NUMERICAL INVESTIGATION OF VENTILATION PROBLEMS USING DISCRETE HEAT AND CONTAMINANT SOURCES

Ph.D. THESIS

by

NEHA GUPTA

DEPARTMENT OF MATHEMATICS
INDIAN INSTITUTE OF TECHNOLOGY ROORKEE
ROORKEE-247667 (INDIA)
APRIL, 2019

NUMERICAL INVESTIGATION OF VENTILATION PROBLEMS USING DISCRETE HEAT AND CONTAMINAT SOURCES

A THESIS

submitted in partial fulfilment of the requirements for the award of the degree

of

DOCTOR OF PHILOSOPHY

in

MATHEMATICS

by

NEHA GUPTA

DEPARTMENT OF MATHEMATICS
INDIAN INSTITUTE OF TECHNOLOGY ROORKEE
ROORKEE-247667 (INDIA)
APRIL, 2019

INDIAN INSTITUTE OF TECHNOLOGY ROORKEE
ROORKEE

CANDIDATE'S DECLARATION

I hereby certify that the work which is being presented in the thesis entitled **"NUMERICAL INVESTIGATION OF VENTILATION PROBLEMS USING DISCRETE HEAT AND CONTAMINANT SOURCES"** in partial fulfilment of the requirements for the award of the degree of **Doctor of Philosophy** and submitted in the Department of Mathematics, Indian Institute of Technology Roorkee, Roorkee is an authentic record of my own work carried out during a period from August, 2014 to April, 2019 under the supervision of Dr. Ameeya Kumar Nayak, Associate Professor, Department of Mathematics, Indian Institute of Technology Roorkee, Roorkee.

The matter presented in this thesis has not been submitted by me for the award of any other degree of this or any other institute.

(NEHA GUPTA)

This is to certify that the above statement made by the candidate is correct to the best of my knowledge.

(Ameeya Kumar Nayak)
Supervisor

The Ph.D. Viva-Voce Examination of **Ms. Neha Gupta,** Research Scholar, has been held on……

Chairperson, SRC

Signature of External Examiner

This is to certify that the student has made all the corrections in the thesis.

Signature of Supervisor

Head of the Department

Dated: ……

Dedicated
to

My Parents

Abstract

This thesis addresses the detailed numerical investigation of double diffusive mixed convection flow within ventilated enclosures equipped with different thermal and solutal boundary conditions. Geometric modulations are included by considering different sizes and locations of inlet port, outlet port, heat sources and contaminant sources. The flow of fluid, heat and contaminants are analyzed by streamlines, isotherms and isoconcentrations for a wide range of flow governing parameters. The trends of average Nusselt number, Sherwood number, entropy generation and cooling efficiency are investigated with the variation of Reynolds number, Richardson number and buoyancy ratio to improve the performance of the ventilated system.

In this thesis, two air distribution forms are studied: one is displacement ventilation and other is mixing ventilation to drive and control the indoor air environment. The mathematical model is formulated based on the pre-assumptions that the fluid is Newtonian, viscous and incompressible and the flow is laminar. A control volume based SIMPLE algorithm is used to solve the flow governing equations, that are represented by a coupled set of non-linear partial differential equations. **Chapter-1** of the thesis includes the basic definitions and various solution algorithms used for fluid flow problems.

Chapter-2 deals with the double diffusive mixed convection flow inside a ventilated enclosure due to the presence of thermosoluted square block at the middle region. The block is at higher temperature and concentration as compared to the inlet cold fluid which is at lower temperature and concentration and is passed through various slots of the left vertical wall and flush-out through the right vertical wall. Effective heat and mass transfer performance is studied by changing the locations of inlet and outlet port with the variation of flow governing parameters which is mostly applicable for building ventilation and cooling of equipments. **Chapter-3** is focused on the numerical simulation of fluid

flow, heat and mass transfer in a ventilated enclosure where a thermo-contaminated square block is placed inside the enclosure. Simulations are performed for different locations and different sizes of the thermo-contaminated block with fixed inlet and outlet port along the vertical walls where coolant air is supplied and contaminated air is flushed out. The heat and contaminant transfer rate along the surface of the block are compared for different block locations with the variation of Richardson number, Reynolds number and buoyancy ratio and found that maximum cooling inside the enclosure is obtained when thermo-contaminated block is placed near the outlet port.

Mixed convection flow in a parallelogrammic shaped ventilated system filled with air-CO_2 mixture with uniform discrete heat and CO_2 contaminant sources is numerically studied in **Chapter-4**. The impact of inclination angle of horizontal walls on average rate of heat transfer and mass transfer, average temperature, entropy generation, Bejan number, cooling efficiency and performance evaluation criterion inside the system is evaluated with respect to the location of inlet port, outlet port and heat sources. **Chapter-5** is focused on maximizing the removal rate of heat and contaminants due to wall heater and a thermosoluted block in a slot-ventilated enclosure. Cold fresh air is infiltrated into the enclosure through an inlet port located along right vertical wall and polluted air is expelled through the chimney shaped outlet port located along the upper wall. The best suited inlet port location along with inclination angle of outlet chimney is determined in terms of maximum heat transfer rate with minimum entropy generation.

Subsequently, a numerical simulation of three-dimensional mixed convection due to thermosolutal gradients in a slot-ventilated enclosure is presented in **Chapter-6** due to discrete heat and contaminant sources under different flow conditions. The numerical simulations are performed for a wide range of flow governing parameters to find the effects of inlet and outlet port locations for achieving acceptable average temperature inside the enclosure to obtain maximum heat and mass transfer rate with minimum entropy generation.

Keywords: Mixed convection; Ventilated enclosure; Finite Volume method; Nusselt number; Sherwood number; average fluid temperature; Cooling efficiency

List of Publications

1. ***Neha Gupta***, A. K. Nayak, "Effects of heat induced pollutants due to thermosolutal exchanger in ventilation system", ***Journal of Thermophysics and Heat Transfer*** *(AIAA)*, July 2017, Volume 32, Issue No. 1, 2018, Pages 172-183, ISSN 0887-8722.

2. ***Neha Gupta***, A. K. Nayak, Sumit Malik, "Conjugate heat and species transport in an air filled ventilated enclosure with a thermo-contaminated block", ***International Journal of Heat and Mass Transfer*** *(Elsevier)*, February 2018, Volume 117, Pages 388-411, ISSN 0017-9310.

3. ***Neha Gupta***, A. K. Nayak, "Performance evaluation of coolant air with buoyancy in a parallelogrammic mixed displacement ventilated system", ***International Journal of Mechanical Sciences*** *(Elsevier)*, December 2018, Volume 149, Pages 38-53, ISSN: 0020-7403.

4. ***Neha Gupta***, A. K. Nayak, "Activity of buoyancy convection and entropy generation in a parallelogrammic shaped mixed displacement ventilated system", ***International Journal of Thermal Sciences*** *(Elsevier)*, March 2019, Volume 137, Pages 86-100, ISSN: 1290-0729.

5. ***Neha Gupta***, A.K. Nayak, "Heat and airborne pollutants removal from a slot-ventilated enclosure due to wall heater and thermosoluted block using a chimney" ***Energy and Buildings*** *(Elsevier)* (Under minor revision).

6. ***Neha Gupta***, A.K. Nayak, "Three-dimensional parametric study of airflow, heat and mass transfer characteristics in a slot-ventilated enclosure", ***International Communications On Heat and Mass Transfer*** (Communicated).

7. K. Venkateshwarlu, A. K. Nayak, Bhupinder Singh, V. K. Katiyar, ***Neha Gupta***, "Thermosolutal Mixed Convection in an Air Filled Ventilated Enclosure With Slot Wise Embedded Heat and Contaminant Sources", ***Journal of Heat Transfer*** *(ASME)*, March 2016, Volume 138, Issue 3, Pages 032501-032501-9, ISSN: 0022-1481.

8. N. Maharana, A. K. Nayak, ***Neha Gupta***, "Generalized higher order Spectral element implementation for reaction-diffusion problems", ***Thermal Science and Engineering Progress*** *(Elsevier)*, September 2017, Volume 3, Pages 150-163, ISSN 2451-9049.

9. ***Neha Gupta***, A.K. Nayak, "Performance of Mixed air distribution in a displacement ventilation system", ***International Journal of Heat and Mass Transfer*** (Communicated).

10. ***N. Gupta***, A Nayak, "Fluid Flow, Heat and Contaminant Transport in a Ventilated Enclosure due to the Presence of Thermosolutal Body" ***ASME 2017 Fluids Engineering Division Summer Meeting***, July 2017, Pages V01CT24A002-V01CT24A002, American Society of Mechanical Engineers.

11. ***Neha Gupta***, A. K. Nayak, "Transient Mixed Convection Flow in Ventilated Parallelogram Enclosure with Partially Active Thermal Zones" ***24th National and 2nd International ISHMT-ASTFE Heat and mass transfer conference (IHMTC-2017)***, December 2017, Pages 2177-2185, ISHMT Digital Library (Begel House Inc.).

12. ***Neha Gupta***, A. K. Nayak, "Numerical study on Transient mixed Convection and entropy generation in a skewed ventilated enclosure" ***3rd Thermal and Fluids Engineering Conference (TFEC)***, January 2018, Pages 1285-1295, ASTFE Digital Library (Begel House Inc.).

Acknowledgements

Through this Thanksgiving note, in the first place, I express my deepest gratitude and heartiest thanks to Almighty God and His blessings for writing and completing this thesis. I am very grateful to my supervisor, Dr. Ameeya Kumar Nayak, Associate Professor, Department of Mathematics, Indian Institute of Technology Roorkee, India who gave me this golden opportunity to pursue higher studies under his guidance. His thoughtful and pertinent skills have taught me a lot not only in Ph.D. program but also in the dire circumstances of my life. No words are enough to express my sincere thanks to my supervisor for his valuable guidance, encouragement and constant support throughout my research work.

I owe my sincere gratitude to Prof. N. Sukavanam, Head of the Department, Prof. V. K. Katiyar and Prof. R. C. Mittal, former heads of the Department of Mathematics, IIT Roorkee, for providing all the necessary facilities and constant support for carry out my doctoral research work. My sincerely thanks to research committee members Dr. Arup Kumar Das, Department of Mechanical Engineering, Prof. Rama Bhargava and Prof. N. Sukavanam, Department of Mathematics for their critic views that helped me in improving the quality of my research work. I am also indebted to the Department of Mathematics, Indian Institute of Technology Roorkee and all its faculty and staff members for their academic support and encouragement at all levels. I gratefully acknowledge the financial support (Grant No. OH-31-23-200-428) given by Ministry of Human Resource Development (MHRD), Government of India.

I am heartily thankful to Prof. S.C. Agrawal, Prof. Jaimala and Dr. Reema Singh, Department of Mathematics, CCS University, Meerut for giving encouragement and motivation to do research in Mathematics. The inspiration, support and cooperation that I

have received from my colleagues and friends are beyond the scope of my acknowledgement. I would like to acknowledge my sincere thanks to my research group Dr. Sumit Malik, Abhishek, Ainul, Bharat, Minakshmi and Lokesh for providing me a helping hand whenever I asked for. Last, but not the least, my candid thanks to my friends Dr. Sumita, Dr. Alka, Dr. Trapti, Nidhi, Renuka, Rachna, Preetika, Baljinder, Sarita, Savita, Astha and Khushboo for their whole-hearted cooperation and support during this memorable stay at IIT Roorkee.

I wish to put on records that whatever I have achieved in my life is due to the blessings and unconditional support of my father Sh. Desh Bandhu Gupta and my mother Smt. Ramita Gupta. I have no words to express my affectionate thanks to my parents, siblings Dr. Abhinav and Ruchita, sister-in-law Vinti and brother-in-law Amit for having faith in me with patience, kindness and unconditional love. Their encouragement has always given me the strength to move ahead in my life. This thesis could not have been possible without their care and support.

At last, I am thankful to everyone who has helped me directly or indirectly for the completion of this work.

Roorkee (Neha Gupta)

April 15, 2019

Table of Contents

List of Tables

List of Figures

Nomenclature

Notation	Description
A	aspect ratio
Br	buoyancy ratio, $Br = \frac{\beta_C(C_h - C_0)}{\beta_T(T_h - T_0)}$
C^*	species concentration, (kg/m^3)
C	dimensionless species concentration, $C = \frac{(C^* - C_0)}{(C_h - C_0)}$
C_h	concentration of the contaminated source, (kg/m^3)
C_i	concentration at the inlet, (kg/m^3)
C_0	reference concentration, (kg/m^3)
D	mass diffusivity, (m^2/s)
k	thermal conductivity, (W/mK)
g	gravitational acceleration (m/s^2)
Gr	Grashof Number, $Gr = \frac{g\beta_T(T_h - T_0)L^3}{\nu^2}$
L	length of horizontal walls of the ventilated enclosure, (m)
H	length of vertical walls of the ventilated enclosure, (m)
L_x	dimensionless distance between y-axis and the center of block
L_y	dimensionless distance between x-axis and the center of block
p^*	pressure (Nm^{-2})
p	dimensionless pressure

Nu_{avg}	average Nusselt number
Pr	Prandtl number, $Pr = \frac{\nu}{\alpha}$
Re	Reynolds number, $Re = \frac{u_i L}{\nu}$
Ri	Richardson number, $Ri = \frac{Gr}{Re^2}$
Sc	Schmidt number, $Sc = \frac{\nu}{D}$
Sh_{avg}	average Sherwood number
S^*_{gen}	entropy generation (W/m^3K)
S_{gen}	dimensionless entropy generation, $S_{gen} = S^*_{gen} \cdot \frac{L^2 T_0^2}{k(T_h - T_0)^2}$
S_T	entropy generation due to thermal diffusion
S_ψ	entropy generation due to fluid friction
S_C	entropy generation due to species diffusion
S_{avg}	average entropy generation
t^*	time, (sec)
t	dimensionless time, $t = \frac{t^* u_i}{L}$
T^*	temperature, (K)
T	dimensionless temperature, $T = \frac{(T^* - T_0)}{(T_h - T_0)}$
T_h	temperature of the heated source, (K)
T_i	temperature of the inlet fluid, (K)
T_0	reference temperature of the fluid, (K)
u_i	velocity of the inlet fluid, (m/s)
u^*, v^*, w^*	components of velocity in x^*, y^* and z^* directions, (m/s)
u, v, w	dimensionless velocity components in x y and z directions
$\overrightarrow{\mathbf{V}}^*$	dimensional velocity vector, (u^*, v^*, w^*)
$\overrightarrow{\mathbf{V}}$	dimensionless velocity vector, (u, v, w)
x^*, y^*, z^*	cartesian coordinates, (m)
x, y, z	dimensionless Cartesian coordinates

Greek letters

α	thermal diffusivity, $(k/(\rho C_p))$ (m^2/s)
β	inclination angle of horizontal walls with x-axis
β_T	thermal expansion coefficient, (K^{-1})
β_C	solutal expansion coefficient, (m^3/kg)
δ	inclination angle of chimney walls with x-axis
μ	dynamic viscosity, (Pa s)
ν	kinematic viscosity, (m^2/s)
ξ, η	transformed co-ordinates in x, y direction
ψ	stream function
ρ	density, (kg/m^3)

Chapter 1

Introduction

1.1 Motivation

In recent decades, public concern about unfavorable health effects of indoor air is a major concern in which occupants of residential and commercial buildings reported health problems analogous with their buildings. Poor indoor environment is the major effectiveness factor that can be improved by upgrading the building structures which may provide a better performance particularly operation and maintenance facilities. Therefore, the most fundamental requirement in the building design is to maintain of good indoor environment conditions which are important for health, thermal comfort and productivity of occupants. Thermal discomfort and higher concentration of carbon dioxide increase the sick building syndrome and decreases the work performance and health of occupants. Sick building syndrome can be identified by symptoms like headache, lethargy, feeling of suffocation, burning eye sensation, skin irritation, nose and throat infection that occur with the occupants of building.

Ventilation is used to provide thermal comfort and good indoor air quality by introducing enough amount of cold fresh air into the space to replenish oxygen, remove excessive heat and eliminating indoor pollutants like moisture, allergens, volatile organic compounds and biological agents. If the outside weather is favorable then indoor air quality can be improved by using natural ventilation with open windows and doors. But for warm and humid weather, external mechanical systems have to be used to ventilate the space. In case of large buildings, acceptable indoor air quality is achieved by using mixed mode ventilation which involves natural ventilation supplemented with mechanical

systems.

In general, there are two trendy air distribution forms that are used to recirculate the indoor air environment; one is displacement ventilation (DV) and other is mixing ventilation (MV). In displacement ventilation, fresh outdoor air is supplied at low velocity from air diffusers located near floor level and exhausted air is extracted near the ceiling by buoyancy forces. Whereas, mixing ventilation is the method in which fresh air is supplied from ceiling level with high velocity to achieve an uniform distribution of temperature and concentration in the space [105]. Mixing ventilation might lead to discomfort in workplaces and can be ineffective in pollutant removal due to high velocity. Whereas, displacement ventilation might lead to excessive air stratification and feet draft discomfort. To overcome these drawbacks, there is a need to analyze different air distribution forms regarding to the location of supplied air and exhausted air at different velocities to obtain a highly desirable ventilation system.

In industrial processes, the performance and work efficiency of mechanical/electrical equipments are highly dependent on their thermal management. The process of miniaturization of electronic gadgets and equipments result higher heat fluxes which needs more efficient cooling strategies [62]. Electronic devices like computers, laptops and their internal components often generate heat during operation that may adversely affect the performance, because some internal components may only function properly below the specified temperature. In order to control the temperature of electronic devices, usually a fan is attached at the inlet or outlet of the cabinet at bottom side that expels heat from the device to control its temperature. The location of heat generating elements also optimizes the performance of electrical devices.

The energy efficiency of a system and its heat and mass transfer characteristics can be improved by minimizing the loss of energy inside the system. The main factors for the loss of available energy inside the system includes the irreversible processes due to thermal gradient, fluid friction, solutal gradient and coupling between heat and mass transfer which are directly proportional to the entropy generation. Therefore, the basic understanding of entropy generation is required for energy efficiency of the thermodynamic system. The entropy generation is based on second law of thermodynamics which states that the entropy in any cyclic process is always non-decreasing. Therefore, the system

should be designed in such a way that it generates minimum entropy to obtain the highly efficient system.

1.2 Fluid flow

Fluid is a substance that continuously deforms after applying some external force and the motion of fluid subjected to stresses or external forces is defined as fluid flow. Both gases and liquids are considered to be in fluids. The flow of water in a river, flow of air over bird's wing, flow of blood in arteries are few examples of fluid flow. The analysis of fluid flow pattern provides some useful information regarding the direction of flow, outputs of any process and mixing of fluids in some industrial process. The velocity of fluid, its direction and presence of some obstacle are the main factors that affect the fluid flow pattern in a domain. In any industrial process, the stable performance of equipments is achieved by the balanced combination of fluid velocity, temperature and location of obstacle. The most important application of fluid flow, heat and mass transfer in our daily life is maintaining the indoor air comfort by using air-conditioner or fan inside the room. The energy consumption in air-conditioner is highly dependent on the location of air-conditioner, exhaust fan, heat generation elements and number of occupants.

1.3 Heat and mass transfer

The transfer of heat in the form of energy from higher temperature region to lower temperature region is known as heat transfer. The heat transfer is classified in three modes: conduction, convection and radiation. Conduction is the mode of heat transfer through molecules when they are in contact with each other. For example; if one end of the metal rod is heated, this heating creates vibration in the molecules due to energy gain, these vibrating molecules transfer their energy to the neighboring molecules, this process occurs throughout the rod and continues till the rod achieves its equilibrium state. Convection is the form of heat transfer through the bulk movement of fluid particles. There are two modes of convective heat transfer: one is natural convection and other is forced convection. Natural convection occurs when fluid moves by buoyancy forces due to the density differences. Natural convection is observed in many real-life situations like in boiling

water, streaming cup of hot coffee, heat transfer from air into the ice and many more. Forced convection refers to the fluid motion that is generated by some external source (such as fan, pump, suction device, etc.) which induces the flow of fluid. Central heating, air conditioning, stream turbines, heat exchangers are few examples of forced convection. The phenomena in which natural convection and forced convection occur at the same time is known as mixed convection. The radiation heat transfer occurs when energy is transferred in the form of electromagnetic waves. A medium is required for heat transfer in conduction and convection processes, whereas any medium is not required in radiation heat transfer. The radiation is elaborated with the examples like transfer of heat from Sun to the Earth's atmosphere through the vacuum of space.

Mass transfer is the process of relative motion of substances (species) in the fluid mixture due to concentration gradients. The species move from higher concentration to lower concentration region. The motion of tea from tea bag into the hot water is the common example of mass transfer. In many industrial or technical processes, mass transfer phenomena occurs simultaneously with the heat transfer processes, for example industrial cooling towers. These cooling towers couple heat transfer with mass transfer by allowing hot water to flow in contact with hotter air and evaporate as it absorbs heat from the air. This form of convection can be visualized in the case of heat and contaminants removal from a ventilated enclosure by using any mechanical device at the inlet or exhaust at the outlet of the enclosure.

Nowadays, a study of mixed convection and heat transfer in enclosures is invariably encountered in many industrial heating or cooling applications including cooling of electronic devices, solar collectors, float glass production, drying technologies, chemical processing equipments, etc. and are of great interest for researchers. There exists a number of flow processes that involves simultaneous effects of heat transfer and mass transfer in practical situations. Such type of flows termed as the double diffusive convection due to simultaneous effect of thermal and concentration gradients [64], [65], [87]. The double diffusive convection flows occur in a wide range of scientific, industrial and technical areas such as oceanography, geology, material processing, biology, astrophysics, chemical processes, etc. [28], [78], [104]. The fluid flow, heat and mass transfer in enclosures is frequently encountered in many industrial applications such as heating and/or cooling of

machines, float glass production, solar collectors etc. [12]. An enormous amount of research is conducted in these fields and substantial efforts in the direction of experimental, theoretical and numerical studies have been made by several researchers ([119, 33, 19]).

1.4 Fundamentals of Fluid Mechanics

Fluid mechanics is a branch of science which deals with the behavior of fluids when they are in state of rest or motion. Fluids are subjected to different forces and different boundary conditions, therefore their behavior depends on these conditions as per their physical and mechanical properties. The characterization and movement of fluid flows are generally described either by using Lagrangian approach or Eulerian approach. In Lagrangian approach, the fluid motion is described by tracking individual fluid particles in terms of their positions and velocities. Whereas, in case of Eulerian approach, a certain control volume is fixed in space through which the fluid flows with the increment of time. Thus, the Eulerian approach for fluid flow refers the description of fluid properties as a function of spatial location and time. These approaches can be imagined with the observation of a flowing water in a river as; if the observer is sitting on a over-bridge of a river and observing the flow of water passing through a fixed point then this represents the Eulerian approach but if the observer is sitting in a boat and observing the flow of water then this represents the Lagrangian approach.

Most of the theories of fluid mechanics are based on the Eulerian approach due to its simplicity from the Lagrangian way of describing the fluid flow. The fluid flow and mechanical properties used in this thesis are based on Eulerian approach. The material derivative is frequently used to describe the basic properties of fluid mechanics in mathematical form. The material derivative represents a link between the Lagrangian and the Eulerian approaches of continuum deformation and formulated as:

$$\underbrace{\frac{D}{Dt}}_{\text{Lagrangian}} = \underbrace{\frac{\partial}{\partial t} + \overrightarrow{\mathbf{V}}^* \cdot \nabla}_{\text{Eularian}}, \tag{1.1}$$

where $\overrightarrow{\mathbf{V}}^*$ is the fluid velocity vector and $\nabla = \hat{\mathbf{i}}\frac{\partial}{\partial x} + \hat{\mathbf{j}}\frac{\partial}{\partial y} + \hat{\mathbf{k}}\frac{\partial}{\partial z}$. In the above equation, D/Dt represents the substantial derivative, whereas $\partial/\partial t$ is the local derivative to measure the time rate of change at a fixed spatial location and $\overrightarrow{\mathbf{V}}^* \cdot \nabla$ is the convective derivative

to measure the time rate of change due to the movement of the fluid element from one location to another in the flow domain.

The physics of fluid mechanics is described by mathematical equations which are based on three fundamental conservation laws namely, conservation of mass, conservation of momentum and conservation of energy. These fundamental laws can be described mathematically as follows:

1.4.1 Conservation of Mass

The continuity equation based on the conservation law of mass states that the net flow rate of mass through a control volume equals to zero, i.e., the time rate of change of mass in the control volume is equal to the difference in cumulative mass inflow and outflow from the control surfaces of the control volume. The differential form of the continuity equation can be written as follows:

$$\frac{\partial \rho}{\partial t^*} + \nabla.(\rho \overrightarrow{\mathbf{V}}^*) = 0, \tag{1.2}$$

where ρ, t^* and $\overrightarrow{\mathbf{V}}^*$ represents fluid density, time and flow velocity vector field respectively. In case of incompressible fluid (i.e. ρ is constant), the continuity equation reduces to

$$\nabla.\overrightarrow{\mathbf{V}}^* = 0. \tag{1.3}$$

In cartesian coordinates, the above equation can be written as:

$$\frac{\partial u^*}{\partial x^*} + \frac{\partial v^*}{\partial y^*} + \frac{\partial w^*}{\partial z^*} = 0, \tag{1.4}$$

where u^*, v^* and w^* denotes the dimensional velocity components in the direction of x^*, y^* and z^* axis respectively. The non-dimensional form of continuity equation can be obtained by using the following dimensionless variables,

$$x = \frac{x^*}{L},\ y = \frac{y^*}{L},\ z = \frac{z^*}{L},\ u = \frac{u^*}{u_i},\ v = \frac{v^*}{u_i},\ w = \frac{w^*}{u_i}, \tag{1.5}$$

where, u_i denotes the characteristic velocity and the non-dimensional form of continuity equation is written by,

$$\frac{\partial u}{\partial x} + \frac{\partial v}{\partial y} + \frac{\partial w}{\partial z} = 0. \tag{1.6}$$

1.4.2 Conservation of Momentum

The conservation of momentum is based on the *Newton's second law of motion*, which states that the time rate of change of momentum of the system is equal to the sum of the external forces acting on the system. The momentum equations was derived in the early 18^{th} century by Claude-Louis Navier [77] and George Gabriel Stokes [114] independently and known as Navier-Stokes equation. Using Reynolds transport theorem, the momentum equation in vector notations can be written as follows:

$$\underbrace{\frac{\partial}{\partial t^*}(\rho\overrightarrow{\mathbf{V}}^*) + \nabla.(\rho\overrightarrow{\mathbf{V}}^*\overrightarrow{\mathbf{V}}^*)}_{\text{Time and Advective acceleration}} = \underbrace{-\nabla p^*}_{\text{Isotropic pressure stress}} + \underbrace{\nabla\cdot\boldsymbol{\tau}}_{\text{Anisotropic viscous stress}}, \tag{1.7}$$

where $\boldsymbol{\tau} = \mu\left[(\nabla\overrightarrow{\mathbf{V}}^*) + (\nabla\overrightarrow{\mathbf{V}}^*)^T - \frac{2}{3}(\nabla\cdot\overrightarrow{\mathbf{V}}^*)\boldsymbol{I}\right]$ is the viscous stress. Using the equation of continuity for an incompressible fluid, the constitutive equation for a Newtonian, viscous, incompressible fluid takes the form

$$\rho\left[\frac{\partial\overrightarrow{\mathbf{V}}^*}{\partial t^*} + (\overrightarrow{\mathbf{V}}^*\cdot\nabla)\overrightarrow{\mathbf{V}}^*\right] = -\nabla p^* + \mu\nabla^2\overrightarrow{\mathbf{V}}^*, \tag{1.8}$$

where p^*, ρ, μ and $\nu(=\mu/\rho)$ denote the pressure, density, viscosity and kinematic viscosity of the fluid, respectively. In cartesian coordinates, the above equation is written as:
u-momentum equation

$$\frac{\partial u^*}{\partial t^*} + u^*\frac{\partial u^*}{\partial x^*} + v^*\frac{\partial u^*}{\partial y^*} + w^*\frac{\partial u^*}{\partial z^*} = -\frac{1}{\rho}\frac{\partial p^*}{\partial x^*} + \nu\left(\frac{\partial^2 u^*}{\partial x^{*^2}} + \frac{\partial^2 u^*}{\partial y^{*^2}} + \frac{\partial^2 u^*}{\partial z^{*^2}}\right), \tag{1.9}$$

v-momentum equation

$$\frac{\partial v^*}{\partial t^*}+u^*\frac{\partial v^*}{\partial x^*}+v^*\frac{\partial v^*}{\partial y^*}+w^*\frac{\partial v^*}{\partial z^*} = -\frac{1}{\rho}\frac{\partial p^*}{\partial y^*}+\nu\left(\frac{\partial^2 v^*}{\partial x^{*^2}}+\frac{\partial^2 v^*}{\partial y^{*^2}}+\frac{\partial^2 v^*}{\partial z^{*^2}}\right)+g\beta_T(T^*-T_0)+g\beta_C(C^*-C_0), \tag{1.10}$$

and w-momentum equation

$$\frac{\partial w^*}{\partial t^*} + u^*\frac{\partial w^*}{\partial x^*} + v^*\frac{\partial w^*}{\partial y^*} + w^*\frac{\partial w^*}{\partial z^*} = -\frac{1}{\rho}\frac{\partial p^*}{\partial z^*} + \nu\left(\frac{\partial^2 w^*}{\partial x^{*^2}} + \frac{\partial^2 w^*}{\partial y^{*^2}} + \frac{\partial^2 w^*}{\partial z^{*^2}}\right). \tag{1.11}$$

The non-dimensional form of the above mentioned governing equations can be obtained by using the variables defined in eq. (1.5) and

$$p = \frac{p^*}{\rho u_i^2}; \quad T = \frac{(T^*-T_0)}{(T_h-T_0)}; \text{ and } C = \frac{(C^*-C_0)}{(C_h-C_0)}, \tag{1.12}$$

as, u-momentum equation

$$\frac{\partial u}{\partial t}+u\frac{\partial u}{\partial x}+v\frac{\partial u}{\partial y}+w\frac{\partial u}{\partial z}=-\frac{\partial p}{\partial x}+\frac{1}{Re}\left(\frac{\partial^2 u}{\partial x^2}+\frac{\partial^2 u}{\partial y^2}+\frac{\partial^2 u}{\partial z^2}\right), \tag{1.13}$$

v-momentum equation

$$\frac{\partial v}{\partial t}+u\frac{\partial v}{\partial x}+v\frac{\partial v}{\partial y}+w\frac{\partial v}{\partial z}=-\frac{\partial p}{\partial y}+\frac{1}{Re}\left(\frac{\partial^2 v}{\partial x^2}+\frac{\partial^2 v}{\partial y^2}+\frac{\partial^2 v}{\partial z^2}\right)+Ri(T+Br.C), \tag{1.14}$$

and w-momentum equation

$$\frac{\partial w}{\partial t}+u\frac{\partial w}{\partial x}+v\frac{\partial w}{\partial y}+w\frac{\partial w}{\partial z}=-\frac{\partial p}{\partial z}+\frac{1}{Re}\left(\frac{\partial^2 w}{\partial x^2}+\frac{\partial^2 w}{\partial y^2}+\frac{\partial^2 w}{\partial z^2}\right), \tag{1.15}$$

where, $Re=\frac{u_i L}{\nu}$, $Gr=\frac{g\beta_T(T_h-T_0)L^3}{\nu^2}$, $Ri=\frac{Gr}{Re^2}$ and $Br=\frac{\beta_C(C_h-C_0)}{\beta_T(T_h-T_0)}$ are the Reynolds number, Grashof number, Richardson number and buoyancy ratio, respectively.

1.4.3 Conservation of Energy

The equation of conservation of energy is based on the first law of thermodynamics, which states that the energy can neither be created nor be destroyed. If, the quantity dQ (heat) is added with the volume ΔV during time Δt and resulting an increment in internal energy dE_T to perform the work done dW, then according to the first law of thermodynamics:

$$dQ=dE_T+dW \quad \text{or} \quad \frac{dQ}{dt}=\frac{dE_T}{dt}+\frac{dW}{dt}. \tag{1.16}$$

In other words

$$\begin{bmatrix} Rate\ \ of \\ heat\ \ transfer \\ into\ \ the\ \ system \end{bmatrix} = \begin{bmatrix} Rate\ \ of \\ increase\ \ of \\ internal\ \ energy \\ of\ \ the\ \ system \end{bmatrix} + \begin{bmatrix} Rate\ \ of \\ work\ \ done \\ by\ \ surface\ \ force \end{bmatrix}$$

Therefore, the energy equation for viscous incompressible fluid can be written as:

$$\frac{\partial T^*}{\partial t^*}+u^*\frac{\partial T^*}{\partial x^*}+v^*\frac{\partial T^*}{\partial y^*}+w^*\frac{\partial T^*}{\partial z^*}=\alpha\left(\frac{\partial^2 T^*}{\partial x^{*^2}}+\frac{\partial^2 T^*}{\partial y^{*^2}}+\frac{\partial^2 T^*}{\partial z^{*^2}}\right)+\phi, \tag{1.17}$$

where, ϕ is the dissipation function given by

$$\phi=2\frac{\mu}{\rho C_p}\left[\left(\frac{\partial u^*}{\partial x^*}\right)^2+\left(\frac{\partial v^*}{\partial y^*}\right)^2+\left(\frac{\partial w^*}{\partial z^*}\right)^2\right]+\frac{\mu}{\rho C_p}\left[\left(\frac{\partial u^*}{\partial y^*}+\frac{\partial v^*}{\partial x^*}\right)^2+\left(\frac{\partial u^*}{\partial z^*}+\frac{\partial w^*}{\partial x^*}\right)^2+\left(\frac{\partial v^*}{\partial z^*}+\frac{\partial w^*}{\partial y^*}\right)^2\right].$$

Here T, α and C_p are the temperature, thermal diffusivity and heat capacity at a constant pressure per unit mass, respectively.

Finally, the non-dimensional form of energy equation with negligible viscous dissipation can be expressed as,

$$\frac{\partial T}{\partial t} + u\frac{\partial T}{\partial x} + v\frac{\partial T}{\partial y} + w\frac{\partial T}{\partial z} = \frac{1}{Re.Pr}\left(\frac{\partial^2 T}{\partial x^2} + \frac{\partial^2 T}{\partial y^2} + \frac{\partial^2 T}{\partial z^2}\right), \tag{1.18}$$

where, $Pr = \frac{\nu}{\alpha}$ is the Prandtl number.

1.5 Solution of Navier-Stokes equations

Generally, the Navier-Stokes (N-S) equations provide a complete description of fluid flow problems in different branches of science, engineering and technology. The solution of Navier-stokes equations after implementing various initial and boundary conditions provide the important flow phenomena and their effects. The unsteady compressible Navier-Stokes equations are a mixed set of hyperbolic-parabolic equations, while the unsteady incompressible Navier-Stokes equations can be treated as a mixed set of elliptic-parabolic equations. However, Navier-Stokes equations show hyperbolic characteristics for convection dominated flow. It is very difficult to obtain the exact solution of Navier-stokes equations due to the presence of highly non-linear terms. As a consequence, different numerical techniques are used to solve the Navier-Stokes equations in the compressible and incompressible flow regimes. Practically, all efficient numerical methods for compressible Navier-Stokes equations have employed the unsteady form of the equations, because of the fact that if the unsteady terms are omitted from these equations, then the resulting equations become a mixed set of hyperbolic-elliptic equations which are difficult to solve due to the differences in numerical techniques required for hyperbolic and elliptic type equations.

In numerical approaches, the linear derivative terms are approximated by Taylor series expansion after neglecting the higher order terms, known as truncation error and the non-linear terms are approximated by suitable linearization techniques. Hence, in place of solving the complex differential equations, an equivalent system of difference equations is to be solved. Both explicit and implicit finite-difference or finite-volume schemes are used to solve the compressible Navier-Stokes equations. Existence and uniqueness of

the solution of Navier-Stokes equation are one of the important issues. Also, a proper choice of numerical method for the solution process need to satisfy three basic necessities; consistency, stability and convergence. The numerical scheme is said to be consistent if the truncation error approaches to zero by reducing the mesh size and time step. For the stability of numerical scheme, the error of approximation must be non-increasing from one step to next step of computation. The numerical scheme is said to be be converged when the numerical solution approaches to the true solution of partial differential equation by decreasing the mesh and time step size to zero.

The accuracy of numerical results for the fluid flow problems is highly dependent on the choice of numerical schemes. Generally, the Navier-Stokes equations comprises of four terms namely, the temporal term, convective term, diffusive terms and source term. Each term can be approximated through various schemes depending on the accuracy of the solution. Several upwind methods have been developed to solve the compressible Navier-Stokes equations in conservative law forms such as the MacCormack method, Beam-Warming method, flux vector splitting scheme, total variation diminishing scheme (TVD), etc. A detailed description about various schemes together with their applications and implementation is provided by many authors such as Anderson et al. [3], Fletcher [35], Anderson [4], Ferzigar and Peric [34] and Lomax et al. [61].

1.5.1 Numerical Methods

The governing equations are needed to be discretized in order to obtain the numerical solution of the Navier-Stokes equations. There are three most common methods for discretization of the flow governing equations which are as follows:

- **Finite difference method**,
- **Finite element method**,
- **Finite volume method**

1.5.1.1 Finite Difference Method

The fundamental approach of finite difference method (FDM) is to replace the partial derivatives by equivalent Taylor series approximation. There are explicit and implicit

schemes to approximate derivatives by using finite difference method. The resulting algebraic system of equations are solved by implementing the boundary conditions. One of the main advantages of using FDM compared to other methods is its ease of implementation. But, on the other hand this method has several drawbacks such as, low order accuracy in the derivative evaluation, difficulty in managing with irregular geometries and in implementation of unusual boundary conditions. The detailed description of FDM is discussed in a book by Smith [110]. The finite difference method has been applied by several authors (Sinha and Admau [109], Deresse and Sinha [30], Admau and Sinha [1], etc.) to solve a broad range of differential equations where they have discussed various ways of approximating the derivatives in finite difference form.

1.5.1.2 Finite Element Method

The finite element method (FEM) is a numerical technique which gives approximate solutions to differential equations that model problems arising in physics and engineering. It provides a piecewise approximation to the differential equations Eg., study the joint inversion of seismic and seismoelectric data in heterogeneous system [52]. A variation of variable with the information on grid point is assumed and the solution is approximated by using interpolation functions between the grid points. Since the assumed variables does not satisfy the differential equations in general, hence, a residual is obtained on substituting the assumed variables in the differential equation. The residual is then multiplied with a set of weight functions and an integration is performed over the considered domain. The most commonly used finite element approximations are the least square method and Galerkin method. The most significant characteristics of FEM is the ability to handle the solution domains having irregular geometry. In general, finite element method requires fewer grid points for a given accuracy of solution as compared to finite difference method. FEM is used by Matle and Sundar [70, 69] to study the heat transfer characteristics for the calibration furnace. The main drawback of finite element method is its complex algorithmic approach of solution and it continue to retain a low-order method. A detailed description of finite element method and its applications to the Navier-Stokes equations are discussed in a number of books written by Oden [84], Chung [25], Baker [11] and Fletcher [35].

1.5.1.3 Finite Volume Method

For the study of mixed convection flow, finite volume method (FVM) is one of the most frequently used numerical technique to solve the flow governing equations for mass, momentum and energy. In this method, the computational domain is divided into a number of non-overlapping control volumes in such a way that there is one control volume neighboring each grid point and the governing differential equations are integrated over each control volume. The variables on the control volume interface are estimated by a linear interpolation between the two neighboring cells to either side of the control volume interface. Here we have used the staggered grid arrangement for allocating the variables because of its advantages in considering the influence of the pressure gradients on fluid flow. The detailed formulation of Finite Volume Method along with applications is discussed by Patankar [86], Anderson et al. [3], Fletcher [35] and Versteeg and Malalasekera [118]. Based on finite volume method, several commercial computational fluid dynamics (CFD) softwares are available in the market like, FLUENT, PHOENICS, STAR-CD and FLOW3D. Finite volume method is used by Guta and Sundar [44] to solve the Navier-Stokes-Brinkman system. All the simulations performed in this thesis are based on FVM and hence a more detailed discussion of FVM is presented in the later part of the thesis.

For more clear understanding of finite volume method, let us consider a two-dimensional convection-diffusion equation for a generic variable φ,

$$\frac{\partial \varphi}{\partial t} + \nabla . \overrightarrow{F} = S_{\varphi}, \tag{1.19}$$

where, $\overrightarrow{F}$ denotes the flux vector consisting of convection and diffusion part and S_{φ} denoted the source term. Integrating eq.1.19 over the finite volume around the grid point (i, j) with volume $V_{i,j}$

$$\int_{V_{i,j}} \frac{\partial \varphi}{\partial t} dV + \int_{V_{i,j}} \nabla . \overrightarrow{F} dV = \int_{V_{i,j}} S_{\varphi} dV.$$

On applying Gauss divergence theorem and rewriting the term $\nabla . \overrightarrow{F}$ as fluxes through the sides of control volume $V_{i,j}$, we get,

$$\int_{V_{i,j}} \frac{\partial \varphi}{\partial t} dx dy + \int_{side} (F_e - F_w) dy + \int_{side} (F_n - F_s) dx = \int_{V_{i,j}} S_{\varphi} dx dy,$$

the subscripts $e,\ w,\ n$ and s refers to the east, west, north and south sides of the control volume $V_{i,j}$ respectively. Finally, the integrals are approximated as,

$$\left(\frac{\partial \varphi}{\partial t}\right)_{i,j} \Delta x \Delta y + (F_{i+1/2,j} - F_{i-1/2,j})\Delta y + (F_{i,j+1/2} - F_{i,j-1/2})\Delta x = (S_\varphi)_{i,j}\Delta x \Delta y + \Delta x \Delta y \mathbf{O}(\Delta x^2, \Delta y^2).$$

The unsteady term, the fluxes and the source term are further discretized with finite differences.

1.5.2 Solution algorithm

The solution of Navier-Stokes (N-S) equations may be attained in many ways. The common algorithms used for the solution methods are,

(a) **Explicit algorithm**

(b) **Implicit algorithm**

(c) **Semi-implicit algorithm**

(a) Explicit algorithm

Explicit algorithm calculates the unknown variable at advanced state of time in a very straight forward manner by using the current state of system. In other words, the value of unknown variable at next time level is represented in terms of variable at current time level which is already known. The explicit algorithms are famous and used because of their simplicity and easy implementation process. But, sometimes, to maintain the stability condition, it require very small time steps, which demand a huge number of iterations to find the converged solution, that leads to a significant increase in calculation time.

(b) Implicit algorithm

In implicit algorithm, the unknown variables are represented in terms of known as well as unknown variables and the solution is achieved by solving simultaneous equations. The solution process may require some extra computations as compared to explicit algorithms but the implicit schemes have clear advantage for not being restricted by stability criteria. As a result, it easily handles the time steps and grid sizes used in the solution process, which enables to lower the computation time of solution.

(b) Semi-implicit algorithm

In semi-implicit algorithm, some variables are treated explicitly and some are treated implicitly. Particularly, for unsteady approaches the velocity components are updated to the new time level in a explicit manner while the pressure may be calculated implicitly by solving the pressure Poisson equation using successive over/under relaxation technique.

1.5.3 Pressure Calculation

Solution of incompressible Navier-Stokes equations is complicated due to the lack of independent equations for pressure, whose gradient contributes to each of the momentum equations. In incompressible flow, density is constant and hence not linked to the pressure. Due to which a coupling between pressure and velocity introduces a constraint on the solution of flow field i.e., if the corrected pressure field is applied in the momentum equation, the resulting velocity field should satisfy the continuity equation. The following three approaches are usually adopted to calculate pressure in incompressible flow:

- **Artificial compressibility approach**
- **Pressure poisson approach**
- **Pressure correction approach**

A brief description of these schemes are presented below.

1.5.3.1 Artificial Compressibility Approach

This is one of the earlier proposed technique for solving incompressible Navier-Stokes equations in primitive variable approach due to Chorin [24]. In this method, the continuity equation was modified by adding an artificial compressibility term which vanishes when the steady state solution is reached. The continuity equation then becomes an evaluation equation for pressure. The introduction of compressibility term in incompressible form enables the use of compressible flow solvers which enhances the convergence characteristics of the solution. Peyret and Taylor [88] recommended the staggered grid arrangement and showed that by using explicit time differencing pseudo-transient artificial compressibility construction can be interpreted as an iterative procedure for the solution of discrete Poisson equation for the pressure.

1.5.3.2 Pressure Poisson Approach

The most common way to combine the continuity and momentum equations is by taking the divergence of the momentum equations. For the incompressible fluid with constant viscosity, the viscous and unsteady terms disappear and by the virtue of continuity equation, the equation is obtained in the following form:

$$\frac{\partial}{\partial x_i}\left(\frac{\partial p}{\partial x_i}\right) = -\frac{\partial}{\partial x_i}\left(\frac{\partial}{\partial x_j}(\rho u_i u_j)\right). \tag{1.20}$$

The above equation for pressure can be solved by using any numerical method for elliptic equation. This type of pressure equation is used to calculate the pressure for both explicit and implicit type solution techniques. To maintain consistency among the approximations used, it is best to derive the equation for the pressure from the discretized momentum and continuity equations rather than by approximating the Poisson equation.

1.5.3.3 Pressure Correction Approach

A number of numerical methods have been developed based on the pressure correction approach out of which SOLA, SIMPLE and PISO are worth mentioning. The method known as SOLA (SOLution Algorithm) is developed by Hirt et al. [46] in which a combined form of central and second order upwinding formulation is used for the discretization of convective terms. The method known as PISO (Pressure-Implicit with Splitting of Operators) is developed by Issa [50] in which the initial velocity field is calculated from momentum equation by using an assumed pressure field and then the calculated velocity is used to compute the new pressure field using the pressure equation. Finally, pressure is used for the correction of the velocity field to provide a second correction for both pressure and velocity fields.

SIMPLE (Semi-Implicit Method for Pressure-Linked Equations) algorithm was introduced by Patankar and Spalding [86] which is based on finite volume discretization using staggered grid arrangement. SIMPLE algorithm is a guess-and-correct iterative procedure for the calculation of pressure to provide the solution for discretized equations. In this method, a pressure equation is derived by using continuity equation together with momentum equations. In numerical computations, a pressure field is guessed initially which is used to obtain the velocity fields after solving the momentum equations,

which may not satisfy the continuity equation. Hence, the pressure and velocity fields are corrected so as to satisfy the continuity equation. A brief discussion about SIMPLE algorithm is provided in the next section.

1.6 SIMPLE algorithm

The acronym, SIMPLE, stands for Semi-Implicit Method for Pressure Linked Equations which is developed by Patankar and Spalding [86] in 1972. The main advantage of SIMPLE algorithm lies in its iterative approach, which is used to solve the whole set of discretized equations. The absence of a separate equation for pressure field is the main difficulty in finding the solution of Navier-Stokes equation, which is tackled by introducing the pressure Poisson equation via continuity equation. Another advantage of SIMPLE method is that it can be applicable for both incompressible and compressible flow problems. In compressible flows, the pressure can be obtained from the density and temperature by using the equation of state where density is regarded as dependent variable of continuity equation as discussed in Versteeg and Malalasekera [118].

This thesis deals with incompressible flow problems, i.e., the density is constant with respect to pressure. There exist a coupling between the pressure and velocity fields which introduces a variation on the solution of flow field. If the correct pressure field is provided in the momentum equations, the resulting velocity field satisfies the continuity equation, else some correction is sought in the values of pressure as well as velocity values.

Implementation of SIMPLE Algorithm for incompressible fluid flow:
The governing equations for a two-dimensional incompressible laminar fluid flow problem in their primitive variables are given by,

$$\frac{\partial u}{\partial x} + \frac{\partial v}{\partial y} = 0, \tag{1.21}$$

$$\frac{\partial u}{\partial t} + \frac{\partial u^2}{\partial x} + \frac{\partial uv}{\partial y} = -\frac{\partial p}{\partial x} + \frac{1}{Re}\left(\frac{\partial^2 u}{\partial x^2} + \frac{\partial^2 u}{\partial y^2}\right), \tag{1.22}$$

$$\frac{\partial v}{\partial t} + \frac{\partial uv}{\partial x} + \frac{\partial v^2}{\partial y} = -\frac{\partial p}{\partial y} + \frac{1}{Re}\left(\frac{\partial^2 v}{\partial x^2} + \frac{\partial^2 v}{\partial y^2}\right). \tag{1.23}$$

Eqs. (1.22) and (1.23), consists of unsteady and convective terms on the left hand side of equation, and the pressure gradient and diffusion term on the right hand side of the equation. The Reynolds number, Re, represents the ratio between inertial forces to viscous forces ([27, 97]).

Discretization process

The very first step in the solution process of above mentioned flow governing equations is the discretization of these equations. Finite volume method is applied to obtain the numerical solution of these equations. In finite volume methodology, the continuity and momentum equations are integrated over the control volumes on a uniform staggered grid (shown in Fig. 1.1). All the scalar variables (p in present case) are stored in the cell center and the velocity components are stored at the cell faces. In particular, the u-velocity components, represented by horizontal arrows ($\rightarrow$), stored at east and west cell faces and the v-velocity, represented by vertical arrows ($\uparrow$), stored at north and south cell faces. Now, integrating the continuity equation [eq. (1.21)] over the $(i,j)^{th}$ scalar control

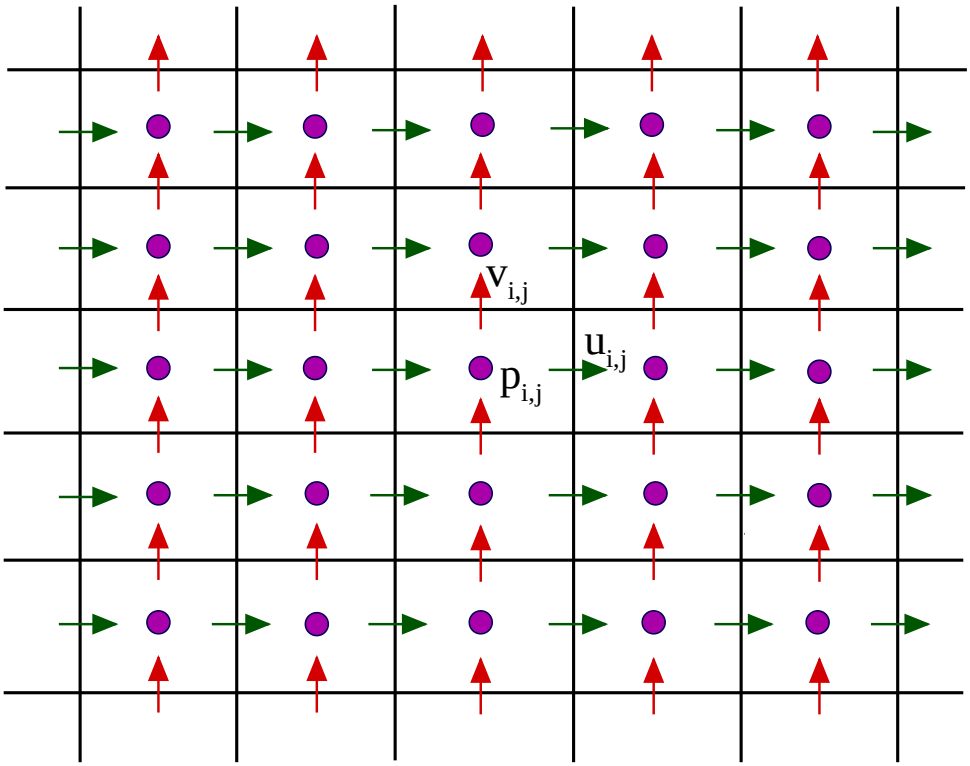

Figure 1.1: Staggered grid arrangement for scalar and vector components.

volume as shown in Fig. 1.2 at $(n+1)^{th}$ time level, we have,

$$(u_{i,j}^{n+1} - u_{i-1,j}^{n+1})\Delta y + (v_{i,j}^{n+1} - v_{i,j-1}^{n+1})\Delta x = 0. \tag{1.24}$$

On integrating the x-momentum equation [eq. (1.22)] at $(n+1)^{th}$ time step over the $(i,j)^{th}$ control volume for u as shown in Fig. 1.3, the discretized equation is obtained as,

$$a_i^u u_{i-1,j}^{n+1} + b_i^u u_{i,j}^{n+1} + c_i^u u_{i+1,j}^{n+1} = d_i^u - \left(p_{i+1,j}^{n+1} - p_{i,j}^{n+1}\right)\Delta y \tag{1.25}$$

Similarly, the integration of y-momentum equation [eq. (1.23)] over $(i,j)^{th}$ control volume for v shown in Fig. 1.4 at $(n+1)^{th}$ time step yields the following algebraic equation,

$$a_i^v v_{i-1,j}^{n+1} + b_i^v v_{i,j}^{n+1} + c_i^v v_{i+1,j}^{n+1} = d_i^v - \left(p_{i,j+1}^{n+1} - p_{i,j}^{n+1}\right)\Delta x \tag{1.26}$$

The aim of SIMPLE algorithm is to establish the pressure link between the continuity and momentum equations by transforming the discretized continuity equation (eq. 1.24) into a pressure Poisson's equation. This pressure poisson equation implements a divergence free velocity field.

SIMPLE is an iterative method which calculates the solution at a next time level using the values at a previous time level. At each control volume, pressure $p_{i,j}$ is unknown at the initial stage. To get a solution for eq. 1.25 and eq. 1.26, a pressure field $p_{i,j}^*$ is guessed. Corresponding to this guessed pressure field $p_{i,j}^*$, the velocity field $(u_{i,j}^*, v_{i,j}^*)$ is determined after solving these discretized momentum equations. Since $u_{i,j}^*$ and $v_{i,j}^*$ satisfy

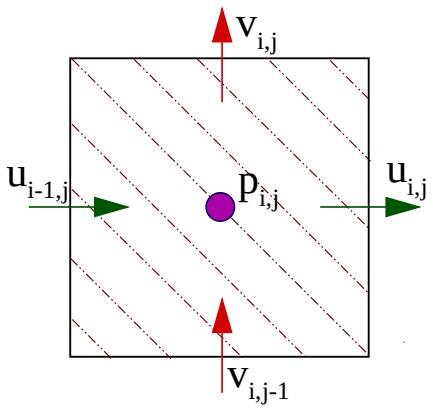

Figure 1.2: Scalar control volume

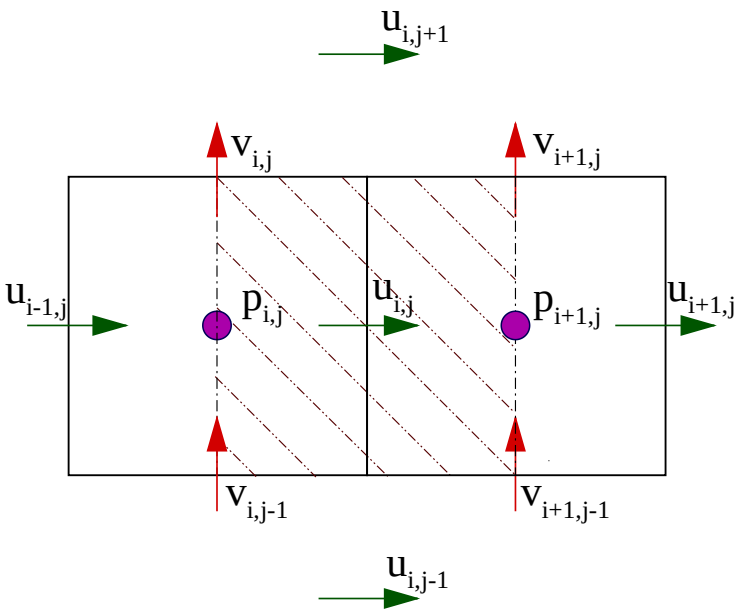

Figure 1.3: u-control volume

the eq. 1.25 and eq. 1.26 respectively, then

$$a_i^u u_{i-1,j}^* + b_i^u u_{i,j}^* + c_i^u u_{i+1,j}^* = d_i^u - \left(p_{i+1,j}^* - p_{i,j}^*\right)\Delta y \tag{1.27}$$

and

$$a_i^v v_{i-1,j}^* + b_i^v v_{i,j}^* + c_i^v v_{i+1,j}^* = d_i^v - \left(p_{i,j+1}^* - p_{i,j}^*\right)\Delta x, \tag{1.28}$$

but, the velocity field $(u_{i,j}^*, v_{i,j}^*)$ may not satisfy the continuity equation [eq. 1.24]. Therefore, a correction is sought in the velocity field and pressure field so as to satisfy the continuity equation [eq. 1.24]. Let $p_{i,j}^c$ be the pressure correction at $(i,j)^{th}$ cell and $(u_{i,j}^c, v_{i,j}^c)$ be the corresponding correction in velocity field. Thus the updated pressure and velocity field can be expressed as:

$$p_{i,j}^{n+1} = p_{i,j}^* + p_{i,j}^c, \tag{1.29}$$

$$u_{i,j}^{n+1} = u_{i,j}^* + u_{i,j}^c, \tag{1.30}$$

$$v_{i,j}^{n+1} = v_{i,j}^* + v_{i,j}^c, \tag{1.31}$$

where, the corrected velocity fields $u_{i,j}^{n+1}$ and $v_{i,j}^{n+1}$ satisfies the continuity equation [eq. 1.24]. Subtracting eq. 1.27 from eq. 1.25 and eq. 1.28 from eq. 1.26, a relation between

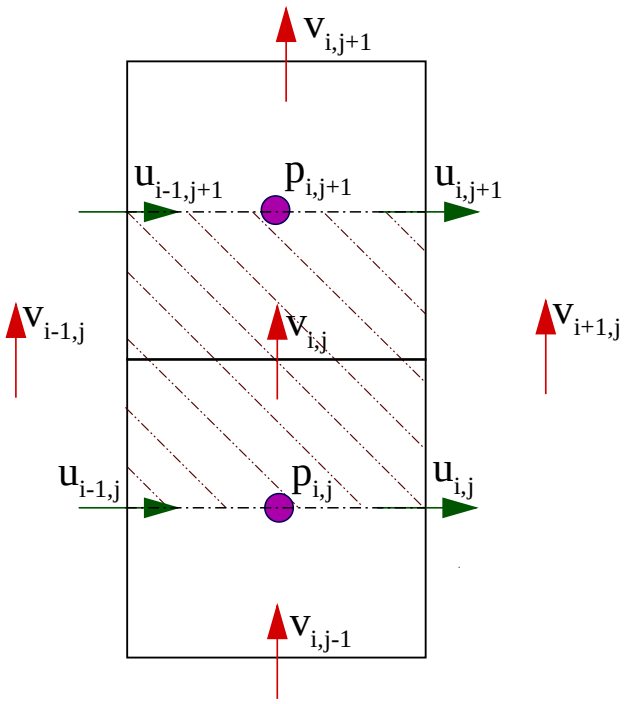

Figure 1.4: v-control volume

pressure correction and velocity correction is obtained as:

$$a_i^u u_{i-1,j}^c + b_i^u u_{i,j}^c + c_i^u u_{i+1,j}^c = -\big(p_{i+1,j}^c - p_{i,j}^c\big)\Delta y, \tag{1.32}$$

$$a_i^v v_{i-1,j}^c + b_i^v v_{i,j}^c + c_i^v v_{i+1,j}^c = -\big(p_{i,j+1}^c - p_{i,j}^c\big)\Delta x. \tag{1.33}$$

Ignoring, the neighboring small correction terms $u_{i-1,j}^c$, $u_{i+1,j}^c$ and $v_{i-1,j}^c$, $v_{i+1,j}^c$, the correction of velocity components can be expressed as

$$u_{i,j}^c = -\left(\frac{\Delta t}{\Delta x}\right)\big(p_{i+1,j}^c - p_{i,j}^c\big), \tag{1.34}$$

$$v_{i,j}^c = -\left(\frac{\Delta t}{\Delta y}\right)\big(p_{i,j+1}^c - p_{i,j}^c\big). \tag{1.35}$$

The derived corrected form of pressure term given in eq. (1.29) sometimes lead to a divergence in the solution. Hence, for the convergence of solution, the pressure field is under-relaxed as:

$$p_{i,j}^{n+1} = p_{i,j}^* + \alpha_p p_{i,j}^c,$$

where α_p is the under-relaxation factor. The relaxation factor is taken between 0 and 1, so that guessed pressure field is added with a fraction of the corrected pressure field

p^c, in order to improve the iteration process to carry forward. Similarly, the velocity components $u_{i,j}^{n+1}$ and $v_{i,j}^{n+1}$ are under-relaxed in the following manner:

$$u_{i,j}^{n+1} = u_{i,j}^{*} - \alpha_u \left(\frac{\Delta t}{\Delta x}\right)\left(p_{i+1,j}^{c} - p_{i,j}^{c}\right), \tag{1.36}$$

$$v_{i,j}^{n+1} = v_{i,j}^{*} - \alpha_v \left(\frac{\Delta t}{\Delta y}\right)\left(p_{i,j+1}^{c} - p_{i,j}^{c}\right). \tag{1.37}$$

Substituting the above corrected velocity field $(u_{i,j}, v_{i,j})$ into the discretized continuity equation (Eq. 1.24), the following Poisson's equation for pressure correction is obtained:

$$\left[2\alpha_u\left(\frac{\Delta t \Delta y}{\Delta x}\right) + 2\alpha_v\left(\frac{\Delta t \Delta x}{\Delta y}\right)\right] p_{i,j}^{c} = -div^{*} + \alpha_u\left(\frac{\Delta t \Delta y}{\Delta x}\right)\left(p_{i-1,j}^{c} + p_{i+1,j}^{c}\right) + \alpha_v\left(\frac{\Delta t \Delta x}{\Delta y}\right)\left(p_{i,j-1}^{c} + p_{i,j+1}^{c}\right) \tag{1.38}$$

where

$$div^{*} = \left(u_{i,j}^{*} - u_{i-1,j}^{*}\right)\Delta y + \left(v_{i,j}^{*} - v_{i,j-1}^{*}\right)\Delta x.$$

Eq. 1.38 can be considered as the discretized form of a Poisson equation, which is referred as Pressure Poisson equation and solved using Gauss-Seidel iterative method. The SIMPLE algorithm contains three relaxation parameters α_p, α_u and α_v. For the problems under consideration in this thesis, a faster convergence is observed for $\alpha_p = 0.8$ or 0.975 and $\alpha_u = \alpha_v = \frac{2}{3}$. The flow chart for SIMPLE algorithm is presented in Fig. 1.5.

SIMPLE algorithm is also extended to compressible two-phase reactive flows (e.g., Steam methane reforming (SMR) and sorption-enhanced steam methane reforming (SE-SMR) processes operated in bubbling fluidized bed reactors by Solsvik et al. [111, 112, 113]). SIMPLE algorithm is one of the most popular algorithm for the solution of incompressible flow problems using simpler grids, but it suffers with a limitation of using the relaxation parameter to overcome the divergence of pressure correction equation. SIMPLE method is modified by several authors to achieve the faster convergence rate. Some revised form of SIMPLE algorithm are known as SIMPLER, SIMPLEC and SIMPLEV. These improved algorithms converges more rapidly than the SIMPLE algorithm but they are more expensive as compared to the SIMPLE algorithm.

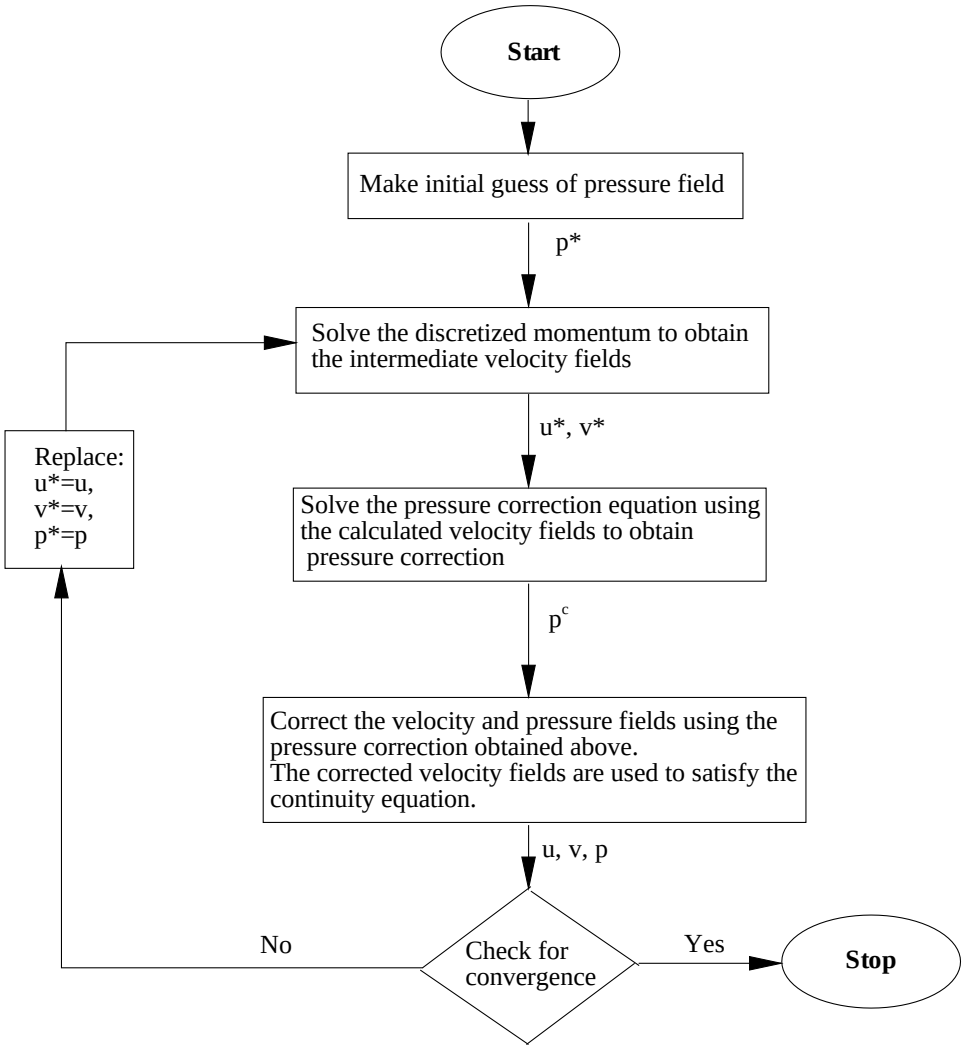

Figure 1.5: Flow chart of SIMPLE algorithm

1.7 Thesis overview

This thesis consists an introductory chapter (Chapter-1) with five main chapters and three appendices. In the introduction section of each chapter, the description of the problem along with brief literature survey, an outline of the motivation and applicability of the problem are addressed. The mathematical description is then presented followed by the detailed description of numerical techniques used to solve the governing equations. The accuracy of our numerical algorithms are validated by comparing with several existing plots of experimental and numerical data in the literature. The results are discussed with the help of relevant data and plots. At the end of each chapter, we have presented the

concluding remarks of each study.

Chapter-1 deals with the general outlines of Computational fluid dynamics (CFD) for double diffusive mixed convection phenomena and its applications in industrial and engineering fields. The governing equations for fluid flow, heat and mass transfer are described. Different numerical estimations for discretization of convective and diffusive terms of governing equations are carried out. Particular attention has been paid to discussion of Navier-Stokes solver in CFD which is a powerful tool for handling the nonlinear partial differential equations in fluid flow. The basic definitions of flow governing parameters such as Reynolds number, Richardson number, Grashof number, Prandtl number etc. which are used in subsequent chapters are explained.

Chapter-2 is focused on the numerical simulation of fluid flow, heat and mass transfer due to a double diffusive mixed convection in air around a thermally and solutally activated square block inside a ventilated enclosure. The block is at higher temperature and concentration than those of inlet fluid which is at ambient temperature and concentration. The inflow is considered through various slots of left vertical wall and outflow through the right vertical wall. Both experimental and numerical confrontations build up in the positioning of air flow source to establish disparity of the reduced effect on velocity and temperature distribution. The objective of the present study is to characterize the mixed air distribution system due to a heated or coolant exchanger in the core of the enclosure combined with inlet cold fluid. Effective cooling and heat transfer performance is studied by changing the locations of inlet and outlet port with the variation of Richardson number (Ri) which is practically applicable for building ventilation and cooling of equipments.

In **Chapter-3**, the flow visualization, thermal and solutal effects in a ventilated enclosure around a thermo-contaminated square block is numerically modeled. Simulations are performed for different locations and different sizes of the thermo-contaminated block with inlet and outlet port along the vertical walls where coolant air is supplied and contaminated air is flush out. The block is maintained at higher temperature and species concentration compared to the injected cold fluid. The walls are assumed as impermeable

and adiabatic to heat and solute. The heat and species transfer rate along the surface of the block is compared for different values of Richardson number, Reynolds number, buoyancy ratio and block positions. Cooling efficiency inside the enclosure and average fluid temperature is calculated for different physical flow parameters to find the most suitable size and position of the block in order to obtain the maximum heat and mass transfer rate inside the enclosure. It is found that maximum cooling inside the enclosure is obtained when thermo-contaminated block is placed near the outlet port.

In **Chapter-4**, the performance of mixed convection inside a ventilated system filled with air-CO_2 mixture with uniform discrete external heat and CO_2 contaminant sources is studied numerically. The lower and upper walls are inclined at different angles with horizontal axis and their respective length is considered as of the order of vertical walls. A suitable co-ordinate transformation is made to solve the coupled nonlinear governing flow equation using finite volume method based SIMPLE algorithm. Injected cold fresh air through the inlet port is considered at different locations of the left vertical wall and flush out through the outlet port along the right vertical wall. Two dimensional projection analysis is made along the middle plane for flow, temperature and concentration in terms of streamlines, isotherms and isoconcentrations with the variation of Richardson number, Reynolds number and inclination angle with a fixed Prandtl number ($Pr = 0.71$) and Schmidt number ($Sc = 1.14$) to study the CO_2 contaminant effect on the ventilation effective factors such as temperature and indoor air quality. The impact of inclination angle and CO_2 concentration level on average rate of heat transfer and mass transfer, average temperature, entropy generation, Bejan number, cooling efficiency and performance evaluation criterion inside the system is evaluated.

In **Chapter-5**, a numerical simulation is performed for double diffusive mixed convection flow in a slot-ventilated enclosure to optimize the removal rate of heat and contaminants due to wall heater and a thermosoluted object. Cold fresh air is infiltrated through the inlet port located along right vertical wall and polluted air is exited through the chimney shaped outlet port located along the upper wall. Vertical walls of the chimney are

considered to be inclined at different angles with horizontal axis. Two dimensional analysis is made for the flow of fluid, heat and species in terms of streamlines, isotherms and isoconcentrations with the variation of Reynolds number (Re) from 50 to 300, Richardson number (Ri) from 0.0 to 10.0 and inclination angle of chimney with the fixed value of Prandtl number ($Pr = 0.71$) and Schmidt number ($Sc = 1.14$). The impact of inlet port locations, Reynolds number, inclination angle and Richardson number on average Nusselt number and Sherwood number, average entropy generation, Bejan number, average temperature, cooling efficiency, air change per hour and performance evaluation criterion of the enclosure is evaluated.

In **Chapter-6**, three dimensional fluid flow, heat and contaminant transport phenomena in a slot-ventilated enclosure is numerically simulated. Inflow of cold air is assumed through the left vertical wall that creates the mixed convection flow when combined with the buoyancy driven flow. Discrete heat sources and contaminant sources are considered along the right vertical face and bottom face, respectively. Three dimensional flow structures and extensive numerical results are obtained for the flow field and cooling efficiency distribution over a wide range of physical parameters namely, Reynolds number, Richardson number and buoyancy ratio to optimize the heat and contaminants removal rate. The trends of thermal Nusselt number and species Sherwood number are analyzed for the variation of Reynolds number (Re) from 100 to 500, Richardson number (Ri) from 0.0 to 10.0 and buoyancy ratio (Br) from -10.0 to 10.0 with fixed Prandtl number (Pr) and Schmidt number (Sc) as 0.71 and 1.14 respectively. Entropy generation, Bejan number, average temperature, cooling efficiency, air change per hour and performance evaluation criterion inside the system are are compared with the most commonly used parameters to find the impact of inflow and outflow port locations. Interactions between inlet airflow and pressure drop resulting a heat loss through the sides of the component with high streamline curvature effect which can not be predicted in 2D flow pattern.

Finally, the summary of the above chapters and future scopes in this direction are included in **Chapter 7**.

1.8 Aims and objectives of thesis

The aim of this thesis is to investigate various flow conditions in a slot-ventilated enclosure which helps to design an efficient industrial or mechanical system. The efficiency of a systems depends on various factors such as flow speed, flow direction, temperature on the boundaries, location of heat sources and contaminant sources. Hence, the objectives of the present work is to simulate the flow behavior, heat and mass transfer phenomena for different configurations for a wide range of flow governing parameters to find the effects of inlet and outlet port locations for achieving acceptable average temperature inside the enclosure. Another objective is to find the optimum values of flow governing parameters with best possible configuration so as to obtain higher heat transfer rate with minimum entropy generation.

Chapter 2

Effects of heat induced pollutants due to thermosolutal exchanger in ventilation system *

2.1 Introduction

Ventilation is the process of providing thermal comfort/dehumidification inside an enclosure by replacing inside air with outside air into the space and is used to control indoor air quality by diluting and displacing indoor pollutants (excessive moisture, unpleasant smell, heat, dust, smoke, etc.) by injecting fresh air through inlet ports. In a ventilated enclosure, two types of convection effects are observed: one is internal buoyancy-induced natural convection due to the presence of heat and contaminant sources and other is external mechanical-driven forced convection due to the injecting air. The combined effect of these two convection effects resulting the double diffusive mixed convection [29]. Double diffusive mixed convection have wide spread applications in space heating/cooling, pollutant removing, thermal comfort, drying technologies, crystal growth, building energy systems, environmental control of buildings and solar energy storage, etc. [100, 75, 108]. Analysis of convection due to thermal and solutal buoyancy effects subject to thermosoluted exchanger in ventilated enclosure is now an important research topic due to the rapid development of air cooled equipments and air conditioner design system. The literature survey shows a sizable number of numerical studies are made on fluid flow and heat transfer in ventilated systems with/without thermosoluted exchanger.

*The contents of this chapter has been published in *Journal of Thermophysics and Heat Transfer, American Institute of Aeronautics and Astronautics, DOI:10.2514/1.T5210*

A numerical study of steady laminar mixed-convection flow in a ventilated square enclosure with a heat conducting solid circular cylinder placed inside the center of the enclosure is made by Rahman et al. [91] to analyze the flow and heat transfer effects inside the enclosure by changing the diameter of the cylinder. It is found that the heat transfer rate is increasing with the increase of Richardson number value at constant cylinder diameter. Subsequently, Rahman et al. [92] studied the effect of heated square cylinder at different positions of the ventilated enclosure where the right vertical wall is maintained with higher temperature compare to other walls and the walls are considered to be adiabatic. Heated block is placed at various locations of the enclosure to study the fluid flow and heat transfer effect and found that average heat transfer rate is maximum in the forced convection dominated area when the cylinder is located near the top wall along the mid-vertical plane. Mamum et al. [68] studied mixed convection heat transfer effect in a ventilated square cavity having a heated hollow cylinder which is placed at the center of the cavity using finite element based Galerkin method. Inflow opening is considered at the bottom of the left vertical wall, whereas the out flow opening is positioned at the top of the opposite side wall. For largest value of the cylinder diameter, average Nusselt number and average fluid temperature is maximum and fluid temperature is increasing with the increasing value of Richardson number with the increment in diameter. It is also observed that heat and mass transfer are largely influenced due to surface interaction in the natural convection process [107].

A numerical study of two-dimensional mixed convection from a heated square solid cylinder located at the center of a vented cavity filled with air is made by Chamkha et al. [23]. They studied the effect of outlet positions (top, middle and bottom of the right vertical wall) with fixed inlet position (center of the left vertical wall) for a wide range of Richardson number ($0 \leq Ri \leq 10$), Reynolds number ($50 \leq Re \leq 500$), locations and aspect ratios of inner square cylinder ($0.25 \leq L_x \leq 0.75, 0.5 \leq L_y \leq 0.75$) and aspect ratios of 0.1, 0.2, 0.3 and 0.4 on the flow and the thermal fields. The average Nusselt number along the heated surface of the square cylinder is found to be increasing with the increasing values of the Reynolds and Richardson numbers. Senthil et al. [58] conducted a

mathematical study of double-diffusive mixed convection in a lid-driven square enclosure with heated block of varying aspect ratio placed at the bottom wall of the enclosure to analyze the heat and mass transfer effect for various flow parameters such as Richardson number, buoyancy ratio, Reynolds number and aspect ratio. The variation of Richardson number and buoyancy ratio produces a maximum heat transfer rate for a fixed aspect ratio and the mass transfer rate decreases with the increase of aspect ratio.

Xu et al. [121] analyzed the double diffusive mixed convection around a heated circular cylinder in an enclosure with different boundary conditions. The inlet flow is considered at low temperature and concentration and is placed at lower-left wall. Out flow is placed at upper-right wall and the heated cylinder is placed at the center of the enclosure with higher temperature and concentration. The results indicate that the flow and heat transfer rate are independent of Lewis number for low Richardson number with $Br = 1.0$. The heat transfer rate around the heated cylinder decreases with the increase of buoyancy ratio and the mass transfer rate increases with the increase of Lewis number at fixed buoyancy ratio. The work is further extended by considering the cylinder locations (lower, middle and upper) to study the effects of Lewis number, buoyancy ratio and cylinder locations on the double diffusive mixed convection with the variation of Richardson number [122]. They concluded that, when the cylinder location is fixed, the mass transfer is increasing significantly and heat transfer rate is almost independent with the increment of Lewis number. Karimi et al. [55] numerically studied the steady-state mixed convection around two heated circular cylinders of equal diameters in a square ventilated enclosure to analyze the effects of cylinder diameter, Reynolds number and Richardson number on the fluid and heat transfer characteristics. It is found that the natural convection is very weak for low Reynolds number and the average Nusselt number over the surface of cylinders is increasing with the increase in cylinder size.

The convection dominated flow with heat and mass transfer effects in a ventilated enclosure with energy activated sources is still a challenge and there needs a complete discussion to deepen the fundamental understanding of transport mechanism. Most of the literature cited above are considering only heat sources along the boundaries and within

enclosures with the variation of inlet and outlet port to find the maximum cooling efficiencies. The problem dealing with the double diffusive convection with a thermosoluted block subjected to a flux-in of cold air and flux-out of contaminated air has not yet been dealt in the literature. In the present chapter, the impact of inlet and outlet port locations due to thermosoluted block inside the ventilated enclosure is simulated, which is a numerical study related to pollutant removing, thermal comfort and industrial drying technologies. Simulations are done for a wide range of buoyancy ratio, Schmidt number and Richardson number and the detailed results are presented in the form of streamlines, isotherms and isoconcentrations. The average Nusselt number and Sherwood number around the block are calculated to find the effective variation of temperature which provides an insight on cooling efficiency factor of the enclosure.

2.2 Problem definition and Mathematical Modeling

In this chapter, two-dimensional mixed convection flow is considered within a square ventilated enclosure of length L filled with air and is shown in Fig. 2.1. A specified square thermosolutal exchanger of length h is placed at the middle portion of the enclosure with reference temperature T_h and concentration C_h. The fluid of the enclosure is maintained with reference temperature T_0 and concentration C_0 where $T_0 < T_h$ and $C_0 < C_h$. Velocities along the top and bottom walls are assumed to be zero and the fluid is assumed to be at rest with uniform temperature T_0 and concentration C_0. In the first configuration, inlet is considered at the lower-left vertical wall and outlet is at the upper-right vertical wall (configuration-I). In the second configuration, inlet is placed at the upper-left vertical wall and outlet is at lower-right vertical wall (configuration-II). The vertical and horizontal walls are considered as impermeable and adiabatic. An inlet flow is considered with uniform temperature T_i and uniform velocity u_i. The outlet flow is assumed to have zero diffusion flux for all the variables i.e. convective boundary condition (CBC). The ratio of block length over the enclosure length is known as aspect ratio and is kept as $A = 0.2$ for the present chapter. The inlet and outlet length is kept as of same size and is equal to $0.1L$.

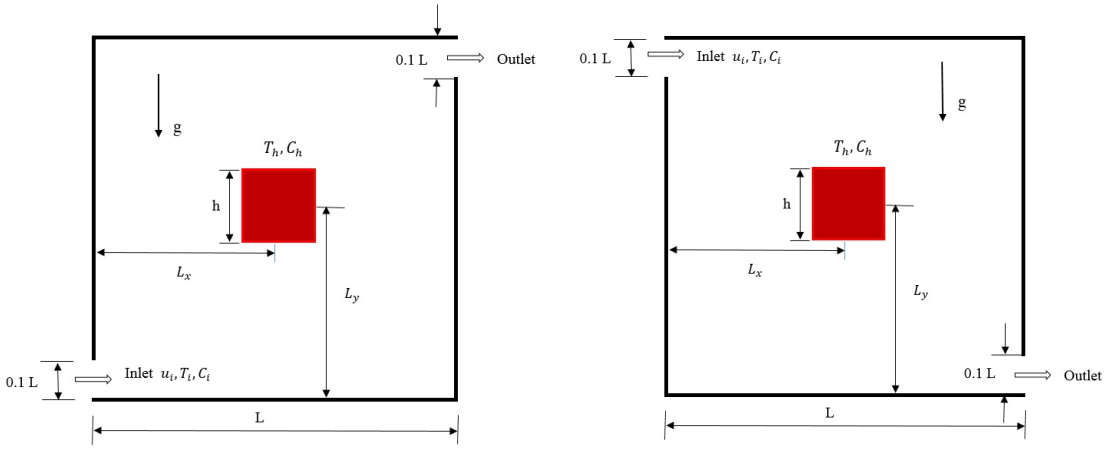

Figure 2.1: Problem Geometry

The flow is assumed to be steady and laminar and the fluid is assumed to be Newtonian, viscous and incompressible. The governing equation for fluid, heat and mass transfer includes continuity equation (conservation of mass), Navier-Stokes equation (conservation of momentum), energy equation (conservation of energy) and concentration equation (conservation of species). The flow is driven due to the buoyancy effects created by the temperature differences and concentration differences inside the enclosure. The density associated in the body force term of y-momentum equation is assumed to be the Boussinesq approximation as:

$$\rho = \rho_0[1 - \beta_T(T^* - T_0) - \beta_C(C^* - C_0)], \tag{2.1}$$

where $\beta_T = -\frac{1}{\rho}\frac{\partial \rho}{\partial T^*}$ and $\beta_C = -\frac{1}{\rho}\frac{\partial \rho}{\partial C^*}$ [79].

The thermal expansion coefficient, β_T is always positive because density decreases with the increasing temperature while the solutal expansion coefficient, β_C may be either positive or negative because, an increase in concentration induces a decrease or an increase in density, respectively [39].

The governing equations in dimensional form with the above mentioned assumptions are given by:

$$\frac{\partial u^*}{\partial x^*} + \frac{\partial v^*}{\partial y^*} = 0, \tag{2.2}$$

$$u^*\frac{\partial u^*}{\partial x^*} + v^*\frac{\partial u^*}{\partial y^*} = -\frac{1}{\rho}\left(\frac{\partial p^*}{\partial x^*}\right) + \nu\left(\frac{\partial^2 u^*}{\partial x^{*2}} + \frac{\partial^2 u^*}{\partial y^{*2}}\right), \tag{2.3}$$

$$u^*\frac{\partial v^*}{\partial x^*}+v^*\frac{\partial v^*}{\partial y^*}=-\frac{1}{\rho}\left(\frac{\partial p^*}{\partial y^*}\right)+\nu\left(\frac{\partial^2 v^*}{\partial x^{*2}}+\frac{\partial^2 v^*}{\partial y^{*2}}\right)+g\beta_T(T^*-T_0)+g\beta_C(C^*-C_0), \quad (2.4)$$

$$u^*\frac{\partial T^*}{\partial x^*}+v^*\frac{\partial T^*}{\partial y^*}=\alpha\left(\frac{\partial^2 T^*}{\partial x^{*2}}+\frac{\partial^2 T^*}{\partial y^{*2}}\right), \quad (2.5)$$

$$u^*\frac{\partial C^*}{\partial x^*}+v^*\frac{\partial C^*}{\partial y^*}=D\left(\frac{\partial^2 C^*}{\partial x^{*2}}+\frac{\partial^2 C^*}{\partial y^{*2}}\right). \quad (2.6)$$

The above mentioned equations can be expressed in non-dimensional form [117] by using the following dimensionless variables:

$$x=\frac{x^*}{L}; \quad y=\frac{y^*}{L}; \quad u=\frac{u^*}{u_i}; \quad v=\frac{v^*}{u_i};$$

$$p=\frac{p^*}{\rho u_i^2}; \quad T=\frac{(T^*-T_0)}{(T_h-T_0)}; \quad C=\frac{(C^*-C_0)}{(C_h-C_0)}. \quad (2.7)$$

$$Re=\frac{u_i L}{\nu}; \quad Pr=\frac{\nu}{\alpha}; \quad Gr=\frac{g\beta_T(T_h-T_o)L^3}{\nu^2};$$

$$Br=\frac{\beta_C(C_h-C_o)}{\beta_T(T_h-T_o)}; \quad Ri=\frac{Gr}{Re^2}; \quad Sc=\frac{\nu}{D}. \quad (2.8)$$

The governing equations in dimensionless form can be described as:

$$\frac{\partial u}{\partial x}+\frac{\partial v}{\partial y}=0, \quad (2.9)$$

$$u\frac{\partial u}{\partial x}+v\frac{\partial u}{\partial y}=-\frac{\partial p}{\partial x}+\frac{1}{Re}\left(\frac{\partial^2 u}{\partial x^2}+\frac{\partial^2 u}{\partial y^2}\right), \quad (2.10)$$

$$u\frac{\partial v}{\partial x}+v\frac{\partial v}{\partial y}=-\frac{\partial p}{\partial y}+\frac{1}{Re}\left(\frac{\partial^2 v}{\partial x^2}+\frac{\partial^2 v}{\partial y^2}\right)+Ri(T+Br.C), \quad (2.11)$$

$$u\frac{\partial T}{\partial x}+v\frac{\partial T}{\partial y}=\frac{1}{Re.Pr}\left(\frac{\partial^2 T}{\partial x^2}+\frac{\partial^2 T}{\partial y^2}\right), \quad (2.12)$$

$$u\frac{\partial C}{\partial x}+v\frac{\partial C}{\partial y}=\frac{1}{Re.Sc}\left(\frac{\partial^2 C}{\partial x^2}+\frac{\partial^2 C}{\partial y^2}\right). \quad (2.13)$$

Influence of boundary conditions on air flow and heat transfer within the enclosure is experimentally and numerically studied by Teodosiu et al. [115] depending on air mean velocity and temperature profiles. Concerning the dynamic and thermal field close to the air supply, the boundary conditions are as:

along the bottom wall,

$$u=0, \quad v=0, \quad \frac{\partial T}{\partial y}=0, \quad \frac{\partial C}{\partial y}=0; \quad y=0, \quad x\in[0,1] \quad (2.14)$$

along the top wall,

$$u = 0, \quad v = 0, \quad \frac{\partial T}{\partial y} = 0, \quad \frac{\partial C}{\partial y} = 0; \qquad y = 1, \quad x \in [0, 1] \tag{2.15}$$

along vertical walls,

$$u = 0, \quad v = 0, \quad \frac{\partial T}{\partial x} = 0, \quad \frac{\partial C}{\partial x} = 0; \qquad x = 0, \quad x = 1 \tag{2.16}$$

along the inlet:

$$u = 1, \quad v = 0, \quad T = -0.5, \quad C = 0 \tag{2.17}$$

along the outlet:

$$\frac{\partial u}{\partial x} = 0, \quad \frac{\partial v}{\partial x} = 0, \qquad \frac{\partial T}{\partial x} = 0, \quad \frac{\partial C}{\partial x} = 0 \tag{2.18}$$

on the surface of square block:

$$u = 0, \quad v = 0, \quad T = 1, \quad C = 1. \tag{2.19}$$

The heat transfer rate on the surface of block is defined by the average Nusselt number (Nu_{avg}) and is given by:

$$\begin{aligned} Nu_{avg} = &- \frac{1}{4A}\Bigg[\int_{L_y-A/2}^{L_y+A/2}\left(\frac{\partial T}{\partial x}\right)_{L_x+A/2} dy + \int_{L_x-A/2}^{L_x+A/2}\left(\frac{\partial T}{\partial y}\right)_{L_y+A/2} dx \\ &+ \int_{L_y-A/2}^{L_y+A/2}\left(\frac{\partial T}{\partial x}\right)_{L_x-A/2} dy + \int_{L_x-A/2}^{L_x+A/2}\left(\frac{\partial T}{\partial y}\right)_{L_y-A/2} dx\Bigg]. \end{aligned} \tag{2.20}$$

The mass transfer rate on the surface of the block is described by the average Sherwood number (Sh_{avg}) and is defined by:

$$\begin{aligned} Sh_{avg} = &- \frac{1}{4A}\Bigg[\int_{L_y-A/2}^{L_y+A/2}\left(\frac{\partial C}{\partial x}\right)_{L_x+A/2} dy + \int_{L_x-A/2}^{L_x+A/2}\left(\frac{\partial C}{\partial y}\right)_{L_y+A/2} dx \\ &+ \int_{L_y-A/2}^{L_y+A/2}\left(\frac{\partial C}{\partial x}\right)_{L_x-A/2} dy + \int_{L_x-A/2}^{L_x+A/2}\left(\frac{\partial C}{\partial y}\right)_{L_y-A/2} dx\Bigg]. \end{aligned} \tag{2.21}$$

The cooling efficiency [85] inside the enclosure is given by

$$\epsilon = 1 - \left(\frac{\overline{T}_{out}}{\overline{T}_{in}}\right), \tag{2.22}$$

where average inlet and outlet temperature are defined as:

$\overline{T}_{in} = \left(\int\limits_{A_{in}} T\ \overrightarrow{V}.\ n\ dA_{in}\right) \Big/ \left(\int\limits_{A_{in}} \overrightarrow{V}.\ n\ dA_{in}\right)$, and

$\overline{T}_{out} = \left(\int\limits_{A_{out}} T\ \overrightarrow{V}.\ n\ dA_{out}\right) \Big/ \left(\int\limits_{A_{out}} \overrightarrow{V}.\ n\ dA_{out}\right)$, where $\overrightarrow{V}$ and n are the velocity vector and the inward normal vector respectively, and A_{in} and A_{out} are the inlet and outlet areas.

2.3 Numerical procedure

The set of governing equations with specified boundary conditions is solved by finite volume approach [86] using the staggered grid arrangement. For solving the discretized equations, a pressure correction based iterative SIMPLE (Semi implicit method for pressure linked equations) algorithm is used. This procedure is based on a cyclic series of guess and correct operations to solve these governing equations. The velocity components are first calculated from the momentum equations using guessed pressure field and then corrected so as to satisfy the continuity equation and this process continues until the solution converges. There is a pressure link between the continuity and momentum equations which is adopted by converting the continuity equation to Poisson equation for pressure. The Poisson equation implements a pressure correction for a divergent velocity field. Throughout the calculations, velocities, temperature and concentration are considered to be converged, if,

$$|\varphi_{i,j}^{n+1} - \varphi_{i,j}^{n}| \leq 10^{-6}, \tag{2.23}$$

where $\varphi = (u, v, T, C)$ are the flow variables, n is the iteration number and (i, j) denote the calculation node point. The desired convergence of flow variables for time step $\Delta t = 0.001$ requires about 60,000 iterations.

2.4 Grid independency test and code validation

A grid independency test is performed for grid sizes varying from 40×40 to 140×140.

Table 2.1: Grid independency test when Ri=1.0 and Re=200.

Grid Point ($n \times m$)	Sh_{avg}	Cooling Efficiency
40×40	11.31041	2.58882
60×60	11.89272	2.57042
80×80	11.95999	2.56315
100×100	12.00160	2.55121
120×120	12.00398	2.55474
140×140	12.00961	2.55821

It is found that there is insignificant change after the grid size 100×100. Therefore, all computations are made with the optimal grid size 100×100.

To validate the accuracy of the numerical code, a comparison is made with the work of Chamkha et al. [23] by considering mixed convection in a square vented cavity with a horizontal heated square block. They have considered a square solid cylinder of width $0.2L$ placed inside a square cavity of length L. Cylinder is considered at high temperature while other walls are kept adiabatic and an inlet opening is considered as fixed at the middle of left vertical wall of length $0.1L$ while outflow opening is varied at the different locations on right vertical wall. Fig. 2.2(a) represents the comparison of average Nusselt number along the block with the variation of Richardson number for Re=200 when outlet is considered at the top of right vertical wall. The Figure represents good agreement of present work with the work done by Chamkha et al. [23].

To validate our result, a comparison is made with the work due to Singh and Sharif [108] by considering the inlet port at the bottom of left vertical wall, outlet along the top of right vertical wall, left vertical wall is maintained at lower temperature compared to right vertical wall at $Re = 300$. Fig. 2.2(b) represents a good agreement of present result with the earlier work done by Singh and Sharif [108].

The present simulation code is also validated with the experimental work done by Minaei et al. [72] by considering a discrete heat source on the right vertical wall and the inflow and outflow openings are considered along the left vertical wall. Fig. 2.2(c) represents the comparison of average Nusselt number for $Re = 320$ with the variation of

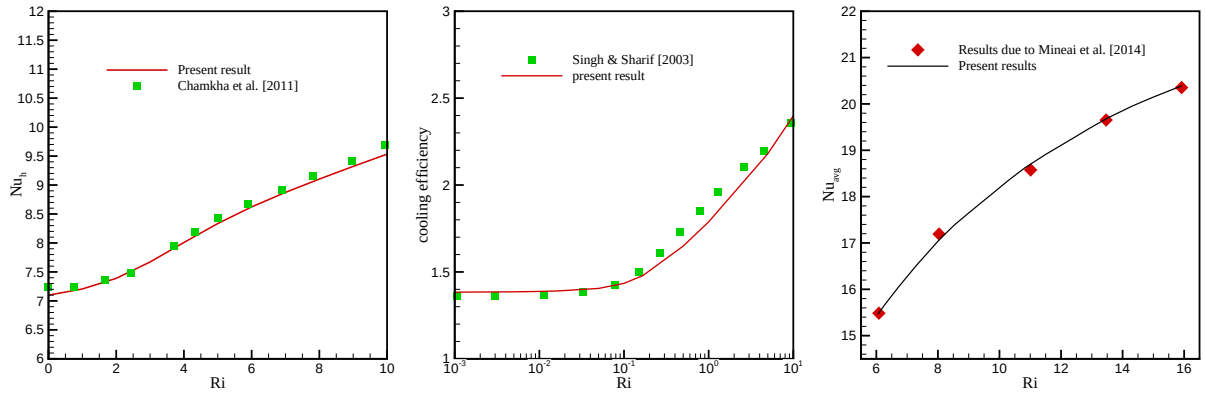

(a) (b) (c)

Figure 2.2: Comparison of (a) Nu_{avg} with the result of Chamkha et al. [23], (b) cooling efficiency with the result of Singh and Sharif [108], (c) Nu_{avg} due to present simulation with the experimental work done by Minaei et al. [72]

Richardson number. The comparison between the present result with the experimental result shows a good agreement.

2.5 Results and discussion

The flow variation and energy transfer is studied inside the ventilated enclosure due to the interaction of buoyancy-induced double-diffusive convection induced by the thermosoluted square block and mechanical-driven forced convection due to the inlet air. Richardson number, buoyancy ratio, Schmidt number, Reynolds number and Prandtl number effects are examined for the flow and heat transfer variation. In the present work, air is considered as working fluid inside the enclosure and the Prandtl number is taken as 0.71 throughout the calculations. For both the configurations an extensive parametric analysis is made to delineate the heat and solute transfer mechanisms for flow variation. Fluid flow is characterized by (i) the primary flow inside the enclosure due to the forced convection effect, (ii) a downstream secondary eddy is formed in the bottom-left corner of the enclosure due to the pressure effect, (iii) an upstream secondary eddy is formed above the main flow stream due to the buoyancy effects, (iv) another secondary eddy is formed near the inlet and outlet port because of high temperature or concentration gradients [73].

2.5.1 Configuration-I: Cold air is injected through the bottom of left vertical wall and outlet is at the upper of right vertical wall

2.5.1.1 Effect of Buoyancy ratio

Buoyancy ratio defines the relative strength of solutal to thermal buoyancy forces causing the density differences. It can be positive, negative or zero values. For zero buoyancy ratio ($Br = 0$), the buoyancy effect is due to temperature gradient and the mass transfer is because of temperature field. For positive buoyancy ratio ($Br > 0$), the thermal and solutal buoyancy forces assist each other (aiding convection). For the negative values of buoyancy ratio ($Br < 0$), thermal and solutal buoyancy forces opposing each other (opposing convection). The current-study deals with the buoyancy induced flow for $-10.0 \leq Br \leq 10.0$. Two different inlet and outlet locations are taken for simulation as shown in Fig. 2.1.

Fig. 2.3 represents the steady flow lines, heat and mass transfer lines of the configuration-I for $Re = 200$, $Ri = 1.0$, $Sc = 5.0$ and $-10.0 \leq Br \leq 10.0$. The flow pattern inside the ventilated enclosure is mainly influenced by the interaction between the buoyancy forces due to temperature, concentration, and the forced convection due to injected air. For negative values of buoyancy ratio, natural convection dominates the flow from inlet to outlet. The effect of flow variation, temperature and concentration transfer for $Br = -10.0$ is presented in the first row of Fig. 2.3. Maximum amount of the inlet fluid flows closed to the left vertical wall and passed through the left-upper side of the heated block towards the outlet and a deformation is observed before the outlet and a clockwise recirculating zone is formed above the upper left corner of the block due to natural convection effect. Two secondary eddies are found along the right vertical wall, one is near the outlet port and second is near the bottom-right corner of the enclosure along the downstream flow. Due to the negative buoyancy ratio, the flow in the enclosure is boundary layer type however the buoyancy resulting a stronger primary eddy around the heated block and this manifests in the formation of secondary upstream region closed to the vertical right wall near the outlet. For $Br = -5.0$, the circulation zone around the block is contrasted while the eddy along the right side of bottom wall is expanded. From the streamlines, it is observed that the deformation force along the upper portion of the enclosure is increased and the secondary eddy formed along the right upper part getting contrasted due to the moving cold fluid and the buoyancy force. As Br shifts from negative to positive, forced convection dominates the flow. For $Br = 1.0$, main streamlines flow from inlet to outlet through the block diagonally in the enclosure because of forced convection effect and two upstream eddies are formed near the left vertical wall and the upper eddy found in case of $Br = -5.0$ driven by the moving fluid and encapsulates a thermal region. This is due to the opposing effect of buoyancy forces where the downstream eddy getting deformed. A small downstream eddy is found along the right corner wall, which is also diminished as Br is increasing in the further cases. As the value of buoyancy ratio increases, three upstream eddies are found near the left vertical wall and a downstream eddy is found just below the outlet port at $Br = 5.0$ which is expanded with the increasing value of Br. As Br increases from 5.0 to 10.0, the flow velocity is getting stronger and the middle vortex created close to the left vertical wall is getting weaker and

the vortex close to right vertical wall is getting stronger. The cold fluid forces the hot fluid towards the outlet and the hot fluid moves upward and getting stacked closed to the outlet end. For all the figures of streamlines in case of $Br = -10.0,\ -5.0,\ 1.0$ and 5.0, hot vortices are formed closed to the bottom wall and for $Br = 10.0$, the cold space is enlarged along the bottom of vicinity due to inertia effect and the vortex is vanished.

Isotherms are generated in the ventilated enclosure because of the interaction between the incoming cold air and thermosoluted block. In Fig. 2.3, the isotherms variation for $Br = -10.0$ and -5.0 are found to be very small and the distribution near the inlet and outlet are almost same. Mostly, the variation is found along the lower part of the block where thermal fluid region getting expanded as Br increases from -10.0 to -5.0. As Br increases, the incoming cold fluid and hot vortex due to the heated block are started to mix up and the uniform distribution of cold fluid is observed. The recirculating zone formed for $Br = -10.0$ and $Br = -5.0$ getting vanished for $Br \geq 1.0$ and a heated plume is formed above the block as Br increases from 1.0 to 10.0.

The isoconcentration lines for $Re = 200, Ri = 1.0$ and $Sc = 5.0$ with $-10.0 \leq Br \leq 10.0$ is presented in the right part of Fig. 2.3. The solutal lines are uniformly distributed along the lower portion of the block for all buoyancy ratios. At $Br = -10.0$, the solutal gradient forms a recirculating zone due to weak inertial forces and the concentration stratification near the lower inlet is more for negative buoyancy effects. The cold fluid flow which enters the enclosure with certain speed, generates an extra force which combine with the buoyancy driven forces. If this force is not sufficient enough to drive the buoyancy forces, then the flow pattern is governed by natural convection and if the buoyancy effect is smaller then the flow pattern is described by forced convection. A solutal plume is also observed above the block as $Br \geq 1.0$ and the lower part of the enclosure has no mass transfer since most of the mass transfer is occurring along the central region of the cavity. Interestingly, for $Br < 1.0$, the isotherms and isoconcentrations shows similar profiles along the upper part of the enclosure, but for $Br \geq 1.0$, the upper profiles differ due to the volume difference.

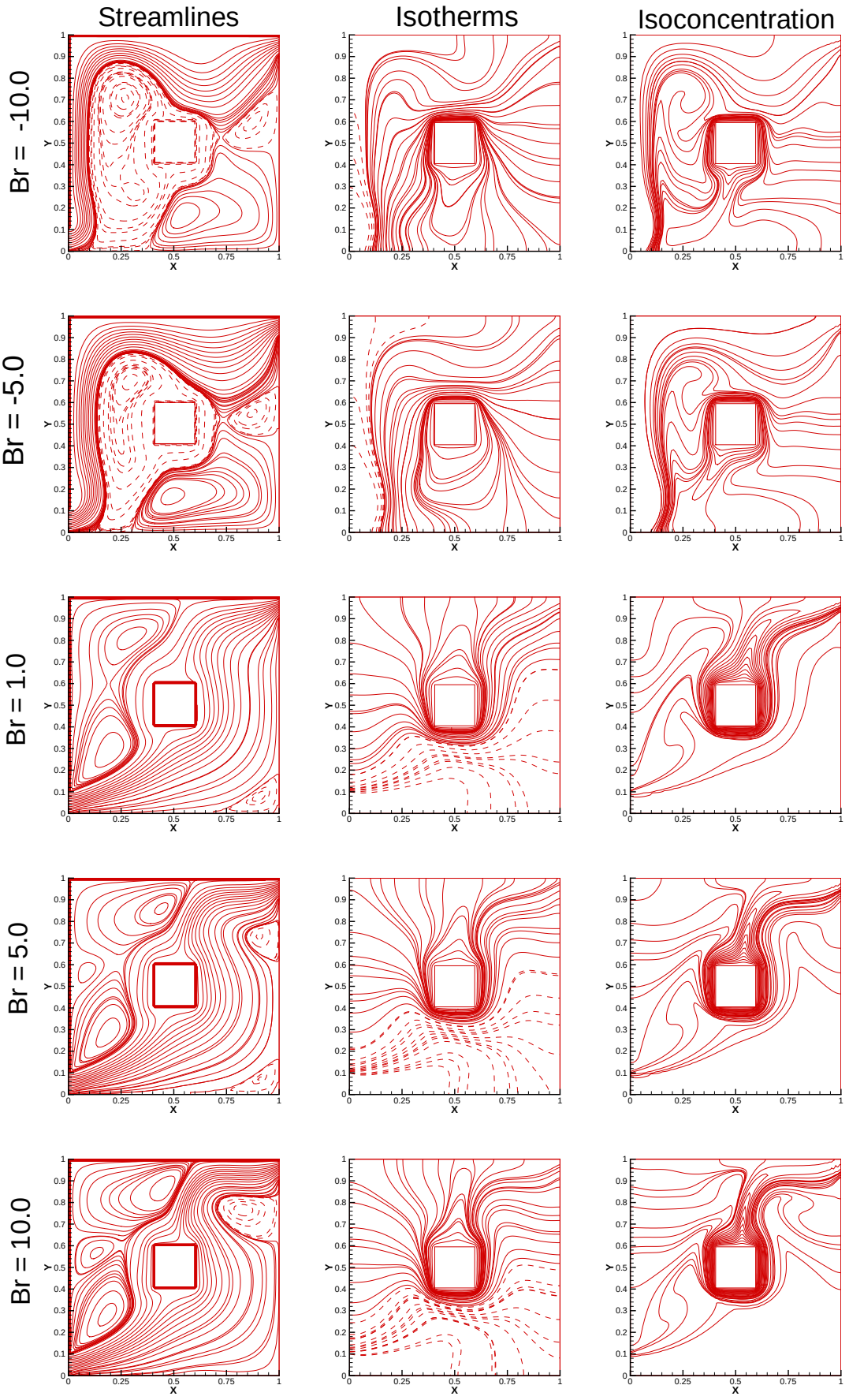

Figure 2.3: Effects of Br on streamlines, isotherms and isoconcentration for configuration-I, ($Sc = 5.0$, $Ri = 1.0$ and $Re = 200$).

2.5.1.2 Effect of Schmidt number

Schmidt number determines the relationship between the thermal and mass diffusivities, which performs as a key parameter for flow variation [122]. Fig. 2.4 represents the streamlines, isotherms and isoconcentrations for Re= 200, $Ri = 1.0$ and $Br = 1.0$ with variation of Schmidt number ($0.07 \leq Sc \leq 7.0$). The streamlines are found to be similar for $Sc < 1.0$ but the variation is mostly found near the right vertical wall. For all the Schmidt numbers, the main streamlines diagonally pass from inlet to outlet through the right side of the block due to the equivalent driving force arisen by the natural and forced convections. For $Sc = 0.07$, two upstream recirculation zones are found near the left vertical wall of the enclosure. As Schmidt number increases to 0.7, the recirculation zone near the left-upper wall is getting increased because of natural convection effect. For $Sc = 0.07$, there is no downstream vortex and as Schmidt number increases to 0.7, a very small vortex is found near the outlet. It is found that the natural convection zone is increased with the increasing value of Schmidt number and the circulating zone formed along the upper left corner is spreading towards the mid-section of the enclosure. As Schmidt number increased from 1.0 to 3.5, the downstream eddy near the outlet port is diminished. For $Sc = 1.0$, a downstream secondary eddy is found in the right-bottom corner of the enclosure which is increased with the increasing value of Schmidt number. For $Sc = 7.0$, the upstream secondary recirculation zone is getting transported towards the outlet and a small eddy is observed in the upper-left corner of the enclosure.

The thermal lines presented in the second column of Fig. 2.4 represents a horizontally stratified region between the block and the vertical walls of the enclosure as forced convection dominates natural convection driven flow. At $Sc = 0.07$, a thermal plume is observed directed towards the upper side of the enclosure and as the value of Schmidt number increases to 0.7, the direction of the thermal plume diverted towards the outlet port. But, afterwards there is no significant change is observed when the Schmidt number increases from 0.7 to 7.0 and dense thermal lines are found around the heated block. Isoconcentration lines are presented in the third column of Fig. 2.4 for various values of Schmidt number. For $Sc = 0.07$, the solutal isoconcentration is uniformly distributed at lower-left zone near the inlet and there is a circulation zone formed around the block

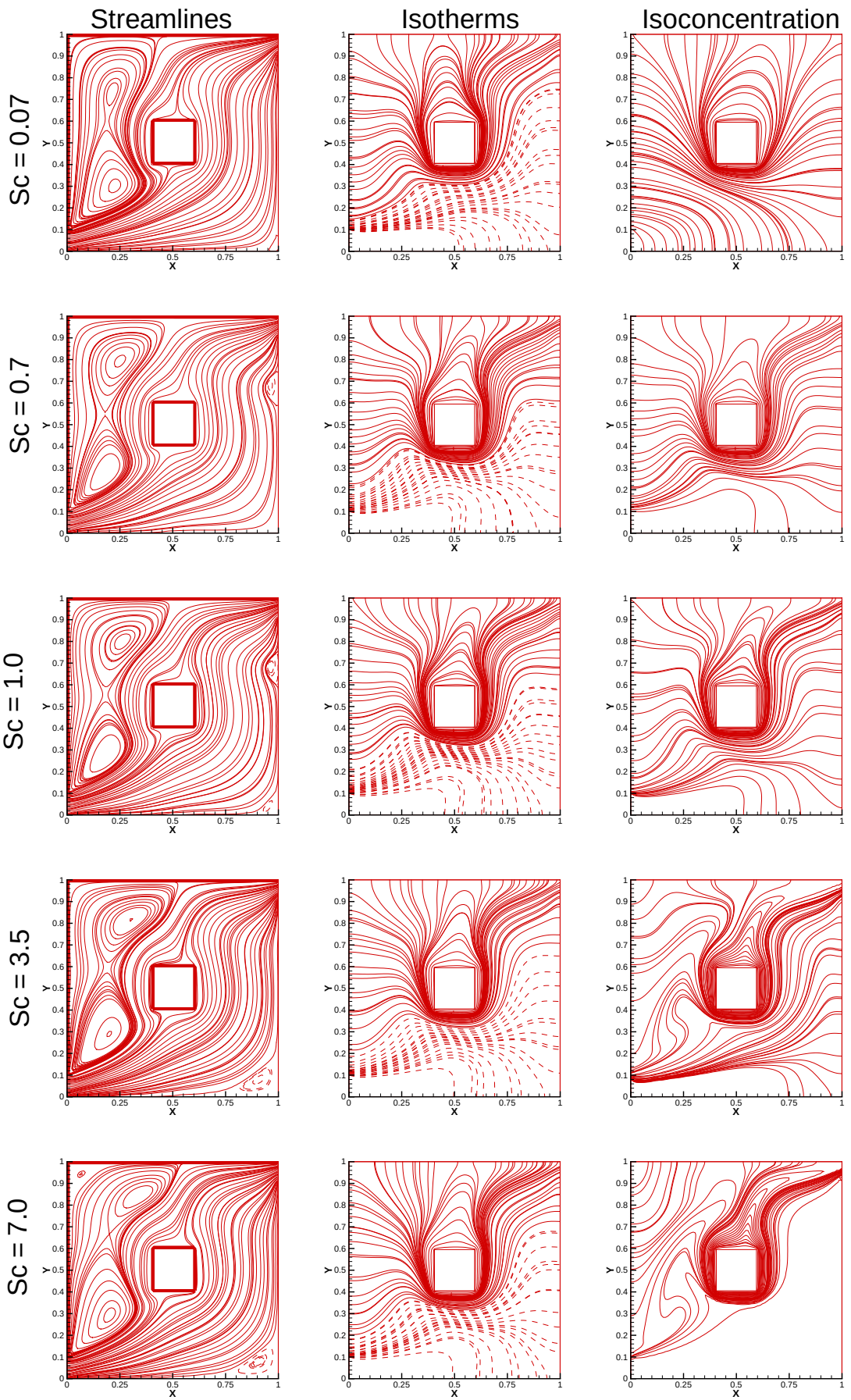

Figure 2.4: Effects of Schmidt number on streamlines, isotherms and isoconcentration for configuration-I, (Br=1.0, Ri=1.0 and Re=200).

towards the upper wall. As the value of Schmidt number increases to 0.7, the isoconcentration lines are horizontally stratified between the vertical walls of the enclosure and the block. Also a solutal plume is formed near the lower part of the block which is directed towards the upper-left corner of the enclosure. For $Sc \geq 1.0$, most of the isoconcentration lines switches to the solutal plume around the block and directed towards the outlet port due to the strong convection effect. At $Sc = 1.0$, the isotherms and isoconcentration lines are almost similar around the block and as Schmidt number increases to 3.5, forced convection is dominating the natural convection flow, hence mass transfer is weak at the inlet section and isoconcentration lines are diagonally pass inside the enclosure. For $Sc = 7.0$, inertial force is weak near the inlet port and a tiny isoconcentration plume is formed and concentration are forced to extract out through outlet due to heavy mass flow rate. It is observed that when Schmidt number increases, the solutal boundary layer around the block becomes thinner which results a larger mass transfer rate.

2.5.1.3 Effect of Richardson number

The flow pattern inside the ventilated enclosure is mainly determined by the interaction between the forced convection due to injected fluid and the buoyancy effects due to thermosoluted block. Richardson number represents the importance of natural convection relative to forced convection. Fig. 2.5 represents the effect of Richardson number on streamlines, isotherms and isoconcentrations for configuration-I at $Br = 1.0$, $Sc = 5.0$ and $Re = 200$. For small values of Richardson number, the buoyancy effects are weak. For $Ri \leq 1$, most of the inlet fluid passes through the right side of the block and a small downstream eddy is found near the bottom-right corner of the enclosure. At $Ri = 0.0$, an upstream anticlockwise circulation zone is observed around the heated block in which two circulation zones are found near the block due to buoyancy effect. As Richardson number increases to 0.1, the flow is dominated by forced convection effect and the upstream circulation zone is contrasted towards the left vertical wall of the enclosure and the vortex near the upper wall of the block is vanished. This is due to the fact that the hot fluid present around the block is driven out by the cold fluid as buoyancy increases. At $Ri = 1.0$, upstream secondary eddy splits into two clockwise rotating cells closed to the left vertical wall due to buoyancy effects and one downstream small eddy is found near the

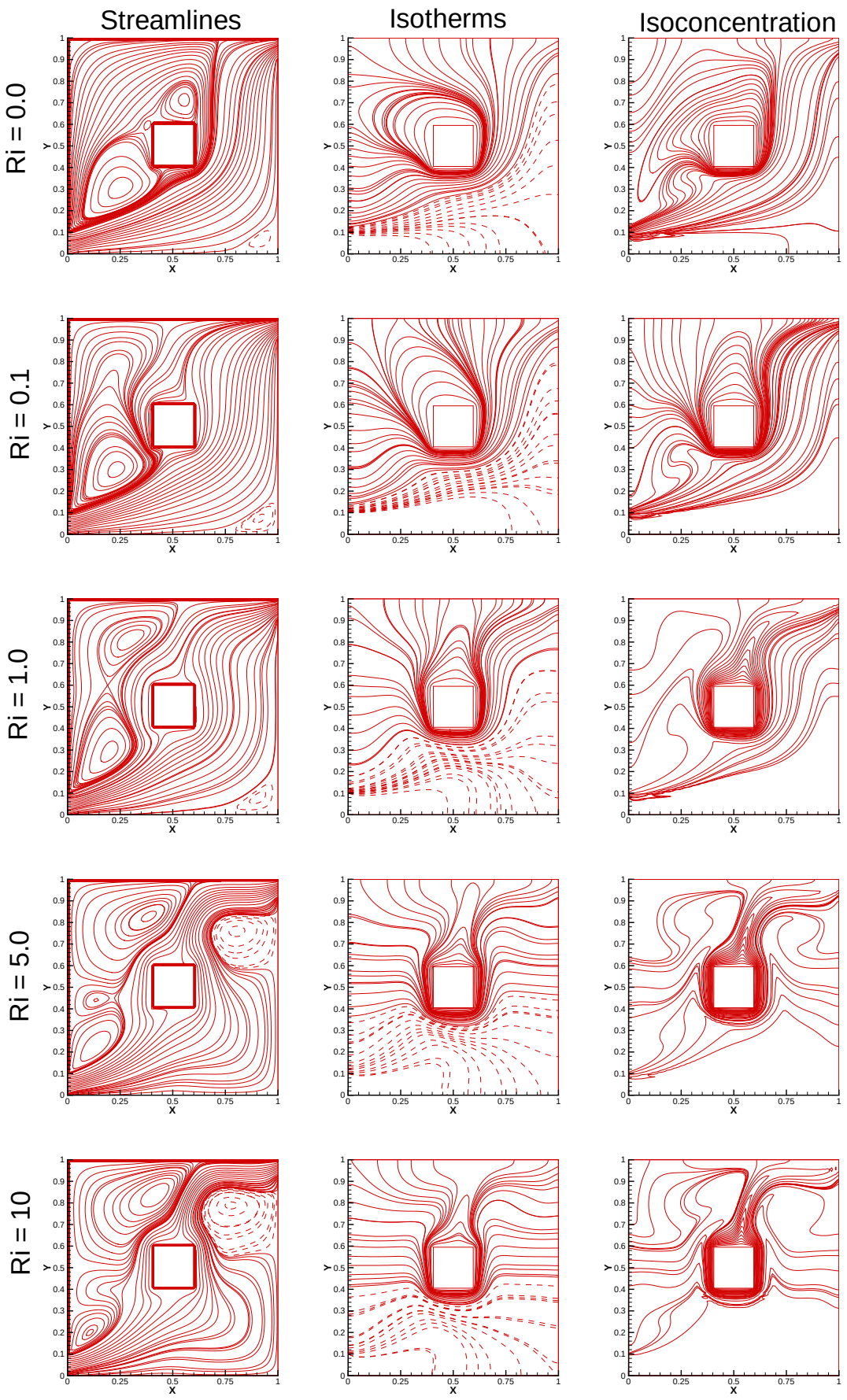

Figure 2.5: Effects of Ri on streamlines, isotherms and isoconcentration for configuration-I, (Sc=5.0, Br=1.0 and Re=200).

bottom-right corner of the enclosure. For $Ri = 5.0$, clockwise rotating cells grows in size and moves towards the boundary and expands more than half of the left wall section. A downstream anticlockwise eddy is found below the outlet port at $Ri = 5.0$ which expands with the increase in Ri. For $Ri = 10.0$, the cold space is enlarged along the bottom-right section of the enclosure due to the convective mode of heat transfer effect. Streamlines are much effected by both forced and natural convections for higher Richardson number.

The effect of Richardson number on isotherms are shown in second column of Fig. 2.5. For low Richardson number, isotherms are found to be uniformly distributed inside the enclosure. A thermal plume directed towards the left vertical wall is observed for $Ri = 0.0$, which is tilted towards upper-left corner for $Ri = 0.1$ inside the ventilated enclosure due to weak convection effect. Thermal lines having lower temperature are observed in the bottom-right region due to forced convection effect. For $Ri \geq 1.0$, the bottom region becomes colder due to mixed convection dominated flow. Thermal lines are found to be horizontally stratified between the block and vertical wall of the enclosure. These thermal lines become denser around the heated square block due to forced flow of inlet fluid and a thermal plume directed towards the upper wall of the enclosure is formed due to forced convection effect.

Effect of Richardson number on isoconcentration lines is presented in Fig. 2.5 (third column). During the computation, it is observed that less dense fluid tends to rise and dense fluid tends to sink which shows the tendency that upper region of fluid composed of lower density materials than lower region. Therefore solutal buoyancy region leads to a configuration of stable stratification. For $Ri < 0.0$, isoconcentration lines are diagonally distributed inside the enclosure and a circulation zone around the block is observed due to low convection effect. At $Ri = 0.1$ this circulation zone is changed to plume directed towards the upper wall of the enclosure. For $Ri \geq 1.0$, isoconcentration plume directed towards the exit port is formed due to the strong convection effect and the mass boundary layer near the block becomes thinner as Richardson number increases, which results in higher mass transfer rate.

2.5.2 Configuration-II: Cold air is injected through the upper of left vertical wall and outlet is at the bottom of right vertical wall

2.5.2.1 Effect of Buoyancy ratio

In Fig. 2.6, the effects of buoyancy ratio on streamlines, isotherms and isoconcentration are shown for configuration-II at $Ri = 1.0$, $Re = 200$ and $Sc = 5.0$. At $Br = -10.0$, the inlet flow dominates the major flow from the inlet to outlet and therefore, streamlines diagonally flow from inlet to outlet passing through the block due to forced convection effect. Three downstream vortex cells are found near the left vertical wall and an upstream eddy is found in the top-right corner of the enclosure. All these eddies are decreased in size as Br increases from -10.0 to -5.0 due to forced convection effect. As Br increases to 1.0, natural convection dominates the flow and the main inlet fluid passes through the left-bottom corner of the enclosure without much penetrating into the enclosure. Streamlines are found recirculated around the block for $Br \geq 1.0$ due to buoyancy effect. At $Br = 1.0$, an upstream secondary eddy is observed in the upper-right corner of the enclosure and as the value of Br increases, this eddy is widen up and a small eddy is found just above the outlet port. For $Br = 10.0$, it is observed that the recirculation zone around the block splits into two recirculating zones in the left side of the block due to the combined thermosolutal effect.

From second column of Fig. 2.6, isotherms are presented for different values of buoyancy ratio. The forced flow, which is entering through the upper inlet with a maximum velocity, creates an additional driving force which combines with the buoyancy forces. If this force is not good enough to supersede the buoyancy forces, then the flow pattern is dominated by natural convection effect, and if the buoyancy forces are small enough then the flow pattern is governed by forced convection effect. It is found that for negative values of Br, thermal field is distributed horizontally between the vertical walls and the block due to forced convection effect, a thermal plume is observed around the block directed towards the bottom wall since the inlet cold fluid is heavier compared to hot fluid. As the value of buoyancy ratio shifts from negative to positive, the thermal plume tilted towards the upper wall and thermal field is stratified between the left vertical wall

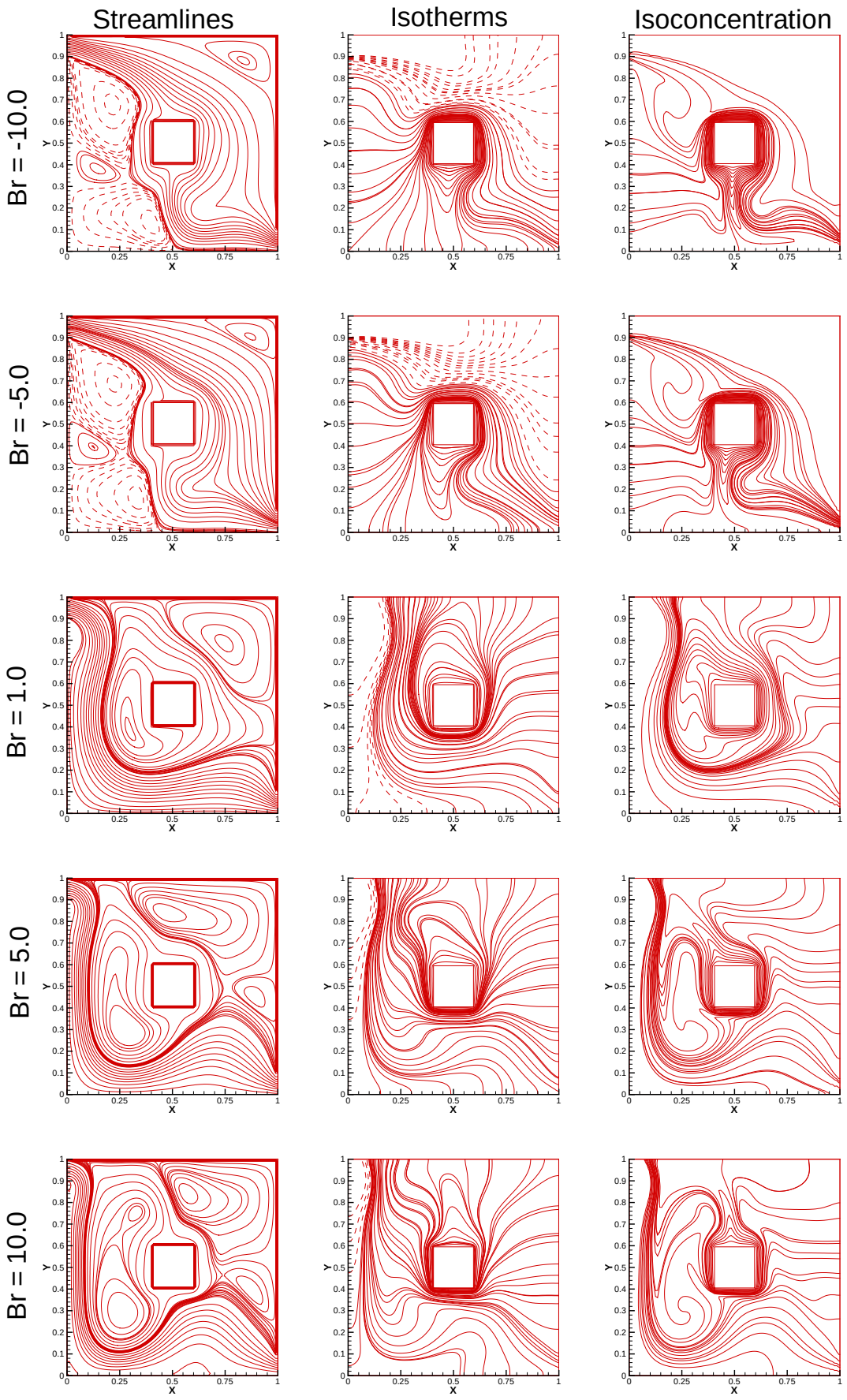

Figure 2.6: Effects of Br on streamlines, isotherms and isoconcentration for configuration-II, (Sc=5.0, Ri=1.0 and Re=200).

and the block due to the tendency of hot and cold air and thermal lines are found to be shifted towards the outlet port.

The isoconcentration lines are shown in Fig. 2.6 (third column) for different values of Br. For negative values of buoyancy ratio, a denser solutal plume is observed in downward direction around the heated block and is directed towards the exit port due to higher forced convection effect and mass transfer rate. As the buoyancy ratio increases to 1.0, the solutal plume disappears and concentration lines are uniformly distributed inside the enclosure due to mixed-convection effect. Isoconcentration lines are found denser near the left side of the block as the inlet fluid mix-up with the buoyancy effects. Again, as the value of buoyancy ratio increases to 5.0, a tiny solutal plume is acted in the upward direction because of higher density difference. Concentration lines are getting stacked at the lower left corner of the enclosure for higher buoyancy ratios.

2.5.2.2 Effect of Schmidt number

The streamlines represented in Fig. 2.7 describes the double diffusive mixed convection of various flow regimes. For $Re = 200$ and $Ri = 1.0$, the induced flow moves parallelly with the left vertical wall passed through horizontal wall to the outlet for all Schmidt numbers ($0.07 \leq Sc \leq 7.0$) as the cold fluid has a tendency to flow downward and hot fluid has a tendency to flow upward due to the density difference. For $Sc = 0.07$, a recirculation zone is found around the heated block and an upstream secondary eddy is formed closed to the upper-right space of the enclosure due to natural convection effect. It is also observed that the recirculation vortex in the upper-right corner of the enclosure gradually increases with the increasing value of Schmidt number while the circulation zone around the block is contrasted with the increasing value of Schmidt number. For $Sc = 0.7$, an eddy is observed near the bottom-left corner of the block which is getting enlarged near the left side of the block due to strong convection effect.

Second column of Fig. 2.7 presented the isotherms distribution for various values of Schmidt number. It is observed that, there is no significant change on isotherms with the variation of Schmidt numbers. Isotherms are found to be stratified between the heated block and vertical walls of the enclosure due to the equivalent effect of forced and natural convections. Dense isotherms occurred around the heated block and are directed towards

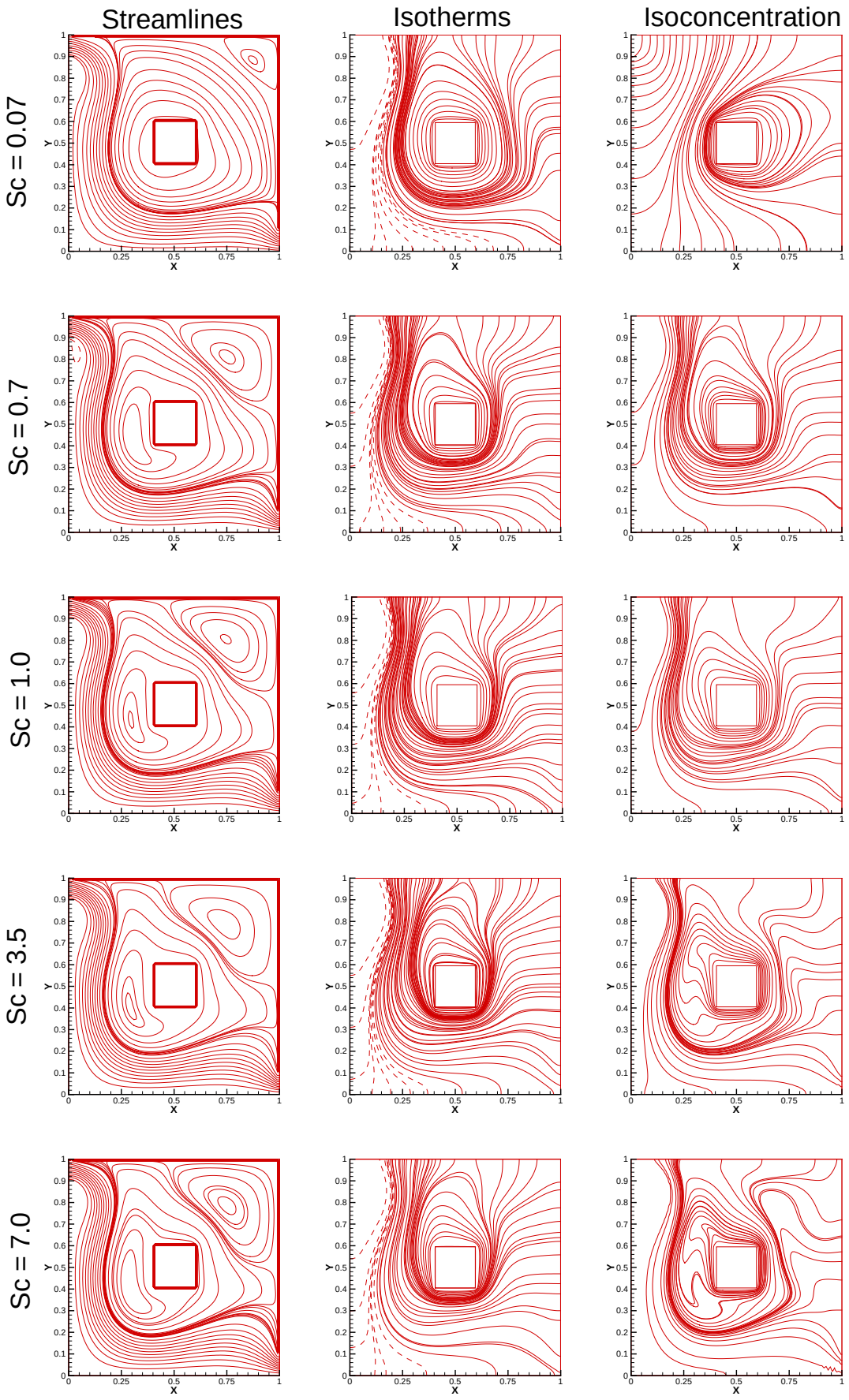

Figure 2.7: Effects of Schmidt number on streamlines, isotherms and isoconcentration for configuration-II, (Br=1.0, Ri=1.0 and Re=200).

the upward direction of the enclosure signifies the higher heat transfer close to the block. As Sc increases, it is found that the temperature lines are moved outward through exit port due to the convection mode of heat transfer. Interestingly, the isotherms are similar to isoconcentration lines for $Sc = 0.7$ and $Sc = 1.0$.

The isoconcentration lines are presented in Fig. 2.7 for various values of Schmidt number at $Re = 200$, $Br = 1.0$ and $Ri = 1.0$ and it is observed that the mass diffusion effect dominates the solutal characteristics since the isoconcentration lines are spirally distributed along the upper-left region near the inlet of the enclosure. A rough solutal plume is observed directed towards the right vertical wall of the enclosure due to weak convection effect. As Schmidt number increases, the stratification of isoconcentration lines near the inlet is vanished and the solutal plume directed towards the upper wall is formed, this may be due to the inlet mass flux condition which significantly differ from the thermal buoyancy conditions. For $Sc = 1.0$, solutal plume vanishes and isoconcentration lines are stratified between the wall of the enclosure and the therosoluted block and denser concentration lines are found in the left region of the enclosure. For $Sc = 3.5$ and $Sc = 7.0$, mass transfer rate is getting higher and concentration lines are circulated between the block and the left vertical wall of the enclosure. This can be concluded that there is a strong assisting flow for the solute to support maximum mass transfer through outlet.

2.5.2.3 Effect of Richardson number

Fig. 2.8 represents the streamlines, isotherms and isoconcentration for $Sc = 5.0$, $Br = 1.0$, $Re = 200$ and $0.0 \leq Ri \leq 10.0$. From the first column of Fig. 2.8, it is observed that the fluid is flowing from inlet to outlet passing through the upper-right side of the block for low Richardson number ($Ri < 1.0$) due to forced convection effect and a small upstream eddy is found in the upper-right corner of the enclosure. Also, two eddies are observed near the heated square block inside the downstream recirculation zone due to buoyancy force. For $Ri = 1.0$, the inlet fluid moves parallel to the left vertical wall and then moves horizontally towards the exit port. Also, an upstream recirculation zone is found around the block due to strong buoyancy effect and a secondary eddy is found in the upper-right corner of the enclosure. As, Richardson number increases to 5.0, the main streamlines

from inlet to outlet is found to be deformed near the outlet port and the secondary eddy in upper-right corner is found to be expanded in the upper region and a small eddy is observed near the outlet port. These circulation zones become larger with the increasing value of Richardson number due to the natural convection effect.

Isotherms are shown in the second column of Fig. 2.8 for various values of Richardson number ($0.0 \leq Ri \leq 10.0$. For low values of Richardson number, isotherms are distributed horizontally as the forced convection dominates the flow and the circulating thermal lines are found around the block directed towards the left vertical wall of the enclosure. The cold fluid is observed to be moving in the upper-right region of the enclosure and the bottom-left region is found to be at higher temperature. As Richardson number increases to 1.0, the cold air move downwards parallel to the left vertical wall due to increased convection effects. Isotherms are observed to be stratified vertically between the block and the vertical walls of the enclosure due to natural convection effect. Also, a tiny thermal plume is formed around the lower-right side of the block which is directed towards the inlet port for higher Richardson number. It is also observed that as Ri increases, diverse isotherms and solutal zones are formed due to increase of flow velocity.

From the right part of Fig. 2.8, it is concluded that for low Richardson number, the isoconcentration lines are found to be concentrated between the block and vertical walls due to strong convection effect. Also a circulation zone of oval shape around the block is observed for $Ri < 1.0$. Induced flow rate increases for $Ri \geq 1.0$ and the fluid is forced to move downwards of the thermosoluted block. As the value of the Richardson number increases to 5.0, a solutal plume around the block directed towards the inlet port is observed and concentration lines are getting stacked at the lower- left corner of the enclosure due to forced convection effect. For $Ri = 10.0$, isoconcentration lines are found to be stratified between left vertical wall and the block due to frictionless of the pressure field. From the visual point of view it can be concluded that the mass transfer boundary layer is formed a little more rapidly than the thermal boundary layer.

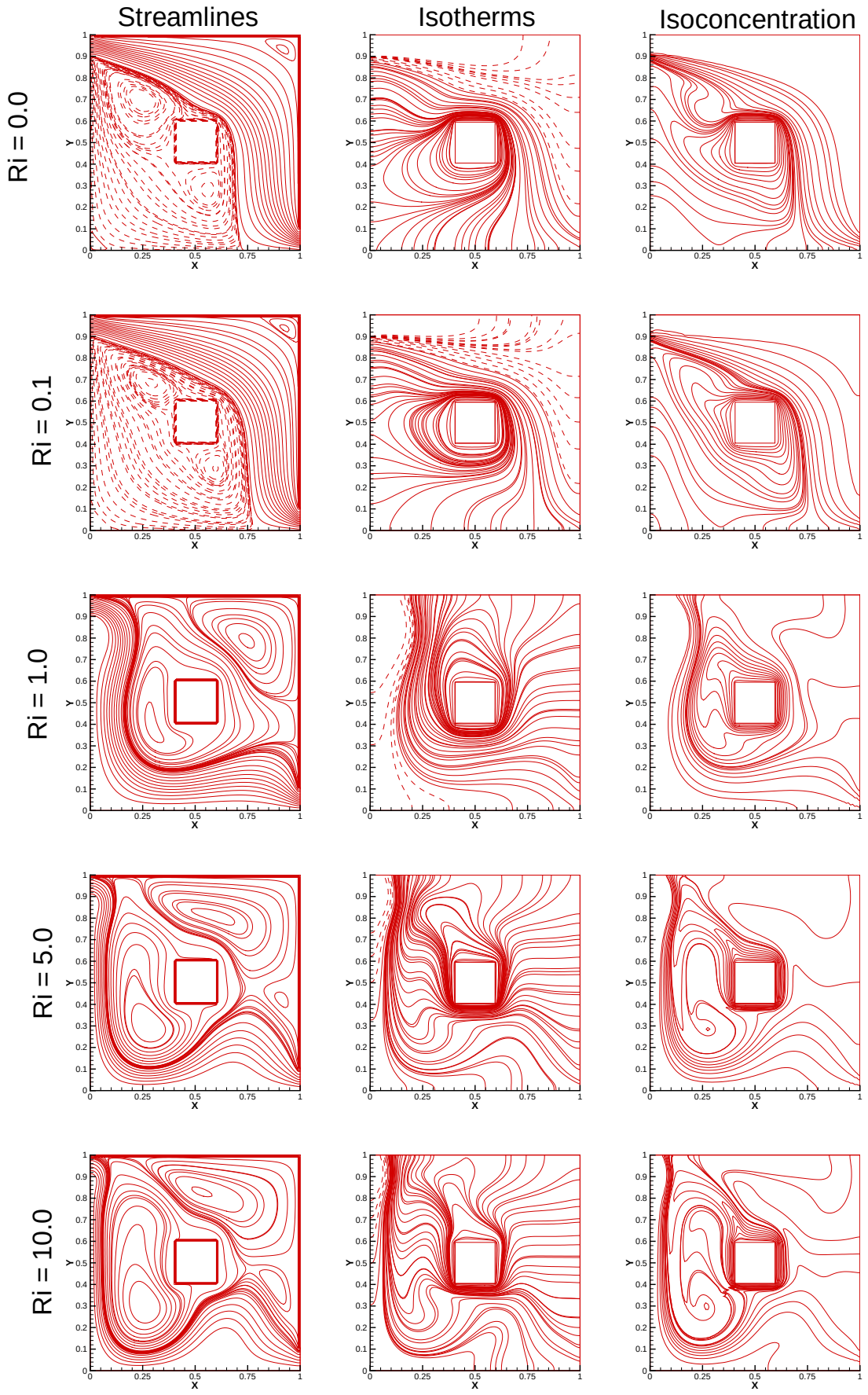

Figure 2.8: Effects of Ri on streamlines, isotherms and isoconcentration for configuration-II, (Sc=5.0, Br=1.0 and Re=200).

2.5.3 Effect of Buoyancy ratio and Richardson number

Fig. 2.9 and 2.10 presents the average Nusselt number, Sherwood number and cooling efficiency for configuration-I & II for different values of Richardson number and buoyancy ratios. At low Richardson number, most of the heat transfer variation is observed along the lower left corner of the block adjacent to the inlet vicinity. A steep temperature and mass flow rate is observed along the lower left corner which causes a sharp variation of temperature and mass transport and weak variation along the upper left section of the enclosure for small Ri values ($Ri < 1.0$) (Fig. 2.9 (a) & (b)). The heat and mass flow rate behaves in a similar fashion, since the isotherms and isoconcentrations represents the same profiles in the inner region of the enclosure due to conduction effects. It is observed from Fig. 2.9 (c) that the increase in Richardson number gives an increment in the cooling efficiency due to the opposing buoyancy effects. When the inlet fluid source is shifted towards the upper end of left vertical wall, then a large effect of inertial force is observed along the cold region. Hence, a very large variation in average Nusselt number is observed for low Richardson number (Fig. 2.10 (a)). It is also observed that as Ri increases, the cold space getting enlarged along the lower part of the enclosure and in the exit vicinity and the mass transfer rate is weak compare to heat transfer rate in configuration-II as observed from Fig. 2.10 (a) & (b). As Br is increasing for any fixed Ri values, the heat and mass flow rate variation is very high along the block due to density variations. Hence cooling efficiency has a large variation when $-10.0 \leq Br \leq -5.0$ (Fig. 2.10(c)). Compare to configuration-I & II, it can be predicted that higher cooling efficiency can be achieved for weak buoyancy forces in configuration-II and strong buoyancy for configuration-I for higher Richardson number values ($Ri > 1.0$).

2.5.4 Effect of Buoyancy ratio and Schmidt number

The combined effect of buoyancy ratio and Schmidt number on average Nusselt number, Sherwood number and cooling efficiency is presented in Fig. 2.11. The variation of buoyancy ratio and Schmidt number is considered in the range of $-10.0 \leq Br \leq 10.0$ and $0.07 \leq Sc \leq 10.0$. At lower buoyancy ratio ($-10.0 \leq Br \leq -5.0$), the temperature variation represents the same profile as observed in the inlet region profiles due to conduction

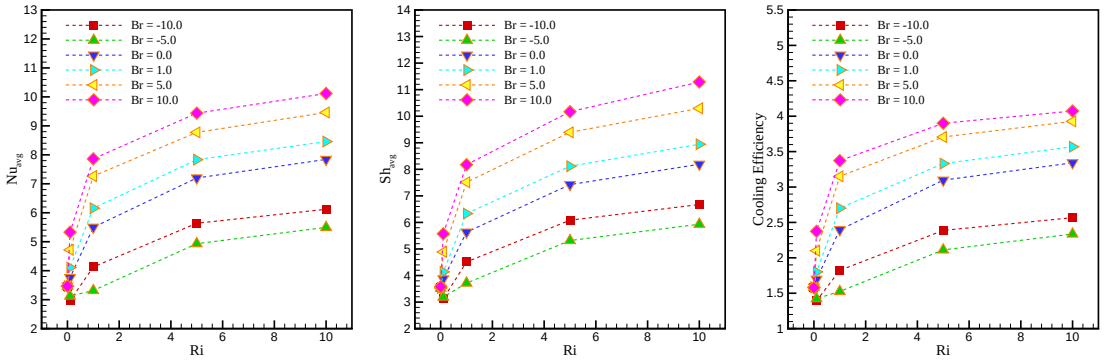

(a) (b) (c)

Figure 2.9: Effect of Br and Ri on (a)Nu_{avg}, (b) Sh_{avg} and (c) cooling efficiency at $Re = 200$, $Sc = 1.0$, $Pr = 0.71$ for Configuration-I.

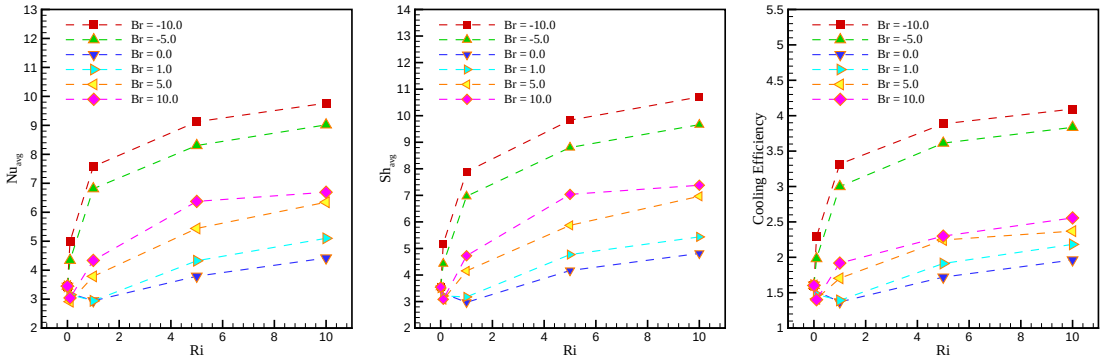

(a) (b) (c)

Figure 2.10: Effect of Br and Ri on (a)Nu_{avg}, (b)Sh_{avg} and (c) cooling efficiency at $Re = 200$, $Sc = 1.0$, $Pr = 0.71$ for Configuration-II.

effects. When the buoyancy effects are small ($-5.0 \leq Br \leq 0.0$), the higher isotherms are clustered closed to the heated block and along the core of the enclosure which causes a steep temperature gradient existence along the left wall of the block and weak temperature gradient along the upper left corner of the enclosure (Fig. 2.11 (a)). This signifies that a large effect of inertial forces along the hot fluid region which overcomes a cold region formed along the lower right corner of the enclosure. The heat transfer is almost constant for all Schmidt numbers at $Br = 0.0$. It is also observed that as Br is increased, the cold space getting mixed with the inlet air in the bottom and flown towards the exit vicinity. The temperature gradients are almost linear for $0.0 \leq Br \leq 10.0$ with $0.7 \leq Sc \leq 10.0$.

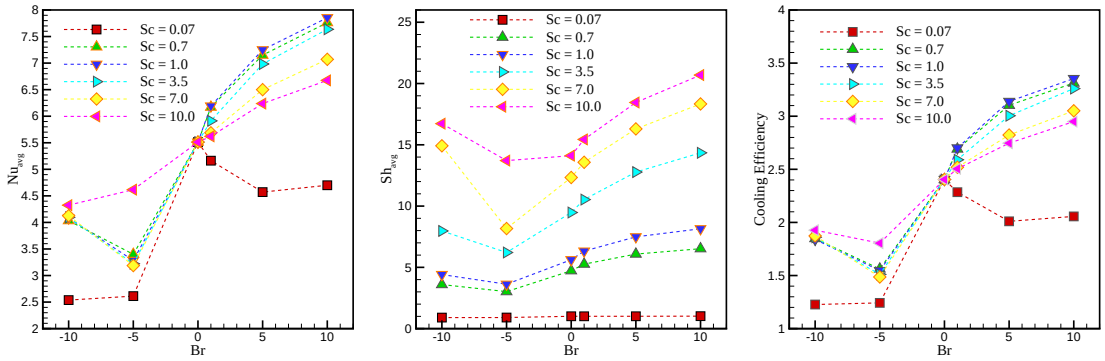

(a) (b) (c)

Figure 2.11: Effect of Buoyancy ratio and Schmidt number on (a) average Nusselt number, (b) average Sherwood number on heated block and (c) cooling efficiency inside the enclosure at $Re = 200$, $Ri = 1.0$, $Pr = 0.71$ for Configuration-I.

But, for $Sc = 0.07$ with $0.0 < Br \leq 10.0$ the temperature gradients goes down linearly as observed from profiles Fig. 2.11 (a). This implies that temperature distribution stratifies near the central region and then temperature variation is very small close to the cold wall. Hence, average Nusselt number going down closed to the outlet. Fig. 2.11 (b) shows the variation of average Sherwood number for different buoyancy ratio and Schmidt numbers. It was found that mass transfer is weak when the buoyancy ratio is small (Fig. 2.11 (b)) because the flow is dominated by natural convection. This is happened naturally in case of weak contaminant sources and it requires a strong heat source to drive the flow to compete with the external forced convection effect. The comparison of efficient cooling for different Schmidt number is made with the variation of buoyancy ratios and is presented in Fig. 2.11 (c). The cooling efficiency is found to be increasing when the Schmidt number is increasing with the Br values. For the cooling efficiency inside the ventilated enclosure, the average Nusselt number closed to the heated block should be lower than the bulk fluid temperature. The variation of Nu_{avg} and cooling efficiency are almost similar for configuration-I. This signifies that mass transfer has little influence over the heat transfer rate for cooling but, the maximum cooling efficiency is achieved for moderate Sc number with largest buoyancy ratio.

A brief analysis of cooling efficiency, average Nusselt number and Sherwood number for configuration-II is made in Fig. 2.12 where the inlet and outlet entrances are exchanged

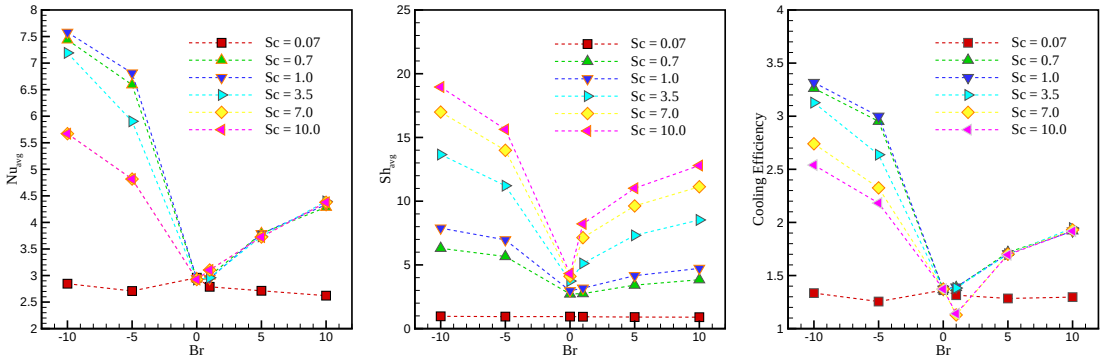

(a) (b) (c)

Figure 2.12: Effect of Buoyancy ratio and Schmidt number on (a) average Nusselt number, (b) average Sherwood number on heated block and (c) cooling efficiency inside the enclosure at $Re = 200$, $Ri = 1.0$, $Pr = 0.71$ for Configuration-II.

for different Sc and Br values. A steep variation of heat and mass transfer rate is observed for low buoyancy ratio (Fig. 2.12(a), (b)). The heat and mass flow rate are found to be same without any buoyancy effects for all Schmidt numbers. Hence, the cooling efficiency is also stabilized at zero buoyancy effects (Fig. 2.12 (c)). For fixed Sc, the cooling efficiency decreases with an increase of Br.

If two different configurations are compared for the same values of Sc number and buoyancy ratios then the maximum cooling efficiency is observed in configuration-I. This signifies that maximum air is cold at the exit when the inlet is placed along the bottom and exit along the top of the enclosure respectively. It is also observed that the maximum variation of Nu_{avg} is 40.72% when the Sc is increased from 0.07 to 10.0 for $Br = 10.0$ and the variation for Sh_{avg} is 92.98%.

2.5.5 Effect of Richardson number and Schmidt number

Fig. 2.13 & 2.14 represents the combined effect of Richardson number and Schmidt number on average Nusselt number, Sherwood number and cooling efficiency inside the enclosure for configuration-I & II. For fixed Richardson number, the isotherm profiles are almost same when $0.07 \leq Sc < 1.0$ and the heat transfer rate is not much effected by the variation in Schmidt number (Fig. 2.13(a)). When Richardson number is small, most of the isothermal lines passing diagonally through the bottom right corner of the block but

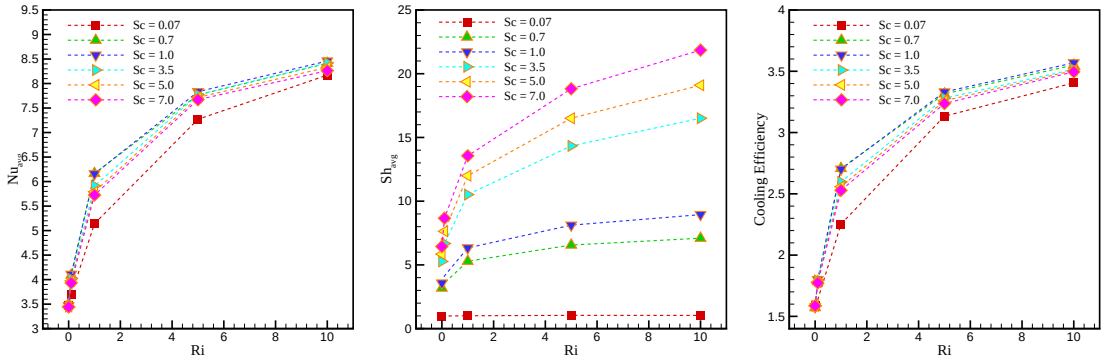

(a) (b) (c)

Figure 2.13: Effect of Richardson number and Schmidt number on (a) average Nusselt number, (b) average Sherwood number on heated block and (c) cooling efficiency inside the enclosure at $Re = 200$, $Br = 1.0$, $Pr = 0.71$ for Configuration-I.

there exist a sharp variation of isoconcentration lines along the lower left corner of the obstacle due to diffusion effect and a recirculation zone is formed towards the left vertical wall which causes higher mass transfer rate. A large variation of mass transfer rate is observed between $Sc > 0.07$ and $Sc \leq 1.0$ with the variation of Richardson numbers (Fig. 2.13 (b)), since recirculation eddy is stronger. With the increase in Ri, most of the isoconcentration lines getting passed through thermosoluted block and higher cooling efficiency is achieved (Fig. 2.13 (c)). The higher thermal, solutal and cooling efficiency is observed at higher Richardson number with higher Sc values. For configuration-I, it is observed that when Sc varies from 0.07 to 10.0, the maximum variation in Nu_{avg} is 16.62 % for $Ri = 1.0$, in Sh_{avg} is 95.25 % for $Ri = 10.0$ and in cooling efficiency is 6.57 % for $Ri = 1.0$ (Fig. 2.13(a), (b) & (c)).

When the flow is dominated by forced convection ($Ri < 1.0$), the heat transfer rate and cooling efficiency is found to be decreasing in case of configuration-II and it is found to be increasing with the increasing value of Richardson number (Fig. 2.14). Due to density difference, cold fluid in the inlet region tries to move downwards and getting retarded by the hot streams close to the obstacle resulting a leading circulating eddy around the block with two hot stream zones. But, the heat transfer is optimized for large Ri and there exist a linear increasing profile for increment of Br & Sc (Fig. 2.14(a)). The isoconcentration has a large deposition along the lower left corner which causes a slow

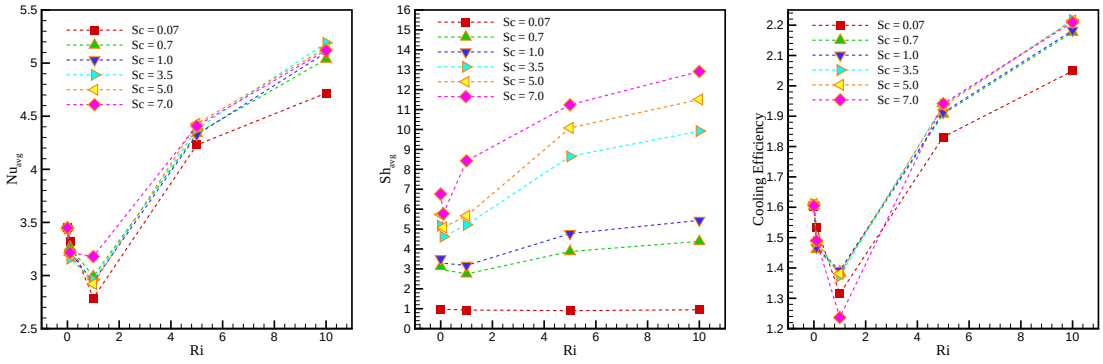

(a) (b) (c)

Figure 2.14: Effect of Richardson number and Schmidt number on (a) average Nusselt number, (b) average Sherwood number on heated block and (c) cooling efficiency inside the enclosure at $Re = 200$, $Br = 1.0$, $Pr = 0.71$ for Configuration-II.

variation of Sherwood number with the increment of Ri values (Fig. 2.14 (b)). Due to the opposing buoyancy effect of heat and mass flow, the cooling efficiency has a very small variation with the increment of Ri (Fig. 2.14 (c)). The maximum cooling efficiency is preserved if configuration-I is considered with higher Richardson number with $Sc = 1.0$. The difference in cooling efficiency is found to be 38.84 % between configuration-I and configuration-II for $Ri = 10.0$ and $Sc = 1.0$.

2.6 Conclusion

Simulations are performed to study the mixed convection effects due to a thermosoluted block in a ventilated enclosure with the variation of flow parameters like buoyancy ratio, Richardson number & Schmidt number. Two different configurations are considered to visualize the heat and mass transfer effect to study the maximum cooling efficiency due to the thermosoluted exchanger. Based on the above results the following remarks can be concluded:

1. The flow is mostly dominated by the convection effects for any fixed values of Br and $Ri \geq 1.0$. If the inlet source is located at the bottom section of left wall of the enclosure then at moderate values of Richardson number ($Ri = 1.0$), a strong hot recirculating zone is found around the block which causes a strong inertial effect with the moving cold fluid.

2. Increment in Ri from 1.0 to 10.0 always produces an increment in average heat transfer rate, mass transfer rate and cooling efficiency for both the configurations due to convection effects.

3. When $Ri = 10.0$ for configuration-I, average Nusselt number and cooling efficiency is found to be maximum for $Br = 10.0$ corresponding to $Sc = 1.0$ but average Sherwood number is higher for $Br = 10.0$ corresponding to $Sc = 10.0$.

4. In case of configuration-II, average Nusselt number and cooling efficiency is found to be maximum for $Ri = 10.0$ corresponding to $Br = -10.0$ and $Sc = 1.0$ and average Sherwood number is higher at $Ri = 10.0$ corresponding to $Br = -10.0$ and $Sc = 10.0$.

5. The maximum variation in average Nusselt number on the surface of thermosoluted block is 40.72 % and in average Sherwood number is 92.98 %, when the Schmidt number varies from 0.07 to 10.0 with $Br = 10.0$.

6. Under simultaneous effect of Schmidt number and Richardson number, average Sherwood number is higher for configuration-I compared to configuration-II and maximum value is obtained for $Sc = 7.0$ with $Ri = 10.0$.

Chapter 3

Conjugate heat and species transport in an air filled ventilated enclosure with different positioning of thermo-contaminated block *

3.1 Introduction

The combined effect of heat and species transfer in ventilated enclosure is receiving significant attention because of its great interest in the phenomena of many practical engineering problems such as solar collectors, heat exchangers, space heating, chemical reactors, energy storage, equipment cooling and biomedical engineering [102, 75, 94, 108]. Many heat sources within a building (people, electronic equipment, heat or pollutant generating obstacles) can be considered as localized and understanding the way in which they stratify a space is very essential to design the efficient ventilation schemes. There are many types of airborne contaminants in buildings and are broadly classified into two types: gaseous and particulate [21]. In the present chapter, gaseous kind of air borne contaminants are assumed, which are usually considered as passive contaminants and followed exactly the air currents in space. Some of these common gaseous contaminants found in buildings are carbon monoxide, carbon dioxide, nitrogen oxide, ozone moisture, sulphur dioxide and its progeny. Many of these gaseous contaminants are combustion by-products. There is increasing concern about the levels of these contaminants in outdoor and consecutively the indoor air after observing the proliferation of transportation and industrial sources.

*The contents of this chapter has been published in *International Journal of Heat and Mass Transfer, Elsevier, DOI:10.1016/j.ijheatmasstransfer.2017.10.028*

In many situations initial pollutant emission and contaminant source information is not known to us. Referring to the up-to-date safety problems of indoor air environment, the 'spying covered' pollutant sources effusing colorless and non-fragrance pollutants will pose a great danger to the occupants and could not easily identified due to their productions or emissions are essentially of no noise, no colour and smell. To detect any chemical or biological agents or infectious viruses, pollutant sensors should be installed to avoid any possible expose of the fatal contaminants to the occupants. The dense distribution of these pollutant sensors in the whole building for detection of these agents are relatively expensive and bulky. Therefore, it is necessary to identify these fatal contaminant or heat sources merely depending on the limited information from the sparsely distributed sensors [60]. In this prospective, a thermo-contaminated block is positioned at different locations in the ventilated room to identify the best possible location to detect or pass the energy flux in a quickest manner. It is also assumed that the third dimension of the enclosure is large enough such that room air and heat transfer are two-dimensional. Numerous experimental and numerical works were conducted in a ventilated enclosure based on the convective effects due to the presence of obstacles or body with various isothermal conditions [90]. During the last decade, numerical investigation on double diffusive natural convection in enclosures due to differentially heated, cooled or different positioning of blocks are carried out for effective cooling or heating [82], [83], [18] [66]. The literature survey shows that for cooling of the heat generating body in which large heat fluxes are to be exhausted, is to allow a low forced convective cooling and buoyancy effect simultaneously. Fans are mostly placed at the exit or at the entrance based on the performance of the system to obtain a pleasant medium. The analysis of the above problem finally motivates to study the mixed convective heat and mass transfer in a vented cavity, however, in the present day scenario, analysis capability plays a vital prerequisite for design even if many commercial softwares are available to analyze the systems.

A mixed convective numerical study in an enclosure with a finite-size heat conducting body is carried by Hsu and How [47]. They observed that heat transfer rate is affected by the change of locations of the outflow openings and the average heat transfer rate is higher when the heat conducting body is existing at far away from the inlet port. Shuja et al. [106] studied the heat transfer effects in a ventilated enclosure where a rectangular

heated solid body is placed along the center and found that maximum variation of heat transfer is observed along the upper section of the cavity when the exit port is placed at the bottom wall. Numerical and experimental studies of mixed convection due to a heat generating element (heater) in a ventilated cavity is carried by Radhakrishnan et al. [90] by varying the heat source location to obtain the optimum thermal performance. They observed that effective cooling can be achieved when heater is placed within the main flow. Rahman et al. [91] numerically investigated the steady laminar mixed-convective flow in a ventilated square enclosure. The right vertical wall is heated and a heat conducting solid circular cylinder is placed inside the center of the enclosure to analyze the flow and heat transfer effects inside the cavity by changing the diameter of the cylinder. It is found that the heat transfer rate is increasing with the increase of Richardson number at constant cylinder diameter. In continuation of that work, Rahman et al. [92] tried to find the effect of heat transfer rate by placing a heat conducting square cylinder at different positions of the ventilated enclosure. The right vertical wall of the enclosure is maintained with high temperature as compared to other walls and the other walls are considered to be adiabatic. The maximum heat transfer is obtained in the forced convection dominated area when the cylinder is located near the top wall along the mid-vertical plane.

Mamum et al. [68] studied mixed convection heat transfer effect in a ventilated square cavity by placing a heated hollow cylinder at the center of the cavity using finite element based Galerkin method. They found that for largest value of the cylinder diameter, maximum average Nusselt number and average fluid temperature can be obtained. Moreover, fluid temperature is increasing with the increasing value of Richardson number for fixed value of cylinder diameter. Literature suggests that for the maximum cooling of heat generating body inside the enclosure, body must be located along the main flow stream near the top wall and highest heat transfer rate can be achieved for increase of Richardson number. A combined numerical and experimental study is performed by Radhakrishnan et. al. [89] in a ventilated cavity to obtain the convective heat transfer effects due to multiple heaters in a staggered arrangement. They evaluated the operating temperature of each heater for a wide range of dimensionless parameters and found that for high values of Reynolds number, the percentage increase in Nusselt number is low for the middle heaters compared to the heaters on either side (left or right).

A numerical investigation of mixed convection from a heated square solid cylinder located near the center of a vented cavity filled with air is made by Chamkha et al. [23]. The flow and the thermal field effect due to varying outlet positions with fixed inlet position is studied for a wide range of Richardson number, Reynolds number, locations and aspect ratios of the inner square cylinder. They observed that average Nusselt number along the heated surface of the square cylinder increases with the increase in Reynolds and Richardson number. They also concluded that average fluid temperature in the enclosure appeared to be constant for a highly buoyancy-dominated convection regime. A numerical study of mixed convection and heat transfer in a ventilated enclosure with a heat-generating solid circular block is made by Rahman et al. [93] to analyze the effects of Reynolds and Prandtl number. They concluded that increasing the Prandtl number results an increase in the heat transfer rate along the block and a decrease in the average temperature of the fluid inside cavity. A numerical study with heat conducting circular block in a ventilated cavity with heated vertical wall is made by Gupta et al. [43] for different values of cylinder diameters. They found that for lower Richardson number, heat transfer rate increases with increase in cylinder diameter while for higher Richardson number, the heat transfer rate decreases with increase in cylinder diameter.

Xu et al. [121] analyzed the double diffusive mixed convection around a heated circular cylinder in an enclosure with different boundary conditions. The inflow opening which is placed along the lower-left wall is considered to be at low temperature and concentration whereas the heated cylinder which is placed at the center of the enclosure is considered at high temperature and concentration. The flow and heat transfer are independent of Lewis number for low Richardson number with buoyancy ratio $Br = 1.0$ and the heat transfer rate around the heated cylinder decreases with the increase of buoyancy ratio for all Lewis numbers. The mass transfer rate increases with the increase in Lewis number for fixed buoyancy ratio. This work is further extended by considering the cylinder locations (lower, middle and upper) to study the effects of Lewis number and buoyancy ratio with the variation of Richardson number [122]. It is found that for a fixed cylinder location, the increase in Lewis number results the significant increment in mass transfer rate whereas the heat transfer rate remains constant.

A mixed convection numerical study related to thermal management in a ventilated

enclosure is made by Biswas et al. [20] by dividing the heating element into multiple equal segments locating on vertical side walls. It is observed that the heat transfer from segmental heating element is always superior to whole heating element. Ren et al. [95] investigated the combined natural and forced convection effects in a ventilated enclosure with discrete heat and airborne pollutants to represent the heat and mass transport phenomena for different flow structures. Karimi et al. [55] numerically studied the mixed convection flow around two heated circular cylinders of equal diameters in a square ventilated enclosure to analyze the effects of cylinder diameter, Reynolds number and Richardson number on the flow and heat transfer characteristics and concluded that the average Nusselt number over the surface of cylinders is increasing with the increase in cylinder size. A numerical investigation on steady and turbulence flow is made by Koufi et al. [57] to analyze the ventilation efficiency for temperature distribution inside the ventilated enclosure. The above cited studies reflect the heat and mass transfer rate variation due to the mixed convection and observed that positioning of obstacle plays a vital role for maximum flow variation.

Very few studies have been carried out so far for the complete discussion of the convection dominated flow with heat and mass transfer effects in a ventilated enclosure with heat and contaminant sources. Most of the recent literature discussed above have considered the discrete heat sources with the variation of inlet and outlet port to find the maximum cooling efficiencies. To the best of authors knowledge, the problem dealing with the double diffusive convection inside an enclosure with a thermo-contaminated square block subjected to a flux-in of cold air and flux-out of contaminated air is not yet been dealt in the literature. In this chapter, the impact of different locations and sizes of thermo-contaminated block is considered inside the ventilated enclosure, which is a numerical study related to pollutant removing, thermal design of buildings, smoke control in tunnels, thermal comfort and industrial drying technologies [108], [75], [90]. Simulations are performed for a wide range of Grashof number, Reynolds number and Richardson number and the detailed findings are presented in the form of streamlines, isotherms and isoconcentrations. Cooling efficiency, average temperature and species transport in the form of average Nusselt number and average Sherwood number around the block are calculated to find the effective variation of temperature and concentration.

3.2 Physical Configuration and Mathematical Modeling

A ventilated square enclosure of length L is considered to investigate two-dimensional double diffusive mixed convection as shown in Fig. 3.1 and a thermally and solutally activated square block of length h is placed inside the enclosure. All walls are considered to be adiabatic and impermeable. Cold fluid is injected through the inlet port placed on the bottom of left vertical wall and contaminated air is exited through the outlet port placed on the top of right vertical wall. Simulations are conducted for different block positions and sizes. Five cases are considered for block positions: in case-I, block is placed in the middle of the enclosure ($L_x = 0.5, L_y = 0.5$), in case-II, block is placed near the right vertical wall ($L_x = 0.75, L_y = 0.5$), in case-III, block is situated near the left vertical wall ($L_x = 0.25, L_y = 0.5$), in case-IV, the block is positioned near the upper wall ($L_x = 0.5, L_y = 0.75$) and in last for case-V, the block is near the bottom wall ($L_x = 0.5, L_y = 0.25$). The aspect ratio (h/L) varies from 0.2 to 0.6 and simulations are performed for various values of Reynolds number, Richardson number, Grashof number and buoyancy ratio for fixed value of Prandtl number, Pr=0.71 and Schmidt number, Sc=1.0 (Methanol diffusing in air).

The fluid is assumed to be Newtonian, viscous and incompressible and the flow is assumed to be laminar. The governing equations for fluid flow, heat and species transfer includes continuity equation (conservation of mass), Navier-Stokes equation (conservation of momentum), energy equation (conservation of energy) and concentration equation (conservation of species). The flow is driven due to the buoyancy effects created by the temperature differences and concentration differences and the forced convection effects by the injected cold air inside the enclosure. The density associated in the body force term of y-momentum equation is assumed to follow the Boussinesq approximation as:

$$\rho = \rho_0[1 - \beta_T(T^* - T_0) - \beta_C(C^* - C_0)], \tag{3.1}$$

where $\beta_T = -\frac{1}{\rho}\frac{\partial \rho}{\partial T^*}$ and $\beta_C = -\frac{1}{\rho}\frac{\partial \rho}{\partial C^*}$ [79]. The thermal expansion coefficient, β_T is always positive because density decreases with the increasing temperate while the solutal expansion coefficient, β_C may be either positive or negative because, an increase in concentration induces a decrease or an increase in density, respectively [39].

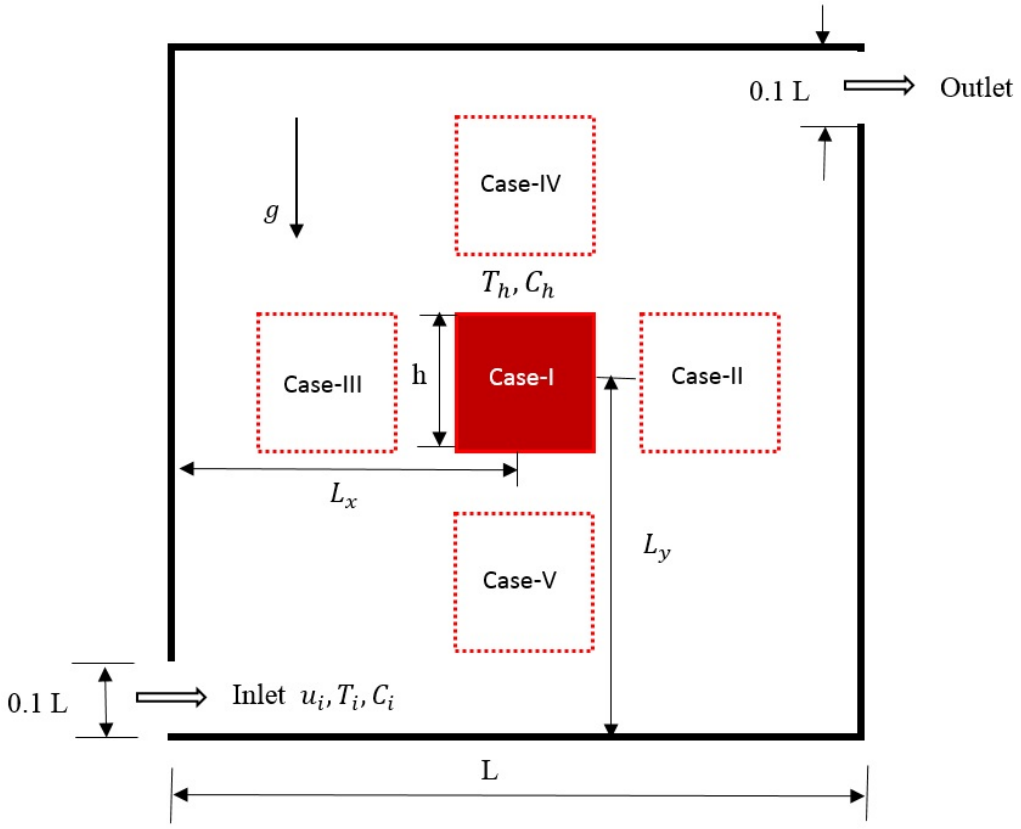

Figure 3.1: Problem Geometry

The governing equations in dimensional form with the above mentioned assumptions are given by:

$$\nabla \cdot \overrightarrow{v} = 0, \tag{3.2}$$

$$\frac{\partial u^*}{\partial t^*} + (\overrightarrow{v} \cdot \nabla)u^* = -\frac{1}{\rho}\left(\frac{\partial p^*}{\partial x^*}\right) + \nu(\nabla^2 u^*), \tag{3.3}$$

$$\frac{\partial v^*}{\partial t^*} + (\overrightarrow{v} \cdot \nabla)v^* = -\frac{1}{\rho}\left(\frac{\partial p^*}{\partial y^*}\right) + \nu(\nabla^2 v^*) + g\beta_T(T^* - T_0) + g\beta_C(C^* - C_0), \tag{3.4}$$

$$\frac{\partial T^*}{\partial t^*} + (\overrightarrow{v} \cdot \nabla)T^* = \alpha(\nabla^2 T^*), \tag{3.5}$$

$$\frac{\partial C^*}{\partial t^*} + (\overrightarrow{v} \cdot \nabla)C^* = D(\nabla^2 C^*). \tag{3.6}$$

The above mentioned equations can be expressed in non-dimensional form by using the following dimensionless variables:

$$x = \frac{x^*}{L}; \quad y = \frac{y^*}{L}; \quad u = \frac{u^*}{u_i}; \quad v = \frac{v^*}{u_i}; \quad t = \frac{t^* u_i}{L};$$

$$p = \frac{p^*}{\rho u_i^2}; \quad T = \frac{(T^* - T_0)}{(T_h - T_0)}; \quad C = \frac{(C^* - C_0)}{(C_h - C_0)}. \tag{3.7}$$

$$Re = \frac{u_i L}{\nu}; \quad Pr = \frac{\nu}{\alpha}; \quad Gr = \frac{g\beta_T(T_h - T_0)L^3}{\nu^2};$$
$$Br = \frac{\beta_C(C_h - C_0)}{\beta_T(T_h - T_0)}; \quad Ri = \frac{Gr}{Re^2}; \quad Sc = \frac{\nu}{D}. \tag{3.8}$$

The governing equations in dimensionless form can be described as:

$$\frac{\partial u}{\partial x} + \frac{\partial v}{\partial y} = 0, \tag{3.9}$$

$$\frac{\partial u}{\partial t} + \frac{\partial (uu)}{\partial x} + \frac{\partial (vu)}{\partial y} = -\frac{\partial p}{\partial x} + \frac{1}{Re}\left(\frac{\partial^2 u}{\partial x^2} + \frac{\partial^2 u}{\partial y^2}\right), \tag{3.10}$$

$$\frac{\partial v}{\partial t} + \frac{\partial (uv)}{\partial x} + \frac{\partial (vv)}{\partial y} = -\frac{\partial p}{\partial y} + \frac{1}{Re}\left(\frac{\partial^2 v}{\partial x^2} + \frac{\partial^2 v}{\partial y^2}\right) + Ri(T + Br.C), \tag{3.11}$$

$$\frac{\partial T}{\partial t} + \frac{\partial (uT)}{\partial x} + \frac{\partial (vT)}{\partial y} = \frac{1}{Re \cdot Pr}\left(\frac{\partial^2 T}{\partial x^2} + \frac{\partial^2 T}{\partial y^2}\right), \tag{3.12}$$

$$\frac{\partial C}{\partial t} + \frac{\partial (uC)}{\partial x} + \frac{\partial (vC)}{\partial y} = \frac{1}{Re \cdot Sc}\left(\frac{\partial^2 C}{\partial x^2} + \frac{\partial^2 C}{\partial y^2}\right). \tag{3.13}$$

The initial conditions for $t = 0$ are given by:

$$u = 0, \quad v = 0, \quad T = 0, \quad C = 0; \quad 0 \leq x, y \leq 1 \tag{3.14}$$

Concerning the dynamic and thermal field close to the air supply, the boundary conditions in dimensionless form for time $t > 0$ associated with the above governing equations are given by:

along the bottom and upper walls,

$$u = 0, \quad v = 0, \quad \frac{\partial T}{\partial y} = 0, \quad \frac{\partial C}{\partial y} = 0; \qquad y = 0, 1; \quad 0 \leq x \leq 1.0 \tag{3.15}$$

along vertical walls,

$$u = 0, \quad v = 0, \quad \frac{\partial T}{\partial x} = 0, \quad \frac{\partial C}{\partial x} = 0; \qquad x = 0, \quad x = 1 \tag{3.16}$$

along the inlet:

$$u = 1, \quad v = 0, \quad T = -0.5, \quad C = 0 \tag{3.17}$$

along the outlet:

$$\frac{\partial u}{\partial x} = 0, \quad \frac{\partial v}{\partial x} = 0, \quad \frac{\partial T}{\partial x} = 0, \quad \frac{\partial C}{\partial x} = 0 \tag{3.18}$$

on the surface of square block:

$$u = 0, \quad v = 0, \quad T = 1, \quad C = 1 \tag{3.19}$$

The heat transfer rate along the surface of block is defined by the average Nusselt number (Nu_{avg}) and is given by:

$$Nu_{avg} = -\frac{1}{4A}\Bigg[\int_{L_y-A/2}^{L_y+A/2}\left(\frac{\partial T}{\partial x}\right)_{L_x+A/2} dy + \int_{L_x-A/2}^{L_x+A/2}\left(\frac{\partial T}{\partial y}\right)_{L_y+A/2} dx + \int_{L_y-A/2}^{L_y+A/2}\left(\frac{\partial T}{\partial x}\right)_{L_x-A/2} dy + \int_{L_x-A/2}^{L_x+A/2}\left(\frac{\partial T}{\partial y}\right)_{L_y-A/2} dx\Bigg]. \tag{3.20}$$

The mass transfer rate along the surface of the block is described by the average Sherwood number (Sh_{avg}) and is defined by:

$$Sh_{avg} = -\frac{1}{4A}\Bigg[\int_{L_y-A/2}^{L_y+A/2}\left(\frac{\partial C}{\partial x}\right)_{L_x+A/2} dy + \int_{L_x-A/2}^{L_x+A/2}\left(\frac{\partial C}{\partial y}\right)_{L_y+A/2} dx + \int_{L_y-A/2}^{L_y+A/2}\left(\frac{\partial C}{\partial x}\right)_{L_x-A/2} dy + \int_{L_x-A/2}^{L_x+A/2}\left(\frac{\partial C}{\partial y}\right)_{L_y-A/2} dx\Bigg]. \tag{3.21}$$

The bulk average temperature [23] is defined as:

$$\theta_{avg} = \int \frac{T\ d\overline{V}}{\overline{V}}, \tag{3.22}$$

where $\overline{V}$ is the enclosure volume.

The cooling efficiency [85] is given by

$$\epsilon = 1 - \left(\frac{\overline{T}_{out}}{\overline{T}_{in}}\right), \tag{3.23}$$

where average inlet and outlet temperature are defined as:

$$\overline{T}_{in} = \left(\int_{A_{in}} T\ \overrightarrow{V}.\ n\ dA_{in}\right) \Big/ \left(\int_{A_{in}} \overrightarrow{V}.\ n\ dA_{in}\right), \tag{3.24}$$

and

$$\overline{T}_{out} = \left(\int_{A_{out}} T\ \overrightarrow{V}.\ n\ dA_{out}\right) \Big/ \left(\int_{A_{out}} \overrightarrow{V}.\ n\ dA_{out}\right), \tag{3.25}$$

where $\overrightarrow{V}$ is the velocity vector, n is the inward normal vector, A_{in} and A_{out} are the inlet and outlet areas, respectively.

3.3 Numerical procedure

The set of flow governing equations with specified boundary conditions are solved by SIMPLE (Semi Implicit Method for Pressure Linked Equations) algorithm based on finite volume approach [86] using the staggered grid arrangement. Finite volume method involves the integration of governing equations over a two-dimensional control volume on a staggered grid (Fig. 3.2) in which different control volumes are considered to discretise different equations. In staggered grid, scalar variables (pressure, temperature and concentration) are stored at the cell center while the velocity components are stored at the cell faces (u-velocity at east and west faces, v-velocity at north and south faces). Continuity equation is discretised over scalar control volume (square ABCD in Fig. 3.2), x-momentum equation is disretised over the $(i,j)^{th}$ control volume for u (square IJKL in Fig. 3.2) and y-momentum equation is disretised over the $(i,j)^{th}$ control volume for v (square EFGH in Fig. 3.2).

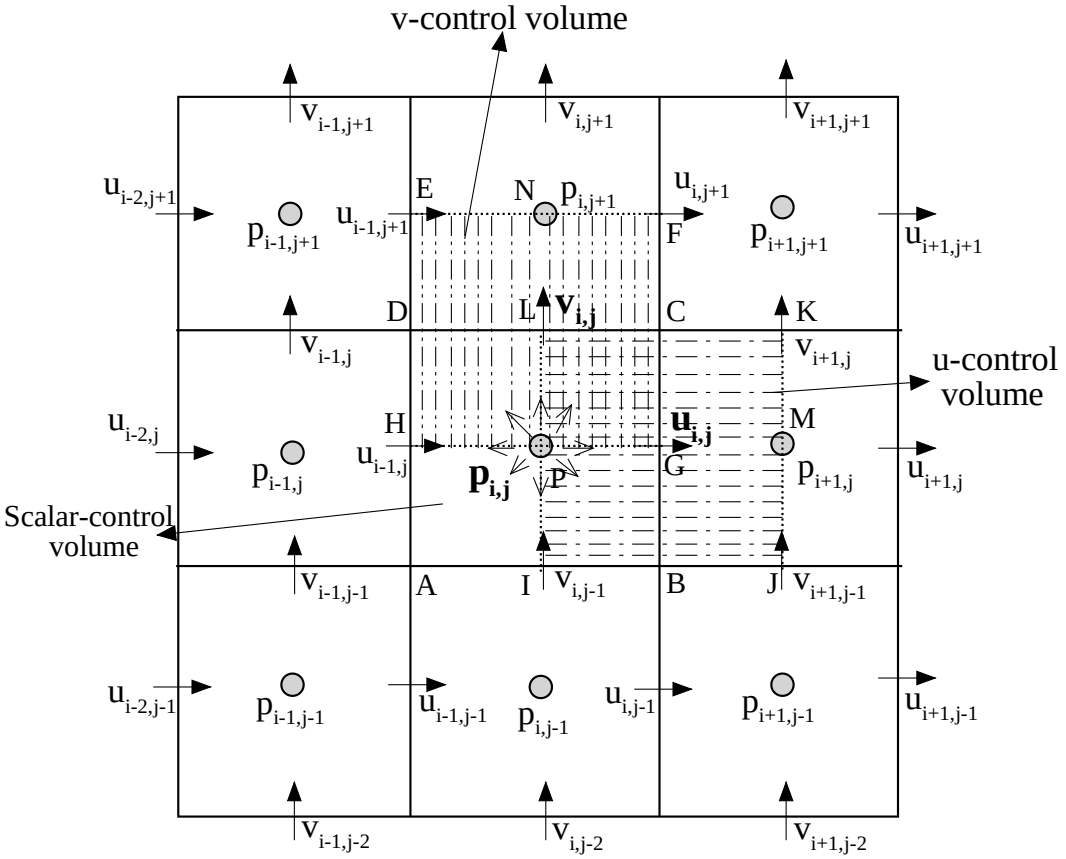

Figure 3.2: Control-volume arrangement for u, v and p in staggered grid

The non-linear terms in the governing equations are tackled by Newton's linearization technique. The non-linear treatments are described as follows:
for x-momentum equation, the non-linear terms are integrated over the u-control volume (square IJKL in Fig. 3.2) as:

$$\begin{aligned}\int \frac{\partial uu}{\partial x} dV &= \frac{(uu)_M - (uu)_P}{\Delta x} \\ &= \frac{1}{\Delta x}\left[(u)_M^{k+1}(u)_M^k - (u)_P^{k+1}(u)_P^k\right] \\ &= \frac{1}{\Delta x}\left[\left(\frac{u_{i,j}^{k+1} + u_{i+1,j}^{k+1}}{2}\right)\left(\frac{u_{i,j}^k + u_{i+1,j}^k}{2}\right) - \left(\frac{u_{i-1,j}^{k+1} + u_{i,j}^{k+1}}{2}\right)\left(\frac{u_{i-1.j}^k + u_{i,j}^k}{2}\right)\right],\end{aligned} \tag{3.26}$$

$$\begin{aligned}\int \frac{\partial uv}{\partial y} dV &= \frac{(uv)_C - (uv)_B}{\Delta y} \\ &= \frac{1}{\Delta y}\left[(u)_C^{k+1}(v)_C^k - (u)_B^{k+1}(v)_B^k\right] \\ &= \frac{1}{\Delta y}\left[\left(\frac{u_{i,j}^{k+1} + u_{i,j+1}^{k+1}}{2}\right)\left(\frac{v_{i,j}^k + v_{i+1,j}^k}{2}\right) - \left(\frac{u_{i,j-1}^{k+1} + u_{i,j}^{k+1}}{2}\right)\left(\frac{v_{i,j-1}^k + v_{i+1,j-1}^k}{2}\right)\right].\end{aligned} \tag{3.27}$$

For y-momentum equation, the non-linear terms are integrated over v-control volume (square EFGH in Fig. 3.2) as:

$$\begin{aligned}\int \frac{\partial uv}{\partial x} dV &= \frac{(uv)_C - (uv)_D}{\Delta x} \\ &= \frac{1}{\Delta x}\left[(v)_C^{k+1}(u)_C^k - (v)_D^{k+1}(u)_D^k\right] \\ &= \frac{1}{\Delta x}\left[\left(\frac{v_{i,j}^{k+1} + v_{i+1,j}^{k+1}}{2}\right)\left(\frac{u_{i,j}^k + u_{i,j+1}^k}{2}\right) - \left(\frac{v_{i-1,j}^{k+1} + v_{i,j}^{k+1}}{2}\right)\left(\frac{u_{i-1,j}^k + u_{i-1,j+1}^k}{2}\right)\right],\end{aligned} \tag{3.28}$$

$$\begin{aligned}\int \frac{\partial vv}{\partial y} dV &= \frac{(vv)_N - (vv)_P}{\Delta y} \\ &= \frac{1}{\Delta y}\left[(v)_N^{k+1}(v)_N^k - (v)_P^{k+1}(v)_P^k\right] \\ &= \frac{1}{\Delta y}\left[\left(\frac{v_{i,j}^{k+1} + v_{i,j+1}^{k+1}}{2}\right)\left(\frac{v_{i,j}^k + v_{i,j+1}^k}{2}\right) - \left(\frac{v_{i,j-1}^{k+1} + v_{i,j}^{k+1}}{2}\right)\left(\frac{v_{i,j-1}^k + v_{i,j}^k}{2}\right)\right].\end{aligned} \tag{3.29}$$

The non-linear terms in temperature and concentration equation are discretised over scalar control volume (square ABCD in Fig. 3.2) as:

$$\int \frac{\partial uT}{\partial x} dV = \frac{(uT)_G - (uT)_H}{\Delta x}$$
$$= \frac{1}{\Delta x}\left[(T)_G^{k+1}(u)_H^k - (T)_H^{k+1}(u)_H^k\right]$$
$$= \frac{1}{\Delta x}\left[\left(\frac{T_{i,j}^{k+1} + T_{i+1,j}^{k+1}}{2}\right)u_{i,j}^k - \left(\frac{T_{i-1,j}^{k+1} + T_{i,j}^{k+1}}{2}\right)u_{i-1,j}^k\right], \tag{3.30}$$

$$\int \frac{\partial vT}{\partial y} dV = \frac{(vT)_L - (vT)_I}{\Delta y}$$
$$= \frac{1}{\Delta y}\left[(T)_L^{k+1}(v)_L^k - (T)_I^{k+1}(v)_I^k\right]$$
$$= \frac{1}{\Delta y}\left[\left(\frac{T_{i,j}^{k+1} + T_{i,j+1}^{k+1}}{2}\right)v_{i,j}^k - \left(\frac{T_{i,j-1}^{k+1} + T_{i,j}^{k+1}}{2}\right)v_{i,j-1}^k\right], \tag{3.31}$$

$$\int \frac{\partial uC}{\partial x} dV = \frac{(uC)_G - (uC)_H}{\Delta x}$$
$$= \frac{1}{\Delta x}\left[(C)_G^{k+1}(u)_H^k - (C)_H^{k+1}(u)_H^k\right]$$
$$= \frac{1}{\Delta x}\left[\left(\frac{C_{i,j}^{k+1} + C_{i+1,j}^{k+1}}{2}\right)u_{i,j}^k - \left(\frac{C_{i-1,j}^{k+1} + C_{i,j}^{k+1}}{2}\right)u_{i-1,j}^k\right], \tag{3.32}$$

$$\int \frac{\partial vC}{\partial y} dV = \frac{(vC)_L - (vC)_I}{\Delta y}$$
$$= \frac{1}{\Delta y}\left[(C)_L^{k+1}(v)_L^k - (C)_I^{k+1}(v)_I^k\right]$$
$$= \frac{1}{\Delta y}\left[\left(\frac{C_{i,j}^{k+1} + C_{i,j+1}^{k+1}}{2}\right)v_{i,j}^k - \left(\frac{C_{i,j-1}^{k+1} + C_{i,j}^{k+1}}{2}\right)v_{i,j-1}^k\right]. \tag{3.33}$$

The discretised algebraic equations are simulated by the SIMPLE algorithm. This procedure is based on a cyclic series of guess and correct operations to solve the governing equations. The velocity components are first calculated from the momentum equations using guessed pressure field and then corrected so that the continuity equation is satisfied and this process continues until the solution converges. Throughout the calculations, velocities, temperature and concentration are considered to be converged, if,

$$|\varphi_{i,j}^{k+1} - \varphi_{i,j}^k| \leq 10^{-6}, \tag{3.34}$$

where $\varphi = (u, v, T, C)$ are the flow variables, k is the iteration number and (i, j) denote the calculation node point. A time-dependent numerical solution is obtained by advancing the flow field variables through a sequence of shorter time steps of duration 0.001. A steady-state is achieved after a transient state, which is independent of the initial conditions and the desired convergence for flow variables requires about 60,000 iterations.

3.4 Grid independency test and code validation

The grid independency test is performed by varying the grid sizes between 60×60 to 140×140 as shown in Table 3.1.

Table 3.1: Grid independency test when $Ri = 1.0$ and $Re = 200$.

Grid Point ($n \times m$)	Sh_{avg}	Cooling Efficiency
60×60	11.89275	2.57042
80×80	11.95991	2.56315
100×100	12.00160	2.55121
120×120	12.00398	2.55474
140×140	12.00961	2.55821

From Table 3.1, it is observed that no significant change is found after the grid size 100×100. Therefore, all computations are made by using the grid size 100×100 as the optimal grid size.

Before the discussion of the results, it is required that the numerical code is tested and verified by the related published research. To validate the accuracy of the numerical code, a comparison is made with the work of Chamkha et al. [23] by considering mixed convection in a square vented cavity with a horizontal heated square block. They considered a square solid cylinder of width $0.2L$ placed inside a square cavity of length L. Cylinder is maintained at higher temperature compared to the inlet air, walls are kept adiabatic and a fixed inlet opening is considered along the middle of left vertical wall of length $0.1L$ while outflow opening is varied at the different locations of the right vertical wall. Fig.3.3 (a) represents the comparison of average Nusselt number along the block with the variation of Richardson number for $Re = 200$, when the outlet port is considered along the upper section of the right vertical wall. The result shows a good agreement of our results with the results due to Chamkha et al. [23].

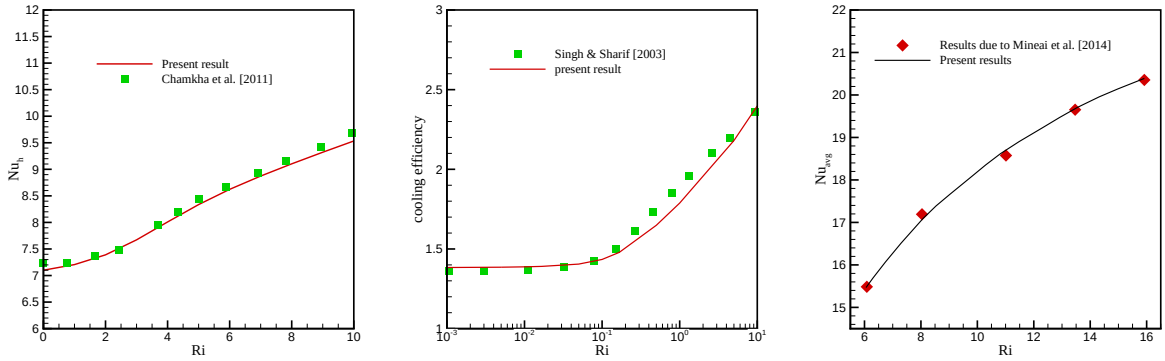

(a) (b) (c)

Figure 3.3: Comparison of (a) average Nusselt number with the result of Chamkha et al. [23] along the heated surface of inner square block, (b) cooling efficiency inside the ventilated enclosure with the result of Singh and Sharif [108] for $Re = 300$, (c) present code with the experimental work done by Minaei et al. [72] for mixed convection flow at $Re = 320$.

For verification and validation of our numerical code, a comparison is made with the work due to Singh and Sharif [108] by considering the inlet port at the bottom of left vertical wall, outlet port is along the top of right vertical wall and the left vertical wall is maintained at lower temperature compared to right vertical wall at $Re = 300$. Fig. 3.3(b) represents the comparison of cooling efficiency with the variation of Richardson number and found that maximum difference of our result with the results of Singh and Sharif [108] is 4.89 % at $Re = 300$. The present code is also validated by the experimental work done by Minaei et al. [72] by considering a discrete heat source on the right vertical wall, inflow and outflow openings are considered on the left vertical wall. Fig. 3.3 (c) presented the comparison of average Nusselt number with the variation of Richardson number for $Re = 320$. The comparison of present result with the experimental result shows a good agreement.

3.5 Results and discussion

The flow variation and energy transfer is observed inside the ventilated enclosure due to the interaction of buoyancy-induced double-diffusive convection induced by the thermo-contaminated square block and the mechanical-driven forced convection generated by the inlet air. Richardson number, buoyancy ratio, Reynolds number and Prandtl number

effects are examined for the flow and heat transfer variation. In the present work, air is considered as working fluid inside the enclosure and Prandtl number is taken as 0.71 throughout the calculations and the value of Schmidt number is taken as $Sc = 1.0$ corresponding to a practically feasible observation (Methanol diffusing in air). The value of buoyancy ratio (Br) equals to 1.0 implies that the thermal and species buoyancy forces are acting in the same direction and equal in magnitude [15]. For all the computations, an extensive parametric analysis is made to delineate the heat and solute transfer mechanisms for flow variation. Fluid flow is characterized by (i) the primary flow inside the enclosure due to the forced convection effect, (ii) a downstream secondary eddy is formed in the bottom-right corner of the enclosure due to the pressure effect, (iii) an upstream secondary eddy is formed above the main stream due to the buoyancy effects, (iv) another secondary eddy is formed near the inlet and outlet port because of high temperature or concentration gradients [73]. The dynamic, thermal and species transport phenomena are depicted through the streamlines, isotherms and isoconcentration lines. In streamline plots, dashed lines represents the clockwise recirculation zone and solid lines represents the anticlockwise recirculation zone. For isotherms and isoconcentration contour plots, solid lines represent the positive values and dashed lines represent the negative values.

3.5.1 Case-I

3.5.1.1 Dynamic Field

The flow pattern inside the ventilated enclosure is the outcome of the interaction between forced convection due to injecting air and buoyancy effects due to thermo-contaminated block. Fig. 3.4 represents the combined effect of Reynolds number and Richardson number on streamlines when the block is placed at the center of the enclosure at $Br = 1.0$ and $Sc = 1.0$. Richardson number shows the importance of natural convection relative to forced convection and varied from 0 to 10 while Reynolds number, Re is considered to be 100, 300 and 500. When $Re = 100$ and $Ri < 1.0$, most of the fluid is flowing diagonally from inlet to outlet as forced convection dominates the flow and an anticlockwise recirculation zone is formed just above the inlet port. In this situation, inflow and boundary conditions strongly favor the physical phenomena of a natural convection and significant increase in negative vortex. For $Re = 300$ and 500, an anticlockwise recirculating zone around

the block is formed and a clockwise recirculating zone is observed in the bottom-right corner of the enclosure while the main streamline from inlet to outlet is flowing between these two circulation zones near the bottom-right section of the enclosure. As Richardson number increases up to 1.0 for $Re = 100$, the recirculation zone is contrasted towards the left vertical wall and splits into two parts due to buoyancy effects and the hot fluid around the block is flushed-out by the injecting cold fluid. For $Ri = 1.0$ and $Re = 300$, the recirculation zone near the left vertical wall is expanded towards the right side and a clockwise eddy is formed near the right vertical wall which is expanded towards the outlet port with increase of Re i.e., for $Re = 500$. For higher values of Richardson number ($Ri \geq 5.0$), flow is dominated by buoyancy induced natural convection effect and a clockwise recirculation zone is formed near the outlet port for all values of Reynolds number which is increasing in size with increasing values of Richardson number. For $Re = 300$, a clockwise eddy is formed near the bottom wall which is increased in size when Re is increased to 500. Moreover, an anticlockwise circulation zone is observed near the upper-left corner of the enclosure and with increase in both the values of Re and Ri, this circulation zone is expanding towards the mid-section of the enclosure. The space with cold fluid is enlarged along the bottom section of the enclosure due to the fact that hot fluid rises above and cold fluid moves downward. There is obvious cause for concern is that, flow driven by buoyancy effects with the heat transfer effects become more intense when Richardson number increases.

3.5.1.2 Thermal Field

Fig. 3.5 depict the isotherm contours for various values of Richardson and Reynolds number for fixed value of $Br(= 1.0)$ and $Sc(= 1.0)$ for case-I. Isotherms are generated inside the enclosure due to the interaction between hot fluid around the thermo-contaminated block and cold fluid passing through the inlet port. For $Ri < 1.0$ and $Re = 100$, the cold fluid is expanded in the bottom-left region of the enclosure near the inlet port and hot fluid rises above in folium shape around the block directed towards the right-upper wall. With the increase of Reynolds number from 100 to 300 and 500, thermal lines with negative values passes from inlet to outlet port through the bottom- right section of the enclosure and an oval shaped recirculation zone is formed around the block due to the

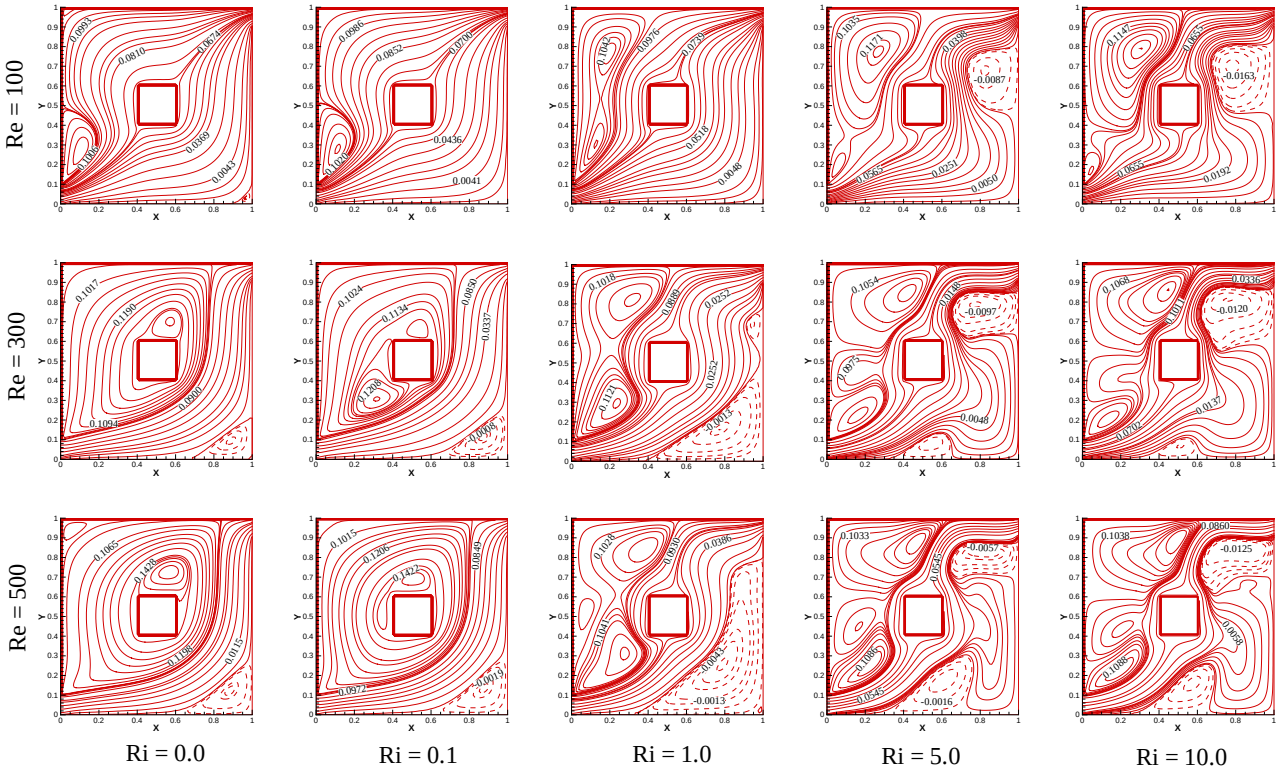

Figure 3.4: Effect of Richardson number for different Reynolds number on streamlines for case-I, (with fixed $Sc = 1.0$, $Br = 1.0$ and $Pr = 0.71$).

high velocity of injected air. For low Richardson number, most of the region of the enclosure is occupied by the hot fluid and inlet cold fluid is stacked near the inlet region. As Richardson number is increased to 1.0 with $Re = 300$ and $Re = 500$, recirculation zone around the block formed a thermal plume directed towards the upper wall and thermal lines with negative values are moving from inlet to outlet port near the bottom wall of the enclosure. The isothermal lines confined to the heated obstacle representing the maximum heat transfer along the central region of the enclosure. In case of $Ri \geq 5.0$, dense thermal lines are observed around the block with tiny thermal plume directed towards the outlet port and lower half region is occupied by cold fluid for higher values of Richardson number and Reynolds number.

3.5.1.3 Solutal Field

Isoconcentration lines for case-I are presented in Fig. 3.6 for various values of Reynolds number and Richardson number. For $Ri < 1.0$, dense solutal lines are found around

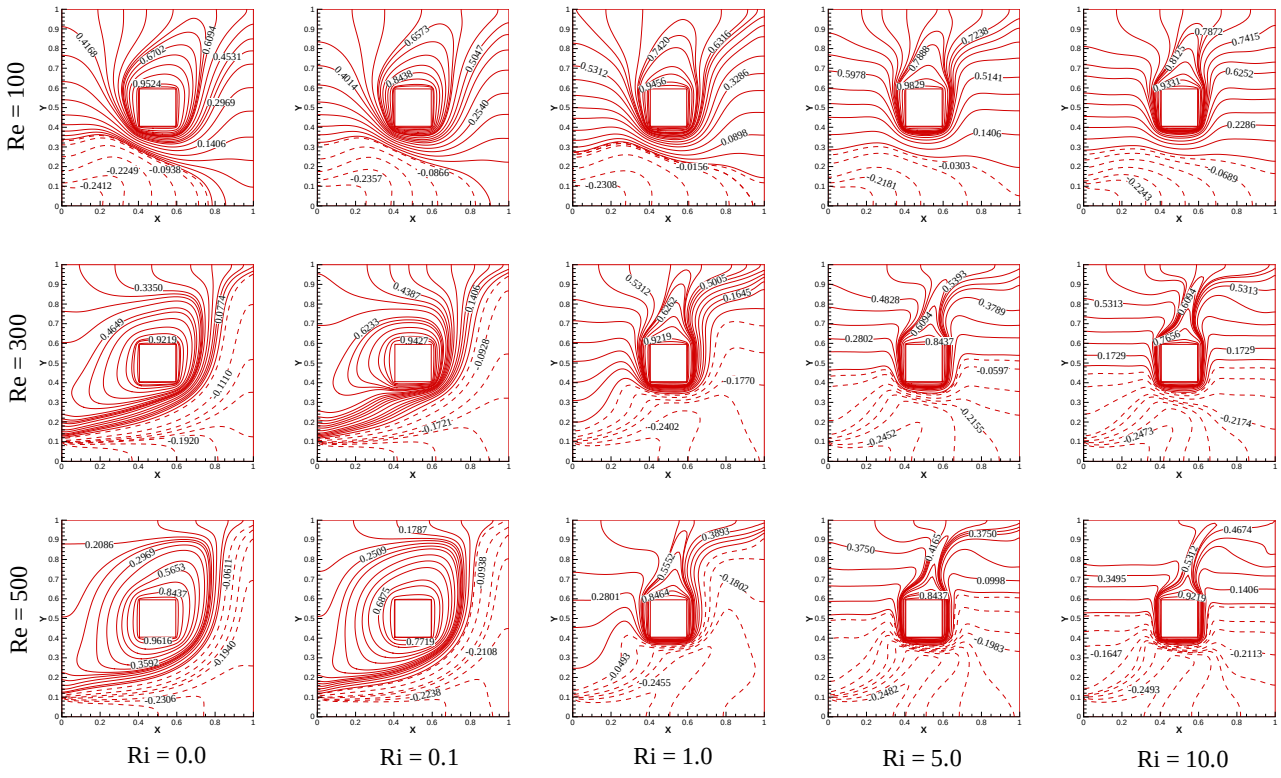

Figure 3.5: Effect of Richardson number on isotherms for case-I for different Reynolds number, (with fixed $Sc = 1.0$, $Br = 1.0$ and $Pr = 0.71$).

the block directed towards the upper-right section of the enclosure for $Re = 100$ and an oval shaped circulation zone around the block is formed for $Re = 300$ and $Re = 500$. For higher Reynolds number, the inlet velocity is high and bottom-right section of the enclosure is dominated by forced convection while the rest part of the enclosure is effected by buoyancy effects. When the Reynolds number increases from $Re = 100$ to $Re = 300$ at low Richardson number ($Ri < 1.0$), the flow bifurcates into two streams: one stream is flowing close to the thermo-contaminated block and another is flowing diagonally from inlet to outlet. For $Ri = 1.0$, the circulation zone formed around the block is converted into solutal plume directed towards the exit port due to the mixed convection effect for $Re = 300$ and 500. In case of higher Richardson number ($Ri \geq 5.0$), there is a tiny solutal plume around the block directed towards the upper wall for low Reynolds number and its direction is shifted towards the exit port for higher Reynolds number due to buoyancy effects. Dense solutal lines are conserved around the block and highly contaminated air is passing out through the outlet port for higher values of Richardson number.

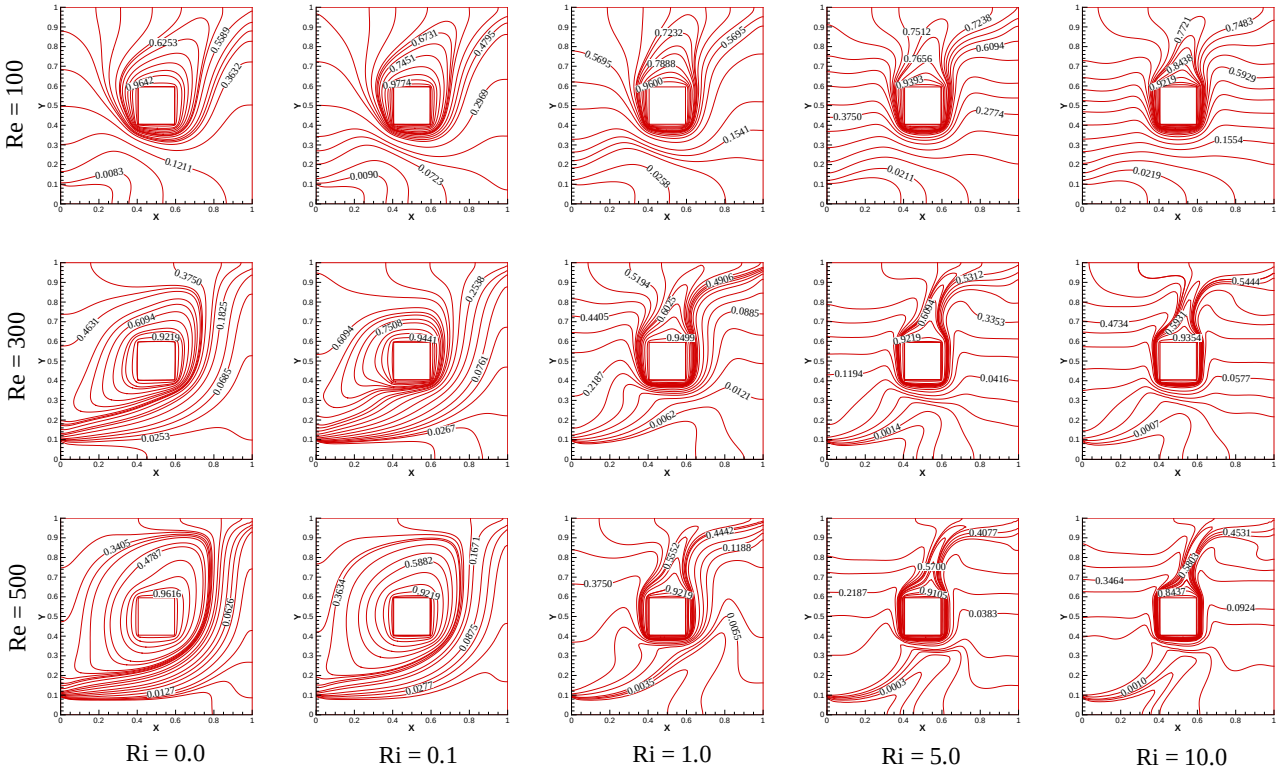

Figure 3.6: Effect of Richardson number on isoconcentrations for different Reynolds number for case-I, (with fixed $Sc = 1.0$, $Br = 1.0$ and $Pr = 0.71$).

3.5.2 Case-II

3.5.2.1 Dynamic Field

Fig. 3.7 represents the combined effect of Reynolds number and Richardson number on streamlines for case-II. As the block is placed near the right vertical wall, anticlockwise recirculation zone are formed near the left vertical wall due to density differences for $Re = 100$ and $Ri < 1.0$. When the Reynolds number is increased up to 300, the recirculation zone is expanded in left half region of the enclosure and a clockwise eddy is formed in the bottom-right corner of the enclosure. A small eddy is found near the thermo-contaminated block for higher values of Reynolds number due to the interaction between cold and hot fluid around the block. For $Ri = 1.0$ and $Re = 100$, main streamlines are passing from inlet to outlet port through the bottom-right section of the enclosure and a circulation zone is formed in upper-left section due to the natural convection effect. This circulation zone is widen up towards the right side and splits into two convective regimes as the

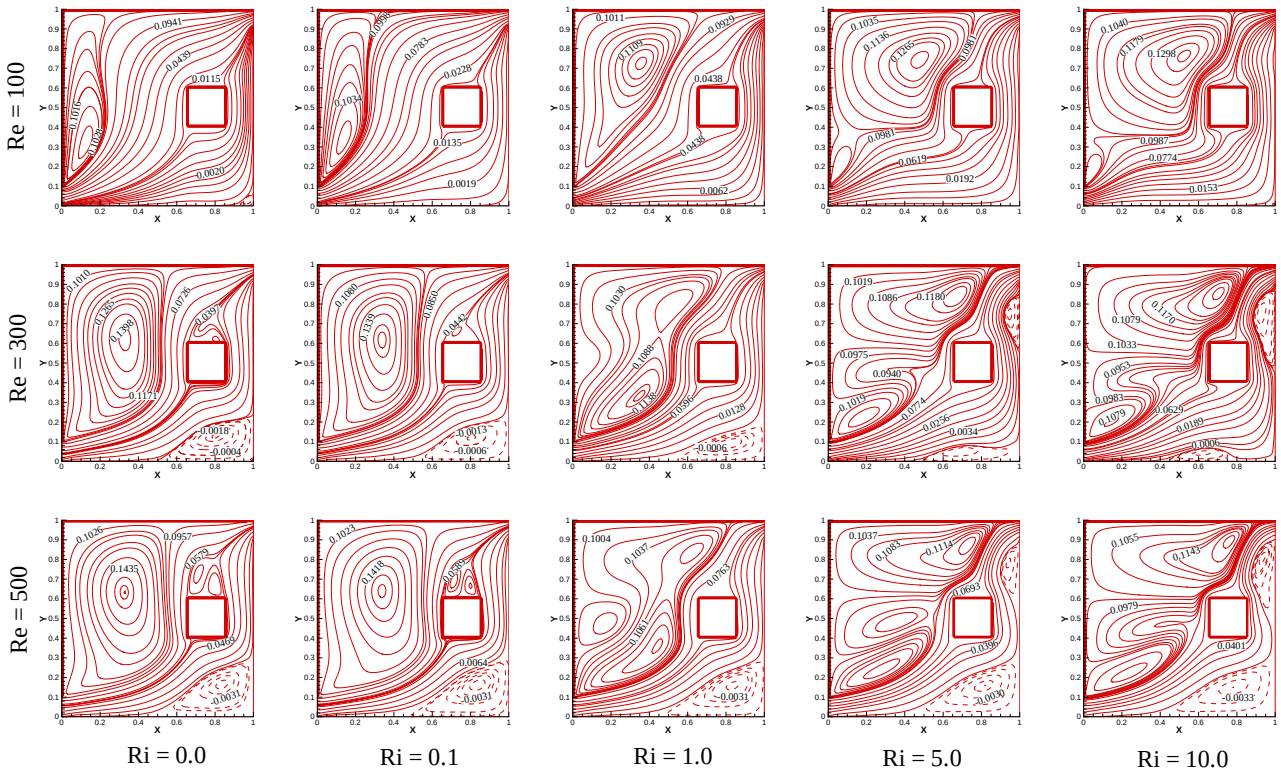

Figure 3.7: Effect of Richardson number on streamlines for case-II for different Reynolds number, (with fixed $Sc = 1.0$, $Br = 1.0$ and $Pr = 0.71$).

Reynolds number increases from 100 to 300 and 500. A small circulation zone near the mid part of the left vertical wall is observed and the size is expanded for $Re = 500$ due to the loss of frictional force. A secondary clockwise eddy is also observed in the lower-right corner of the enclosure at $Re = 300$ which is increasing in size with the increasing value of Reynolds number. As Richardson number is larger i.e. $Ri \geq 5.0$, the recirculation zone occupies the most portion of the upper-left section of the enclosure for $Re = 100$ and the main streamlines are passing parallel to the bottom wall and then turned towards the outlet port passing over the block. As Reynolds number increases to 300, the size of the anticlockwise circulation zone near the upper-left wall is getting shrunk towards the upper wall and an eddy is formed just above the inlet port which is growing in size since the inlet cold fluid forced the hot fluid to move towards the exit port. Another circulation zone is formed between these two zones as Reynolds number increases to 500. For $Re = 300$, two clockwise small eddies are formed: one is near the outlet port and another is in the bottom-right corner of the enclosure which are getting increased in size

for $Re = 500$, this reveals that majority of the inlet stream passes around the block.

3.5.2.2 Thermal Field

Fig. 3.8 represents the thermal lines for various values of Reynolds number and Richardson number. As the block shifts towards right vertical wall, thermal lines with high temperature are moving towards the exit port and more than half region of the enclosure is strongly cooled by inlet air. In case of low Richardson number ($Ri < 1.0$) with $Re = 100$, thermal lines are vertically distributed inside the enclosure and thermal lines with high temperature near the block are moving towards the right vertical wall due to dominating forced convection effect. As Reynolds number increases to 300 and 500, thermal lines around the block is observed in folium shape directed towards the outlet port due to the higher velocity of injected air. It is concluded that for $Ri < 1.0$ and $Re \geq 300$, approximately three-fourth region of the enclosure is occupied by isotherms with negative values which results a maximum cooling inside the enclosure. For $Ri = 1.0$, these thermal lines around the block are converted to thermal plume which results the higher heat transfer rate. In case of high Richardson number ($Ri \geq 5.0$), thermal plume around the block becomes more sharper than before and the cooling efficiency inside the enclosure is also increasing. From Fig. 3.8, it is observed that the thermal boundary layer near the thermo-contaminated block becomes thinner with the increment in Reynolds number.

3.5.2.3 Solutal Field

Isoconcentration lines for case-II is presented in Fig. 3.9 for different values of Richardson number and Reynolds number with $Br = 1.0$ and $Sc = 1.0$. For low Richardson number with $Re = 100$, circulation zone of high concentrated isoconcentration lines around the block follows a straight path towards the right vertical wall and as Reynolds number increases, the direction is shifted towards the outlet port due to increased forced convection effect. For $Ri \geq 1.0$, a tiny solutal plume is formed around the block with dense solutal lines which are directed towards the outlet port. The sharpness of the solutal plume is getting stronger with the increasing values of the Reynolds number and Richardson number which results the high mass transfer rate.

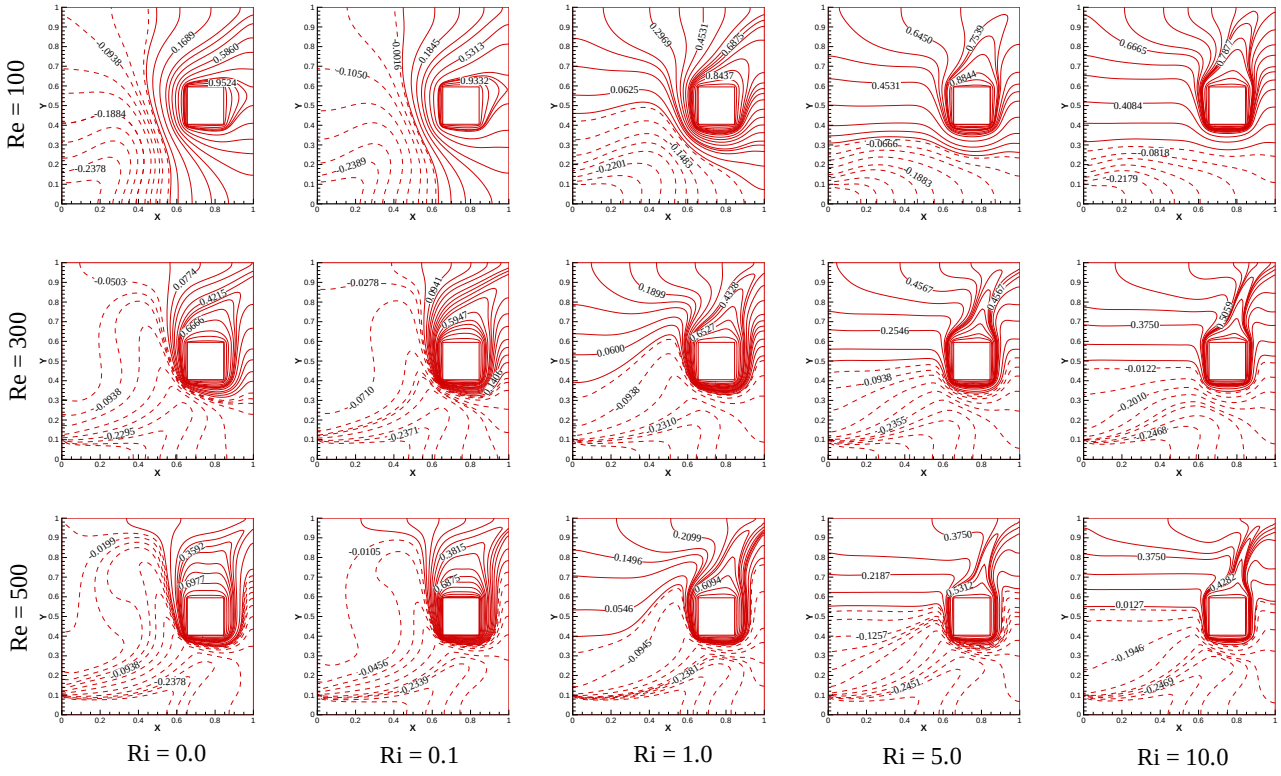

Figure 3.8: Effect of Richardson number with different Reynolds number on isotherms for case-II, (with fixed $Sc = 1.0$, $Br = 1.0$ and $Pr = 0.71$).

3.5.3 Case-III

3.5.3.1 Dynamic Field

Streamlines for case-III in which block is placed near the left vertical wall ($L_x = 0.25, L_y = 0.5$) are presented in Fig. 3.10. The injected cold fluid is interacted with thermo-contaminated block and eddies are formed near the block due to buoyancy induced convection effects. For $Re = 100$ and $Ri = 0.0$, main streamlines passes from inlet to outlet without any interaction to the block following a diagonal path from inlet to outlet while an anticlockwise circulation zone is formed around the block with two eddies near the block which are expanded towards the right side wall of the enclosure with the increment of Reynolds number. A clockwise smaller circulation zone is formed in the bottom-right corner of the enclosure which is increasing in size with increase in the Reynolds number. As Richardson number increases from 0.0 to 0.1, the recirculation zone around the block diminishes for $Re = 100$ and a small circulation zone is observed just above the inlet port.

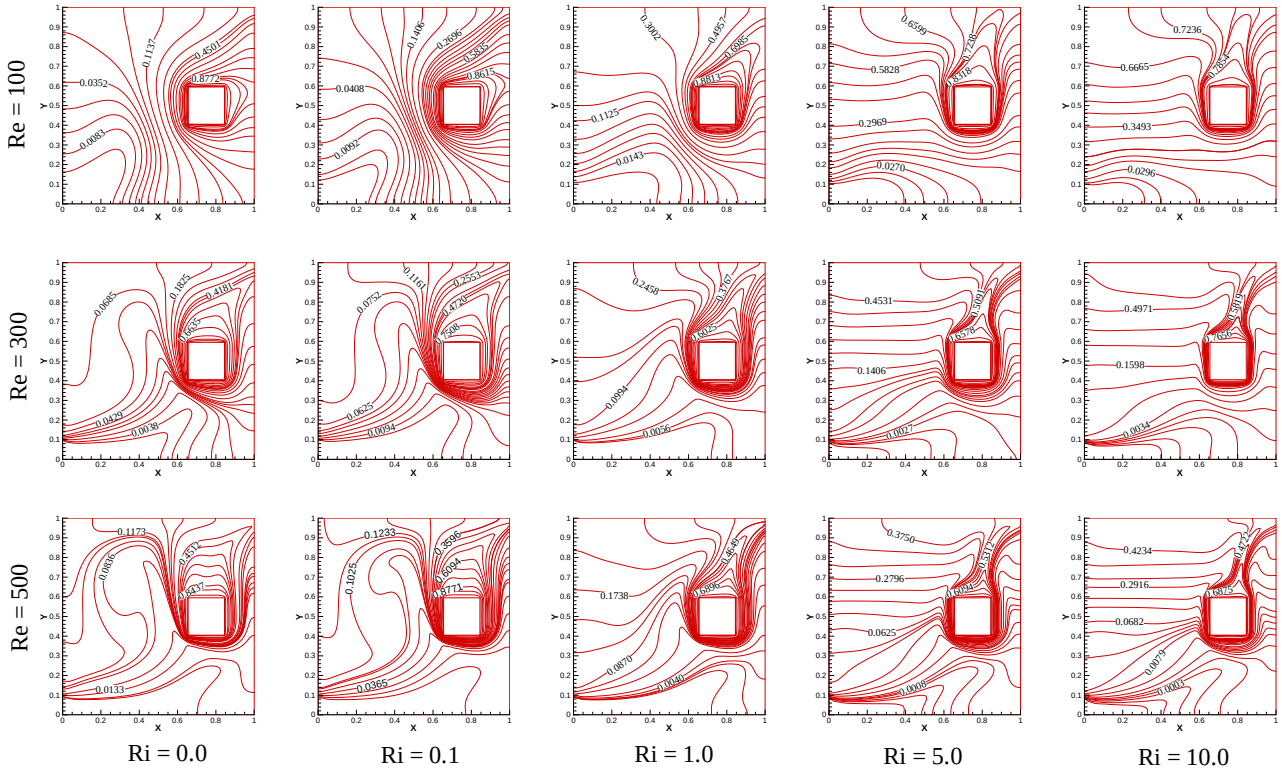

Figure 3.9: Effect of Richardson number with different Reynolds number on isoconcentrations for case-II, (for fixed $Sc = 1.0$, $Br = 1.0$ and $Pr = 0.71$).

As Re increases from 100 to 300 with fixed $Ri(= 0.1)$, streamlines are divided into three different zones; first is clockwise circulation zone in the bottom-right corner of the enclosure due to frictional force observed by the inlet fluid, second is the main streamlines from inlet port to outlet port and the third is anticlockwise recirculation zone around the block due to weak buoyancy effects and pressure loss. As Re increases to 500, the main streamlines follow a tortuous path from inlet to outlet through the bottom-right region and a circulation zone around the block is contracted towards the upper region and another circulation zone is found between these two zones due to combined forced convection and buoyancy effects. For $Ri = 1.0$ and $Re = 100$, the induced flow is dominated by forced convection and fluid moves diagonally from inlet port to outlet with a small upstream eddy near inlet port. For $Re = 300$, injected fluid interacted with heated block and a clockwise recirculation zone is formed near the bottom wall which is expanded towards upper side for $Re = 500$ and a downstream eddy is formed in the bottom-right corner of the enclosure. For higher Richardson number $Ri \geq 5.0$ with $Re = 100$, a clockwise

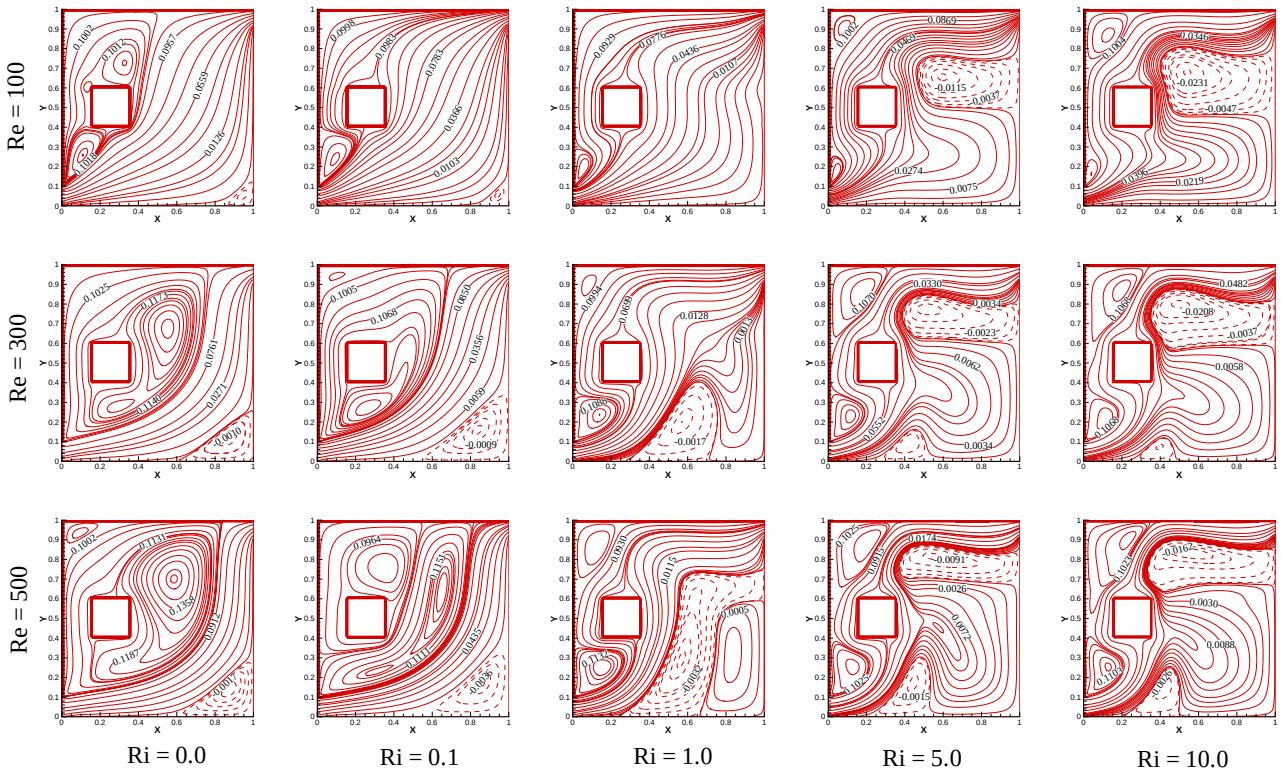

Figure 3.10: Effect of Richardson number with different Reynolds number on streamlines for case-III, (for fixed $Sc = 1.0$, $Br = 1.0$ and $Pr = 0.71$).

downstream eddy is formed just below the main streamlines near the outlet port and as Re increases, this eddy shrinks towards the upper section of the enclosure and a secondary clockwise eddy is grown up near the mid-section of bottom wall. Two upstream eddies are formed, one is near the inlet port and the other is in the upper-left corner of the enclosure which are increasing in size with increasing values of Reynolds number and Richardson number due to natural convection effect.

3.5.3.2 Thermal Field

Fig. 3.11 represents the thermal lines for case-III at $Br = 1.0$ with various values of Richardson and Reynolds number. For $Re = 100$, the injected fluid is not much influenced with the thermo-contaminated block due to which the cold air moves in bottom section of the enclosure and thermal lines with higher temperature forms a circulation zone around the block. As Richardson number increases from 0.0 to 10.0, thermal lines with higher temperature switches from left side to right side and exited through the outlet port due

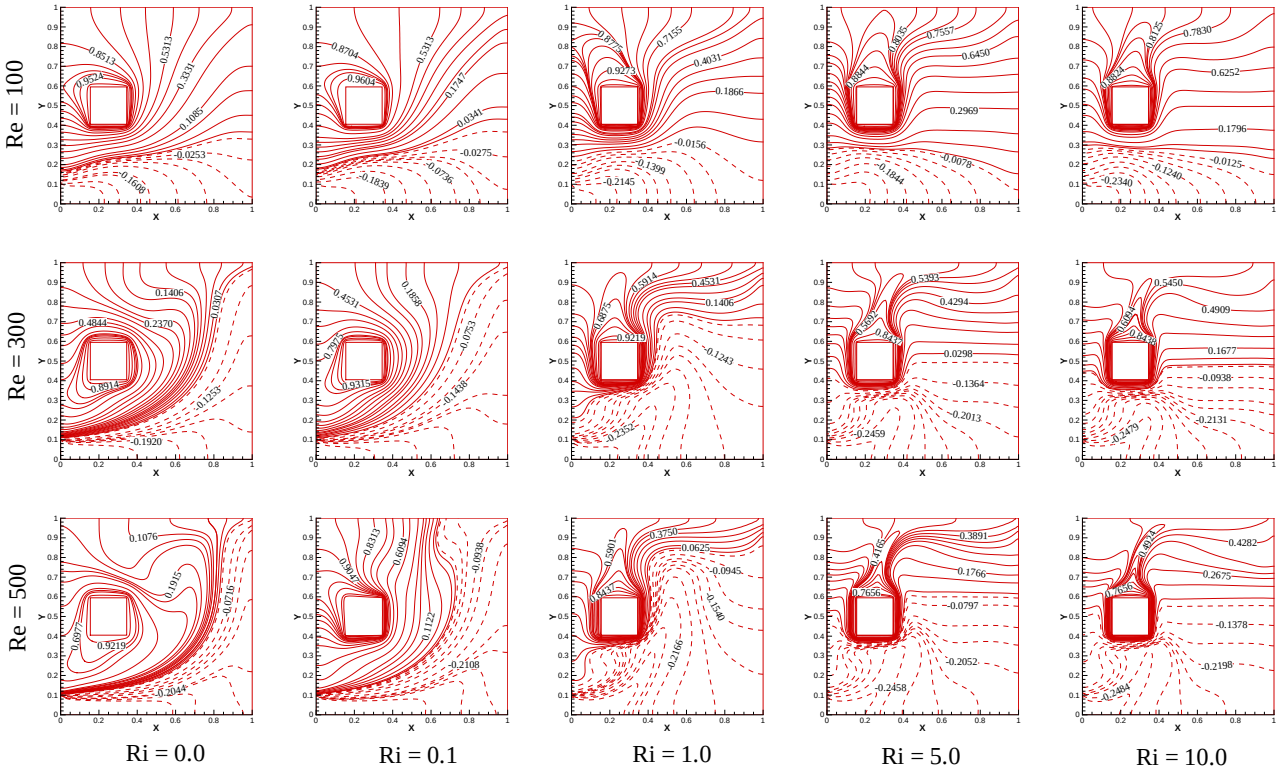

Figure 3.11: Effect of Richardson number for different Reynolds number on isotherms for case-III, (with fixed $Sc = 1.0$, $Br = 1.0$ and $Pr = 0.71$).

to density difference. For high Reynolds number ($Re = 300,\ 500$) and $Ri < 1.0$, the cold fluid moves from inlet port to outlet port through the bottom-right section of the enclosure and the thermal lines with higher temperature forms a circulation zone around the block which are directed towards the left vertical wall and keeps the left region at high temperature. The bottom-right section of the enclosure is occupied by cold fluid due to forced convection effects. For $Ri \geq 1.0$, circulation zone is transformed to a thermal plume around the block and dense thermal lines with high temperature move towards the exit port due to which heat transfer rate is always higher for higher Richardson number. For $Re = 300,\ 500$ and $Ri \geq 1.0$, the bottom section of the enclosure is at lower temperature due to increased volume of cold fluid inside the enclosure.

3.5.3.3 Solutal Field

Isoconcentration lines for different Reynolds number and Richardson number are represented in Fig. 3.12. Due to shifting of thermo-contaminated block from right to left part

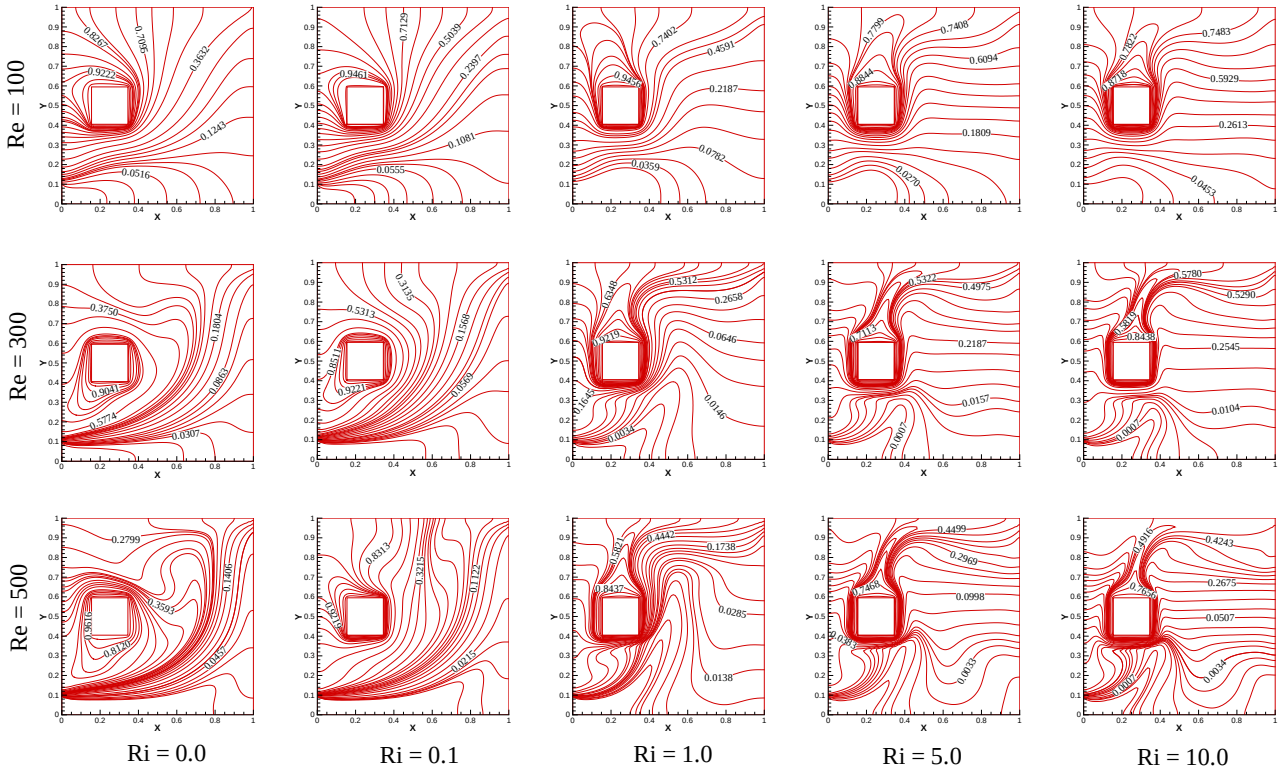

Figure 3.12: Effect of Richardson number for different Reynolds number on isoconcentrations for case-III, (with fixed $Sc = 1.0$, $Br = 1.0$ and $Pr = 0.71$).

of the enclosure, higher concentrated solutal lines spread in the left region around the block while low concentrated lines passes diagonally from inlet to outlet port in case of low Richardson number values ($Ri < 1.0$), since dense fluid stacked along the lower part. At $Ri = 1.0$, a solutal plume directed towards the upper wall is formed around the block for $Re \geq 300$ due to faster movement of inlet fluid which results the faster removal of contaminants from the enclosure. For $Ri \geq 5.0$, a dense solutal plume around the block directed towards the upper wall is found for $Re = 100$. By further increase in Reynolds number to 300 and 500, it is found that the solutal plume around the block becomes denser and the direction of solutal plume is shifted from upper wall to the exit port due to forced convection dominated flow. In case of higher Reynolds number, the solutal lines around the block are getting thicker due to formation of thicker solutal boundary layer. It is also observed that with increasing velocity of injected fluid, the value of the concentration lines near the outlet port is decreasing while the increasing value of Richardson number resulting an increment in the value of concentration lines near the outlet port.

3.5.4 Case-IV

3.5.4.1 Dynamic Field

Fig. 3.13 represents the effect of Reynolds number and Richardson number on streamlines for case-IV (when block is placed near the upper wall). For $Ri < 1.0$ and $Re = 100$, streamlines are flowing from inlet to outlet through the block and an upstream anticlockwise circulation zone is formed near the left vertical wall just above the inlet port because the flow characteristics are dominated by forced convection effect. As Re increases up to 300, major flow is passing directly from inlet port to outlet port parallel to the bottom-right section of the enclosure. Also, an upstream recirculation eddy is found around the block due to density differences which is getting increased in size as Re is increased to 500. A clockwise eddy is formed in the bottom-right corner of the enclosure at $Re = 100$ and its size is increasing with the increase in Reynolds number. In case of $Ri = 1.0$ and $Re = 100$, the injected cold fluid is flowing from inlet to outlet port in the bottom-right

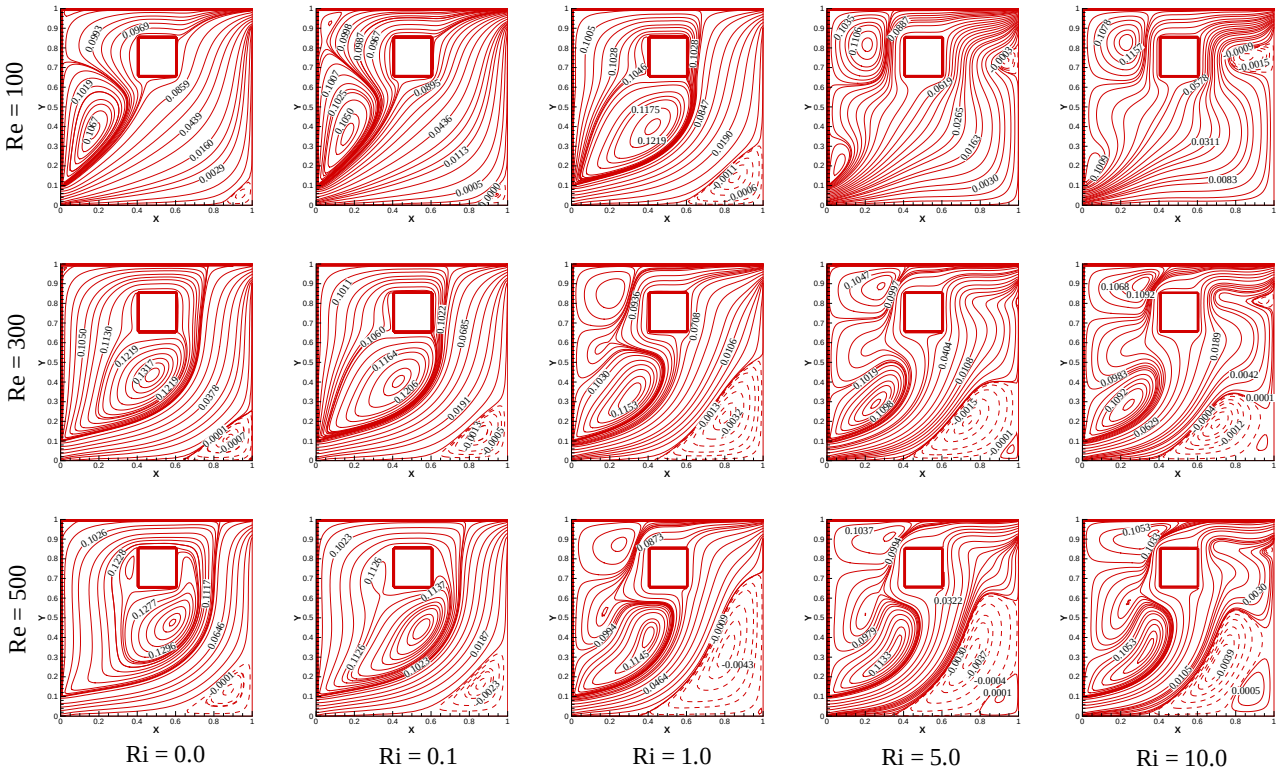

Figure 3.13: Effect of Richardson number for different Reynolds number on streamlines for case-IV, (with fixed $Sc = 1.0$, $Br = 1.0$ and $Pr = 0.71$).

region of the enclosure and cold air have no interaction with the block due to weak inertial force of injected fluid. A circulation zone is also formed around the block in upper-left region and a clockwise downstream eddy is formulated in the bottom-right corner of the enclosure. With the increment in Reynolds number and Richardson number, the rate of heat and mass transfer along the block is increasing due to the strong interaction of inlet fluid with the thermo-contaminated block. For $Re \geq 300$, a clockwise downstream eddy is formed in the bottom-right corner of the enclosure which is decreased in size with increased value of Ri due to natural convection effect. Upstream anticlockwise eddies are formed near the left vertical wall of the enclosure due to buoyancy effects.

3.5.4.2 Thermal Field

For case-IV, the temperature distribution inside the enclosure for different parametric values for fixed buoyancy ratio $Br(= 1.0)$ and Schmidt number $Sc(= 1.0)$ are presented in Fig. 3.14. Temperature profiles for low Richardson number values i.e. $Ri < 1.0$ with $Re = 100$ shows that hot fluid around the block is moving in upward direction due to inflow of cold fluid which is placed in the lower region of the enclosure. As Re increases from 100 to 300 and 500, the hot fluid around the block is moving downwards due to larger inlet fluid velocity which forces the fluid to move towards the outlet port since fluid density is not sufficient enough to keep the fluid in the lower level. For $Ri = 1.0$, a circulation zone of thermal lines with high temperature around the block is formed which is directed towards the upper wall at $Re = 100$ and injected cold fluid flows in the bottom-right region of the enclosure towards the outlet port. Increase of Reynolds number shows that the heat transfer rate is increased and a tiny thermal plume around the block is formed which moves toward the outlet port. For $Ri > 1.0$, the role of convection in heat transfer becomes more prominent and the hot fluid moves towards the upper region and getting stacked closed to the outlet port. Consequently, the thermal boundary layer on the surface of the block becomes thinner. For $Re = 100$, the region below the block is getting cooled for all values of Ri. As Reynolds number increases, the region occupied with cold fluid is expanded for $Ri \geq 1.0$ due to density difference inside the enclosure. Cooling inside the enclosure is increasing with the increasing value of Reynolds number as well as Richardson number, since the air moves faster with increasing convection effects.

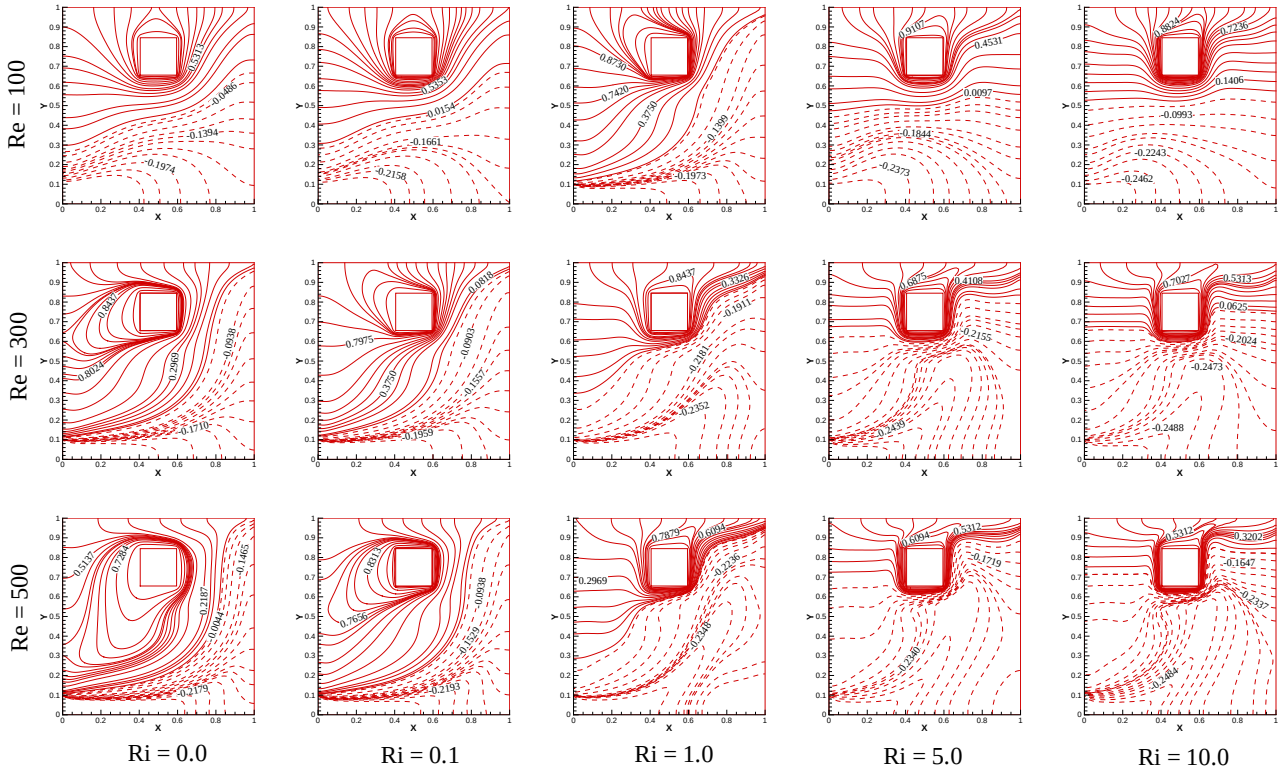

Figure 3.14: Effect of Richardson number for different Reynolds number on isotherms for case-IV, (with fixed $Sc = 1.0$, $Br = 1.0$ and $Pr = 0.71$).

3.5.4.3 Solutal Field

In case-IV, the block is positioned near the upper wall and the solutal lines for different values of Reynolds number and Richardson number are presented in Fig. 3.15. For $Re = 100$, the circulation zone is formed around the block and flow lines with lower concentration are distributed uniformly in the lower section of the enclosure dominated by the forced convection effect ($Ri < 1.0$). When the Reynolds number is increased, the isothermal circulation zone of high concentrated solutal lines around the block are forced to move in the left section of the enclosure due to the forced convection effect. As the block shifts close to the upper wall, the highly concentrated solutal lines are moving faster towards the outlet port for $Ri > 1.0$ where natural convection dominates the flow. A tiny solutal plume around the block is found in the upward direction for higher values of Reynolds and Richardson number due to the stronger solutal gradient in the upper part of the enclosure. For $Re \geq 300$, the solutal lines are getting dense close to the block

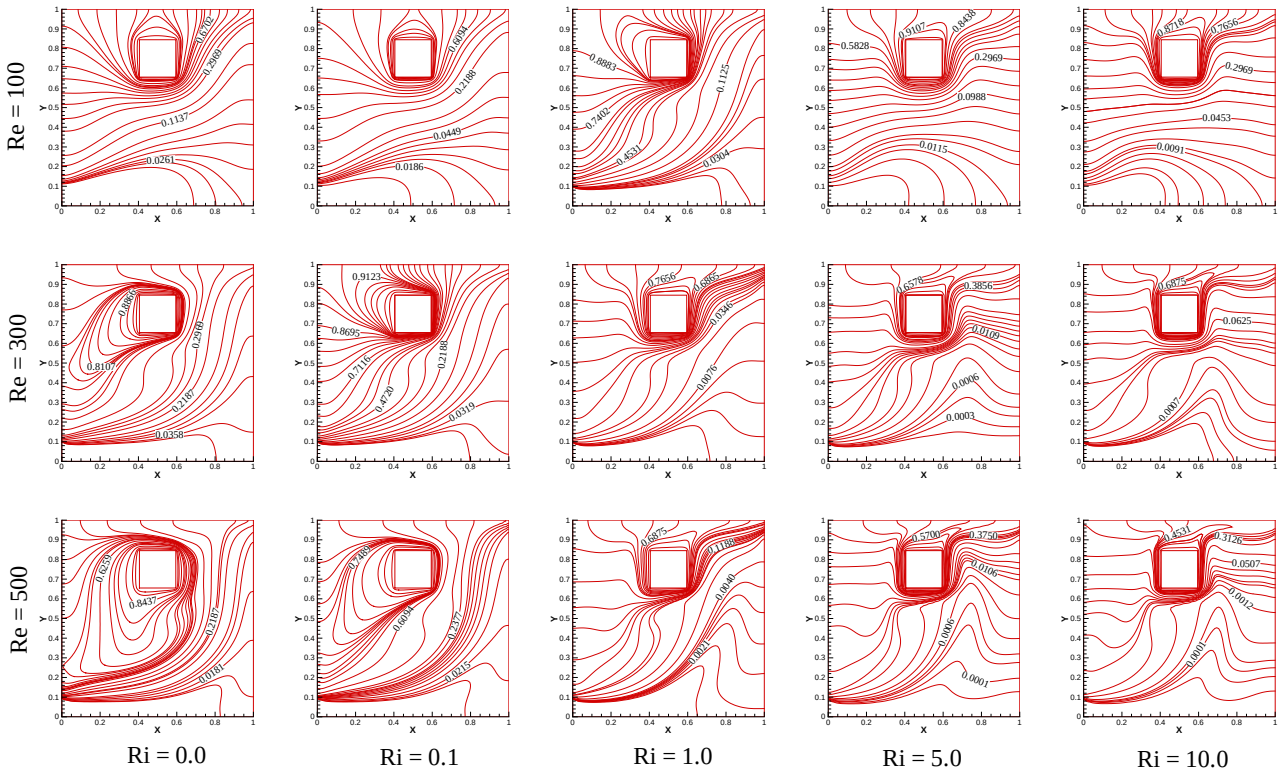

Figure 3.15: Effect of Richardson number for different Reynolds number on isoconcentrations for case-IV, (with fixed $Sc = 1.0$, $Br = 1.0$ and $Pr = 0.71$).

dominated by the natural convection effect. The contaminated air moves towards the outlet port in case of higher Reynolds and Richardson number.

3.5.5 Case-V

3.5.5.1 Dynamic Field

In case-V, the block is placed near the bottom wall and the flow pattern for various values of Reynolds number and Richardson number is presented in Fig. 3.16. For $Re = 100$ (first row of Fig. 3.16), injected fluid move towards the outlet port through the block for $Ri < 1.0$ and two very small upstream vortices are formed: one is above the inlet port and other is in the upper-left corner of the enclosure. As the Richardson number increases to 1.0, main streamlines are getting stratified in the lower section and the fluid flows diagonally towards the outlet port and an upstream anticlockwise recirculation zone is also formed in the upper-left section of the enclosure. This is because of mixing of the fluid due to buoyancy force and the convection current in the enclosure.

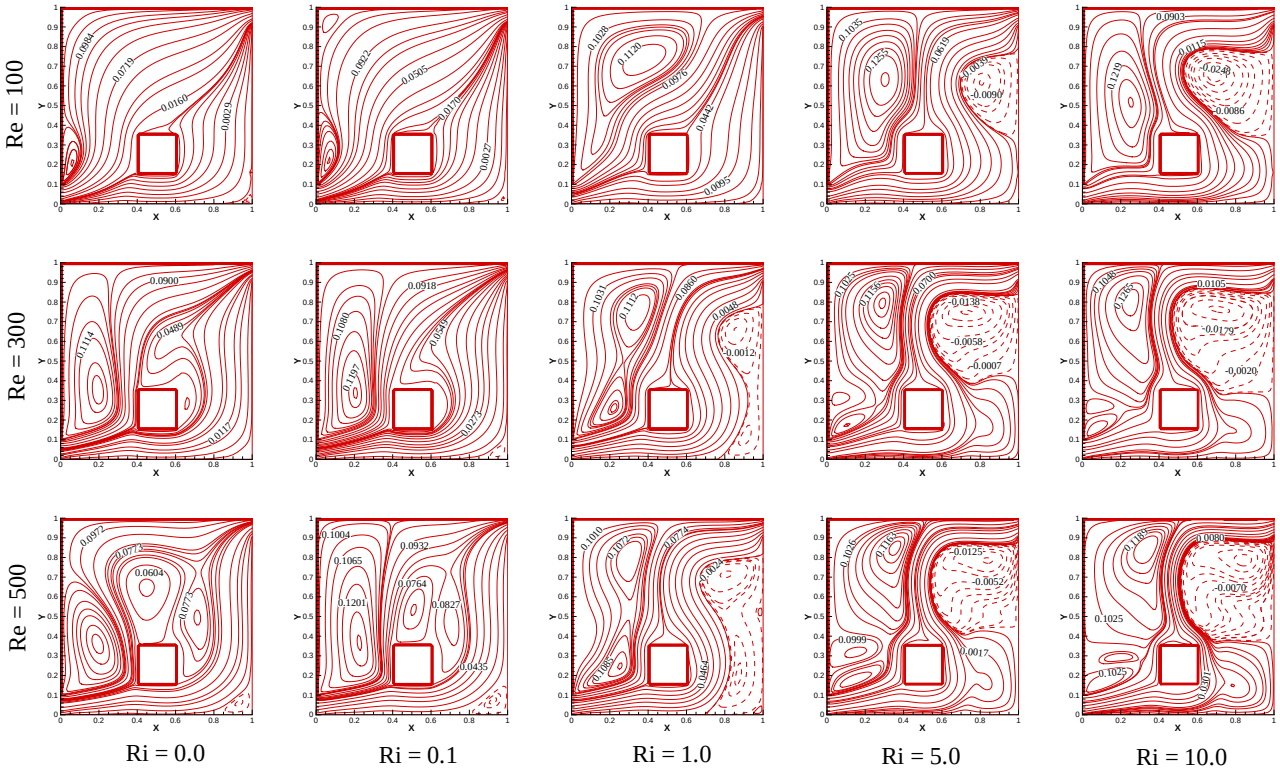

Figure 3.16: Effect of Richardson number with different Reynolds number on streamlines for case-V, (for fixed $Sc = 1.0$, $Br = 1.0$ and $Pr = 0.71$).

As Richardson number increases to 5.0, the natural convection dominates the flow and a clockwise recirculation zone is formed below the outlet port near the right vertical wall. For $Ri = 10.0$, the clockwise eddy is getting stronger while the anticlockwise recirculation zone is getting weaker towards left side due to density difference. For higher values of Reynolds number ($Re = 300, 500$) with $Ri < 1.0$, the injecting fluid is directly interacted with thermo-contaminated block and then moved towards the outlet port resulting an upstream recirculation zone adjacent to the left vertical wall. Near the upper wall of the thermo-contaminated block, eddies are formed due to temperature differences and getting larger in case of $Re = 500$. The upstream recirculation zone is found to be identical with the shape as formed for $Re = 300$ at $Ri = 0.1$. As the Richardson number increases to 1.0, a clockwise eddy is observed adjacent to the right vertical wall due to the density differences for $Re = 300$ and it is expanded in size when Reynolds number is increased to 500. The size of upstream recirculation zone formed near the left wall is increased and split up into two cells. For $Ri > 1.0$, the hot fluid around the block is driven by injecting

cold fluid towards the outlet port and the upper section of the enclosure is much effected by the density differences that causes a clockwise eddy adjacent to the right vertical wall below the outlet port and the anticlockwise eddies are formed adjacent to the left vertical wall, since the role of heat transfer becomes more significant.

3.5.5.2 Thermal Field

Temperature distribution inside the enclosure for different values of Reynolds and Richardson number is presented in Fig. 3.17 for case-V in which block is placed near the bottom wall. For $Ri < 1.0$, the injected cold fluid interacts with the block and forces the hot fluid to move towards the upper section of the enclosure. For $Re = 100$ with $Ri < 1.0$, thermal lines with higher temperature forms an oval shaped circulation zone around the block which directs toward the bottom-right section of the enclosure and for $Ri = 1.0$, direction shifts toward the upper-right section of the enclosure due to density difference. By further increase in Richardson number ($Ri > 1.0$), a thermal plume around the block is observed which is directed towards the upper wall and thermal lines with high temperature is expanded in the upper section of the enclosure. In case of $Ri < 1.0$ with $Re = 300$, oval shaped thermal lines directed towards the outlet port are observed around the block, while for $Re = 500$, thermal lines around the block are observed in obcordate shape directed towards the upper wall inside the enclosure due to forced convection effect. In case of $Ri \geq 1.0$, natural convection effect dominates the flow characteristics and the convective region above the block reduces to a sharp thermal plume which moves towards the upper section of the enclosure for $Re = 300$ and 500. Thermally activated line with value 0.4247 lies just above the block at $Ri = 1.0$ whereas, it moves towards the outlet when Ri increases to 10.0. The vertical mid section of the enclosure is at higher temperature compared to the core section of the enclosure due to mixed convection effect.

3.5.5.3 Solutal Field

Fig. 3.18 represents the isoconcentration lines of case-V for different values of Reynolds number and Richardson number. In case of $Re = 100$ with low Richardson number values ($Ri < 1.0$), high concentrated lines are distributed in the lower-right section of the enclosure around the block. As Ri increases from 0.1 to 5.0, these highly concentrated

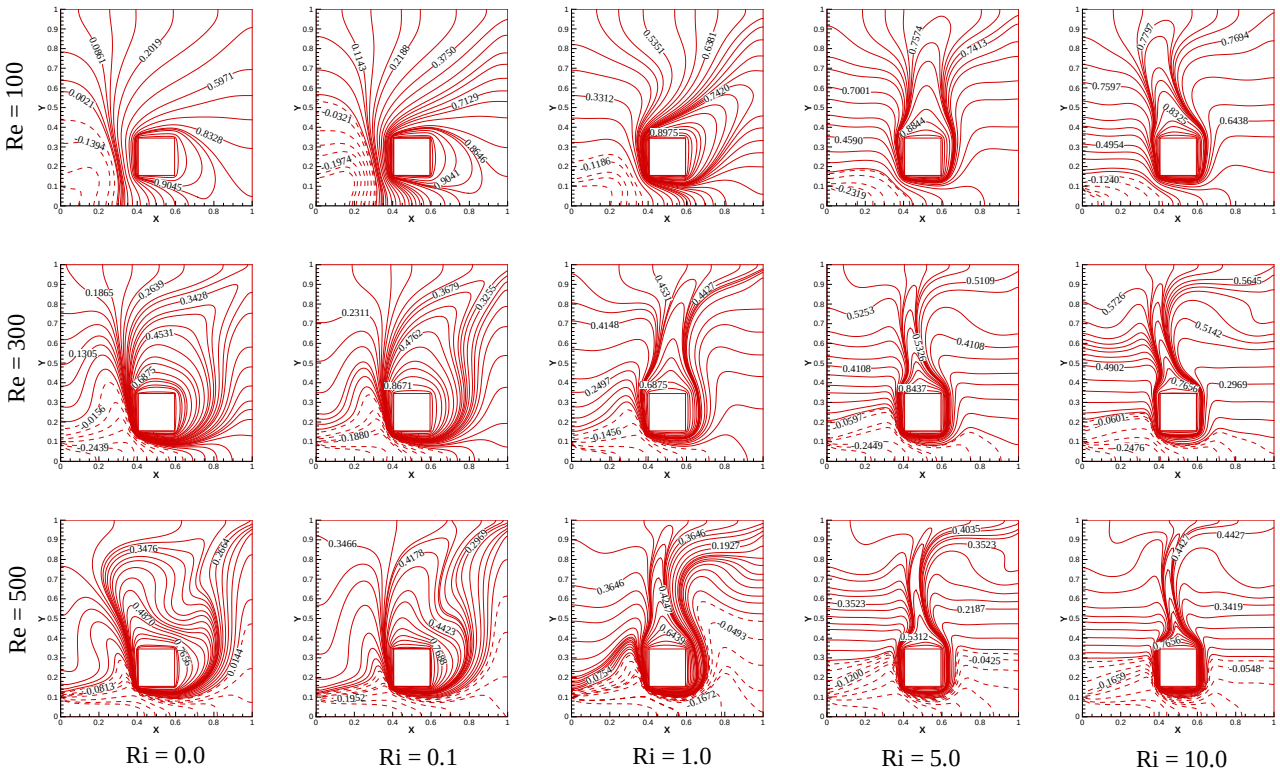

Figure 3.17: Effect of Richardson number with different Reynolds number on isotherms for case-V, (for fixed $Sc = 1.0$, $Br = 1.0$ and $Pr = 0.71$).

lines are moved towards the upper section of the enclosure and for $Ri = 10.0$, these lines maintain a uniform distribution of mass inside the enclosure. For higher Reynolds number ($Re = 300$ and 500) with $Ri < 1.0$, dense isothermal lines are observed along the bottom and left side of the block and highly concentrated lines are diffused in the upper right section of the enclosure above the block due to forced convection effect. For $Ri \geq 1.0$, isoconcentration lines around the block are converted to solutal plume and move towards the upper part of the enclosure. It is observed that the mass transfer rate along the block is higher in case-V as compared to other remaining cases but the species concentration is minutely exited through the outlet port and higher concentrated air is assembled in the upper section of the enclosure. One can observe the rapid change occurring in the concentration continuously and their shape changes significantly to non-uniform nature as Ri shifts from 1.0 to 5.0 which indicates the effect of increase in Richardson number on the species transfer process.

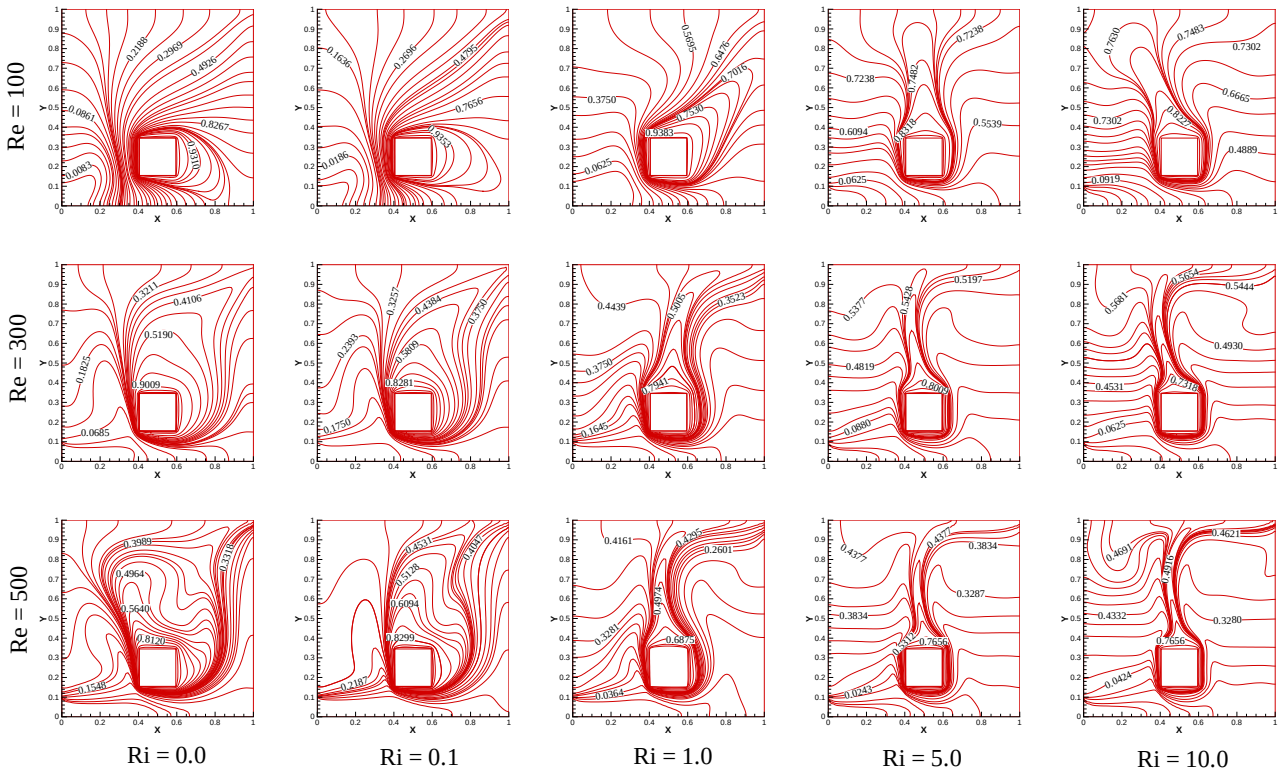

Figure 3.18: Effect of Richardson number with different Reynolds number on isoconcentrations for case-V, (for fixed $Sc = 1.0$, $Br = 1.0$ and $Pr = 0.71$).

3.5.6 Effect of Block Length Variation

3.5.6.1 Dynamic Field

Simulations are performed for different values of aspect ratios and results are presented for dynamic field in Fig.3.19 for various values of Reynolds number with the fixed value of Richardson number $Ri = 1.0$. As the block size increases, the heat transfer inside the enclosure increases and the space available for the buoyancy-induced recirculation zone is reduced, therefore the upstream and downstream secondary eddies are found to be decreased in size. For $Re = 100$, two convective regimes are found adjacent to left vertical wall when $A = 0.2$ and as aspect ratio is increased to 0.4, the eddy which is formed in the upper-left corner is diminished. Further increase in aspect ratio resulting a decrease in the size of eddy near the inlet port due to the inlet cold fluid whereas increase in Reynolds number results the increase in size of the eddy. From the figure, it is depicted that with increase in the Reynolds number, the main flow from inlet to outlet

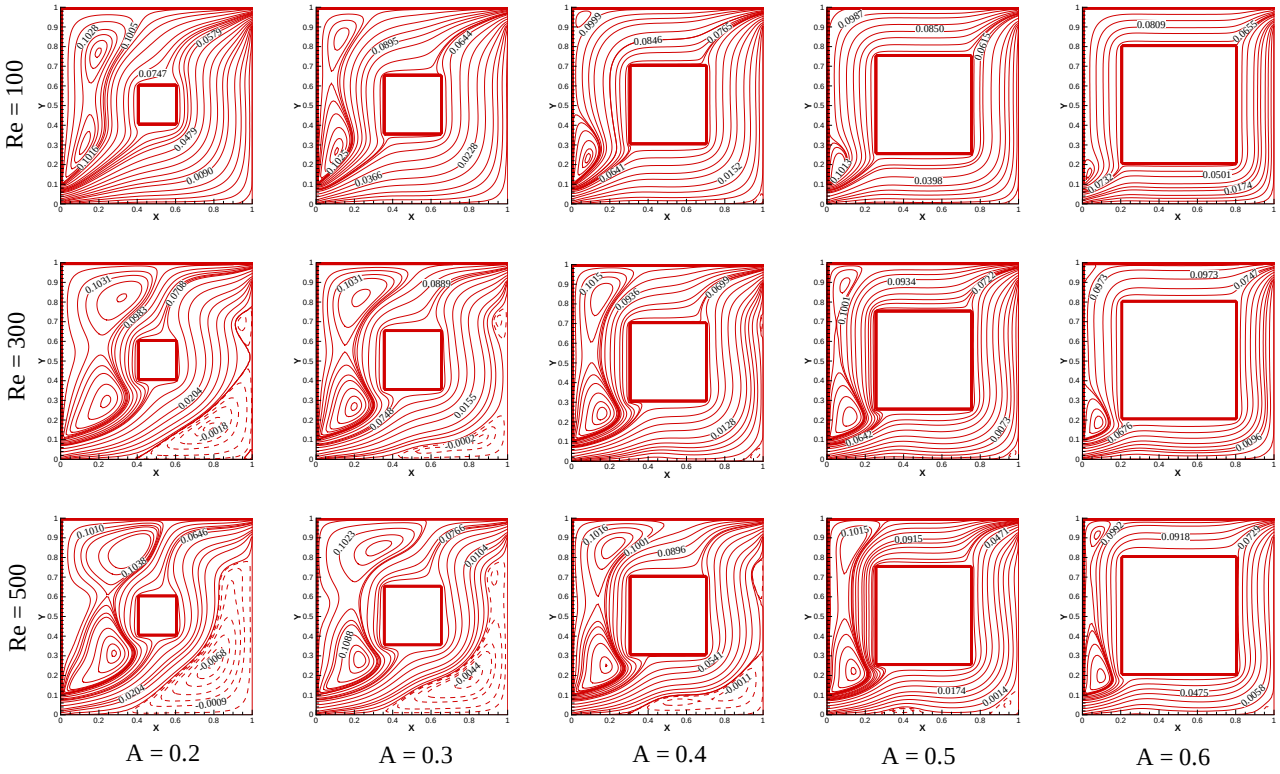

Figure 3.19: Effect of Reynolds number and aspect ratios on streamlines for case-I (with fixed $Ri = 1.0$, $Sc = 1.0$, $Br = 1.0$ and $Pr = 0.71$).

port is getting compressed due to forced convection and secondary recirculation zones are formed. Mostly, the thermal conductivities influence the fluid variation as the value of aspect ratio is increased. The streamlines are found to be straight for higher aspect ratios ($A = 0.4,\ 0.6$) due to the decreased space between the block and the enclosure wall.

3.5.6.2 Thermal Field

Isotherm contours are represented in Fig. 3.20 for different aspect ratios and Reynolds number with fixed $Ri = 1.0$. Increase in aspect ratio implies the decreased flow space with larger amount of heat and contaminants inside the enclosure due to increased size of thermo-contaminated block. With increasing value of aspect ratio, the heat transfer along the block is increasing and thermal lines are clustered along the lower part of the block. The bottom right section is occupied by cold fluid for higher values of Reynolds number and isotherms with higher temperature are moving towards the upper section of the enclosure. It is obvious that the size of recirculation zone effectively reduces and

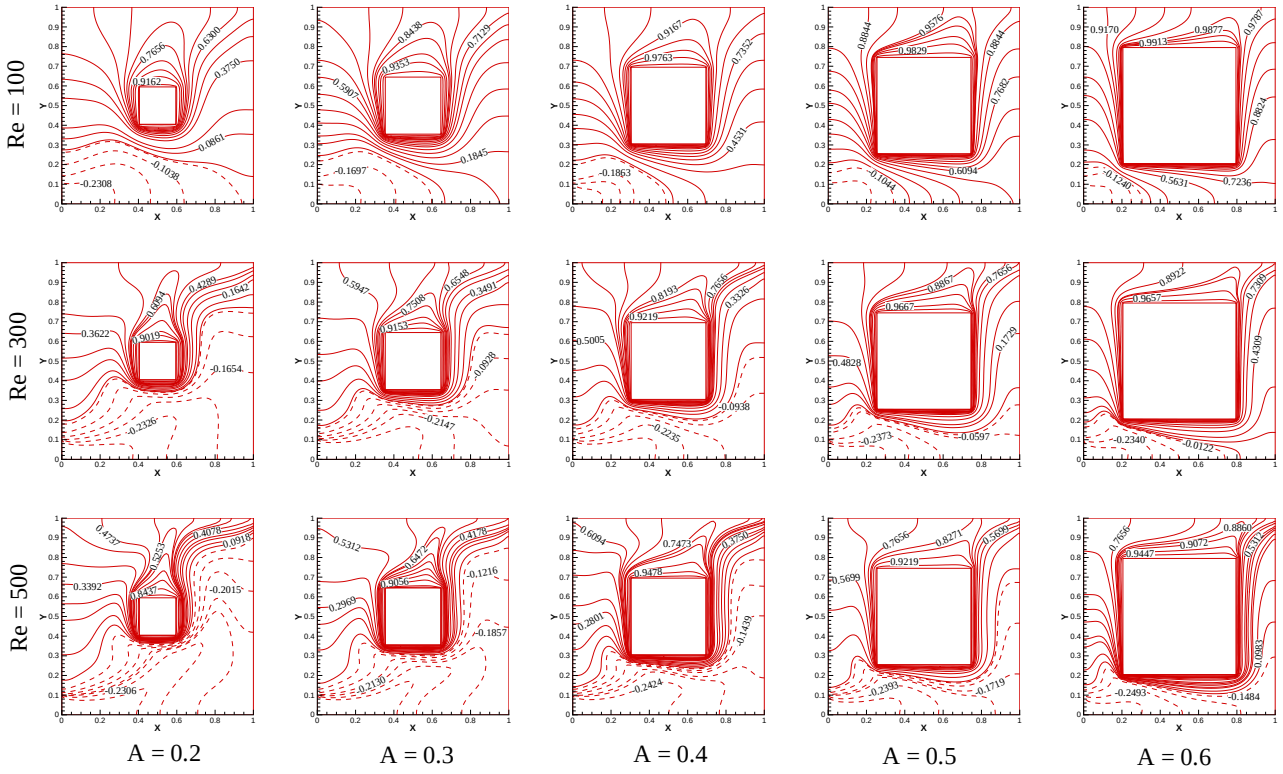

Figure 3.20: Effect of Reynolds number and aspect ratios on isotherms for case-I (with fixed $Ri = 1.0$, $Sc = 1.0$, $Br = 1.0$ and $Pr = 0.71$).

the fluid traverses through limited area with available inertia as the block size increases. Along the upper side of the thermo-contaminated block, some deviation in the isothermal lines are observed due to convection effect and hot fluid moves toward the outlet port. For higher values of Reynolds number, the lower region becomes colder due to forced convection effect.

3.5.6.3 Solutal Field

Fig. 3.21 represents the isoconcentration distribution inside the enclosure for various values of aspect ratios and Reynolds number. Concentration level is rapidly increasing inside the enclosure with the increase in aspect ratio due to increased size of thermo-contaminated block. Contaminant removal rate is found to be higher in case of higher Reynolds number due to forced convection effect. For aspect ratio 0.2, oval shaped solutal lines directed towards the upper section around the block is observed at $Re = 100$. The concentration level near the left vertical wall is observed to be decreasing with the

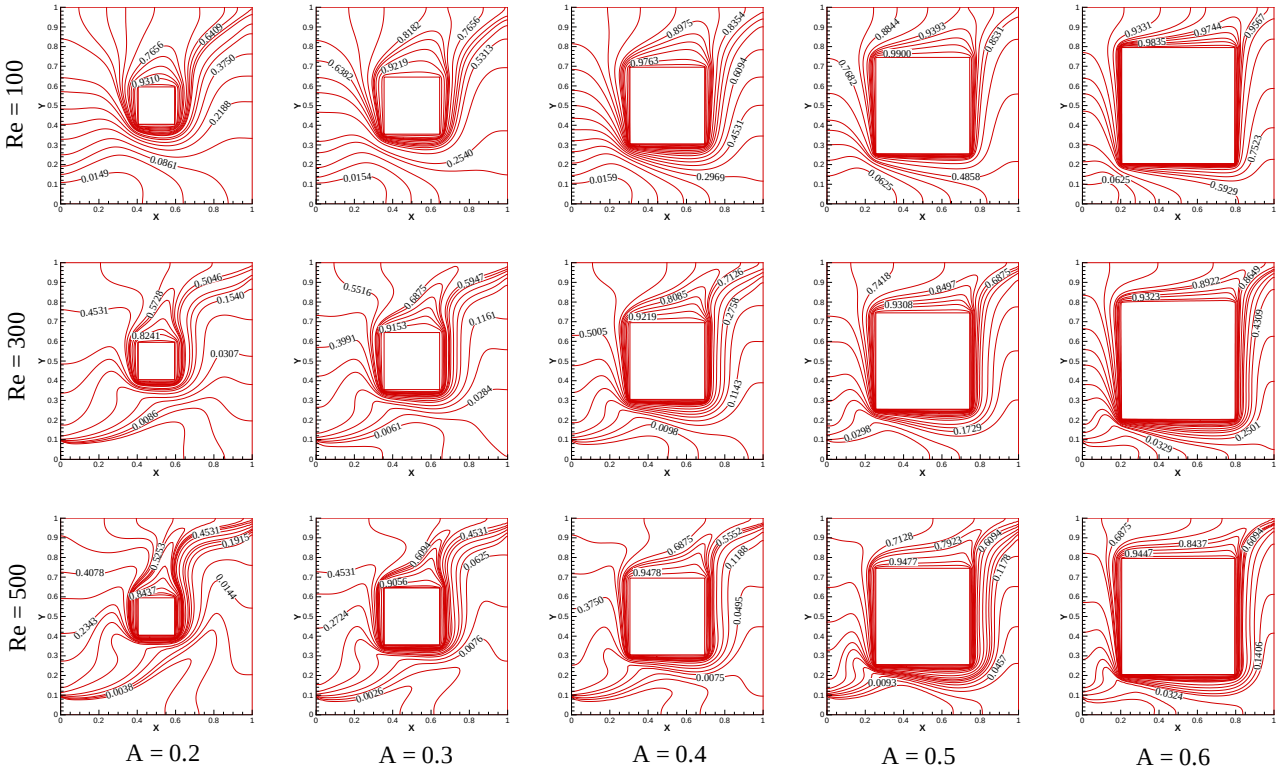

Figure 3.21: Effect of Reynolds number and aspect ratios on isoconcentrations for case-I (for fixed $Ri = 1.0$, $Sc = 1.0$, $Br = 1.0$ and $Pr = 0.71$).

increase in Reynolds number. For higher Reynolds number, a solutal plume is formed around the block directed towards the upper-right section of the enclosure and highly concentrated isoconcentration lines are found to be assembled near the block. As the block size increases, the contaminated region also increases which results the higher mass transfer rate along the block. It is also observed that for higher Reynolds number, the isoconcentration lines shows small values towards the outlet due to fast movement of fresh air and the concentration level is larger near the block in case of low Reynolds number.

3.5.7 Average Nusselt number, Sherwood number, temperature and cooling efficiency

Fig. 3.22 (a) and (b) represents the comparison of average heat transfer rate with the variation in Richardson number for different block locations inside the enclosure. From the figure, it is observed that average Nusselt number is increasing with the increasing value of Richardson number in all the cases for $Re = 100$. The heat transfer rate is found

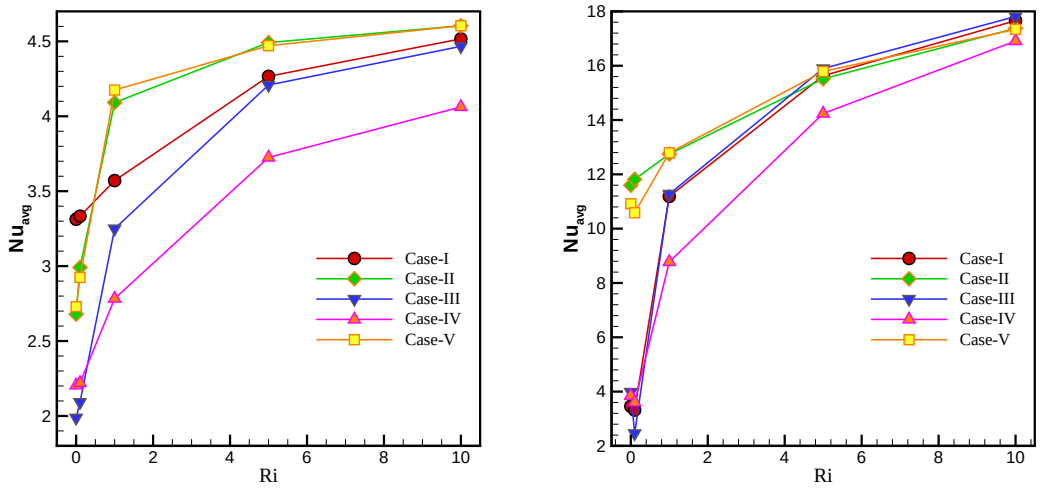

Figure 3.22: Variation of average heat transfer rate along the block with the variation of Richardson numbers for (a) $Re = 100$ and (b) $Re = 500$ with fixed $Br = 1.0$ for different locations of the block.

to be higher for case-II and case-V in which the block is placed near the outlet port and inlet port, respectively and thermo-contaminated block is directly affected by inlet fluid. From Fig. 3.22 (b), no effective variation in heat transfer rate is found around the block for $Ri > 6.0$. When the block is located in the upper section near the exit port, the heat transfer rate is less because the distance between the block and the inlet port is large. The effect of Richardson number on average mass transfer rate along the block is shown in Fig. 3.23 (a) for $Re = 100$ and in Fig. 3.23 (b) for $Re = 500$. It is observed that average Sherwood number is higher for higher Reynolds number due to forced convection effect. With the increasing values of Richardson number, average rate of mass transfer is also increasing in all the cases due to increased density differences. When $Re = 100$, the value of Sh_{avg} is maximum in case-II and case-V for $Ri \geq 1.0$ and when $Re = 500$, maximum Sh_{avg} is achieved in case-III.

To obtain the maximum cooling effect inside the enclosure, the value of average temperature must be smaller. A comparison between Richardson number and average temperature inside the enclosure is represented in Fig. 3.24 (a), (b) and (c) for different values of Reynolds number. The cooling inside the enclosure is increasing with the increasing value of Reynolds number due to increasing amount of cold air. The average temperature

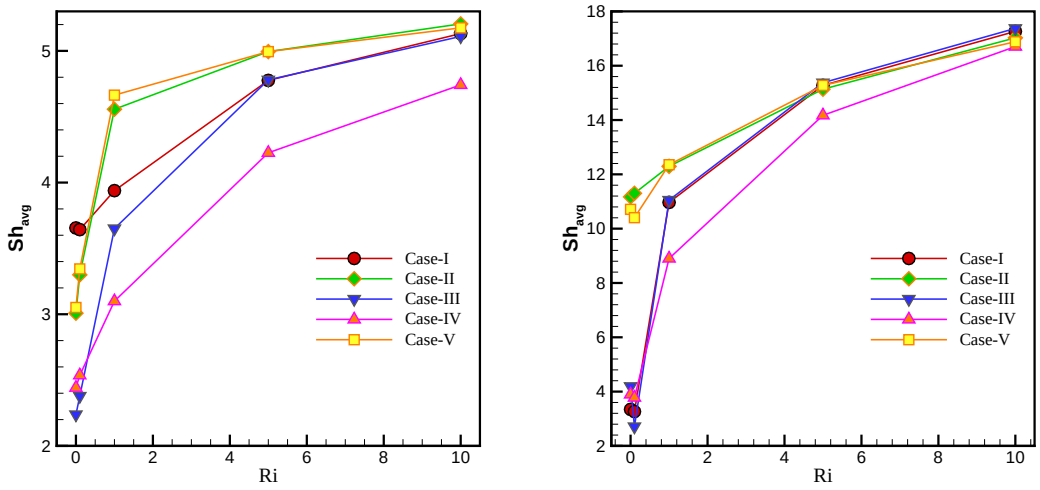

Figure 3.23: Variation of average mass transfer rate along the block with the variation of Richardson numbers for (a) $Re = 100$ and (b) $Re = 500$ with fixed $Br = 1.0$ for different locations of the block.

is found to be maximum in case-V, in which the block is placed in the lower section near the inlet port and heat from thermo-contaminated block is forced by inlet fluid to move upwards and thus thermal lines with higher temperature are found to be spread in the upper region. This concludes that to achieve the maximum heating inside the enclosure, block must be placed in the bottom section of the enclosure near the inlet port with low Reynolds number value. Whereas, for the cooling inside the enclosure, block must be located in the upper section near the outlet port with higher Reynolds number value. This happens because the heat source is affected by strong external flow. It is observed from the figure that maximum cooling is obtained in case-IV, in which the block is placed in the upper region near the outlet port. Moreover, the average temperature is found to be decreasing with increase in Richardson number for case-IV. Fig. 3.25 represents the variation in average temperature of the enclosure and cooling efficiency due to the change in buoyancy ratio at $Ri = 1.0$ and $Re = 500$. In case of negative buoyancy ratio, thermal and solutal buoyancy forces oppose each other and this results the higher variation in average temperature while for positive buoyancy ratio, thermal and solutal buoyancy effects assist each other produces low temperature dissipation inside the enclosure for case-IV. Thus for the effective cooling inside the enclosure, the block must be placed near the

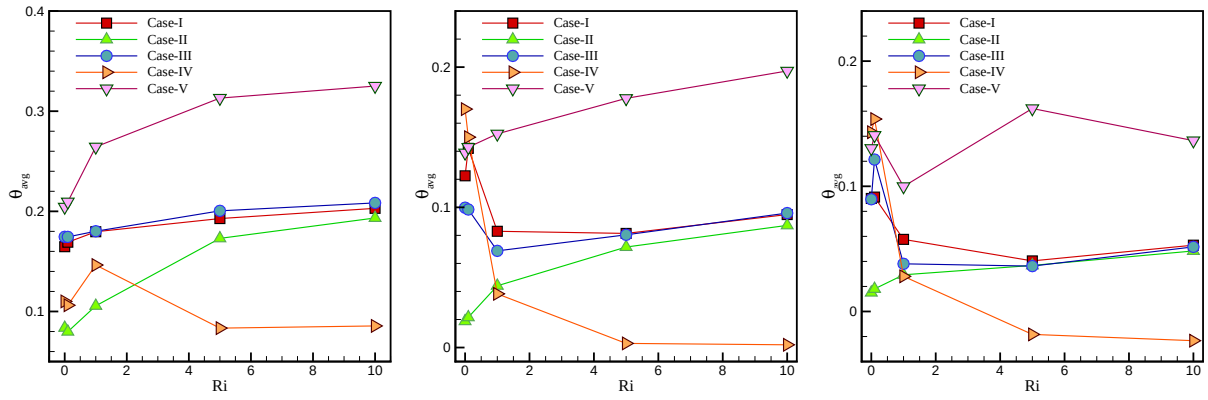

Figure 3.24: Comparison of bulk average temperature inside the enclosure with the variation of Richardson number for (a) $Re = 100$, (b) $Re = 300$ and (c) $Re = 500$ (with fixed $Sc = 1.0$, $Br = 1.0$ and $Pr = 0.71$).

outlet for aiding convection with the forced convection i.e. for higher Reynolds number. This is because the fluid with highest Reynolds number is capable to carry more heat away from the heat source and dissipated through the outlet port of the enclosure.

It is observed that for the efficient cooling inside the enclosure, the block must be placed near the outlet port, this is due to the tendency of hot air which moves in the upward direction towards the outlet port due to density difference. A comparison is made between the Case-II and case-IV for different values of Reynolds number in Fig. 3.26. With increasing value of Richardson number from 1.0 to 10.0, the cooling efficiency inside the enclosure is increasing monotonically for both the cases. The average temperature for case-IV is found to be decreasing with the increase in Richardson number as well as Reynolds number due to convection effects. For small Reynolds number, the injected cold air moves slowly and getting heated when it comes in contact with the thermo-contaminated block due to which the upward region of the block is surrounded by this hot air and thus the average temperature of the enclosure is getting intensified. As the velocity of the injected air is increased, the heat transfer rate is also increased which results efficient cooling inside the enclosure. The average temperature of the enclosure is minimum in case-IV relative to $Re = 500$ in natural convection dominated region.

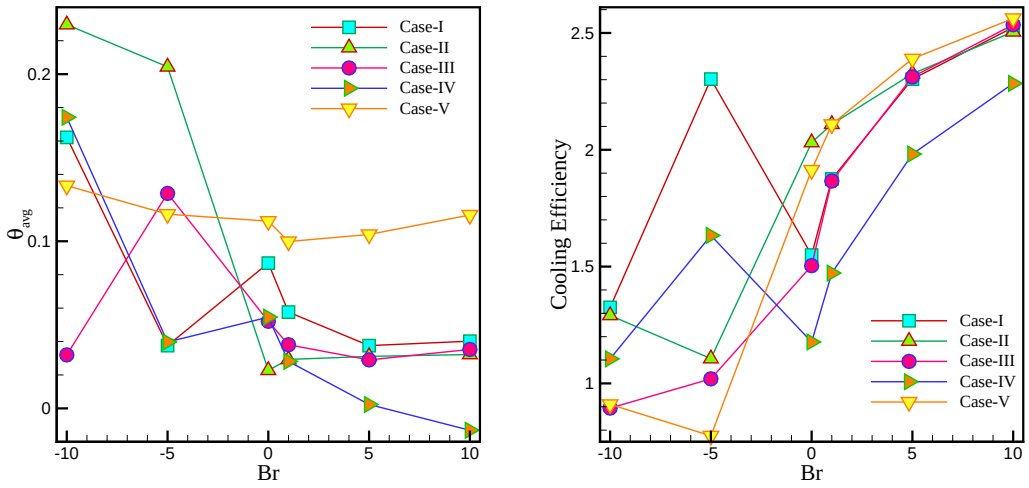

(a) (b)

Figure 3.25: Comparison of (a) average temperature and (b) cooling efficiency inside the enclosure with the variation of buoyancy ratio for fixed $Re = 500$, $Sc = 1.0$, $Ri = 1.0$ and $Pr = 0.71$.

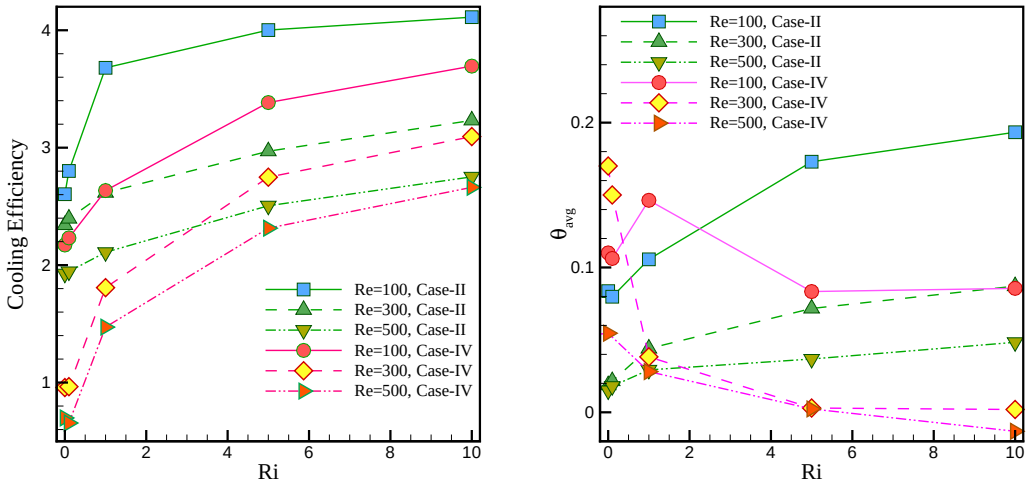

(a) (b)

Figure 3.26: Comparison of the simulated results of case-II and Case-IV for (a) cooling efficiency and (b)average temperature inside the enclosure with the variation of Richardson number (with fixed $Sc = 1.0$, $Br = 1.0$ and $Pr = 0.71$.)

3.6 Conclusion

The present study is performed for the double diffusive mixed convection due to different locations and various aspect ratios of a thermo-contaminated block inside the ventilated enclosure with the variation of flow parameters like Richardson number, Reynolds number and buoyancy ratio. Five different locations and five different aspect ratios of the block are considered to visualize the heat and species transfer effect to study the average temperature and effective cooling inside the enclosure. Based on the numerical simulations, the conclusions are summarized as follows:

1. When the block is placed in bottom section of the enclosure, thermal lines with higher temperature are rising above the block and most of the upper section fluid is getting heated, resulting the higher bulk average temperature inside the enclosure.

2. Cooling efficiency is higher when the Reynolds number is 100 and Richardson number is 10.0 for case-II whereas, it is minimum when the Reynolds number is 500 and Richardson number is 0.0 for case-IV.

3. The average temperature inside the enclosure is minimum when Reynolds number is 500 for case-IV, whereas, the average temperature of the fluid is found to be maximum when Reynolds number is 100 for case-V.

4. For the maximum cooling inside the enclosure, block must be placed near the outlet port in the upper section of the enclosure. The heat and species transport rate along the block is increasing with the increase of Reynolds and Richardson number.

5. In case-III, the major portion of lower-mid section is occupied by cold fluid for higher Richardson number and Reynolds number.

6. When the block is placed at the middle section of the enclosure, the average Nusselt number along the thermo-contaminated block achieves its maximum value when the inlet port is located along the middle section of the left vertical wall, and further increased with the increase in inlet port size and Reynolds number value because of injected cold air.

Chapter 4

Performance evaluation of coolant air with buoyancy in a parallelogrammic mixed displacement ventilated system *

4.1 Introduction

Mixed convection in an enclosure refers to the convection process occurring due to the combined effects of buoyancy force and the mechanically driven force which has large scale applications in industrial and commercial heating or cooling applications like cooling of electronic devices, solar systems, thermal comfort, drying technologies, chemical processing equipments, power electronics, furnace design and building applications. Mixed convection in rectangular ventilated enclosures due to discrete heating and cooling effects are broadly investigated by several authors [29, 108, 57, 54]. However, very few research papers on mixed convection dealt with differential geometries are available in the literature. The parallelogrammic shaped geometry is widely applicable in various areas such as electronics, building, aeronautics and solar energy and the fluid flow, heat and mass transfer behavior varies with the variation in inclination angle of the enclosure for different values of flow governing parameters [10]. The idea is brought from the ventilation in a theatre of the institution which is 60 feet in chord, 44 feet deep; more correctly, it is a semi circle of 30 feet radius, applied to a parallelogram of 60 by 14. Usually in the upper part of the theatre, it is observed that 3% of the carbonic acid in it, produced by vitiation and

*The contents of this chapter has been published in *Journal of Mechanical Sciences, Elsevier, DOI:10.1016/j.ijmecsci.2018.08.040*

imperfect ventilation [49]. The thermal behavior and indoor air quality due to air-CO_2 mixture inside the ventilated cavity is analyzed by Xaman et al. [120] for better design of buildings in order to achieve acceptable microclimate. Heat transfer processes generates irreversibility, resulting in process efficiency loss. This efficiency loss is related to the entropy generation, which exists in all heat transfer and fluid flow processes. In recent scenario, the optimal design criteria for thermal systems by minimizing their entropy generation is a topic of great interest, especially in the fields related to geometry of a duct, natural convection in enclosure has gained attraction of many researchers [53, 22, 32].

Hyun and Choi [48] studied the transient natural convection effects with heat transfer in parallelogrammic-shaped enclosure to analyze the time history patterns of fluid flow and thermophoretic effects. The average Nusselt number along the heated vertical sidewalls are presented at different time levels with the variation of inclination angle of horizontal walls. Study on double-diffusive natural convection in a parallelogrammic shaped enclosure is numerically studied by Costa [26] to find the influence of heat and mass transfer inside the enclosure and their dependence on flow governing parameters like Rayleigh number, aspect ratio and inclination angle. The variation in heat and mass transfer was found to be significant by increasing either Rayleigh number or the buoyancy ratio. Bairi [6] discussed about the Nusselt number evaluation criteria for closed enclosures and concluded that the evaluation criteria based on the distance between active walls is not suitable for closed enclosures of non-rectangular sections. He had proposed a definition of Nusselt number for closed enclosures of parallelogrammic section for natural convection flows. The flow circulation and temperature distribution in a trapezoidal shaped enclosure due to uniform and non-uniform temperature along the bottom wall with various inclination angle was analyzed by Basak et al. [13] and it was observed that the higher temperature variations can be obtained with the increment in inclination angle.

A combined experimental and numerical analysis of flow dynamics and heat transfer effects in a parallelogrammic shaped closed enclosure applicable for building design was made by Bairi [9] to find the thermal effects produced by the interpolation of two vertical thermally active walls connected by a channel of insulating material. Two dimensional temperature fields and flow lines at different instant of time are demonstrated to visualize

the temporal evolution of heat transfer rate which is used for the time dependent convection exchange occurring between the wall made up of air-filled inclined cells. Garcia de Maria et al. [38] experimentally and numerically tested the steady-state natural convection phenomena in a 2D air-filled enclosure of parallelogrammic section with isothermal discrete heat sources and shown that the average Nusselt number can be formulated as a function of Rayleigh number and inclination angle. Bairi [7] studied numerically the transient natural convection effects in an air-filled parallelogrammic enclosure to determine the convective exchanges at the heated wall that consists of five alternated isothermal and adiabatic horizontal bands. The results for fluid flow and temperature were presented in the form of streamlines, thermal lines and average Nusselt number at each band of the hot wall for several values of the inclination angle throughout the transient phase and steady phase. Bairi [8] had proposed Nusselt-Rayleigh-Fourier type correlation for the flow simulation through an enclosure of parallelogrammic section to find the heat transfer by transient natural convection. From the literature it is observed that several studies has been done on natural convection in closed enclosure of parallelogrammic section but very few studies are available for mixed convection, which has large scale applications in engineering problems.

In the present chapter, mixed convection in a ventilated parallelogrammic enclosure is numerically studied to find the maximum heat transfer with minimum entropy generation due to the presence of discrete heat and solutal sources, where solutes are considered to be contaminant in nature. Computations are performed with the variation of flow governing parameters like Reynolds number, Richardson number and inclination angle with a fixed value of Prandtl number, Schmidt number and buoyancy ratio. The results are presented in the form of streamlines, isotherms, isoconcentrations, average Nusselt number, Sherwood number, cooling efficiency entropy generation and performance evaluation criteria to find the best suited configuration for optimized cooling/heating.

4.2 Problem formulation and governing equations

The physical structure of the proposed problem consists a ventilated enclosure of parallelogrammic section (Fig. 4.1) where, the horizontal walls are placed at an angle β with the

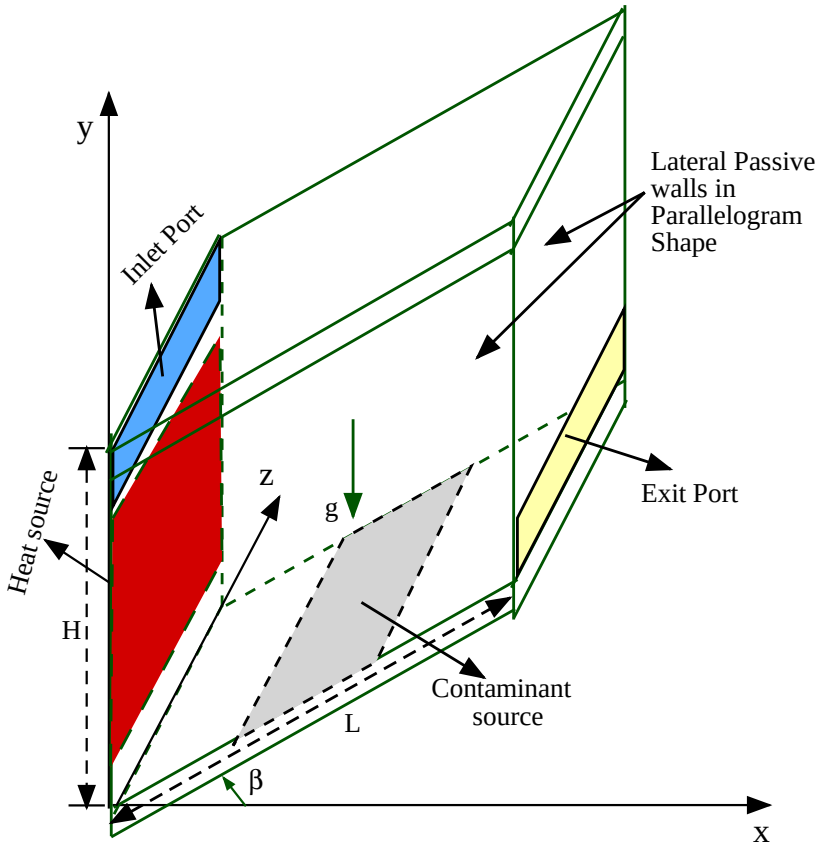

Figure 4.1: Schematic diagram of the fluid flow configuration.

horizontal axis. The length of vertical and horizontal walls of the enclosure are considered as L. An inlet port with cold air entrant is considered along the left vertical wall and exit through the right vertical wall of the parallelogrammic shaped enclosure. The length of inlet and outlet port is considered to be equal and taken as $0.1L$. A discrete heat source is considered along the vertical walls and contaminant source along the bottom wall (shown in Fig. 4.1). The length of the heat source and contaminant source is taken as $0.6L$ for the simulations. The enclosure is assumed to be filled with air and the walls are considered as insulated and adiabatic. The inclination angle is chosen in both positive and negative sense i.e., different angular values are considered as, 0^0, $\pm 15^0$, $\pm 30^0$, $\pm 45^0$, $\pm 60^0$ for the simulation.

Four different cases (Fig. 4.2) are considered with the variation of the position of heat source, inlet port and outlet port. In case-I, the heat source is considered along the left vertical wall, inlet port is along the upper section of the left vertical wall and outlet

is considered along the lower section of the right vertical wall; In case-II, the heat source is considered along the right vertical wall, inlet port is along the upper section of the left vertical wall and outlet is along the lower section of the right vertical wall; In case-III, the heat source is considered along the left vertical wall, inlet port is along the lower section of left vertical wall and the outlet is along the upper section of the right vertical wall; In case-IV, the heat source is considered along the right vertical wall, inlet port is along the lower section of the left vertical wall and the outlet is along the upper section of the right vertical wall.

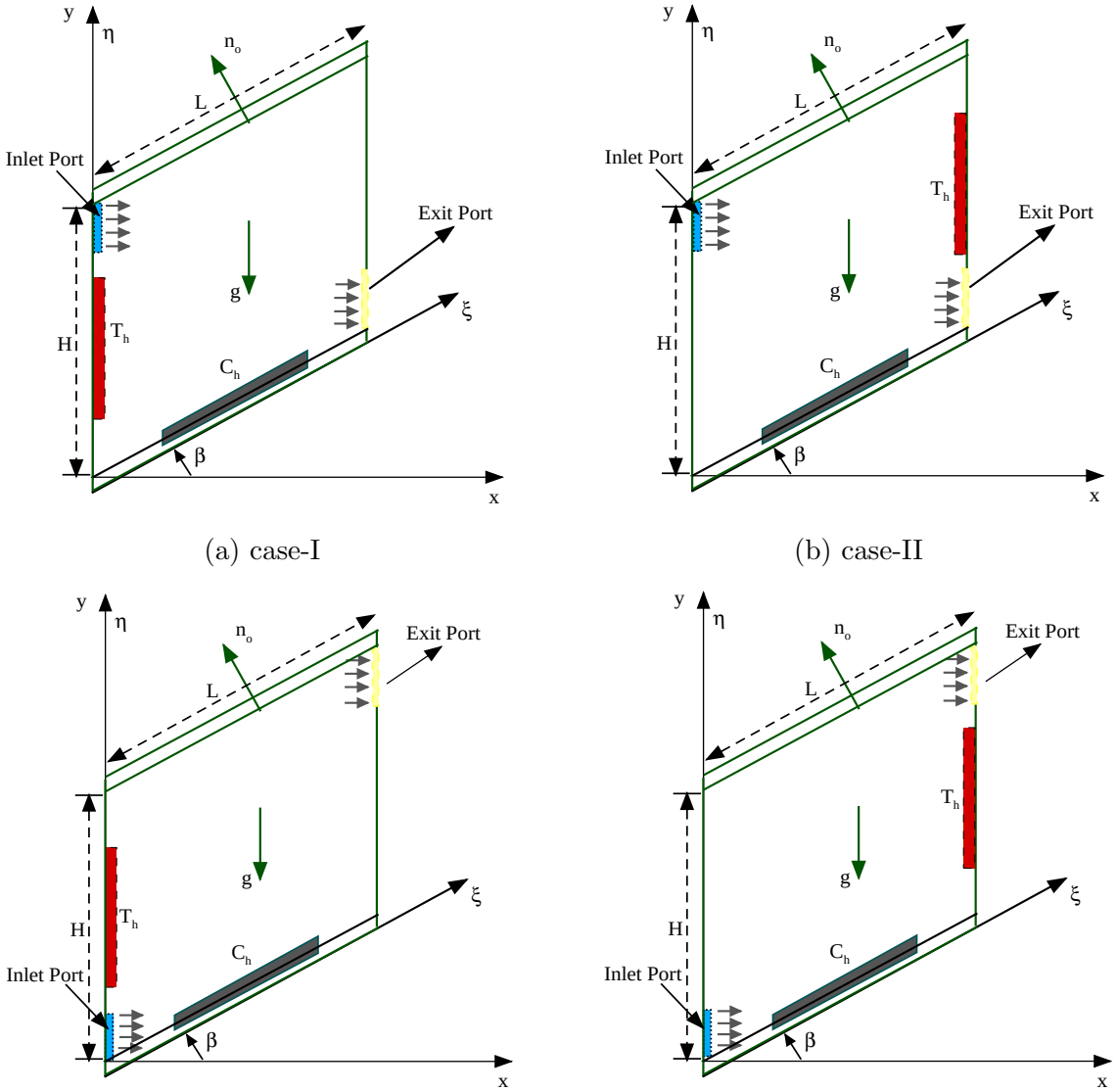

(a) case-I

(b) case-II

(c) case-III

(d) case-IV

Figure 4.2: Sketching of different computational domain for the simulation

The fluid is assumed to be Newtonian, viscous and incompressible and the flow is assumed to be laminar. The governing equation for fluid flow, heat and mass transfer includes the equation of continuity i.e., (conservation of mass), Navier-Stokes equations for momentum (conservation of momentum), energy equation (conservation of energy) and concentration equation (conservation of species). The flow is driven by the buoyancy effects generated due to the temperature and concentration differences and the forced convection effects due to the injected cold air. The density variation due to temperature and concentration is approximated due to the Boussinesq approximation as:

$$\rho = \rho_0[1 - \beta_T(T^* - T_0) - \beta_C(C^* - C_0)], \tag{4.1}$$

where $\beta_T = -\frac{1}{\rho}\frac{\partial \rho}{\partial T^*}$ and $\beta_C = -\frac{1}{\rho}\frac{\partial \rho}{\partial C^*}$ represents the thermal expansion coefficient and solutal expansion coefficient, respectively. The thermal expansion coefficient, β_T is always positive as density decreases with the increase of temperature while the solutal expansion coefficient, β_c may be either positive or negative because an increase in concentration induces a decrease or an increase in density, respectively [39]. The flow governing equations in dimensional form are considered as:

$$\nabla \cdot \overrightarrow{v} = 0, \tag{4.2}$$

$$\frac{\partial u^*}{\partial t^*} + (\overrightarrow{v} \cdot \nabla)u^* = -\frac{1}{\rho}\left(\frac{\partial p^*}{\partial x^*}\right) + \nu(\nabla^2 u^*), \tag{4.3}$$

$$\frac{\partial v^*}{\partial t^*} + (\overrightarrow{v} \cdot \nabla)v^* = -\frac{1}{\rho}\left(\frac{\partial p^*}{\partial y^*}\right) + \nu(\nabla^2 v^*) + g\beta_T(T^* - T_0) + g\beta_C(C^* - C_0), \tag{4.4}$$

$$\frac{\partial T^*}{\partial t^*} + (\overrightarrow{v} \cdot \nabla)T^* = \alpha(\nabla^2 T^*), \tag{4.5}$$

$$\frac{\partial C^*}{\partial t^*} + (\overrightarrow{v} \cdot \nabla)C^* = D(\nabla^2 C^*). \tag{4.6}$$

The characteristic length and reference inlet velocity are considered as L and u_i, respectively and u^*, v^*, t^*, T^*, C^* represents the dimensional horizontal velocity, vertical velocity, time, temperature and concentration, respectively. The above mentioned equations can be expressed in non-dimensional form by using the following dimensionless variables:

$$x = \frac{x^*}{L}; \quad y = \frac{y^*}{L}; \quad u = \frac{u^*}{u_i}; \quad v = \frac{v^*}{u_i}; \quad p = \frac{p^*}{\rho u_i^2}; \quad T = \frac{(T^* - T_o)}{(T_h - T_o)}; \quad C = \frac{(C^* - C_o)}{(C_h - C_o)};$$

$$Br = \frac{\beta_C(C_h - C_o)}{\beta_T(T_h - T_o)}; \quad Gr = \frac{g\beta_T(T_h - T_o)L^3}{\nu^2}; \quad Re = \frac{u_i L}{\nu}; \quad Ri = \frac{Gr}{Re^2}; \quad Pr = \frac{\nu}{\alpha}; \quad Sc = \frac{\nu}{D}.$$

The computational domain does not coincide with the co-ordinate lines in the physical space and therefore the implementation of boundary conditions required a complicated interpolation of the data along the boundary points. To avoid this difficulty, a suitable co-ordinate transformation is made for physical space (x, y) and the transformed co-ordinates are represented in the form of (ξ, η) so that the boundary of physical space coincides with the boundary of the computational domain. The transformed co-ordinate system is considered as,

$$\xi = x/cos\beta, \ \eta = y - x \ tan\beta \tag{4.7}$$

Under the above transformation, the governing equations and the boundary conditions reduces to:

$$\frac{1}{cos\beta}\frac{\partial u}{\partial \xi} - tan\beta\frac{\partial u}{\partial \eta} + \frac{\partial v}{\partial \eta} = 0, \tag{4.8}$$

$$\frac{\partial u}{\partial t} + \frac{1}{cos\beta}\frac{\partial (uu)}{\partial \xi} - tan\beta\frac{\partial (uu)}{\partial \eta} + \frac{\partial (vu)}{\partial \eta} = -\left(\frac{1}{cos\beta}\frac{\partial p}{\partial \xi} - tan\beta\frac{\partial p}{\partial \eta}\right) + \frac{1}{Re.cos^2\beta}\left(\frac{\partial^2 u}{\partial \xi^2} + \frac{\partial^2 u}{\partial \eta^2} - 2sin\beta\frac{\partial^2 u}{\partial \xi \partial \eta}\right), \tag{4.9}$$

$$\frac{\partial v}{\partial t} + \frac{1}{cos\beta}\frac{\partial (uv)}{\partial \xi} - tan\beta\frac{\partial (uv)}{\partial \eta} + \frac{\partial (vv)}{\partial \eta} = -\frac{\partial p}{\partial \eta} + \frac{1}{Re.cos^2\beta}\left(\frac{\partial^2 v}{\partial \xi^2} + \frac{\partial^2 v}{\partial \eta^2} - 2sin\beta\frac{\partial^2 v}{\partial \xi \partial \eta}\right) + \frac{Gr}{Re^2}(T + Br.C), \tag{4.10}$$

$$\frac{\partial T}{\partial t} + \frac{1}{cos\beta}\frac{\partial (uT)}{\partial \xi} - tan\beta\frac{\partial (uT)}{\partial \eta} + \frac{\partial (vT)}{\partial \eta} = \frac{1}{Re.Pr.cos^2\beta}\left(\frac{\partial^2 T}{\partial \xi^2} + \frac{\partial^2 T}{\partial \eta^2} - 2sin\beta\frac{\partial^2 T}{\partial \xi \partial \eta}\right), \tag{4.11}$$

$$\frac{\partial C}{\partial t} + \frac{1}{cos\beta}\frac{\partial (uC)}{\partial \xi} - tan\beta\frac{\partial (uC)}{\partial \eta} + \frac{\partial (vC)}{\partial \eta} = \frac{1}{Re.Sc.cos^2\beta}\left(\frac{\partial^2 C}{\partial \xi^2} + \frac{\partial^2 C}{\partial \eta^2} - 2sin\beta\frac{\partial^2 C}{\partial \xi \partial \eta}\right). \tag{4.12}$$

The initial conditions at $t = 0$ are given by:

$$u = 0, \;\; v = 0, \;\; T = 0, \;\; C = 0; \qquad 0 \leq \xi, \eta \leq 1 \tag{4.13}$$

Boundary conditions at $t > 0$ for the computational domain are defined as:
along horizontal Walls:

$$u = 0, \; v = 0, \; \frac{\partial T}{\partial \eta} = 0, \; \frac{\partial C}{\partial \eta} = 0 \quad \text{at} \;\; \eta = 0 \text{ or } 1;$$

along vertical walls:

$$u = 0, \; v = 0, \; \frac{\partial T}{\partial \xi} = sin\beta \frac{\partial T}{\partial \eta}, \; \frac{\partial C}{\partial \xi} = sin\beta \frac{\partial C}{\partial \eta} \quad \text{at} \;\; \xi = 0 \text{ or } 1;$$

for inlet port:

$$u = 1, \; v = 0, \; T = -0.5, \; C = 0;$$

for outlet port:

$$\frac{\partial u}{\partial \xi} = sin\beta \frac{\partial u}{\partial \eta}, \; \frac{\partial v}{\partial \xi} = sin\beta \frac{\partial v}{\partial \eta}, \; \frac{\partial T}{\partial \xi} = sin\beta \frac{\partial T}{\partial \eta}, \; \frac{\partial C}{\partial \xi} = sin\beta \frac{\partial C}{\partial \eta};$$

for heat source along the vertical wall:

$$u = 0, \; v = 0, \; T = 1, \; \frac{\partial C}{\partial \xi} = sin\beta \frac{\partial C}{\partial \eta};$$

for contaminated section of the bottom wall:

$$u = 0, \; v = 0, \; \frac{\partial T}{\partial \eta} = 0, \; C = 1.$$

The average heat transfer rate along the heated portion of the wall is defined by average Nusselt number as,

$$Nu_{avg} = -\int \frac{\partial T}{\partial \xi} d\eta. \tag{4.14}$$

The average mass transfer rate along the contaminated portion of the bottom wall is defined by average Sherwood number as,

$$Sh_{avg} = -\int \frac{\partial C}{\partial \eta} d\xi. \tag{4.15}$$

In the mixed convection system, the main factors for irreversible flow are heat transfer and fluid friction [99]. Based on the local thermodynamic equilibrium of the linear transport

theory, the entropy generation due to heat transfer irreversibility is denoted by S_T and is given as:

$$\begin{aligned} S_T &= \left(\frac{\partial T}{\partial x}\right)^2 + \left(\frac{\partial T}{\partial y}\right)^2 \\ &= \left(\frac{1}{cos\beta}\frac{\partial T}{\partial \xi} - tan\beta\frac{\partial T}{\partial \eta}\right)^2 + \left(\frac{\partial T}{\partial \eta}\right)^2, \end{aligned} \tag{4.16}$$

and the entropy generation due to fluid friction irreversibility is denoted by S_ψ which is given as:

$$\begin{aligned} S_\psi &= \phi\left[2\left\{\left(\frac{\partial u}{\partial x}\right)^2 + \left(\frac{\partial v}{\partial y}\right)^2\right\} + \left\{\frac{\partial v}{\partial x} + \frac{\partial u}{\partial y}\right\}^2\right] \\ &= \phi\left[2\left\{\left(\frac{1}{cos\beta}\frac{\partial u}{\partial \xi} - tan\beta\frac{\partial u}{\partial \eta}\right)^2 + \left(\frac{\partial v}{\partial \eta}\right)^2\right\} + \left\{\left(\frac{1}{cos\beta}\frac{\partial v}{\partial \xi} - tan\beta\frac{\partial v}{\partial \eta}\right) + \frac{\partial u}{\partial \eta}\right\}^2\right]. \end{aligned} \tag{4.17}$$

The total entropy generation inside the system is obtained by summation of the total entropy generation due to heat transfer and the total entropy generation due to fluid friction [99], i.e.,

$$S_{gen} = S_T + S_\psi \tag{4.18}$$

and the average entropy generation inside the enclosure is given by:

$$S_{avg} = \frac{1}{V}\int_V S_{gen} dV. \tag{4.19}$$

The relative dominance of entropy generation due to heat transfer and fluid friction is given by Bejan number which is formulated as [98]:

$$Be_T = \frac{S_T}{S_{gen}}, \tag{4.20}$$

and the average Bejan number inside the enclosure is given by:

$$Be_{avg} = \frac{1}{V}\int_V Be_T \; dV. \tag{4.21}$$

Roy et al. [98] observed that for $Be < 0.5$, the entropy generation is dominated by fluid friction irreversibility while $Be > 0.5$ implies the dominance of heat transfer irreversibility and $Be = 0.5$ implies the equal contribution of heat transfer and fluid friction irreversibility to the entropy generation.

In order to find the maximum heat transfer rate with minimum entropy generation, we have discussed the performance evaluation criterion (PEC) which is the ratio of Nusselt number and entropy generation [67] i.e.,

$$PEC = \frac{Nu_{avg}}{S_{avg}}. \tag{4.22}$$

The cooling efficiency [85] inside the enclosure is given by

$$\epsilon = 1 - \left(\frac{\overline{T}_{out}}{\overline{T}_{in}}\right) \tag{4.23}$$

where $\overline{T}_{in}$ is the average inlet temperature and $\overline{T}_{out}$ is the average outlet temperature.

4.3 Numerical procedure and Code Validation

The transformed nonlinear governing equation with specified boundary conditions are solved numerically by finite volume based SIMPLE algorithm [86] using staggered grid arrangement. The method involves the integration of governing equations over each control volumes which involves a pressure link between the continuity and momentum equations which is adapted by the justification of continuity equation to the Poisson equation for pressure. The Poisson equation implements a pressure correction for the divergent velocity field. The velocity field $u^*_{i,j}$ and $v^*_{i,j}$ are obtained from the momentum equations using the guessed pressure field $p^*_{i,j}$ (which is equal to the previous time step solution) at any intermediate stages which may not satisfy the continuity equation. The continuity equation is justified through a pressure correction $p^c_{i,j}$ at each cell (i, j) as

$$p^{n+1}_{i,j} = p^*_{i,j} + p^c_{i,j}$$

which implies a correction in the velocity field $u^c_{i,j}$ and $v^c_{i,j}$ as

$$u^{n+1}_{i,j} = u^*_{i,j} + u^c_{i,j}$$

$$v^{n+1}_{i,j} = v^*_{i,j} + v^c_{i,j}$$

where $u^{n+1}_{i,j}$ and $v^{n+1}_{i,j}$ are satisfied by the continuity equation. The corrected velocity fields $(u^{n+1}_{i,j},\ v^{n+1}_{i,j})$ can be obtained from the momentum equation as,

$$u^{n+1}_{i,j} = u^*_{i,j} + \alpha_u\left[-\frac{\Delta t}{\Delta\xi}\frac{1}{cos\beta}(p^c_{i+1,j} - p^c_{i,j}) + \frac{\Delta t}{4\Delta\eta}tan\beta(p^c_{i,j+1} - p^c_{i,j-1} + p^c_{i+1,j+1} - p^c_{i+1,j-1})\right] \tag{4.24}$$

$$v_{i,j}^{n+1} = v_{i,j}^{*} + \alpha_v \left[- \frac{\Delta t}{\Delta \eta} (p_{i,j+1}^{c} - p_{i,j}^{c}) \right] \tag{4.25}$$

α_u and α_v are considered as the relaxation parameters and the convergence is achieved for the relaxation parameter $\frac{2}{3}$. With the substitution of the corrected velocity fields $(u_{i,j}^{n+1},\ v_{i,j}^{n+1})$ in the discretized continuity equation, Poisson equation reduces to,

$$\begin{aligned}
&\left[2 \left\{ \alpha_u \left(\frac{\Delta t \Delta \eta}{\Delta \xi} \right) \frac{1}{cos^2 \beta} + \alpha_v \left(\frac{\Delta t \Delta \xi}{\Delta \eta} \right) \right\} + \alpha_u \left(\frac{\Delta t \Delta \xi}{4 \Delta \eta} \right) tan^2 \beta \right] p_{i,j}^{c} \\
&\quad = - \left[\frac{\Delta \eta}{cos \beta} (u_{i,j}^{*} - u_{i-1,j}^{*}) + \Delta \xi (v_{i,j}^{*} - v_{i,j-1}^{*}) \right] + \alpha_u \left(\frac{\Delta t \Delta \eta}{\Delta \xi} \right) \frac{1}{cos^2 \beta} \left(p_{i+1,j}^{c} + p_{i-1,j}^{c} \right) \\
&\quad + \alpha_v \left(\frac{\Delta t \Delta \xi}{\Delta \eta} \right) \left(p_{i,j+1}^{c} + p_{i,j-1}^{c} \right) + \frac{\Delta \xi}{4} tan \beta \left(u_{i,j+1}^{*} + u_{i-1,j+1}^{*} - u_{i-1,j-1}^{*} - u_{i,j-1}^{*} \right) \\
&\quad + \alpha_u \left(\frac{\Delta t \Delta \xi}{16 \Delta \eta} \right) tan^2 \beta \left(2 p_{i,j+2}^{c} + p_{i+1,j+2}^{c} - 2 p_{i+1,j}^{c} + p_{i-1,j+2}^{c} - 2 p_{i-1,j}^{c} + p_{i-1,j-2}^{c} \right. \\
&\quad \left. + 2 p_{i,j-2}^{c} + p_{i+1,j-2}^{c} \right) - \alpha_u \left(\frac{\Delta t}{2} \right) \frac{tan \beta}{cos \beta} \left(p_{i+1,j+1}^{c} - p_{i+1,j-1}^{c} - p_{i-1,j+1}^{c} + p_{i-1,j-1}^{c} \right).
\end{aligned} \tag{4.26}$$

In the computation, velocities, temperature and CO_2 concentration are considered to be converged, if, $|\varphi_{i,j}^{k+1} - \varphi_{i,j}^{k}| \leq 10^{-6}$, where $\varphi = (u,\ v,\ T,\ C)$ are the flow variables, k is the iteration number and (i, j) denote the grid nodes.

Numerical validation of the present work is made with the experimental and numerical results due to Garcia de Maria et al. [38] by considering the natural convective flow in a closed enclosure of parallelogrammic section. Left vertical wall is divided in five horizontal bands which are assumed to be alternatively maintained at higher temperature and adiabatic, whereas the right vertical wall is maintained at low temperature. The Nusselt number is calculated along the hot bands of the left vertical wall for various values of inclination angle at $Ra = 10^4$ and the average Nusselt number (Nu_{avg}) is presented in Fig. 4.3 (a). The grid independency test is performed by considering different grid sizes 80×80, 100×100, 150×150, 200×200 and 250×250. A good agreement of the present result is found with Garcia de Maria et al. [38] and 200×200 is found to be optimal grid size (Fig. 4.3 (a)). The maximum error for average Nusselt number (grid size 200×200) with the result due to Garcia de Maria et al. [38] is found to be 4.05 %. The present code is also validated by the experimental work done by Minaei et al. [72] to investigate

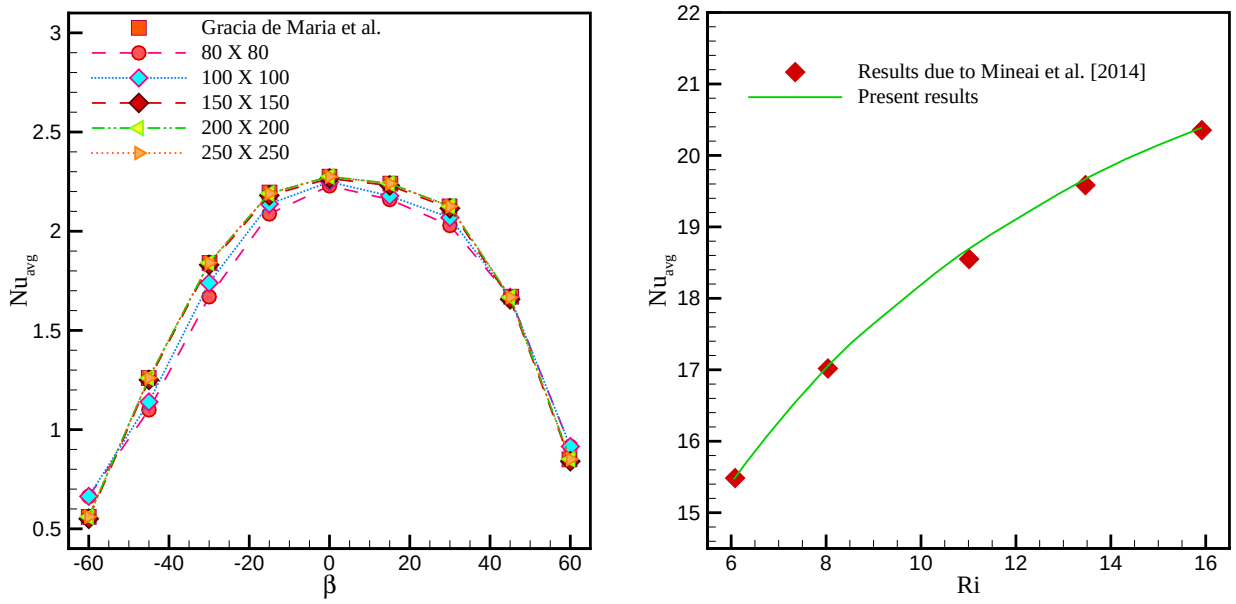

(a) (b)

Figure 4.3: Comparison of average Nusselt number along the hot wall using present code with the results due to (a) Garcia de Maria et. al. [38] and (b) Minaei et al. [72].

the mixed and natural convection heat transfer in a ventilated enclosure by considering the inflow and outflow openings along the left vertical wall and a discrete heat source along the right vertical wall. Fig. 4.3(b) represents the comparison of average Nusselt number along the right vertical wall with the variation in Richardson number values for fixed $Re = 320$. Figure shows a good agreement of present result with the experimental results done by Minaei et al. [72].

4.4 Results and discussion

A numerical investigation is made for mixed convection flow in a ventilated enclosure of parallelogrammic section filled with air. The upper and bottom walls are inclined at an angle β with the horizontal axis. A discrete heat source is considered along the vertical wall and a contaminant source is assumed to be placed along the bottom wall. The fluid flow, heat and mass transfer is studied with the variation of Reynolds number, Richardson number and inclination angle with fixed Prandtl number, Schmidt number and buoyancy ratio ($Br = 1.0$). In the present study, air is considered as working fluid

($Pr = 0.71$) and carbon dioxide ($Sc = 1.14$) is assumed to be diffusing in the air [41]. Four different configurations are chosen based on the location of inlet port, outlet port and heat source. The value of the Richardson number varies from 0.0 to 10.0, inclination angle from -60^0 to 60^0 and Reynolds number is taken as 50 and 100. The fluid is driven with the combined influence of forced convection due to injected fresh air and buoyancy forces due to temperature and concentration differences i.e., density variation inside the enclosure. The emphasis has been given on the influence of CO_2 contaminant and temperature source on the indoor air quality and flow distribution in the ventilated inclined enclosure.

4.4.1 Dynamic Field

The fluid flow variation is obtained due to the interaction of the buoyancy force and forced convection due to inlet coolant air. The streamlines for $Re = 100$ and $Ri = 1.0$ is presented in Fig. 4.4 (a) and Fig. 4.4 (b) for case-I and case-III respectively to study the effectiveness of the angle of inclination in the horizontal wall. The hot fluid tends to flow in upward direction and the cold fluid flows in downward direction since the density of cold fluid is higher than the hot fluid. For case-I, the cold fluid moves from inlet port to outlet port through the upper-right section and a downstream circulation zone of less dense fluid is formed in the bottom-left region of the enclosure for $\beta = 0^0$ due to higher temperature along the left vertical wall. As the horizontal wall is inclined in positive direction, the right vertical wall tends to move in upward direction which results the decreased distance between inlet and outlet port. Also the increasing value of inclination angle implies the decreasing distance between adjacent walls like left vertical wall and bottom wall so that the circulation zone is getting shrunk with the increase of angle from 0^0 to 60^0. For $\beta = 15^0$, an upstream eddy is formed in upper-right corner due to density effect which is increasing in size with the increase of inclination angle. When inclination angle is increased in negative direction i.e. from 0^0 to -60^0, the circulation zone is getting shrunk towards the left vertical wall and the upper right region is occupied by the cold fluid.

For case-III (Fig. 4.4 (b)), the cold fluid passes from inlet port to outlet through the bottom-right section of the enclosure while the upper-left section is occupied with heated fluid when $\beta = 0^0$. A small upstream eddy is observed near the upper wall for $\beta = 15^0$

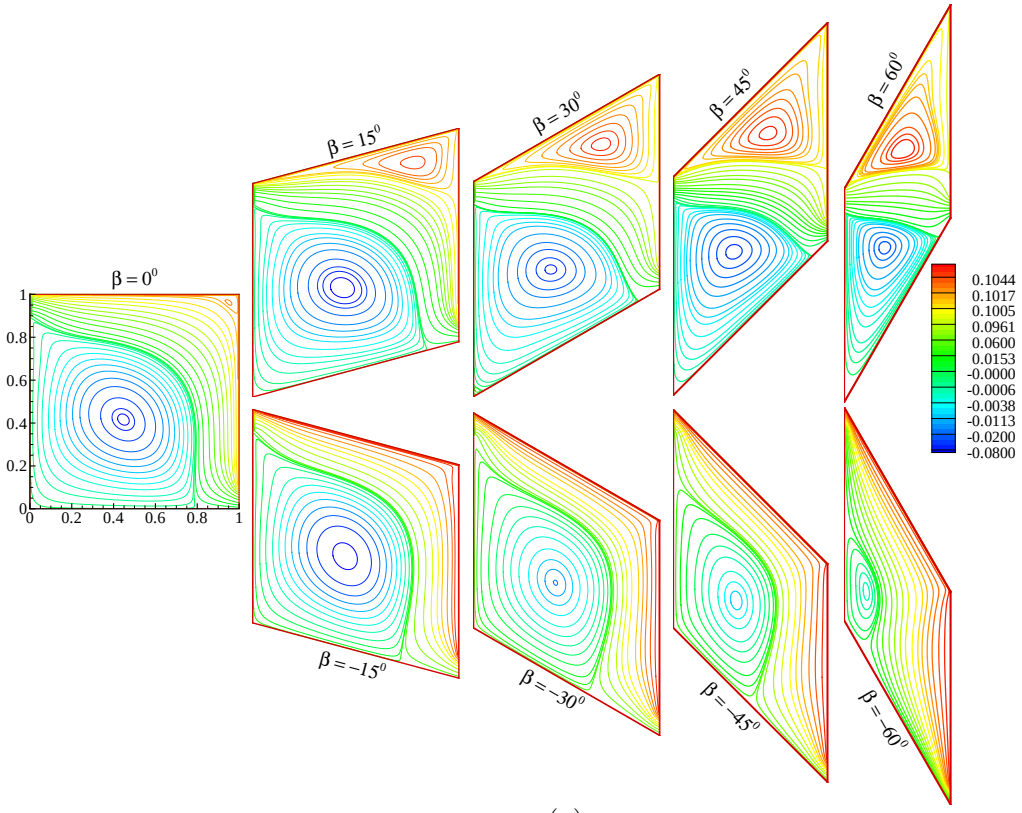

(a)

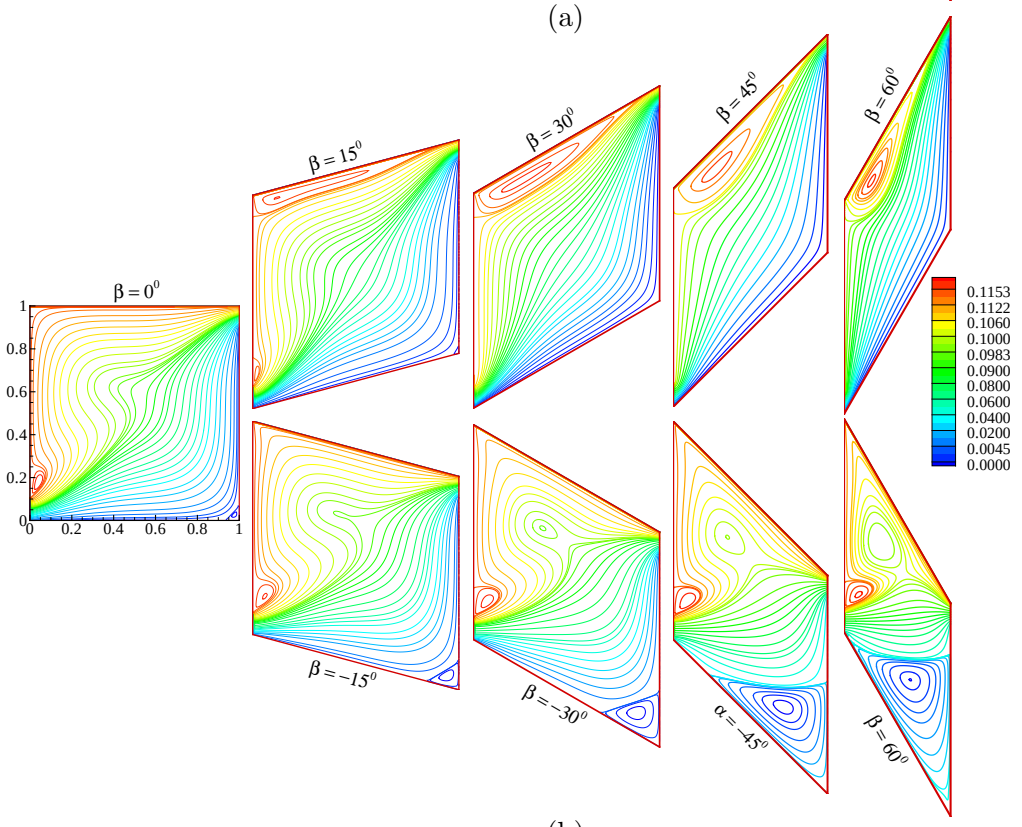

(b)

Figure 4.4: Effect of inclination angle on streamlines for (a) case-I and (b) case-III with fixed $Re = 100$, $Ri = 1.0$ and $Br = 1.0$.

due to density difference and this eddy is growing in size when inclination angle is further increasing up to 60^0. The fact behind this phenomena is that the distance between inlet and outlet port is increasing with the increase in inclination angle. The region affected by cold fluid is shrinking when the value of β is decreasing from 0^0 to -60^0 due to the reduction in distance between inlet port and outlet port. Thus, the hot fluid has gathered in the upper-left portion of the enclosure for negative value of inclination angle.

Fig. 4.5 (a) represents the effect of inclination angle on streamlines for case-I and Fig. 4.5 (b) for case-II when $Re = 100$, $Ri = 5.0$ and $Br = 1.0$. For case-I, the streamlines flow parallelly to the upper wall and then turns back to the downward direction. As the position of heat source is shifted from left wall to right wall (case-II), the fluid flows in the downward direction from the inlet parallel to left vertical wall and then move towards the outlet port due to the effect of buoyancy. A downstream circulation zone is formed in the lower-left region of the enclosure for case-I while an upstream circulation zone is formed in the upper-right region for case-II. As the inclination angle is increasing from 0^0 to 60^0, the main flow lines are shifting downwards following the diagonal path and an upstream eddy is formed in the upper-right corner for case-I (Fig.4.5 (a)). As the value of inclination angle is increasing from 15^0 to 60^0, the distance between inlet port and outlet port is decreasing which results an increase in size of the upstream eddy and decrease in size of the downstream eddy. From Fig. 4.5 (a), it is observed that the natural convection dominated region is getting decreased with the decreasing value of the inclination angle from -15^0 to -60^0. For case-II, the circulation zone is decreasing in size with the increase of inclination angle from 0^0 to 60^0 due to the decreasing area between upper wall and right vertical wall of the enclosure. It is observed that the forced convection dominated region for case-II is getting enlarged when inclination angle is increased either in positive direction i.e., from 0^0 to 60^0 or in negative direction i.e., 0^0 to -60^0.

For low Reynolds number value $Re = 50$ and Richardson number $Ri = 0.1$, the effect of inclination angle on streamlines are presented in Fig.4.6 for case-III and case-IV. For square enclosure, usually the streamlines are passing diagonally and dominated by forced convection effect for case-III and an upstream circulation zone is formed near the upper wall when $\beta \geq 15^0$. But in case-IV, circulation zone is also formed for $\beta = 0^0$ due to density differences. Also, it is observed that the size of the circulation zone is getting

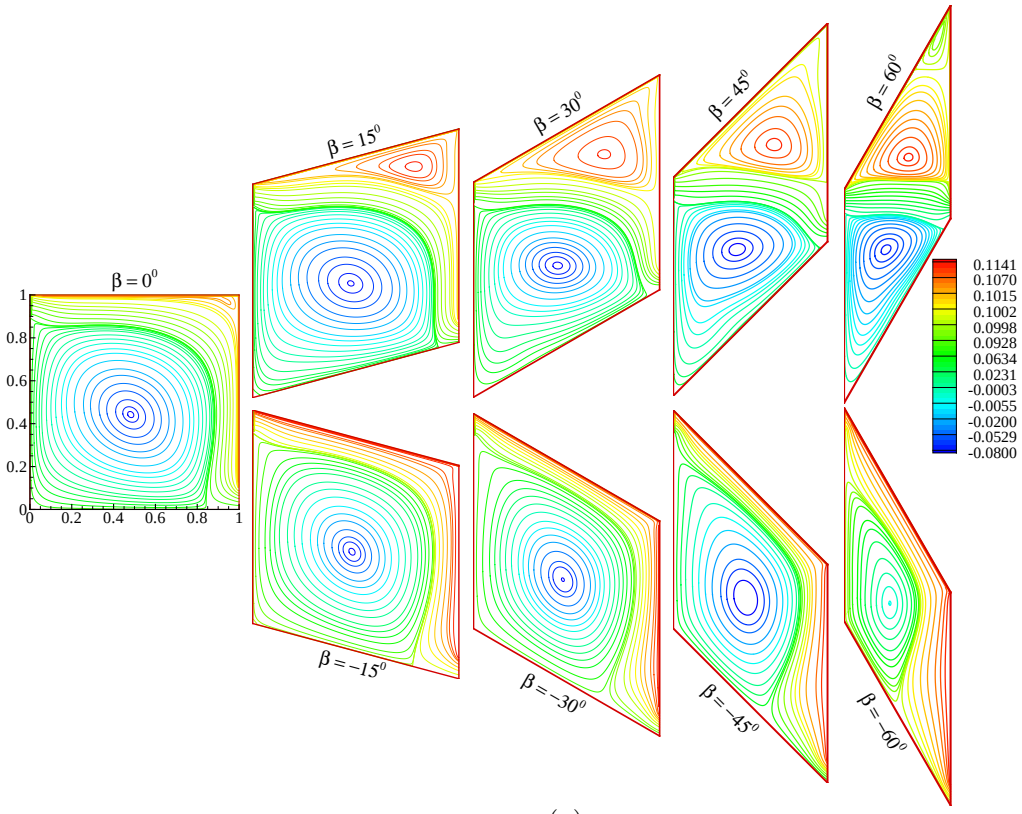

(a)

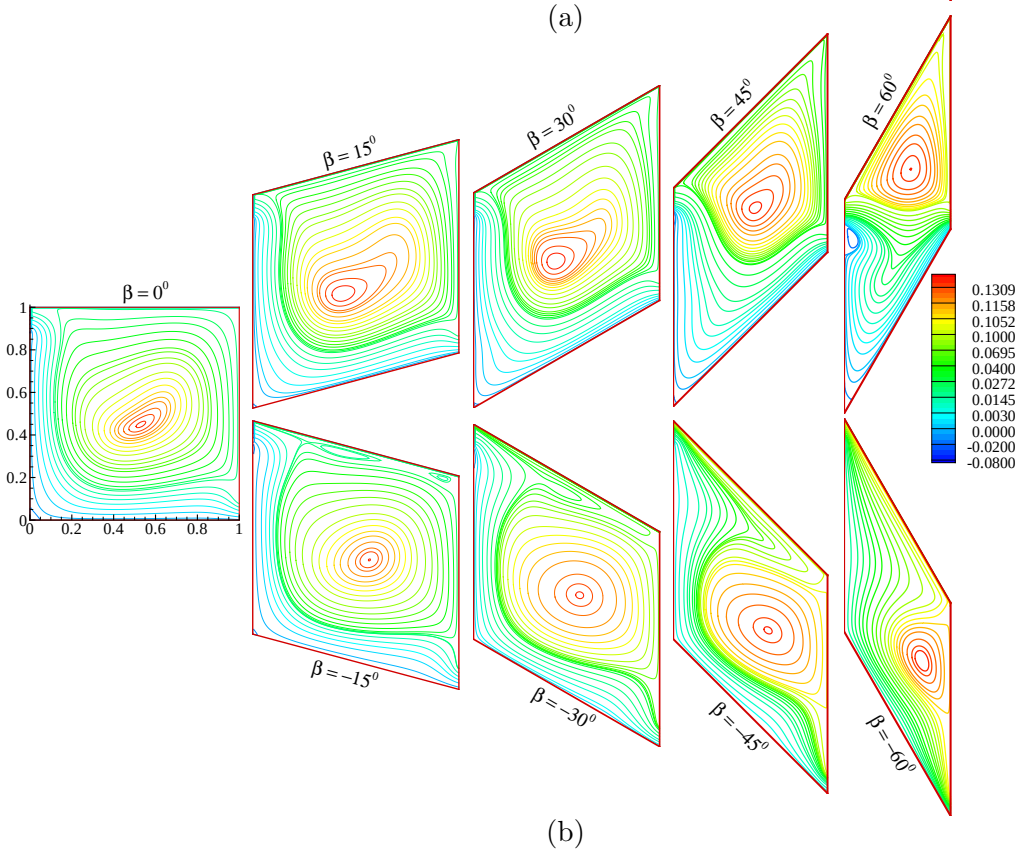

(b)

Figure 4.5: Effect of inclination angle on streamlines for (a) case-I and (b) case-II with fixed $Re = 100$, $Ri = 5.0$ and $Br = 1.0$.

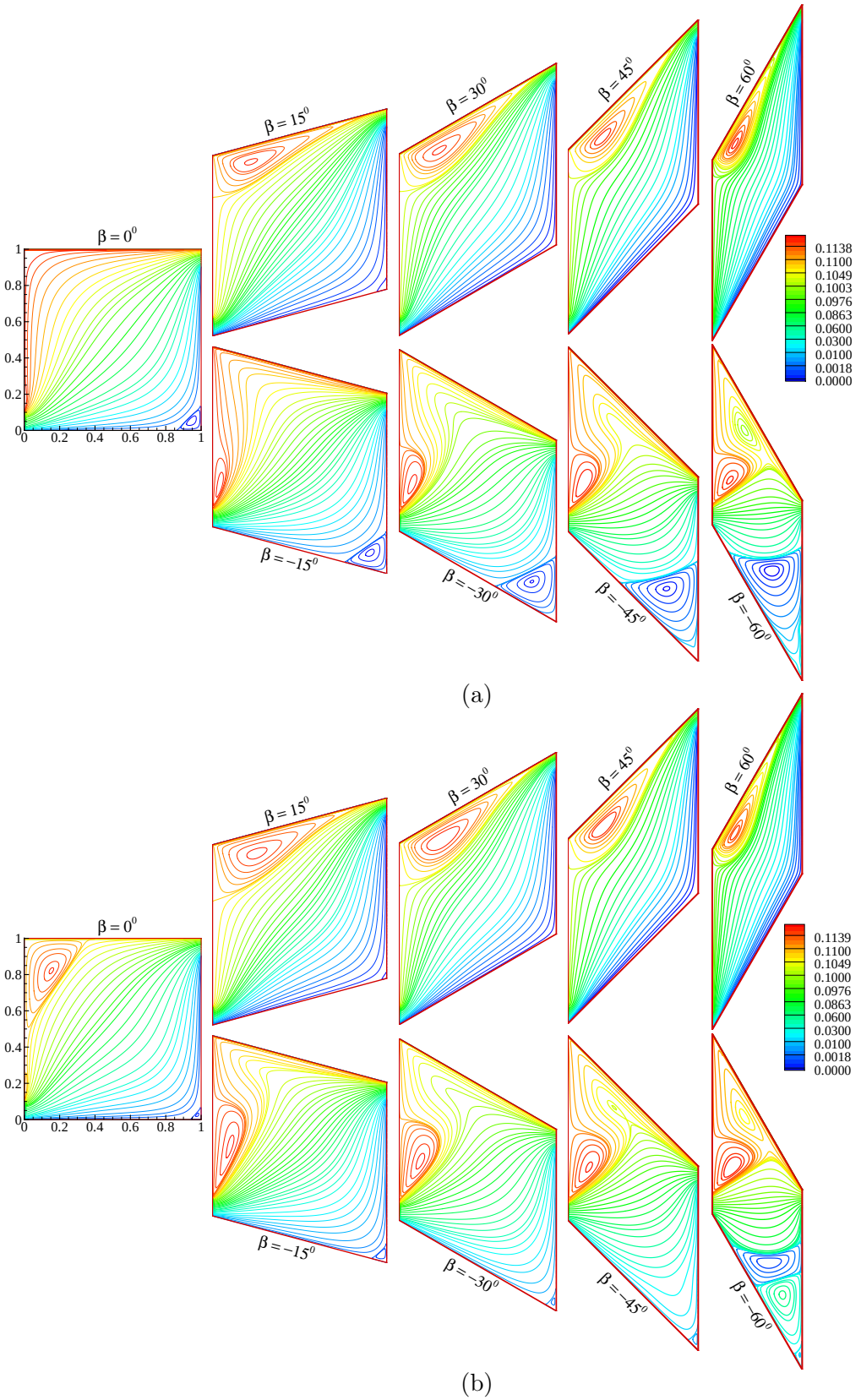

Figure 4.6: Effect of inclination angle on streamlines for (a) case-III and (b) case-IV with fixed $Re = 50$, $Ri = 0.1$ and $Br = 1.0$.

decreased with the increasing value of inclination angle from 15^0 to 60^0. When inclination angle is -15^0, an eddy is formed near the inlet port for both these cases as the distance is decreased between the inlet and outlet port. For case-III, a downstream eddy is formed in the bottom-right corner of the enclosure due to the occurrence of acute angle between bottom and right vertical wall. Declined in inclination angle from $\beta = -15^0$ to $\beta = -60^0$, resulting an increment in the size of downstream eddy in bottom-right corner due to the slope effect of bottom wall and reduction of distance between inlet and outlet port.

4.4.2 Thermal Field

Variation in thermal lines due to change in inclination angle for case-I and case-II are presented in Fig. 4.7 with fixed values of Reynolds number and Richardson number ($Re = 50,\ Ri = 0.1$). Isotherms are formed in the ventilated domain due to the density differences inside the enclosure. The heat transfer effect is mostly depended on the position of heat source and inlet opening of the cold fluid. For $\beta = 0^0$, thermal lines with higher temperature is found to be stacked near the heat source due to weak natural convection effect and the injected cold fluid is found to be moving in the upper-right region due to forced convection effect. As inclination angle increases, thermal lines with higher temperature are moving towards the right section whereas, the cold air is moving in the upper-right section of the enclosure which causes the bottom-left region to be at higher temperature. With the variation in inclination angle from $\beta = 0^0$ to $\beta = -60^0$, it is observed that thermal lines with higher temperature are moving towards the outlet port which results the increase in heat transfer rate.

For case-II (Fig. 4.7 (b)), a thin and compact layer of thermal boundary is observed near the right vertical wall for $\beta = 0^0$. The variation in inclination angle from $\beta = 0^0$ to $\beta = 60^0$ resulting the increment in the density of thermal lines with higher temperature which are moving in upward direction and assembled in the upper-right corner of the enclosure due to the friction loss and tendency of hot fluid. The decreasing value of inclination angle from $\beta = 0^0$ to $\beta = -60^0$ resulting the reduction of distance between vertical walls which resulting the flow domination by forced convection effect and the injecting air which forces the hot air to move downwards. Thus thermal lines with higher values tends to move in downward direction and exit through the outlet port.

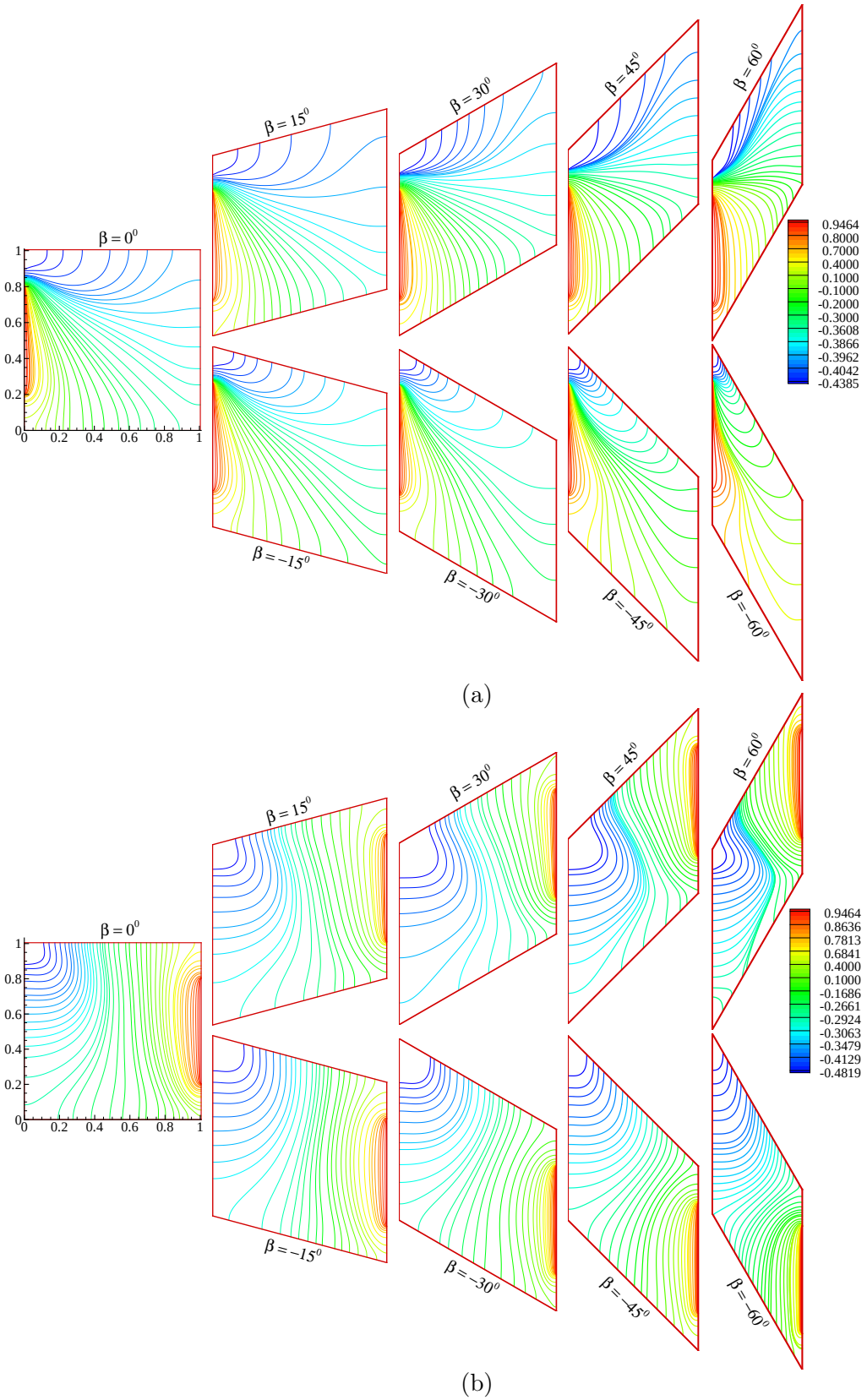

Figure 4.7: Effect of inclination angle on isotherms for (a) case-I and (b) case-II with fixed $Re = 50$, $Ri = 0.1$ and $Br = 1.0$.

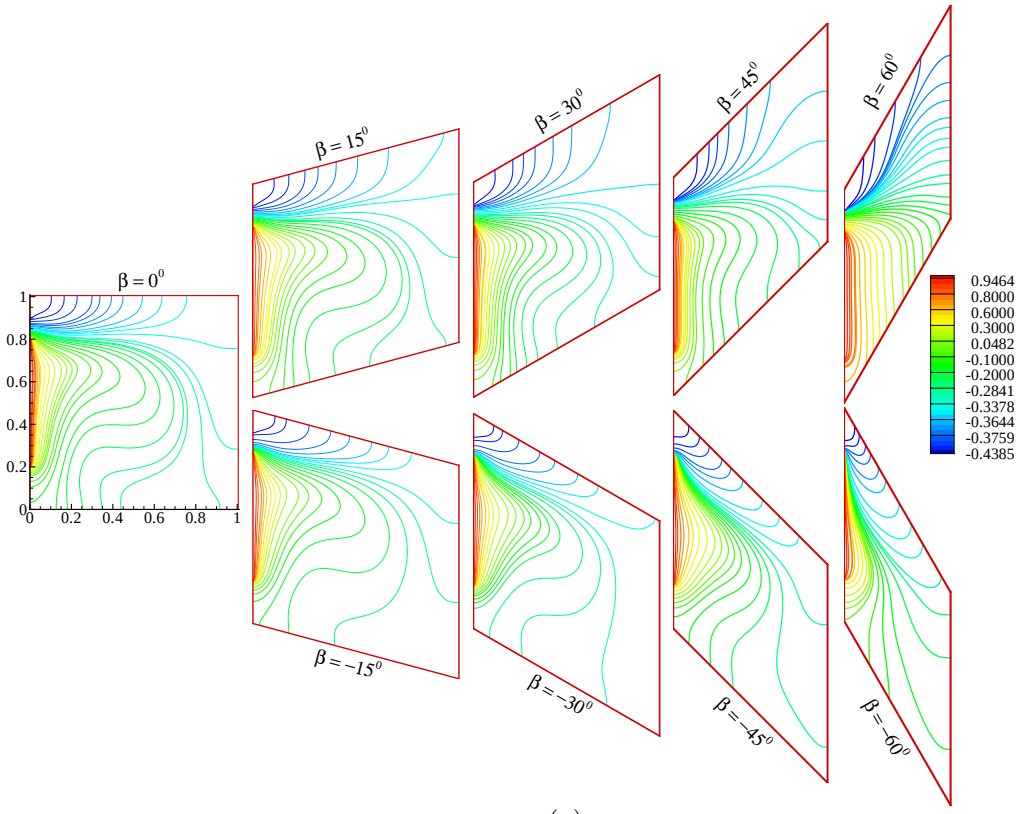

(a)

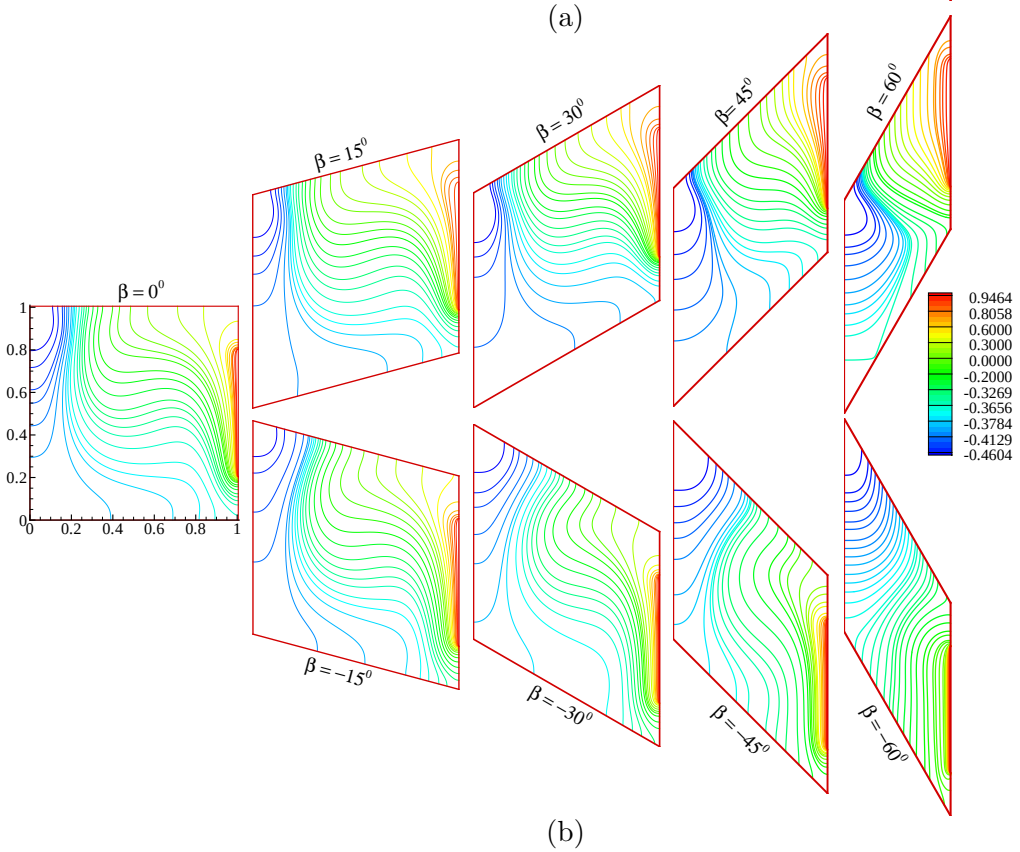

(b)

Figure 4.8: Effect of inclination angle on isotherms for (a) case-I and (b) case-II with fixed $Re = 50$, $Ri = 5.0$ and $Br = 1.0$.

As the Richardson number increases from 0.1 to 5.0, the variation of temperature for various values of inclination angle in case-I and case-II are presented in Fig. 4.8 with a fixed value of Reynolds number ($Re = 50$). The injected cold air is moving parallel to the upper wall for case-I and temperature field is found to be dominated by the natural convection effect due to the density differences. As the position of heat source is changed from left vertical wall to right vertical wall, the cold fluid is found to be moving in the downward direction towards the right section near the heat source which is at higher temperature. With the increasing value of inclination angle, isotherms with higher temperature are observed to be moving in upward direction so that the bottom-left region is occupied by cold fluid. It is also found that overall temperature inside the enclosure is less for case-II compare to case-I.

The effect of inclination angle on thermal lines for case-III and case-IV are presented in Fig. 4.9 with fixed value of Reynolds number and Richardson number ($Re = 50,\ Ri = 0.1$). For $\beta = 0^0$, thermal lines with higher values of temperature are moving in upward direction from heat source and the upper-left region is occupied by fluid of higher temperature for case-III. As the heat source is shifted from left wall to right wall i.e., case-IV, the temperature is found to be uniformly distributed around the heat source and the left section of the enclosure is getting colder due to inlet air. With the increasing value of inclination angle, the overall temperature inside the enclosure is also increasing and it is higher for $\beta = 60^0$. For case-IV, when angle β increases in the positive direction, thermal lines with higher temperature are moving in upper-right section whereas when β decreases from 0^0 to -60^0, thermal lines are moving in the lower-right section of the enclosure due to the convection effects.

Fig. 4.10 represents the heat transfer effect due to inclination angle, location of inlet and outlet port for fixed values of Reynolds number and Richardson number ($Re = 100,\ Ri = 5.0$) for case-I and case-III. In case of $\beta = 0^0$, the fluid in the upper-right section is dominated by forced convection effect and thermal lines with higher temperature is found to be moving towards the mid section from the heat source due to natural convection effect. Highly compressed thermal lines are present near the heat source due to major density variation. Increasing value of inclination angle from 0^0 to 60^0 results an increase in the heat transfer rate which shows that the overall temperature inside the enclosure

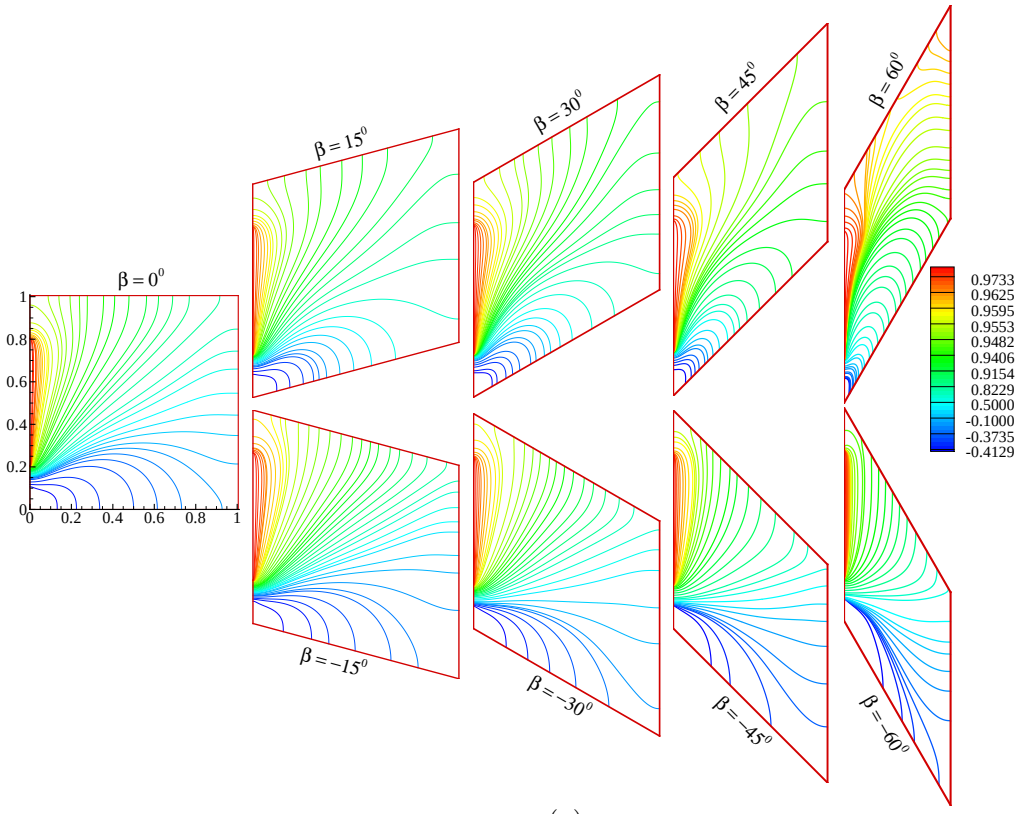

(a)

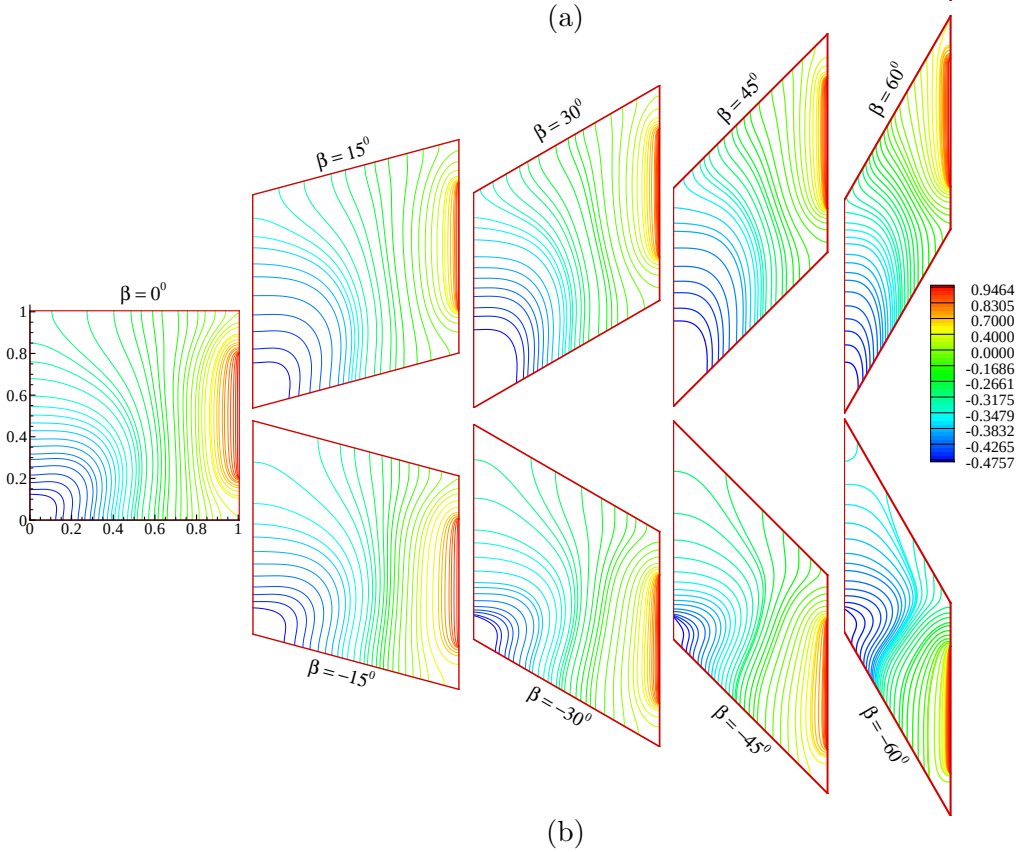

(b)

Figure 4.9: Effect of inclination angle on isotherms for (a) case-III and (b) case-IV with fixed $Re = 50$, $Ri = 0.1$ and $Br = 1.0$.

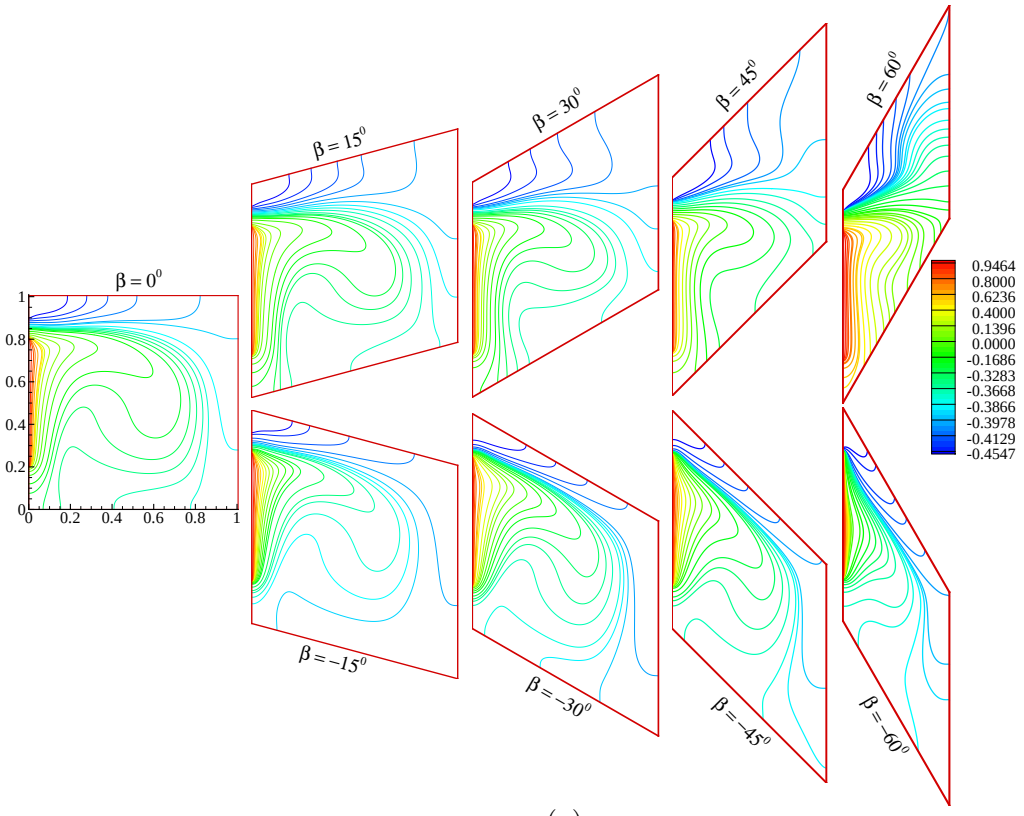

(a)

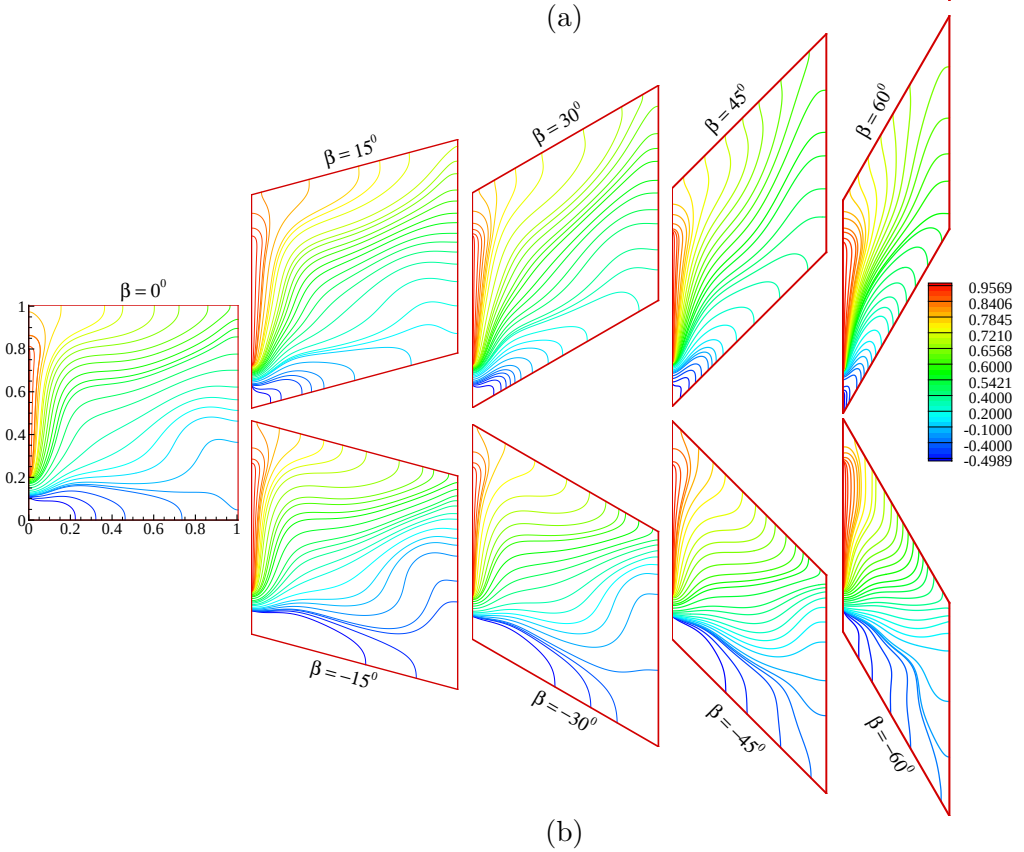

(b)

Figure 4.10: Effect of inclination angle on isotherms for (a) case-I and (b) case-III with fixed $Re = 100$, $Ri = 5.0$ and $Br = 1.0$.

is decreasing. By changing the location of inlet and outlet port, the heat transfer effects in the lower portion of the enclosure is dominated by forced convection effect while the upper-left region is dominated by natural convection effect (Fig. 4.10 (b)). As the cold air is entered through the bottom section of the left wall, it forced the reference fluid to move in upward direction and the associated hot fluid is moved in the upward direction due to low density. When the inclination angle is increasing from 0^0 to 60^0, the distance between the inlet and outlet opening is also increasing which results the domination of natural convection effects inside the enclosure. If the inclination angle is varying from 0^0 to -60^0 (i.e., in decreasing order), thermal lines with higher temperature is found to be compressed near the upper-left section and lower section is occupied by cold air due to density differences.

4.4.3 Concentration Field

The effect of inclination angle on isoconcentration profiles are presented in Fig. 4.11 for case-I and case-III with fixed $Re = 50$ and $Ri = 0.1$. Cold air through the inlet port is entering inside the enclosure which creates an additional force and combines with the buoyancy forces. If this force is sufficient enough to overcome the buoyancy forces, then the the flow pattern is governed by forced convection effect and if this force is not sufficient enough then the flow pattern is governed by natural convection. For case-I, fresh air is entering through the upper section of the left vertical wall and stacking in the upper-right region of the enclosure. The bottom region is spanned by contaminated air due to the presence of carbon-dioxide along the bottom wall. With the increasing value of inclination angle, the contaminated air is moving towards the left section of the enclosure whereas by varying the inclination angle from 0^0 to -60^0, inclined wall forces the contaminated air to move towards the right section and exited through the outlet port. By changing the location of inlet and outlet port i.e., case-III, contaminated air is moving towards the right part of the enclosure and upper-left section is occupied by fresh air (Fig. 4.11 (b)). In case of $\beta > 0^0$, a thin boundary layer of contaminated air is observed near the bottom wall. Whereas, for negative values of inclination angle, the contaminated air is gathering in the bottom-right corner of the enclosure due to slope of the bottom wall. Mass transfer rate is increasing with the decreasing value of inclination angle due to decreased distance

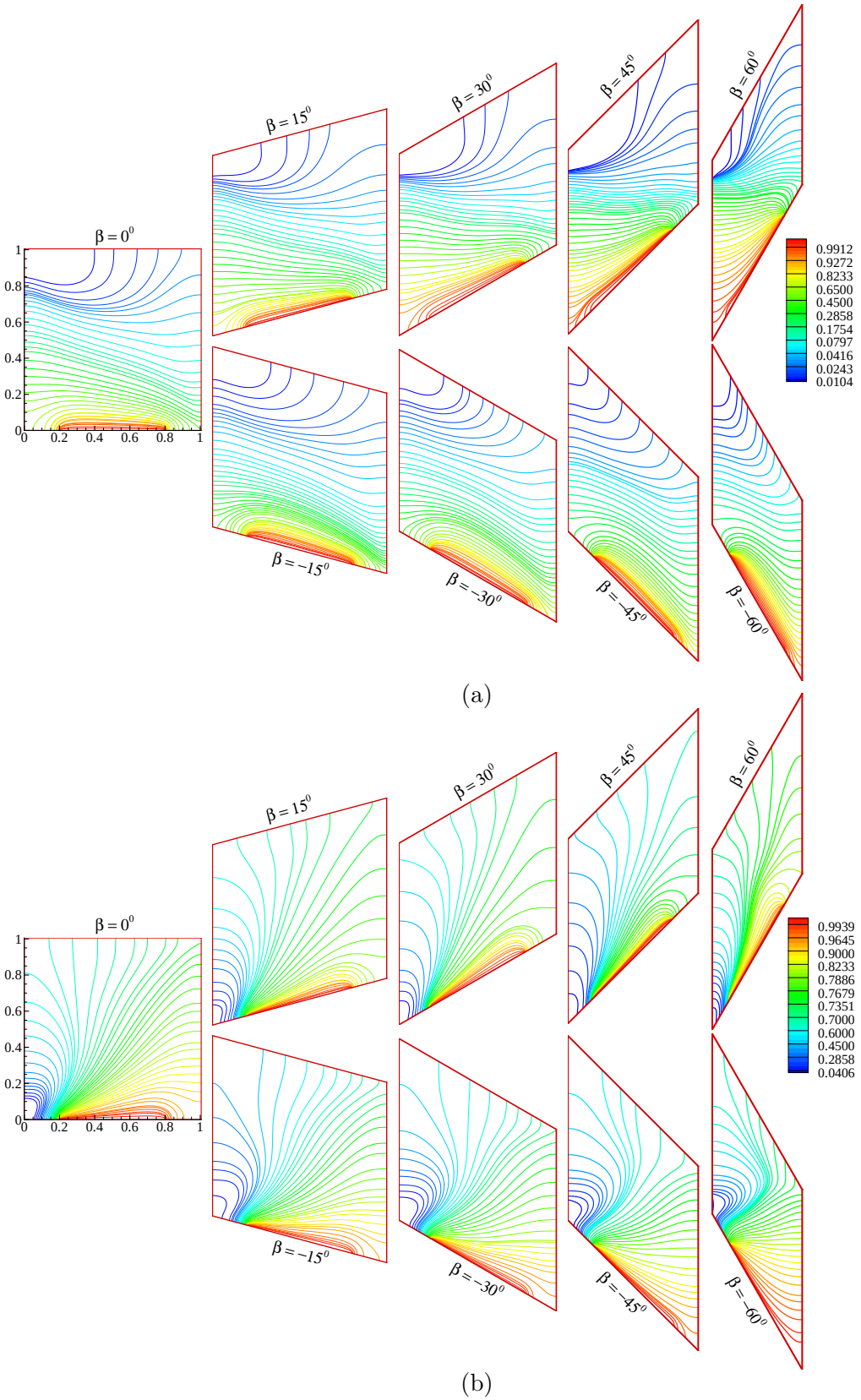

Figure 4.11: Effect of inclination angle on isoconcentrations for (a) case-I and (b) case-III with fixed $Re = 50$, $Ri = 0.1$ and $Br = 1.0$.

between contaminated source and exit port.

For higher Richardson number ($Ri = 5.0$) with different values of inclination angle, isoconcentration field is presented in Fig. 4.12 for case-I and case-III. Increase in Richardson number inferred that the density differences is increased which results natural convection dominated flow inside the enclosure. Dense isothermal lines are found to be stratified close to the contaminated source due to mixed convection effect for both the cases. For increasing value of β, the contaminated air is moving towards the left region of the enclosure for case-I while these lines are observed to be moving towards the right region of the enclosure for case-III due to the dominance of forced convection effect as well as slope of the horizontal wall. The decreasing value of β from 0^0 to -60^0 is intensifying the contaminated air to move towards the exit port due to density effects for case-I and hence, the removal rate of contaminated air is higher for $\beta = -60^0$. For case-III, the variation in inclination angle from 0^0 to -60^0 results the stratification of contaminated air in the bottom-right corner due to decreased distance between bottom wall and the right vertical wall. Also, the upper-left region is occupied by inlet air and contaminated air is forced to move towards the right wall.

Forced convection effect can be increased by the increment in Reynolds number which dominates the natural convection effect inside the enclosure. The effect of inclination angle on isoconcentration profiles for $Re = 100$ is presented in Fig. 4.13. A thick solutal boundary layer is found near the bottom wall for case-I with $Ri = 0.1$ due to contaminant source and mass transfer is dominated by forced convection effect along the upper section due to inlet air. From the figure, It is analyzed that removal rate of contaminants is increasing with the decreasing value of β for case-I. Fig. 4.13(b) represents the isoconcentration profiles for case-III with $Ri = 5.0$. Upper-left region is dominated by forced convection effect and mass transfer rate is found to be increasing with the increasing value of Reynolds number as well as Richardson number. Contaminated air is found to be assembled in the bottom-right section of the enclosure due to the decrement of distance between bottom and right wall when inclination angle varies from 0^0 to -60^0, whereas the contaminated air is getting preserved near the bottom wall when inclination angle varies from 15^0 to 60^0 due to the dominance of forced convection.

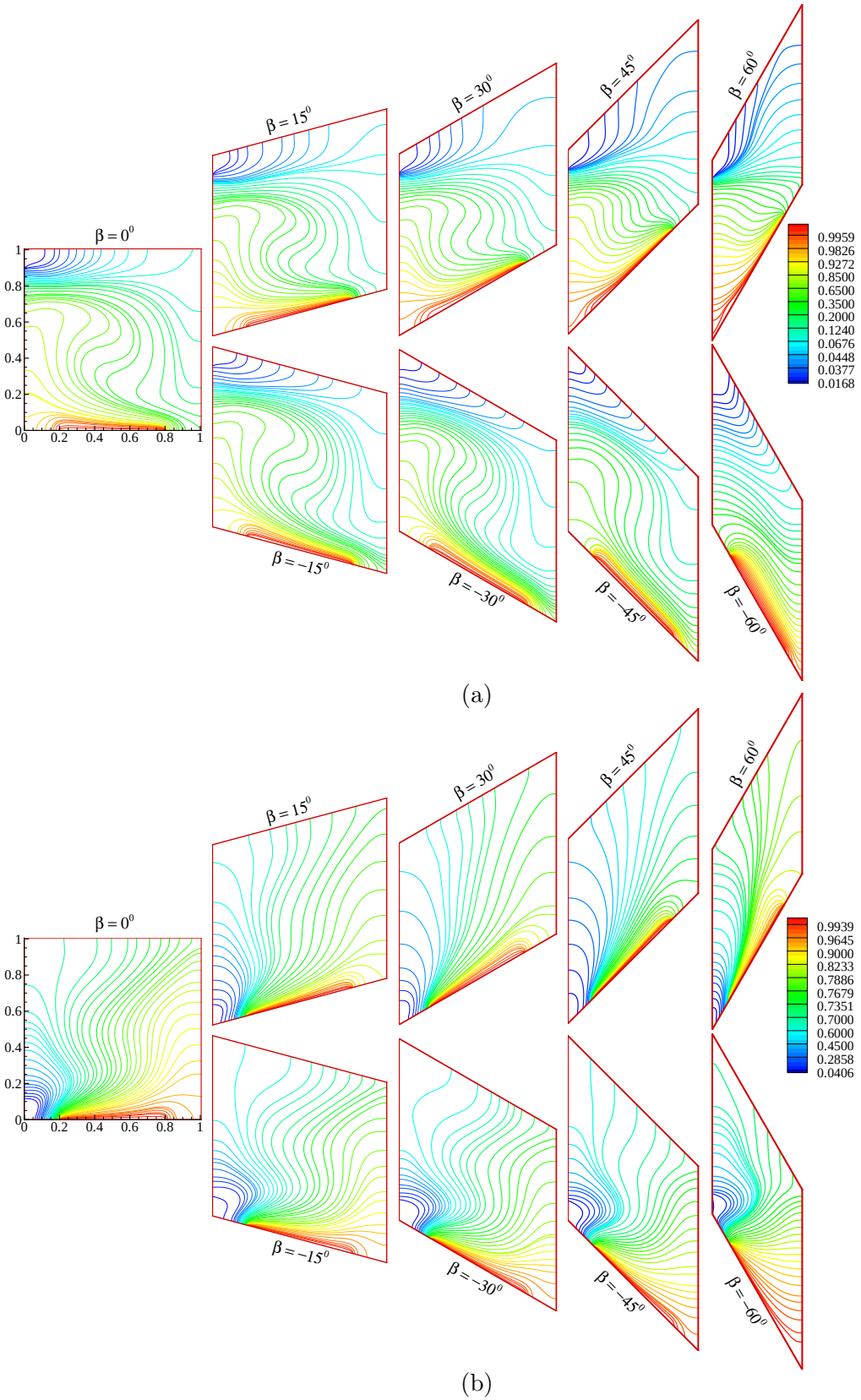

Figure 4.12: Effect of inclination angle on isoconcentrations for (a) case-I and (b) case-III with fixed $Re = 50$, $Ri = 5.0$ and $Br = 1.0$.

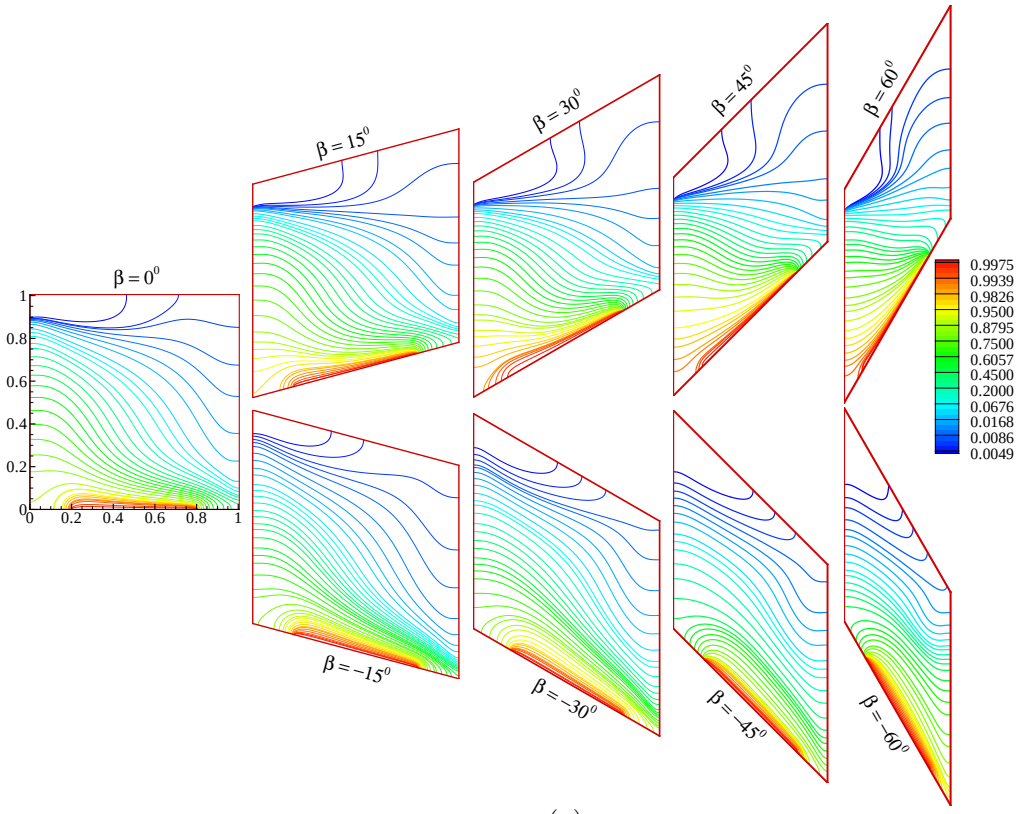

(a)

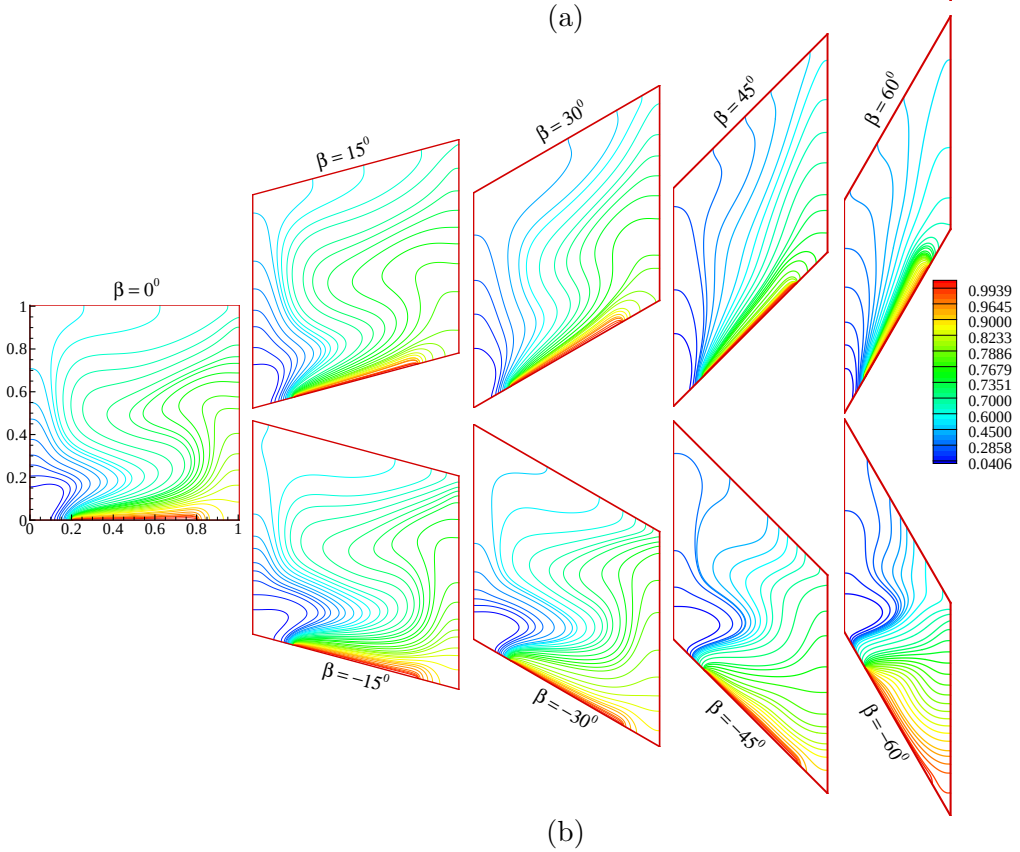

(b)

Figure 4.13: Effect of inclination angle on isoconcentrations for (a) case-I with $Ri = 0.1$ and (b) case-III for $Ri = 5.0$ with fixed $Re = 100$ and $Br = 1.0$.

4.4.4 Average Nusselt number, Entropy Generation, Bejan number and Performance evaluation Criterion

A comparison is made for average heat transfer rate, average entropy generation, average Bejan number and performance evaluation criteria for fixed value of Richardson number $Ri = 0.1$ and presented in Fig. 4.14 to find the effectiveness of inclination angle. It is observed that heat transfer rate is higher for high Reynolds number ($Re = 100$) due to forced convection effect. The average Nusselt number is higher for case-II corresponding to $\beta = -30^0$, whereas the maximum value of Nu_{avg} is obtained for case-III with $\beta = 15^0$. From Fig. 4.14 (b), the average entropy generation is found to be minimum in case-III for $-60^0 \leq \beta \leq 0^0$, while S_{avg} is minimum in case-I for $0^0 \leq \beta \leq 60^0$ corresponding to $Re = 50$ due to weaker forced convection effect. The average energy loss is higher for case-I and case-II when $\beta = -60^0$ with $Re = 100$. The increasing value of inclination angle from -60^0 to 0^0 produce an increase in the effective area of the enclosure and from 0^0 to 60^0 signifies the decrease in the effective area of the enclosure.

The flow field is dominated by heat transfer irreversibility for all these cases because $Be > 0.5$ (Fig. 4.14 (c)). When β varies from -60^0 to 0^0, average Bejan number is greater than 0.95 for case-III with $Re = 50$ which implies that there is insignificant energy loss due to fluid friction. Similarly, for case-II with low Reynolds number and $0^0 < \beta \leq 60^0$, there is major contribution of heat transfer irreversibility in average entropy generation. The motivation of the present work is to find the maximum heat transfer with respect to minimum entropy generation i.e., maximum performance evaluation criteria. It is concluded from the Fig. 4.14 (d) that case-I gives better performance for $-30^0 \leq \beta \leq -15^0$ whereas case-III gives better performance for $0^0 \leq \beta \leq 45^0$ corresponding to $Re = 50$. The value of PEC is increasing with the increase in β from -60^0 to 0^0 and it is decreasing with further increase in β due to slope of the horizontal wall.

The buoyancy effects are increasing with the increase in Richardson number and a comparison is presented in Fig. 4.15 with $Ri = 5.0$ to show the effectiveness of inclination angle on average Nusselt number, average entropy generation, average Bejan number and performance evaluation criteria. The rate of heat transfer is found to be higher in case-IV with $Re = 100$ because heated air is moving in upward direction due to density and

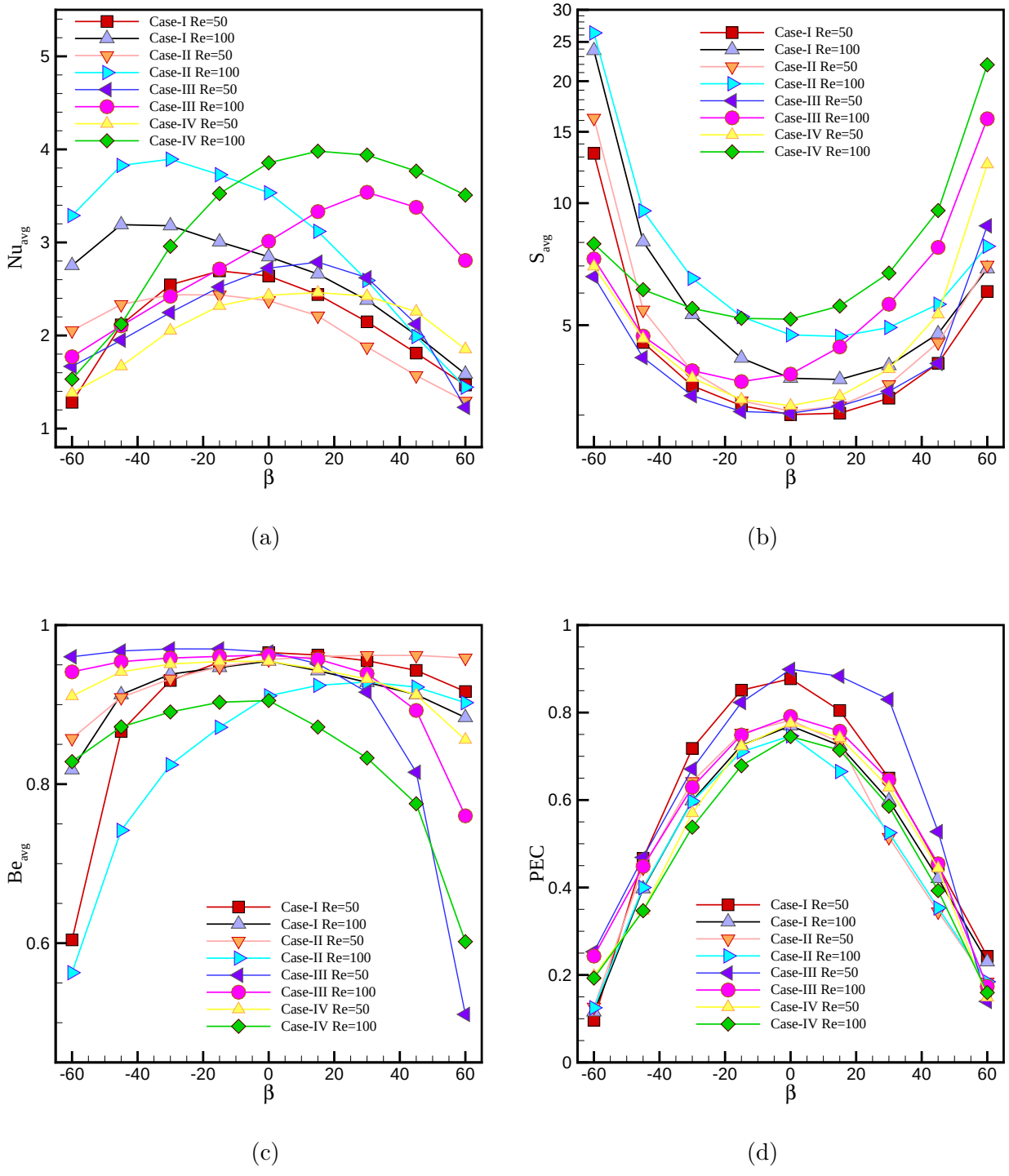

Figure 4.14: Comparison of average (a) heat transfer rate, (b) entropy generation, (c) Bejan number and (d) performance evaluation criterion with the variation of inclination angle for fixed $Ri = 0.1$.

exit through the outlet port which is placed just above the heat source. The minimum entropy generation is observed in case-III corresponding to weak forced flow ($Re = 50$) due to negligible fluid friction irreversibility.

The dominance of heat transfer irreversibility is found for all the cases except in case-IV corresponding to $\beta = 60^0$ for $Re = 100$ (Fig. 4.15 (c)). Increasing buoyancy effects produced maximum rate of heat transfer corresponding to higher Reynolds number while the minimum energy loss is achieved corresponding to lower Reynolds number. The ratio of average Nusselt number to average entropy is presented in Fig. 4.15 (d) to find the maximum heat transfer with minimum entropy generation for $Ri = 5.0$. Minimum performance is obtained in case-II due to the location of heat source, inlet port and outlet port. The performance of the system can be increased by changing the location of heat source as well as inlet and outlet opening. It is observed that for $-60^0 \leq \beta \leq -30^0$, the value of PEC is higher in case-III at $Re = 100$, while for $15^0 \leq \beta \leq 30^0$, the value of PEC is higher in case-IV corresponding to $Re = 50$. Maximum value of heat transfer with respect to minimum entropy generation is achieved in case-IV with $Re = 100$ and $\beta = 0^0$.

Fig. 4.16 (a) and (b) represents the comparison of average Nusselt number and average entropy generation for fixed value of Reynolds number ($Re = 100$) at $\beta = 0^0$ with the variation of Richardson number (Ri). It is analyzed from the figure that both the average heat transfer rate as well as average energy loss are increasing with the increase of Richardson number from 1.0 to 10.0 due to the dominance of heat transfer irreversibility and buoyancy effects. Average Nusselt number is higher in case-IV, while the energy loss is minimum in case-I and case-II. A comparison is presented for performance evaluation criterion in Fig. 4.16 (c) and (d) with the variation in Richardson number to find the optimum configuration for maximum heat transfer with minimum energy loss. In case-I, the value of PEC is higher for low Reynolds number ($Re = 50$) as compared with the values at $Re = 100$. At $Ri = 1.0$ with $Re = 50$, the value of performance evaluation criterion is higher in case-III, whereas for $Re = 100$, the value is higher in case-IV. The maximum value of PEC is observed for case-III for low Richardson number i.e., forced convection dominating flow, whereas for higher Richardson number ($Ri > 1$), maximum value of PEC is found in case-IV due to the dominance of buoyant forces.

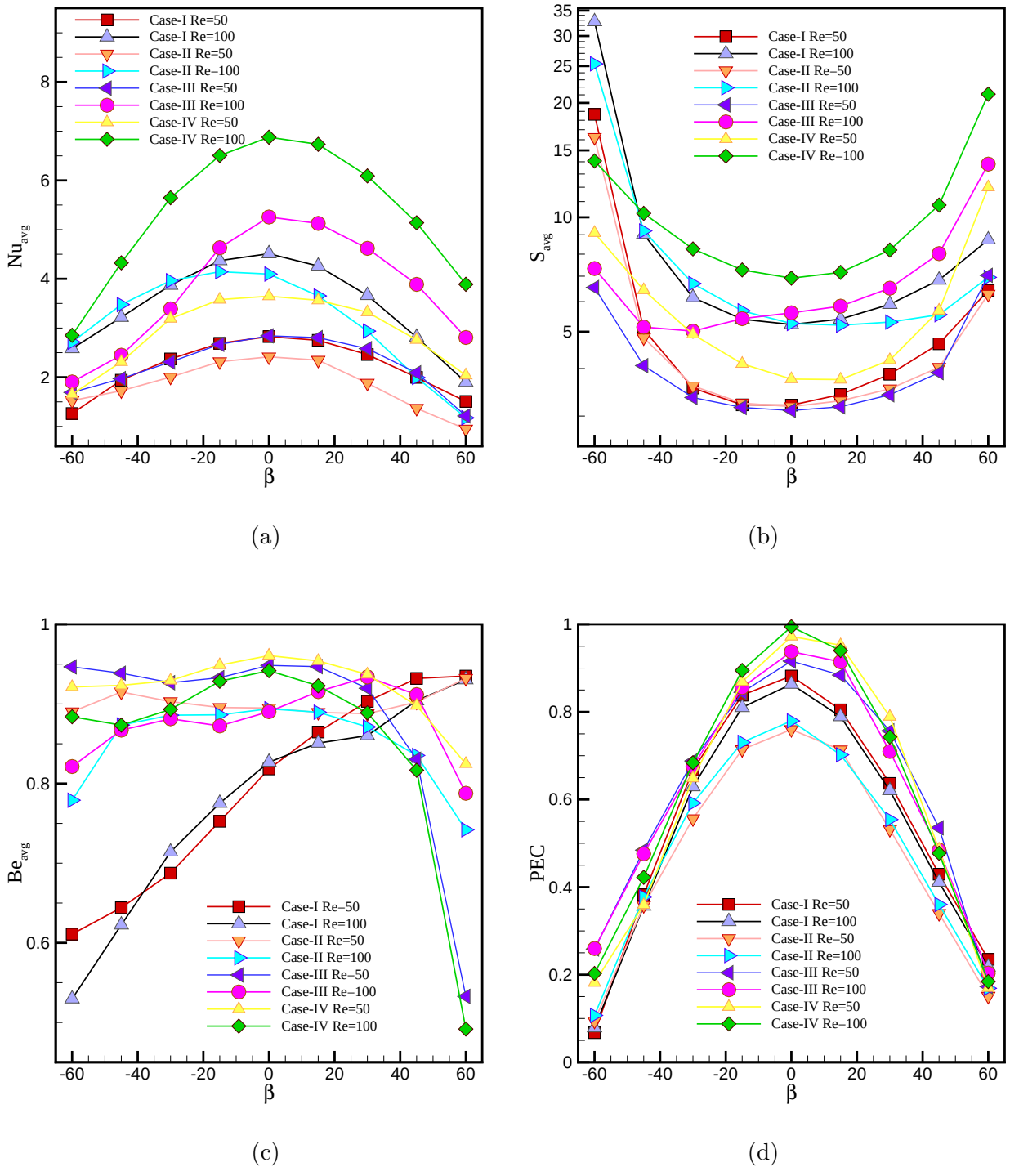

Figure 4.15: Comparison of average (a) heat transfer rate, (b) entropy generation, (c) Bejan number and (d) Performance evaluation criterion with the variation of inclination angle for fixed $Ri = 5.0$.

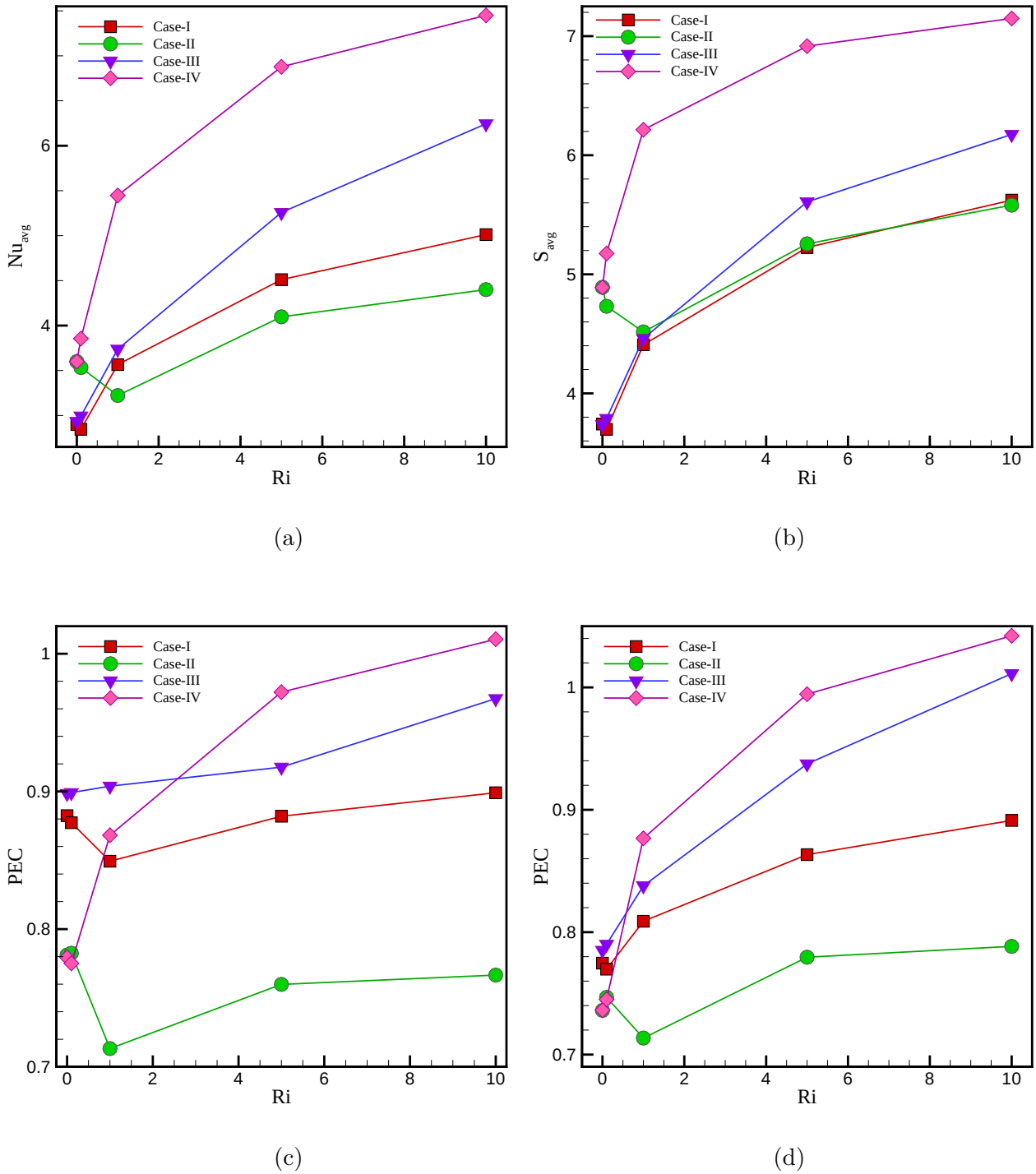

Figure 4.16: Comparison of (a) average heat transfer rate ($Re = 100$), (b) average entropy generation ($Re = 100$), (c) performance evaluation criterion ($Re = 50$) and (d) performance evaluation criterion ($Re = 100$) with the variation of Richardson number for square cavity ($\beta = 0^0$)

4.4.5 Average Sherwood number, Average Temperature and Cooling Efficiency

The average Sherwood number variation for CO_2 concentration with $Ri = 0.1$ is presented in Fig. 4.17 (a), where the angle of inclination is varied from -60^0 to 60^0 for different Reynolds number. It is observed that for low Richardson number, mass transfer rate is higher in case-II for $-60^0 \leq \beta \leq -30^0$ because distance between contaminant source and outlet port is very small. If the inclination angle lies within the range $-15^0 \leq \beta \leq 60^0$, average Sherwood number is found to be higher in case-IV with $Re = 100$. For case-I and II, mass transfer rate is found to be decreasing with the increasing value of β from -45^0 to 60^0 because in flow direction is changing from right to left of the contaminant source. For higher Richardson number $Ri = 5.0$, the effect of inclination angle on mass transfer rate is calculated and presented in Fig. 4.17 (b) for all the simulated cases. The average mass transfer rate is higher for higher Reynolds number ($Re = 100$) compared to low Reynolds number ($Re = 50$) because forced convection effect is increasing with the increase in velocity of inlet air. Mass transfer rate is found to be increasing in case-II and case-III with the increase in β from -60^0 to 0^0 and then decreasing when β varies from 0^0 to 60^0. For case-I, maximum mass transfer rate is found for $\beta = -15^0$ with $Re = 100$ due to buoyancy effect. For $-60^0 \leq \beta \leq 15^0$ maximum value of average Sherwood number is obtained in case-II, and for further increase in β from 30^0 to 60^0, maximum mass transfer is obtained in case-IV corresponding to $Re = 100$.

The variation in average temperature inside the enclosure due to change in β from -60^0 to 60^0 is presented in Fig. 4.18 for different Reynolds number. For $Ri = 0.1$, overall temperature inside the enclosure is found to be minimum for case-II when β varies from -60^0 to -15^0, and for case-IV when β varies from 0^0 to 60^0 (Fig. 4.18 (a)) corresponding to $Re = 100$. It is concluded that maximum cooling can be preserved inside the enclosure when the heat source is placed along the right wall and to obtain more heating inside the enclosure, heat source must be placed along the left vertical wall. In case of higher Richardson number $Ri = 5.0$, maximum cooling inside the enclosure is obtained in case-IV at $\beta = 60^0$ corresponding to $Re = 100$ due to forced convection dominated flow (Fig. 4.18 (b)). For case-I, average heating inside the enclosure is found to be decreasing with the increase of β from -60^0 to 60^0 due to the slope of horizontal wall. For case-III, average

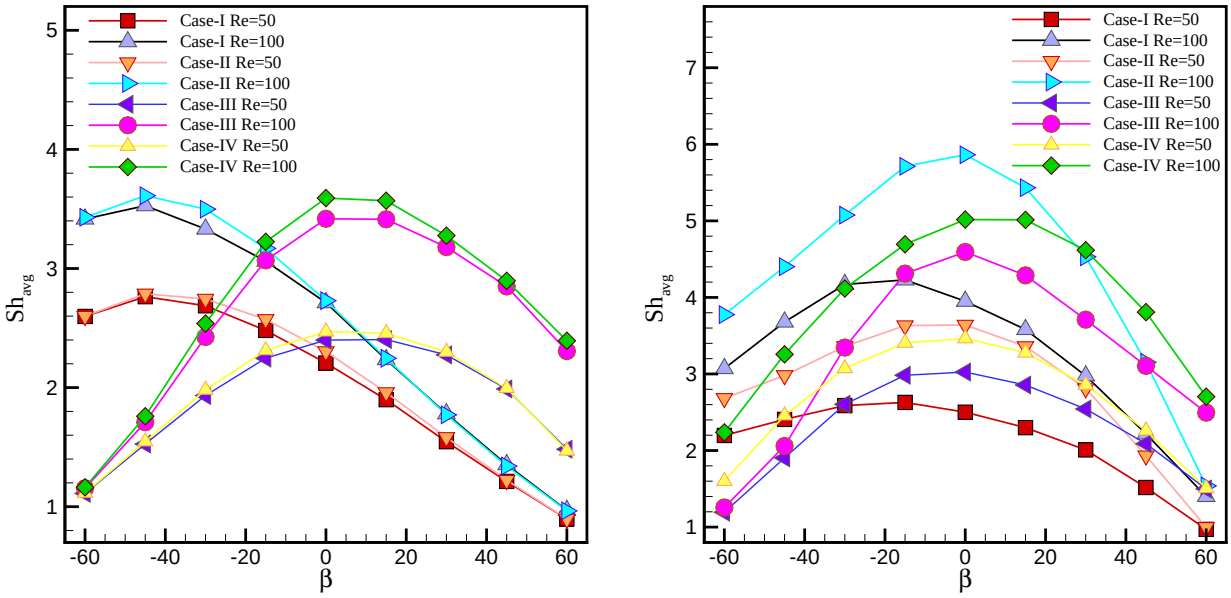

Figure 4.17: Effect of the variation of inclination angle on average Sherwood number with fixed (a) $Ri = 0.1$ and (b) $Ri = 5.0$ for different Reynolds number and configurations.

cooling is decreasing with the increase of inclination angle due to dominance of mixed convection. For $-45^0 \leq \beta \leq -15^0$, minimum average temperature inside the enclosure is found in case-III, while for $0^0 \leq \beta \leq 60^0$, minimum average temperature is obtained in case-IV. It is also observed that maximum cooling inside the enclosure is obtained for higher Reynolds number values since the flow is dominated by forced convection.

The inclination angle effect on cooling efficiency inside the enclosure is calculated and presented in Fig. 4.19 (a) for $Ri = 0.1$ and Fig. 4.19 (b) for $Ri = 5.0$, respectively. Cooling efficiency inside the enclosure is found to be decreasing with the increase of β from -60^0 to 60^0 for case-I whereas the value of cooling efficiency is increasing with the increasing value of β for case-III. In case of lower Richardson number ($Ri = 0.1$), cooling efficiency is higher for case-I corresponding to $\beta < -15^0$, whereas its higher value is obtained for case-III corresponding to $\beta > 15^0$ with $Re = 50$ due to the location of inlet and outlet port. For $Ri = 5.0$, the cooling efficiency is higher in case-IV for $-30^0 \leq \beta \leq 30^0$ with $Re = 50$. Maximum cooling efficiency inside the enclosure at $\beta = -60^0$ is obtained for case-I due to buoyancy dominated flow whereas maximum

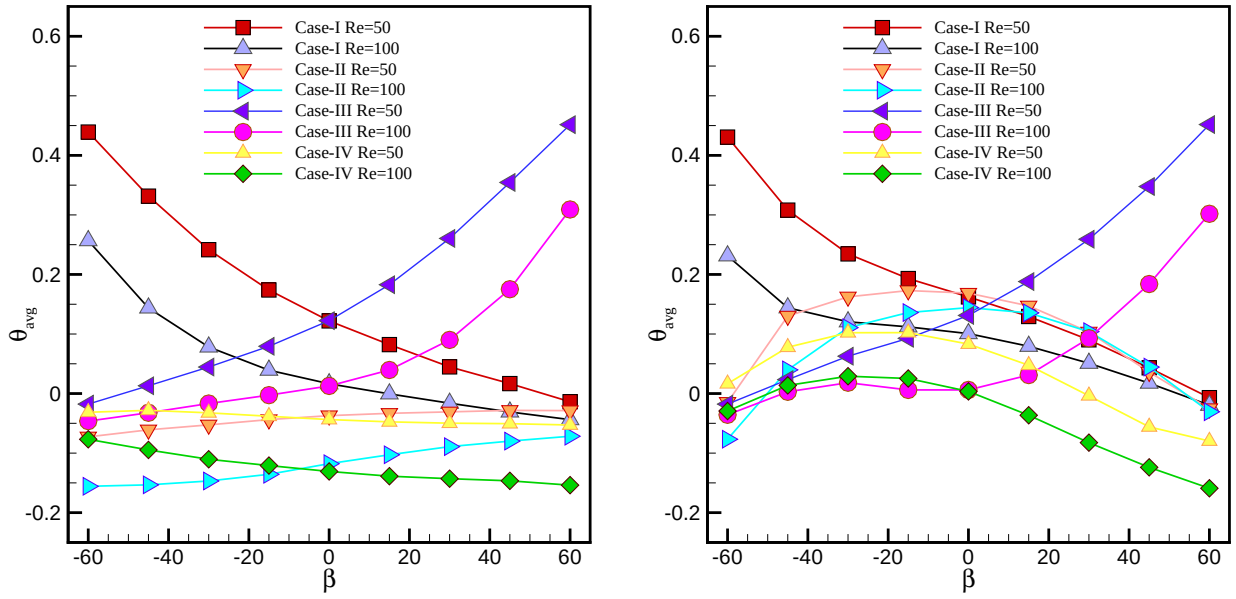

(a) (b)

Figure 4.18: Effect of inclination angle on average temperature inside the enclosure for (a) $Ri = 0.1$, (b) $Ri = 5.0$ for different values of Reynolds number.

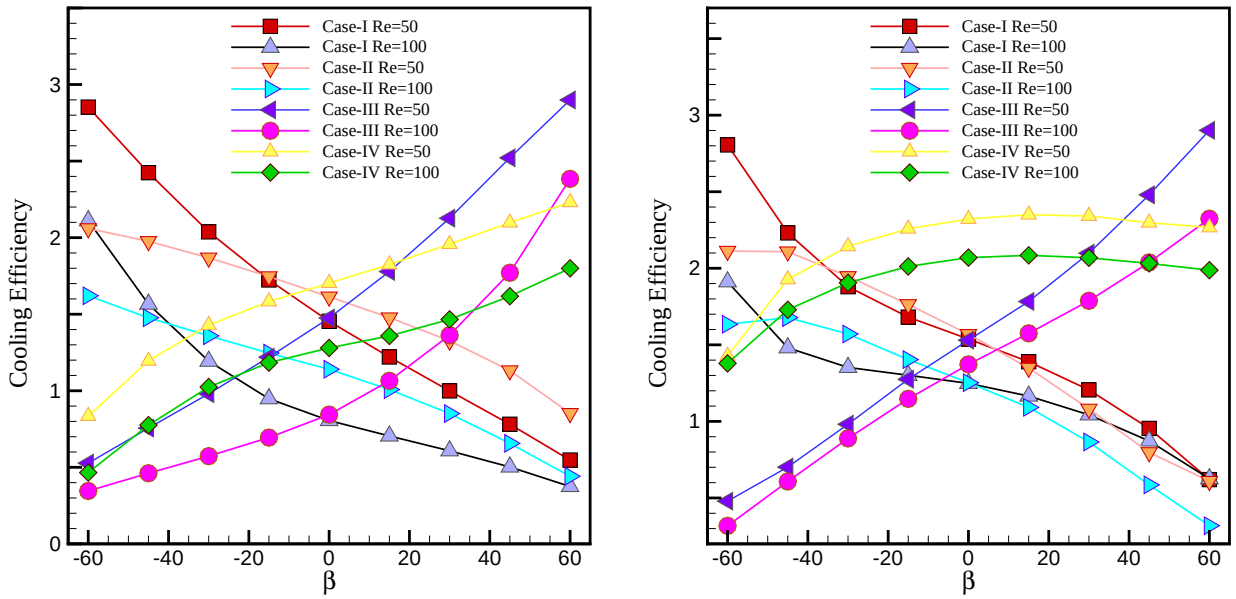

(a) (b)

Figure 4.19: Effect of inclination angle on Cooling Efficiency inside the enclosure for (a) $Ri = 0.1$, (b) $Ri = 5.0$ for different values of Reynolds number for all the cases.

cooling at $\beta = 60^0$ is obtained for case-III corresponding to $Re = 50$. Cooling efficiency is found to be optimum for small values of Reynolds number.

4.5 Conclusion

Simulations are performed to study the mixed convection flow in a ventilated enclosure of parallelogrammic section with the variation of flow parameters like Reynolds number, Richardson number and inclination angle of horizontal wall with the x-axis. Four different configurations are chosen by changing the heat source location, inlet and outlet port to visualize the heat and mass transfer effect to find the optimum performance of the system. Fluid flow, heat and species transport are largely influenced by wall inclination angle, since effective area of the enclosure is increasing when β varies from -60^0 to 0^0, whereas effective area is decreasing when β varies from 0^0 to 60^0. Based on the above mentioned facts, following remarks can be concluded:

1. Heat transfer rate is higher in case-IV for higher Richardson number with $\beta = 0^0$ and $Re = 100$, since thermal lines with larger values from the heat source are moving directly towards the outlet port.

2. For low Richardson number ($Ri = 0.1$), average Nusselt number is higher for case-II when $\beta < 0^0$ and for case-IV when $\beta \geq 0^0$ with $Re = 100$, because heat transfer effect is dominated by forced convection.

3. Increase in Richardson number value directly increase the buoyancy effects which reduces the thickness of thermal boundary layer and thus increasing the heat transfer rate.

4. Average energy loss is observed to be smaller when β varies from -30^0 to 30^0 with low Reynolds number. For higher Richardson number ($Ri = 5.0$), average energy loss is minimum in case-III for $Re = 50$, while for $\beta = \pm 60^0$, energy loss is maximum because the effective area of the enclosure is smaller.

5. For $Ri = 0.1$, maximum heat transfer rate with respect to minimum energy loss i.e., maximum value of PEC is obtained for case-III when β varies from 0^0 to 15^0

with $Re = 50$. For higher Richardson number ($Ri = 5.0$), maximum value of PEC is obtained in case-IV when $-30^0 \leq \beta \leq 30^0$ corresponding to $Re = 100$.

6. Fluid flow is dominated by the heat transfer irreversibility compared to the fluid friction irreversibility because Bejan number is greater than 0.5 for all the cases when $-60^0 \leq \beta \leq 45^0$.

7. For low Richardson number ($Ri = 0.1$), mass transfer rate is higher in case-II for $\beta < -15^0$ due to smaller distance between contaminant source and outlet port, while mass transfer rate is higher in case-IV if $\beta \geq -15^0$ with $Re = 100$. For $Ri = 5.0$, mass transfer rate is higher for case-II when β varies from -60^0 to 15^0 at $Re = 100$.

8. To obtain maximum cooling inside the enclosure, heat source must be kept along the right vertical wall, whereas for maximum heating, the heat source must be placed along the left vertical wall.

Chapter 5

Heat and airborne pollutants removal from a slot-ventilated enclosure due to wall heater and thermosoluted block using a chimney

5.1 Introduction

Heat and mass transfer phenomena driven by the mechanical-driven force combined with buoyancy force in ventilated enclosures are extensively studied in the civil and industrial environment such as thermal and pollution control, electronic cooling, chemical processing and building applications [101, 108, 29, 125]. The primary challenge in recent innovations in building design for ventilation is to provide thermal comfort and high indoor air quality because utmost people spend most of their time inside the commercial or residential buildings. Ventilation is proved to be the most convenient way to improve the quality of indoor air for optimal heating/cooling. There are two modes to ventilate the space, one is buoyancy driven flow and other is mechanical driven flow by introducing fresh air at low velocities and the combination of these two modes introduce the mixed convection problem inside the ventilated space. The researchers search for better ways to improve indoor environment quality using mixing ventilation approach which is considered as highly desirable provided exterior environment cooling. The boundary features usually composed of absorber wall, air gap and cover with high transmissivity to improve the ventilation rates.

To visualize the behavior of heat and fluid flow by mixed convection inside the

ventilated enclosure, a number of experimental and numerical studies have been done so far. Deng et al. [29] analyzed the characteristics of fluid flow, heat and contaminant transport structures in a displacement ventilated enclosure due to discrete heat and contaminant sources for different values of Reynolds and Richardson number. Air flow and temperature distribution in a room with fixed inlet and outlet port was studied by Tripathi et al. [116] and concluded that the intensity of air circulation increased due to inlet flow velocity and buoyancy which leads to the uniformity in temperature. Mixed convection in the presence of heat generating element (heater) in a ventilated cavity was numerically and experimentally investigated to obtain the optimal thermal performance by Radhakrishnan et al. [90] and effective cooling inside the cavity was obtained when heating element is placed within the main stream. The space where fresh outdoor air is entered via windows or doors can be ventilated naturally by using solar chimney in which flow is driven due to the buoyancy force. Bassiouny and Korah [14] investigated the flow patterns inside a room attached with the solar chimney to obtain the optimum air flow rate. They have discussed the effect of solar chimney inclination angle on air change per hour and correlate the air change per hour to the solar intensity, air gap width and absorber inclination angle. The indoor air quality depends on the humidity, temperature and CO_2 concentration of the space.

In general, displacement ventilation (DV) and mixing ventilation (MV) are two trendy air distribution forms that are used to recirculate the indoor environment. In displacement ventilation, fresh outdoor air is supplied at low velocity from air supply diffusers located near floor level and exhausted air is extracted near the ceiling level by buoyancy forces. The mixing ventilation is the method in which fresh air is supplied from ceiling level with high velocity to achieve an uniform distribution of temperature and concentration in the space [105]. Due to high velocity, mixing ventilation might lead to discomfort in workplaces and ineffective in pollutant removal. A numerical investigation was done by Ren et al. [95] for flow mixing and displacement flow inside a slot ventilated enclosure in the presence of heated and airborne polluted strip. The path followed by heat and airborne pollutants are visualized and their efficiencies are compared for displacement flow and mixing. Also, a numerical study due to heated and polluted strip in the presence of conducting baffle inside an open enclosure was presented by Ren et al. [96] to optimize

the removal rate of heat and pollutants. They found that heatlines and masslines are largely affected by the location and length of the baffle and it is concluded that the rate of heat and mass transfer can be intensified by the baffle only when the distance between bottom wall and baffle varies from 0.2 to 0.5 and thermal Rayleigh number is greater than the critical value.

A numerical simulation of heat transfer due to heating floor inside the ventilated cavity in steady and turbulence regime was developed by Koufi et al. [57]. The main focus was to find the better configuration in terms of inlet and outlet location to obtain the optimum ventilation efficiency for temperature distribution and heating intensity. In the literature, wind catchers were used for natural ventilation in buildings as either extract system or air supply to provide thermal comfort. Montazeri et al. [74] investigated the impact of size and location of outlet openings using wind-catchers for the analysis of fluid flow characteristics of cross-ventilation in a isolated building to achieve maximum performance of the wind catcher and indoor air quality. Zhang et al. [125] conducted a numerical investigation to remove the airborne pollutants from a slot-ventilated enclosure in which a contaminant source is located in the lower section of the enclosure and two discrete heat sources are placed along the bottom and right vertical walls. Optimal configuration is obtained in terms of position of the outlet port, heat source and higher efficiency of contaminant removal from the enclosure. It is also concluded that fluid flow, heat and contaminant transport phenomena are strongly dependent on the Reynolds number and Grashof number.

In the literature, there exist enough research work related to slot-ventilation for different combination of inlet and outlet port with heat and contaminant sources. But for the best of authors' knowledge there is a lack of research considering outlet port in the form of chimney which is applicable in various industrial heating and cooling processes and removal of indoor pollutants from residential buildings. In this chapter, a new module is developed for the simulation of a square slot-ventilated enclosure with chimney as outlet port with a wall heater and a thermosoluted rectangular block. Simulations are performed to find the optimum inclination angle of chimney with best suited position of inlet port to obtain the acceptable average temperature of the enclosure and maximum performance evaluation criteria for heat transfer for different range of fluid flow parameters.

5.2 Problem description and Mathematical Modelling

A slot-ventilated enclosure (Fig. 5.1) of length L, breadth B and height H filled with air-CO_2 mixture is considered in the present chapter. Fresh cold air is infiltrated into the enclosure via an inlet port of height $0.15L$ located along right vertical wall and polluted air is expelled naturally via an outlet chimney located along the upper wall. The height and width of outlet chimney are taken as $0.5L$ and $0.15L$, respectively. The vertical walls of outlet chimney are assumed to be inclined at an angle δ with the x-axis. A discrete heater and a rectangular thermosoluted block having higher temperature and higher concentration are considered to be located along the left vertical wall and lower-right region of the enclosure, respectively (shown in Fig. 5.1). The length of wall heater is taken as $0.3L$ for the simulations. Also, the length and height of thermosoluted block is taken as $0.1L$ and $0.2L$ respectively. The walls of the enclosure are assumed to be adiabatic and insulated. The inclination angle values are varied as, 45^0, 60^0, 75^0 and 90^0 for the simulation.

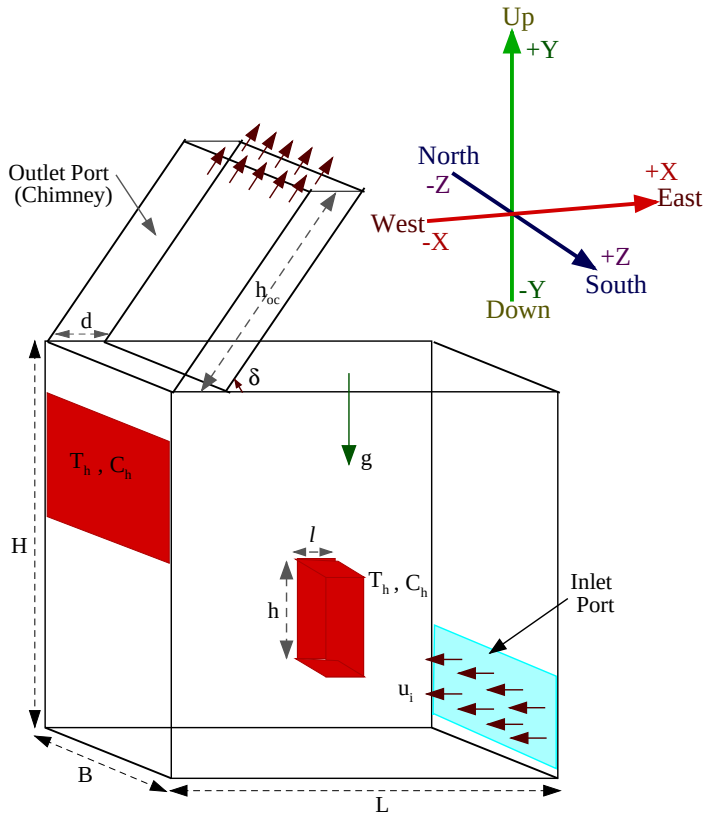

Figure 5.1: Schematic diagram of the fluid flow configuration.

Three different cases (Fig. 5.2) are simulated with respect to the variation in position of inlet port. In case-I, case-II and case-III, inlet port is considered along the lower section, middle section and upper section of the right vertical wall, respectively.

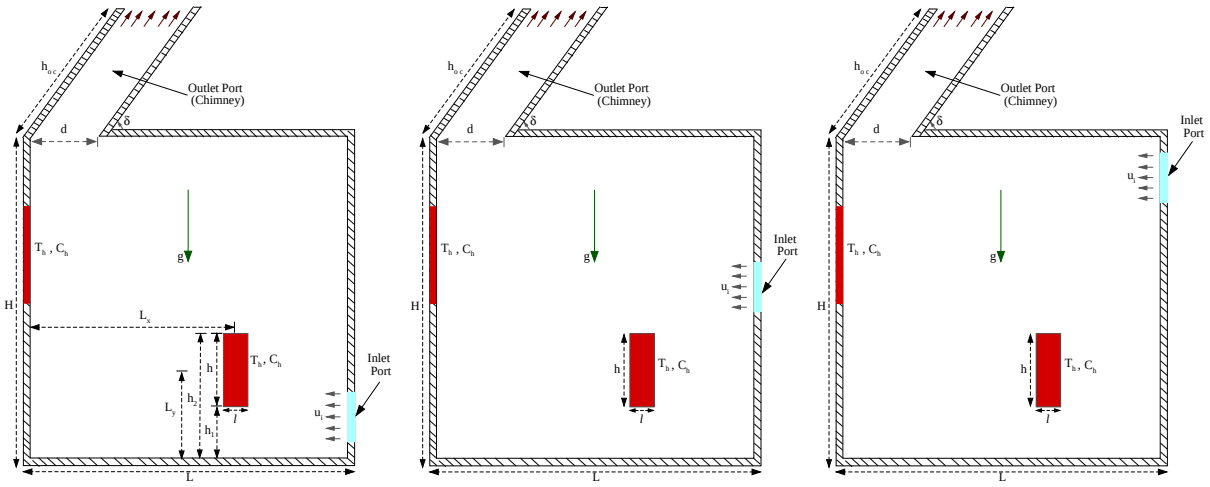

(a) Case-I (b) Case-II (a) Case-III

Figure 5.2: Geometry of different computational domains for the simulation

The governing equations for the flow of fluid, heat and mass inside the slot-ventilated enclosure includes the continuity equation (conservation of mass), Navier-Stokes equations (conservation of momentum), heat equation (conservation of energy) and concentration equation (conservation of species) which are based on the preassumptions that the fluid is Newtonian, viscous and incompressible and the fluid flow is laminar. Thermal radiation inside the system is assumed to be negligible and the physical properties except density variations are independent of temperature and concentration. Therefore, Boussinesqs approximation is used for density variation due to temperature and concentration as:

$$\rho = \rho_0[1 - \beta_T(T^* - T_0) - \beta_C(C^* - C_0)], \tag{5.1}$$

where $\beta_T = -\frac{1}{\rho}\frac{\partial \rho}{\partial T^*}$ is the coefficient of thermal expansion and $\beta_C = -\frac{1}{\rho}\frac{\partial \rho}{\partial C^*}$ is the coefficient of solutal expansion. The value of β_T is always greater than zero, since the density decreases with the increase of temperature. Whereas, the value of β_c shows random nature, since an increase in concentration induces a decrease or an increase in density, respectively [39].

The dimensionless form of flow governing equations can be expressed as:

$$\frac{\partial u}{\partial x} + \frac{\partial v}{\partial y} = 0, \tag{5.2}$$

$$\frac{\partial u}{\partial t} + u\frac{\partial u}{\partial x} + v\frac{\partial u}{\partial y} = -\frac{\partial p}{\partial x} + \frac{1}{Re}\left(\frac{\partial^2 u}{\partial x^2} + \frac{\partial^2 u}{\partial y^2}\right), \tag{5.3}$$

$$\frac{\partial v}{\partial t} + u\frac{\partial v}{\partial x} + v\frac{\partial v}{\partial y} = -\frac{\partial p}{\partial y} + \frac{1}{Re}\left(\frac{\partial^2 v}{\partial x^2} + \frac{\partial^2 v}{\partial y^2}\right) + Ri(T + Br.C), \tag{5.4}$$

$$\frac{\partial T}{\partial t} + u\frac{\partial T}{\partial x} + v\frac{\partial T}{\partial y} = \frac{1}{Re.Pr}\left(\frac{\partial^2 T}{\partial x^2} + \frac{\partial^2 T}{\partial y^2}\right), \tag{5.5}$$

$$\frac{\partial C}{\partial t} + u\frac{\partial C}{\partial x} + v\frac{\partial C}{\partial y} = \frac{1}{Re.Sc}\left(\frac{\partial^2 C}{\partial x^2} + \frac{\partial^2 C}{\partial y^2}\right). \tag{5.6}$$

The initial conditions for time $t = 0$ in computational domain are given as:

$$u = 0,\ v = 0,\ T = 0,\ C = 0;$$

and the boundary conditions related to computational domain for $t > 0$ are defined as: along the inlet port:

$$u = -1, \quad v = 0, \quad T = -0.5 \quad C = 0;$$

outlet port:

$$\frac{\partial u}{\partial y} = 0, \quad \frac{\partial v}{\partial y} = 0, \quad \frac{\partial T}{\partial y} = 0; \quad \frac{\partial C}{\partial y} = 0;$$

solid walls:

$$u = 0, \quad v = 0, \quad \frac{\partial T}{\partial n} = 0, \quad \frac{\partial C}{\partial n} = 0;$$

wall heater and thermosoluted block:

$$u = 0,\ v = 0,\ T = 1,\ C = 1.$$

The implementation of boundary conditions for outlet chimney is complicated because the computational domain of outlet chimney does not coincide with the coordinate lines. In order to ignore this complexity, independent variables (x, y) in the physical domain are transformed into (ξ, η) in computational domain by using the formula:

$$\xi = x - (y/tan\delta),\ \eta = (y - 1)/sin\delta$$

Under the above transformation, the governing equations for outlet chimney can be represented as:

$$\frac{\partial u}{\partial \xi} - \frac{1}{tan\delta}\frac{\partial v}{\partial \xi} + \frac{1}{sin\delta}\frac{\partial v}{\partial \eta} = 0, \tag{5.7}$$

$$\frac{\partial u}{\partial t} + u\frac{\partial u}{\partial \xi} - \frac{v}{tan\delta}\frac{\partial u}{\partial \xi} + \frac{v}{sin\delta}\frac{\partial u}{\partial \eta} = -\frac{\partial p}{\partial \xi} + \frac{1}{Re.sin^2\delta}\left(\frac{\partial^2 u}{\partial \xi^2} + \frac{\partial^2 u}{\partial \eta^2} - 2cos\delta\frac{\partial^2 u}{\partial \xi \partial \eta}\right), \tag{5.8}$$

$$\begin{aligned}\frac{\partial v}{\partial t} + u\frac{\partial v}{\partial \xi} - \frac{v}{tan\delta}\frac{\partial v}{\partial \xi} + \frac{v}{sin\delta}\frac{\partial v}{\partial \eta} &= \frac{1}{tan\delta}\frac{\partial p}{\partial \xi} - \frac{1}{sin\delta}\frac{\partial p}{\partial \eta} \\ &+ \frac{1}{Re.sin^2\delta}\left(\frac{\partial^2 v}{\partial \xi^2} + \frac{\partial^2 v}{\partial \eta^2} - 2cos\delta\frac{\partial^2 v}{\partial \xi \partial \eta}\right) + Ri(T + Br.C),\end{aligned} \tag{5.9}$$

$$\frac{\partial T}{\partial t} + u\frac{\partial T}{\partial \xi} - \frac{v}{tan\delta}\frac{\partial T}{\partial \xi} + \frac{v}{sin\delta}\frac{\partial T}{\partial \eta} = \frac{1}{Re.Pr.sin^2\delta}\left(\frac{\partial^2 T}{\partial \xi^2} + \frac{\partial^2 T}{\partial \eta^2} - 2cos\delta\frac{\partial^2 T}{\partial \xi \partial \eta}\right), \tag{5.10}$$

$$\frac{\partial C}{\partial t} + u\frac{\partial C}{\partial \xi} - \frac{v}{tan\delta}\frac{\partial C}{\partial \xi} + \frac{v}{sin\delta}\frac{\partial C}{\partial \eta} = \frac{1}{Re.Sc.sin^2\delta}\left(\frac{\partial^2 C}{\partial \xi^2} + \frac{\partial^2 C}{\partial \eta^2} - 2cos\delta\frac{\partial^2 C}{\partial \xi \partial \eta}\right). \tag{5.11}$$

The boundary conditions for outlet chimney in the computational domain are transformed as:

along inclined walls of the chimney:

$$u = 0,\ v = 0,\ \frac{\partial T}{\partial \xi} = 0,\ \frac{\partial C}{\partial \xi} = 0; \qquad \text{at } \xi = 0 \ \&\ 0.15;$$

and along the exit of outlet chimney:

$$\frac{\partial u}{\partial \eta} = cos\delta\frac{\partial u}{\partial \xi},\ \frac{\partial v}{\partial \eta} = cos\delta\frac{\partial v}{\partial \xi},\ \frac{\partial T}{\partial \eta} = cos\delta\frac{\partial T}{\partial \xi},\ \frac{\partial C}{\partial \eta} = cos\delta\frac{\partial C}{\partial \xi}; \qquad \text{at } \eta = 0.5$$

The average Nusselt number along the heater is defined as,

$$Nu_h = -\frac{1}{h_2 - h_1}\int_{h_1}^{h_2}\frac{\partial T}{\partial x}dy, \tag{5.12}$$

and the average heat transfer rate along the thermosoluted block is defined as:

$$\begin{aligned}Nu_{avg} = -\frac{1}{2(l+h)}\Bigg[&\int_{L_y-h/2}^{L_y+h/2}\left(\frac{\partial T}{\partial x}\right)_{L_x+l/2}dy + \int_{L_x-l/2}^{L_x+l/2}\left(\frac{\partial T}{\partial y}\right)_{L_y+h/2}dx \\ &+ \int_{L_y-h/2}^{L_y+h/2}\left(\frac{\partial T}{\partial x}\right)_{L_x-l/2}dy + \int_{L_x-l/2}^{L_x+l/2}\left(\frac{\partial T}{\partial y}\right)_{L_y-h/2}dx\Bigg].\end{aligned} \tag{5.13}$$

The average mass transfer rate along the thermosoluted block is defined by average Sherwood number as,

$$Sh_{avg} = -\frac{1}{2(l+h)}\Bigg[\int_{L_y-h/2}^{L_y+h/2}\left(\frac{\partial C}{\partial x}\right)_{L_x+l/2}dy + \int_{L_x-l/2}^{L_x+l/2}\left(\frac{\partial C}{\partial y}\right)_{L_y+h/2}dx + \int_{L_y-h/2}^{L_y+h/2}\left(\frac{\partial C}{\partial x}\right)_{L_x-l/2}dy + \int_{L_x-l/2}^{L_x+l/2}\left(\frac{\partial C}{\partial y}\right)_{L_y-h/2}dx\Bigg]. \quad (5.14)$$

The fluid flow is always accompanied by entropy generation due to irreversible flow generated by imposed boundary conditions. The main factors for irreversible flow in the mixed convection system are fluid friction, heat transfer and mass transfer. Based on the local thermodynamic equilibrium of the linear transport theory, the entropy generation in dimensional form can be expressed as [76, 17, 5]:

$$\begin{aligned} S^*_{gen} =& \frac{k}{T_0^2}\left[\left(\frac{\partial T^*}{\partial x^*}\right)^2 + \left(\frac{\partial T^*}{\partial y^*}\right)^2\right] + \frac{\mu}{T_0}\left[2\left\{\left(\frac{\partial u^*}{\partial x^*}\right)^2 + \left(\frac{\partial v^*}{\partial y^*}\right)^2\right\} + \left(\frac{\partial v^*}{\partial x^*} + \frac{\partial u^*}{\partial y^*}\right)^2\right] \\ &+ \frac{RD}{C_0}\left[\left(\frac{\partial C^*}{\partial x^*}\right)^2 + \left(\frac{\partial C^*}{\partial y^*}\right)^2\right] + \frac{RD}{T_0}\left[\left(\frac{\partial T^*}{\partial x^*}\right)\left(\frac{\partial C^*}{\partial x^*}\right) + \left(\frac{\partial T^*}{\partial y^*}\right)\left(\frac{\partial C^*}{\partial y^*}\right)\right]. \end{aligned} \quad (5.15)$$

In the above equation, first term represents the dimensional entropy generation due to thermal diffusion (S^*_T), the second term represents the dimensional entropy generation due to fluid friction (S^*_ψ), the third term represents the dimensional entropy generation due to species diffusion (S^*_C) and the last term represents the dimensional entropy generation due to coupling between thermal and species diffusion ($S^*_{T,C}$). By using the dimensionless parameters, the entropy generation in non-dimensional form can be expressed as:

$$\begin{aligned} S_{gen} =& \left[\left(\frac{\partial T}{\partial x}\right)^2 + \left(\frac{\partial T}{\partial y}\right)^2\right] + \phi_1\left[2\left\{\left(\frac{\partial u}{\partial x}\right)^2 + \left(\frac{\partial v}{\partial y}\right)^2\right\} + \left(\frac{\partial v}{\partial x} + \frac{\partial u}{\partial y}\right)^2\right] \\ &+ \phi_2\left[\left(\frac{\partial C}{\partial x}\right)^2 + \left(\frac{\partial C}{\partial y}\right)^2\right] + \phi_3\left[\left(\frac{\partial T}{\partial x}\right)\left(\frac{\partial C}{\partial x}\right) + \left(\frac{\partial T}{\partial y}\right)\left(\frac{\partial C}{\partial y}\right)\right], \end{aligned} \quad (5.16)$$

where ϕ_1, ϕ_2 and ϕ_3 are the irreversibility distribution ratios and they are given by

$$\phi_1 = \frac{\mu T_0}{k}\left(\frac{u_i}{\Delta T}\right)^2, \quad \phi_2 = \frac{RD}{k}\frac{T_0^2}{C_0}\left(\frac{\Delta C}{\Delta T}\right)^2, \quad \phi_3 = \frac{RDT_0}{k}\left(\frac{\Delta C}{\Delta T}\right)$$

Eq. 6.17 can also be written as:

$$S_{gen} = S_T + S_\psi + S_C + S_{T,C} \quad (5.17)$$

where S_T, S_ψ, S_C and $S_{T,C}$ denotes the dimensionless entropy generation due to thermal gradients, viscosity effects, concentration gradients and the combined effect of thermal and concentration gradients, respectively. The average entropy generation can be calculated by using the formula:

$$S_{avg} = \frac{1}{V}\int_V S_{gen} dV \tag{5.18}$$

The relative dominance of entropy generation due to heat and mass transfer irreversibility to the total irreversibility is given by Bejan number which is formulated as [40, 98]:

$$Be_{T,C} = \frac{S_T + S_C + S_{T,C}}{S_{gen}}, \tag{5.19}$$

and the average Bejan number inside the enclosure is given by:

$$Be_{avg} = \frac{1}{V}\int_V Be_{T,C}\ dV. \tag{5.20}$$

Roy et al. [98] concluded that, the fluid friction irreversibility is dominant for $Be < 0.5$ whereas the heat and mass transfer irreversibility is dominant for $Be > 0.5$ and $Be = 0.5$ implies the equal contribution of heat and mass transfer irreversibility and fluid friction irreversibility to the entropy generation.

Performance evaluation criterion (PEC) is calculated in this study to find the maximum rate of heat transfer with minimum entropy generation, which is defined as the ratio of average Nusselt number to total entropy generation [67] i.e.,

$$PEC = \frac{(Nu_h + Nu_{avg})/2}{S_{avg}}. \tag{5.21}$$

Air change per hour (ACH) [56] is specified by the ventilation rate which is calculated as:

$$ACH = \frac{Q \times 3600}{V}, \tag{5.22}$$

where Q is the volumetric flow rate and V denotes the volume of enclosure.
The cooling efficiency [42] inside the enclosure is formulated as:

$$\epsilon = 1 - \left(\frac{\overline{T}_{out}}{\overline{T}_{in}}\right), \tag{5.23}$$

where $\overline{T}_{in}$ is the average temperature along inlet port and $\overline{T}_{out}$ is the average temperature along outlet port.

5.3 Numerical procedure and Code Validation

The nonlinear governing equations for slot ventilated enclosure along with the reconstructed equations for outlet chimney with specified boundary conditions are numerically solved by using finite volume method [86] using staggered grid arrangement. In the first step, above mentioned governing equations are integrated over the control volumes and converted into a set of algebraic equations. These algebraic equations are simulated using the SIMPLE (Semi Implicit Method for Pressure Linked Equations) algorithm which is based on a cyclic procedure of guess and correct operations. Momentum equations are solved to obtain the velocity using the guessed pressure and then a correction is introduced so that the equation of continuity is satisfied. A pressure link between the continuity and momentum equations is involved in this procedure which is established by the conversion of continuity equation into the Poisson equation for pressure. The procedure is completely discussed in chapter 1. Computational values for flow variables are assumed to be converged, if,

$$|\varphi_{i,j}^{k+1} - \varphi_{i,j}^{k}| \leq 10^{-6},$$

where $\varphi = (u,\ v,\ T,\ C)$ denotes the flow variables, k is the iteration number and (i, j) denotes the computational grid nodes. The flow field variables are upgraded through the succession of shorter time steps of duration 0.001. Thus, a steady-state numerical solution is obtained, which is independent of the initial conditions. The desired convergence of flow variables is achieved after 54,000 iterations approximately.

The simulation code of present work is numerically validated with the research work done by Singh & Sharif [108] by considering the mixed convection flow inside the ventilated enclosure. They have assumed that the right vertical wall is maintained at higher temperature, whereas the left vertical wall is maintained at lower temperature and rest walls are taken as adiabatic. Inlet and outlet ports are considered to be located along the bottom section of the left vertical wall and upper section of the right vertical wall, respectively. Nusselt number is calculated along the hot wall for various values of Richardson number at $Re = 100$ and the average Nusselt number (Nu_{avg}) is presented in Fig. 5.3 (a) corresponding to different Richardson number values. The grid independency test is also performed by taking different grid sizes 60×60, 80×80, 100×100, 120×120

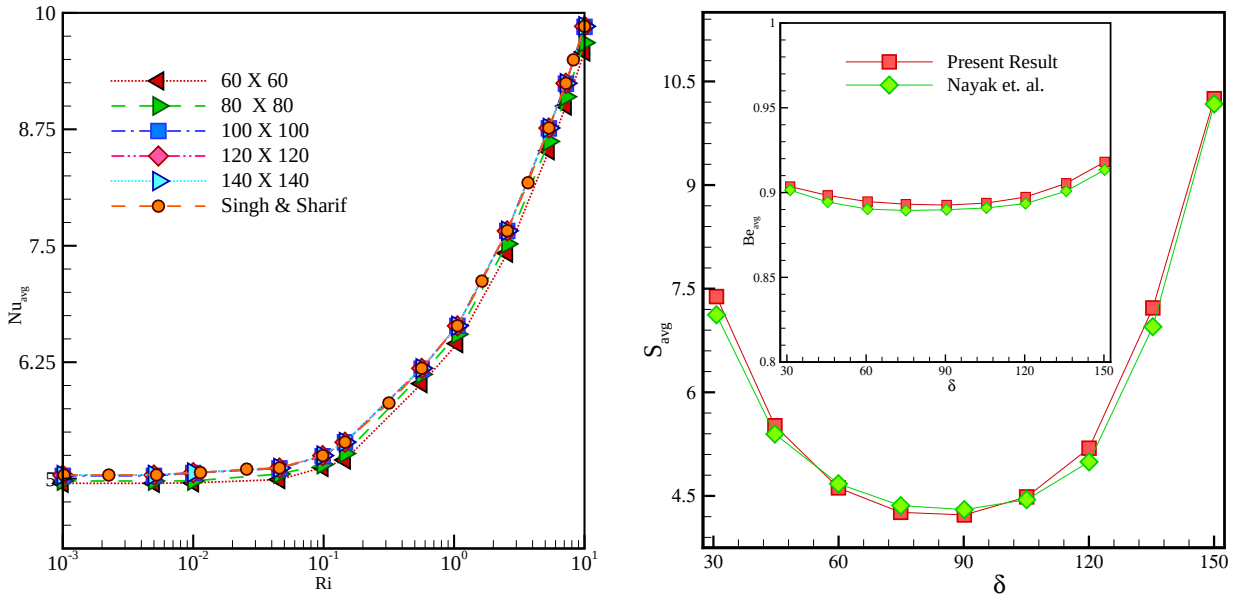

(a) (b)

Figure 5.3: Comparison of the present simulated results with the result due to (a) Singh et. al. [108] for average Nusselt number along the hot wall and (b) Nayak et al. [81] for average entropy generation when $Ri = 0.1$ and for Bejan number when $Ri = 5.0$ with fixed $Re = 100$.

and 140×140. Figure indicates the good agreement of present result with the results due to Singh & Sharif [108] and 100×100 is observed to be the optimal grid size (Fig. 5.3 (a)). For the present simulation, grid size is taken as 100×100 for the enclosure and 10×50 for the chimney shaped outlet.

The accuracy of present code is also validated with the work done by Nayak et al. [81] by taking the case of normal fluid. They considered the mixed convection flow inside a differentially heated enclosure whose top lid is sliding in the x-direction with a uniform velocity. The vertical walls of enclosure are assumed to be inclined at an angle δ with the horizontal-axis. The temperature of left vertical wall is higher as compared to the right vertical wall, while the horizontal walls are kept adiabatic. Average entropy generation for $Ri = 0.1$ and average Bejan number for $Ri = 5.0$ are calculated with the variation of inclination angle at $Re = 100$ and represented in Fig. 5.3 (b). Figure indicates a good coordination between the present results and the result due to Nayak et al. [81] and therefore, the present code is validated. The maximum percentage difference between the

present results and results due to Nayak et al. [81] for average entropy generation is 3.587 %.

5.4 Results and discussion

A numerical simulation is performed for mixed convection flow inside a slot-ventilated enclosure due to wall heater with a thermosoluted block for the removal of heat and contaminants. An inlet port for the infiltration of cold air is placed along the right vertical wall and a chimney shaped outlet port is attached along the upper wall to flush out the polluted air. Vertical walls of the chimney are considered to be inclined at different angles with the horizontal axis. The 2D geometry is selected on the basis of 3D geometry since x-y planes are considered to be similar along the North-South axis. The air enters through the east side windows, while the north and south windows are considered to be closed and a portion of the upper level of the west wall is warmed. Air is assumed as the working fluid for the present work, therefore, Pr is taken to be 0.71 and carbon dioxide is diffusing in to the air which results $Sc = 1.14$ [41]. Three different cases are chosen based on the location of inlet port with the variation of Richardson number from 0.0 to 10.0, Reynolds number $Re = 50,\ 100,\ 300$ and inclination angle of outlet chimney $45^0 \leq \delta \leq 90^0$. The impact of inlet port locations, Reynolds number, inclination angle and Richardson number on average Nusselt number and Sherwood number, bulk average temperature, entropy generation, Bejan number, cooling efficiency, air change per hour and performance evaluation criterion inside the system are evaluated.

5.4.1 Dynamic Field

The interaction between buoyancy forces and infiltrated air executes the variation of fluid flow inside the enclosure. The effects of inlet port location and variation of infiltrated air velocity on streamlines are represented in Fig. 5.4 for $Ri = 0.1$ and $\delta = 60^0$ to study the patterns of fluid flow. For low Reynolds number ($Re = 50$), infiltrated fluid is flowing very smoothly from inlet port to outlet chimney by covering the whole area of the enclosure in case-I due to weak natural convection effect. A slight/minute change in injected fluid velocity (i.e., $Re = 100$) inferred the formation of a tiny clockwise eddy just above the

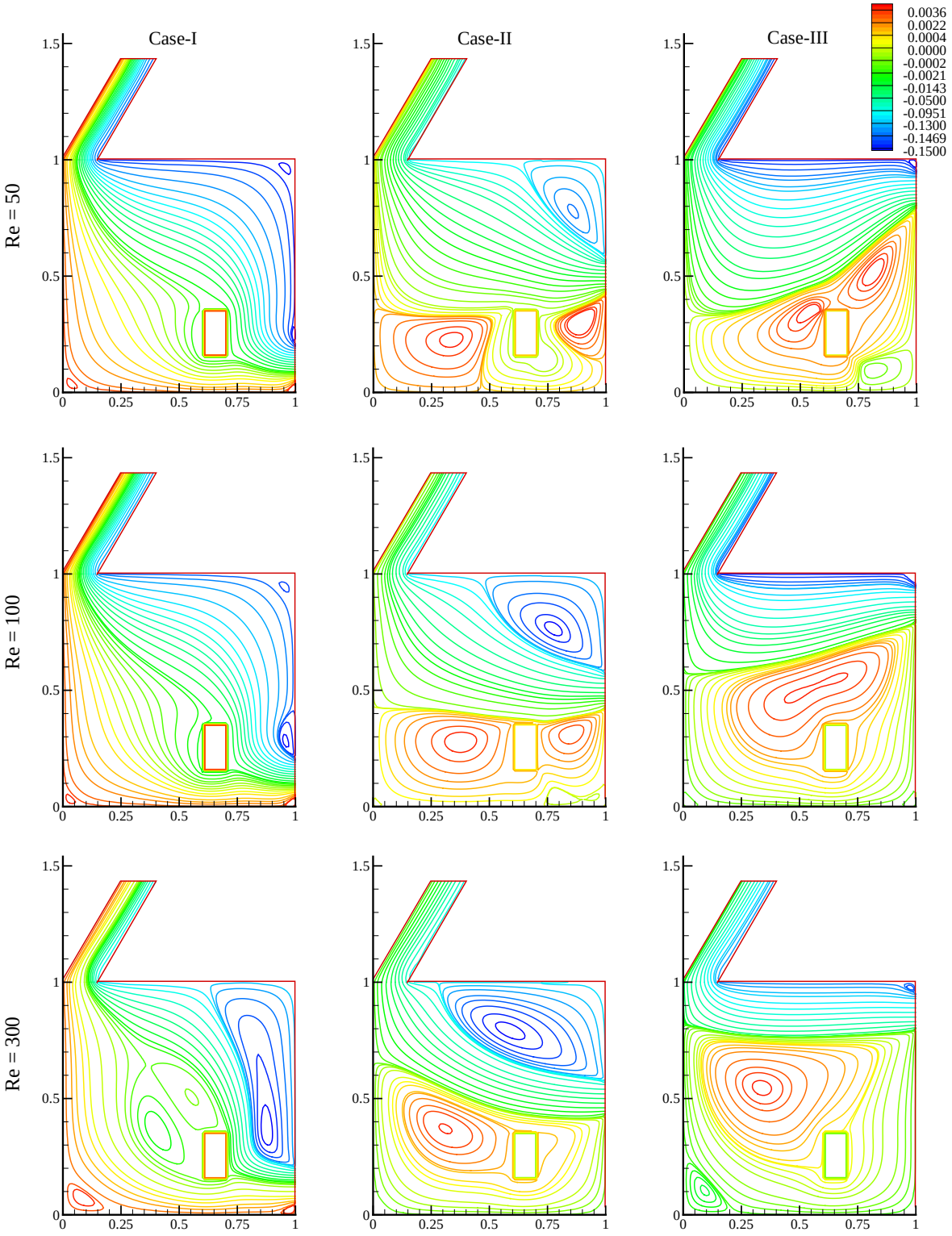

Figure 5.4: Effects of inlet port locations and Reynolds number on streamlines for $Ri = 0.1$ and $\delta = 60^0$.

inlet port due to forced convection and this eddy is getting enlarged when the injected fluid velocity is very high i.e., $Re = 300$. There are two circulation zones close to the upper-left faces of the block because the inlet fluid is not interacted with block completely due to higher velocity. By changing the inlet port location from bottom section to mid section (second column of Fig. 5.4), it is observed that cold fluid is moving towards the block only for low Reynolds number ($Re = 50$), whereas a downstream recirculation zone around the block is found for higher Reynolds number. This phenomena is occurred because the weaker flow velocity is unable to carry the cold air towards the block and hence the fluid moves downwards due to higher density whereas higher velocity forced the cold air to move straight towards the chimney. For case-III (third column of Fig. 5.4), the infiltrated fluid moves in the upper-left region of the enclosure and turned towards the outlet chimney due to the location of inlet port. An anticlockwise circulation zone of reference fluid is found around the block in the lower region of the enclosure for $Re = 50$. The size of this anticlockwise recirculation zone is getting larger for the increased value of Reynolds number and injected cold fluid is found to be moving parallel to the upper wall and then turned towards the outlet chimney for higher Reynolds number due to forced convection effect. It is visualized from the figure that for low Richardson number, infiltrated fluid is getting interacted with the block either when the inlet port is located in the bottom section of the right vertical wall or when the velocity of infiltrated cold fluid is weaker ($Re = 50$).

Fig. 5.5 presents the fluid flow structures for different values of Reynolds number when Ri is considered as 5.0. For case-I, the infiltrated air is entered along the bottom section of the right vertical wall and is moving from inlet port to outlet chimney through the thermosoluted block forming an upstream clockwise recirculation zone of reference fluid in the upper-right section of the enclosure for $Re = 50$. The circulation zone is getting shrink towards the right vertical wall when inlet fluid velocity is increased (Re=100 & 300) due to forced convection dominance. Fluid flow is found to be stacked in the left region near the block due to the density difference created by the heat sources for higher values of Reynolds number. It is observed that the fluid is flowing very smoothly, when infiltrated air is entering with low velocity i.e., $Re = 50$ for all the cases. The upstream clockwise circulation zone existing in the upper-right corner for case-I is shifted

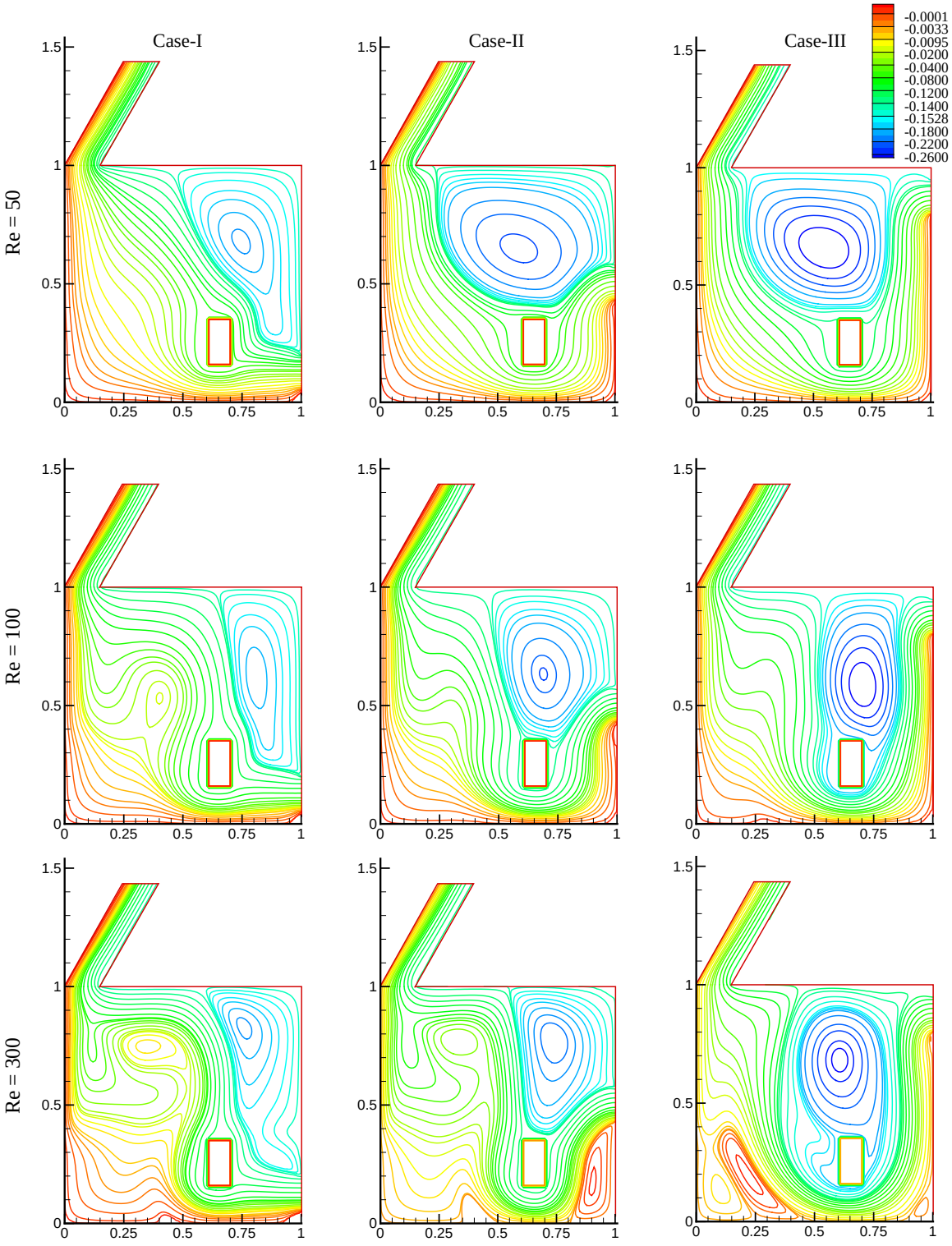

Figure 5.5: Effects of inlet port locations and Reynolds number on streamlines for $Ri = 5.0$ and $\delta = 60^0$.

towards the upper region for case-II and getting stuck between inlet and outlet flow stream for case-III due to the change of forced convection effect because of inlet port location. For case-II, the inlet fluid is not much incorporated with the thermosoluted block for $Re = 100$ and the upper-right region of the enclosure is occupied by low density fluid via upstream circulation zone due to buoyant forces. With the increasing velocity of the inlet fluid ($Re = 300$), the streamlines in the left region of the enclosure are observed to be dominated by some deformation force and an anticlockwise eddy is formed in the bottom right corner due to friction loss. In case-III, as the inlet port is located along the upper section of the right vertical wall, the cold fluid moves in the downward direction due to higher density and then turns back towards the left region of the enclosure for higher Reynolds number. A clockwise recirculation zone of thermosoluted fluid is formed above the block due to the lack of interaction with cold air. Two more downstream eddies are developed near the bottom wall for $Re = 300$ because of the strong density difference. It is concluded that the hidden reason for the formation of eddies of reference fluid is due to higher inlet fluid velocity which forces the fluid to move straight way without interacting the fluid in corners and boundary layers.

5.4.2 Thermal Field

The effects of infiltrated air velocity as well as inlet port location on isotherms are presented in Fig. 5.6 for $Ri = 0.1$ and $\delta = 60^0$. When the cold fluid enters with low velocity ($Re = 50$), the bottom-left region of the enclosure is found to be dominated by natural convection effect for all the cases. For case-I with $Re = 50$, heated thermal lines in folium shape around the block is found to be moving towards the left side and the direction is shifted towards the outlet chimney as Reynolds number increased to 100. Heated thermal lines from the wall heater is observed to be moving in the downward direction for $Re = 50$ that implicate heating in the lower-left region. As the Reynolds number is increased from 50 to 100, the temperature between wall heater and thermosoluted block is slightly decreased due to the forced convection effect. By further increment in inlet fluid velocity ($Re = 300$), thermal obcordate around the block is formed directed towards the outlet chimney due to forced air and the temperature is decreased inside the enclosure. For case-II, heated thermal lines from the block are moving towards the bottom

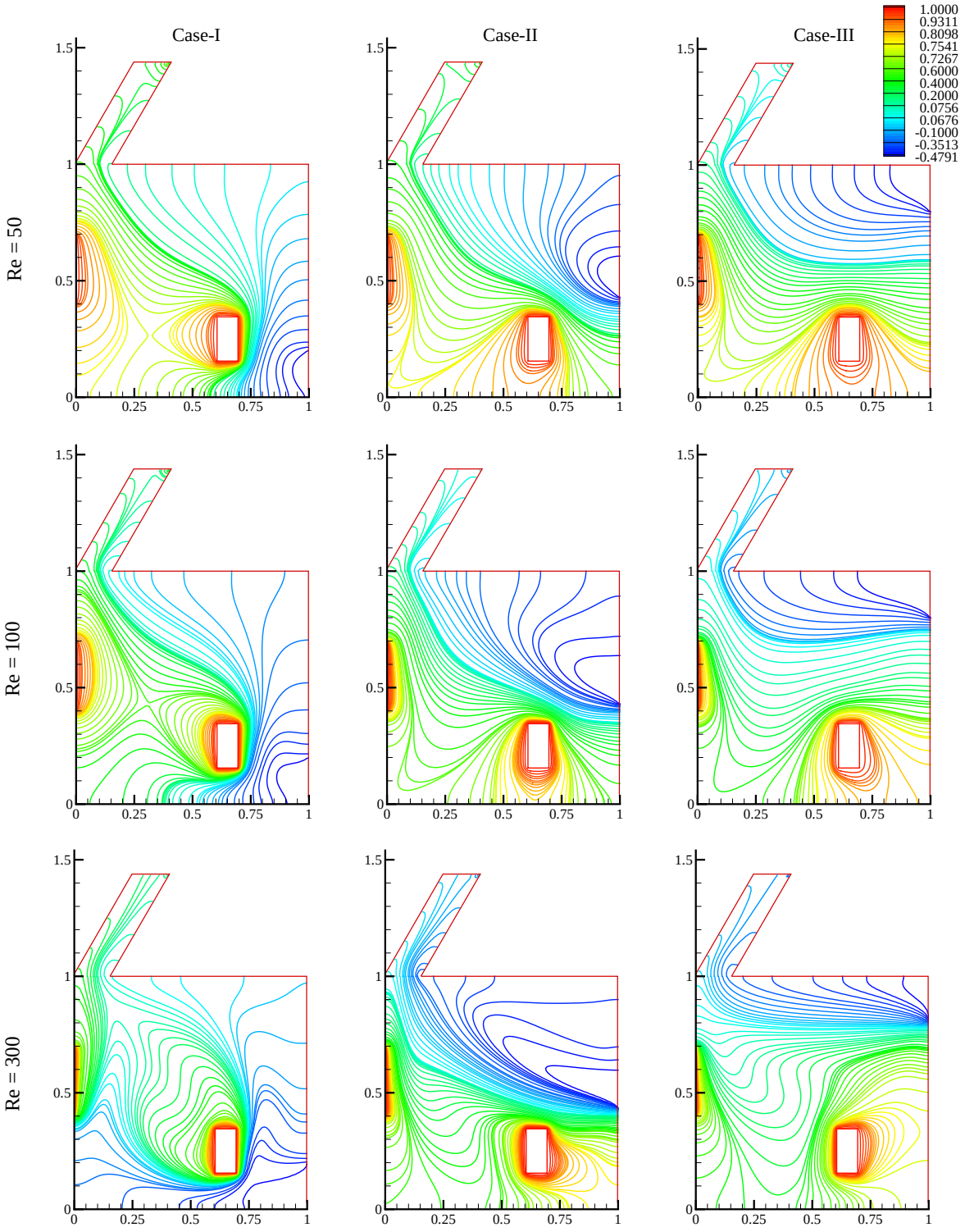

Figure 5.6: Effect of inlet fluid velocity i.e., Reynolds number on isotherms with $Ri = 0.1$ and $\delta = 60^0$ for all cases.

wall for $Re = 50$ & 100 while the direction of the flow shifts towards the right wall for higher Reynolds number since the volume of cold air from inlet port is increased. The upper region is occupied by colder thermal lines due to forced convection effect and the temperature inside chimney is getting decreased with the increase in Reynolds number. When the inlet port is located along the upper section of the right vertical wall (case-III), the cold air is flowing in the upper region without any interaction with the heat sources resulting higher temperature in lower region of the enclosure. It is observed that for higher Reynolds number, upper and mid section section of the enclosure is colder than the bottom-right section because the heated air around the block is forced to move towards the bottom-right section. By comparing the effect of inlet port location, the region near the bottom wall and right vertical wall is observed to be colder in case-I for $Re = 300$ than other cases.

Fig. 5.7 represents the temperature profiles when $Ri = 1.0$ for different inlet port locations and variation of Reynolds number. From the first row, it is observed that the heat is flowing from thermosoluted block in the form of folium shaped lines and their directions are changing from left wall to bottom wall with the changing of location of the inlet port from bottom section to upper section of the right vertical wall for $Re = 50$. These folium shaped lines are getting sharper when Reynolds number is increased from 50 to 100, and the direction is shifted from upper-left section to the right wall with the change of inlet port location which signify the forced convection dominance (second row of Fig. 5.7). For case-III, the upper region is found to be colder than the lower region which is at higher temperature due to forced flow of infiltrated air. Ovate shaped thermal plumes are generated directing towards the upper wall when $Re = 300$ for case-I, and heat lines are flowing from wall heater to the outlet chimney due to higher velocity of cold air. The lower section of the enclosure is occupied by heated thermal lines for case-III when $Re = 300$ because of higher velocity of infiltrated air and the cold air is forced to move directly towards the outlet port without interacted with the heat sources.

Thermal field for $Ri = 5.0$ with various values of Reynolds number are shown in Fig. 5.8 for all the cases. The bottom-right region is occupied by cold air because oval shaped hot thermal lines from thermosoluted block are moving towards the upper-left region for $Re = 50$ and the heat released from wall heater is shifted towards the outlet chimney

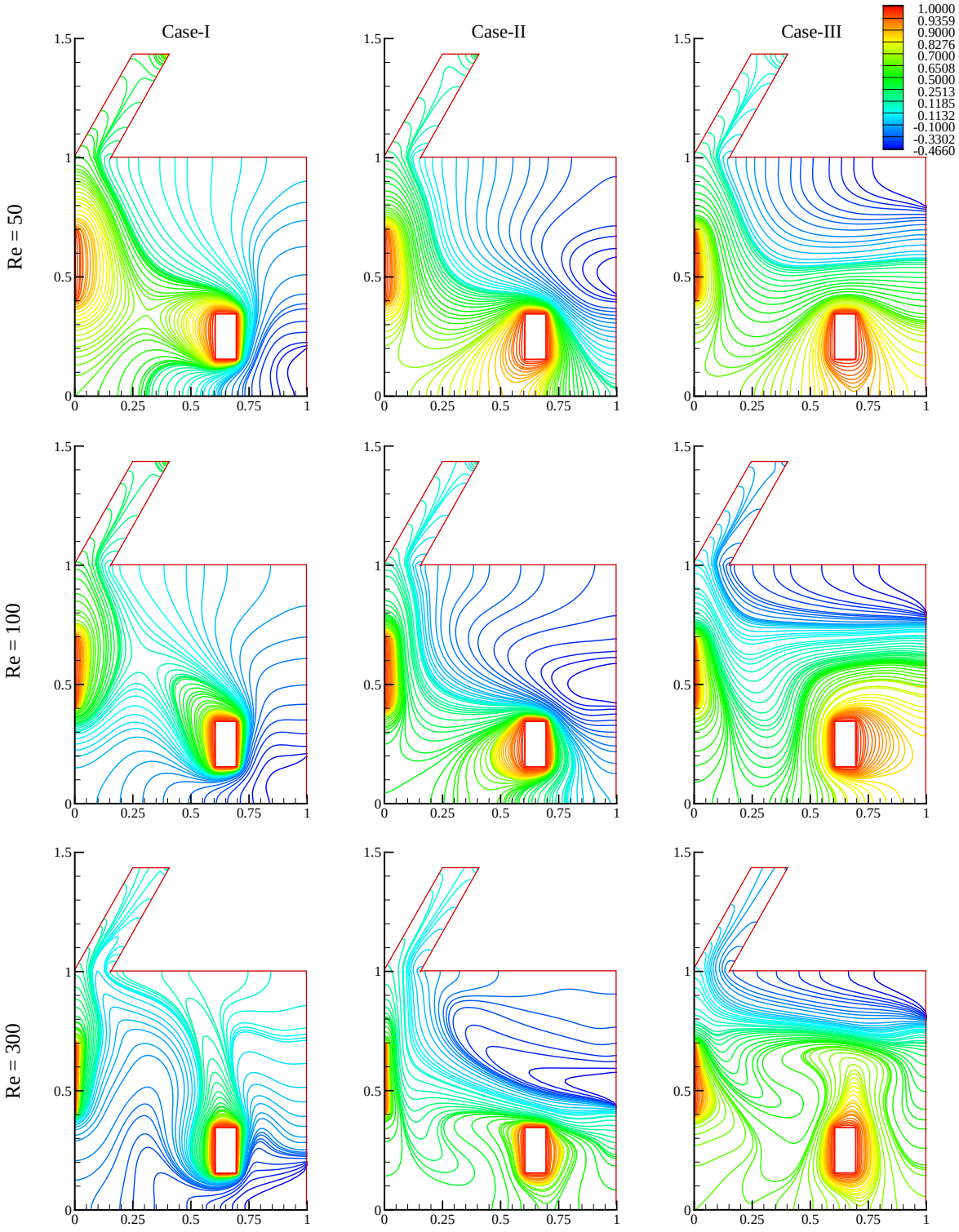

Figure 5.7: Effect of inlet fluid velocity i.e., Reynolds number on isotherms with $Ri = 1.0$ and $\delta = 60^0$ for all cases.

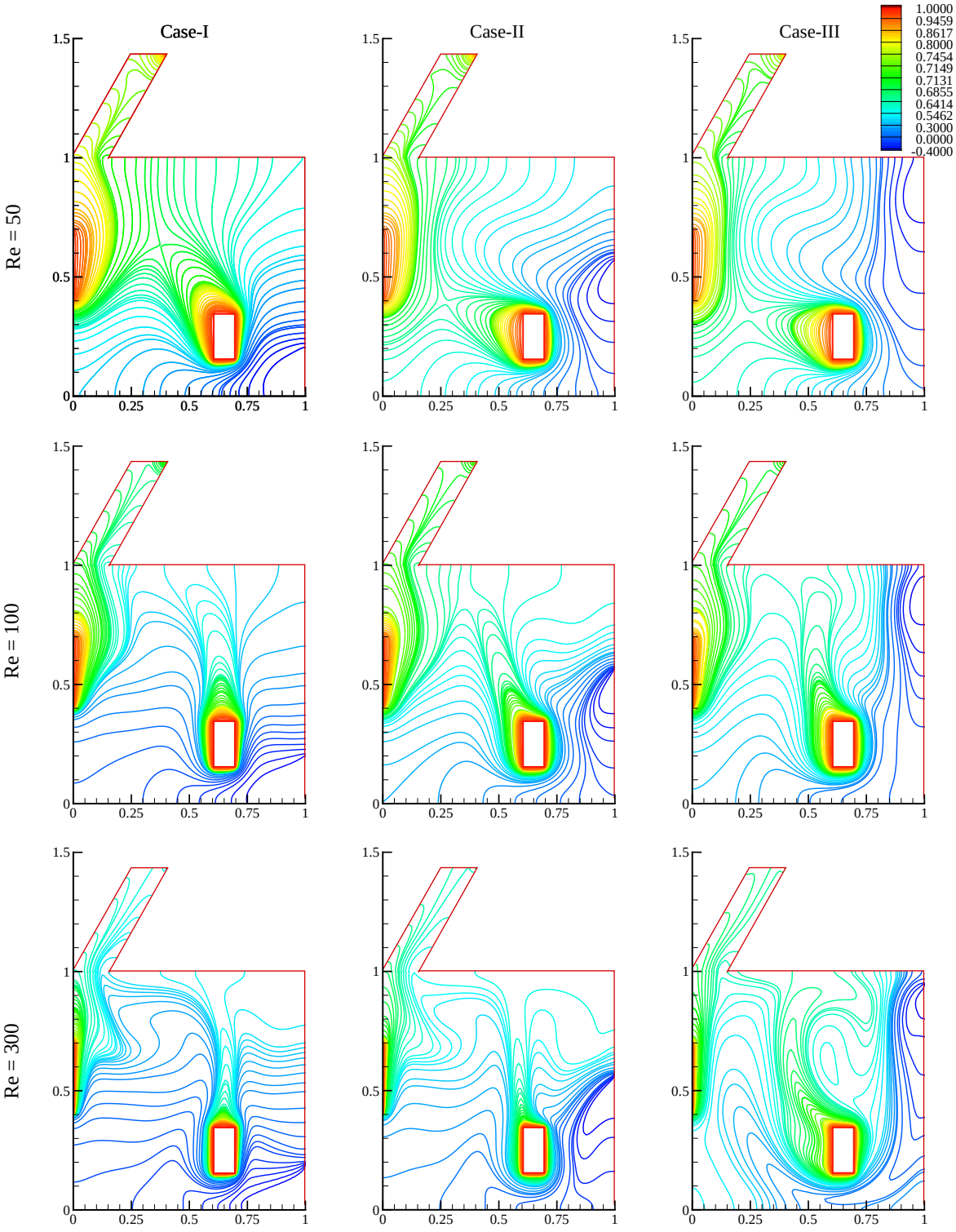

Figure 5.8: Effect of inlet fluid velocity i.e., Reynolds number on isotherms with $Ri = 5.0$ and $\delta = 60^0$ for all cases.

due to weak density of hot air. With the increase in infiltrated air velocity ($Re = 100$), a thermal plume of hot air directed towards the upper wall is formed around the block for all the cases. It is analyzed that the bottom region is colder for case-II compared to case-I and the overall temperature inside the enclosure is colder for case-III. By further increase in Reynolds number, the plume around the block is getting sharper and the hot lines encapsulate near the block and the wall heater for which the temperature variation inside the enclosure is weak in comparison to lower Reynolds number. Thermal lines near the wall heater are observed to be slightly deformed for case-I and case-II, and these lines are moving straight towards the outlet chimney for case-III. The above mentioned results conclude that maximum cooling inside the enclosure can be preserved when the infiltration of the cold fluid will occurred through upper section of the right vertical wall of the enclosure.

5.4.3 Concentration Field

The effect of Reynolds number as well as location of inlet port on solutal profiles are represented in Fig. 5.9 for $Ri = 0.1$ and $\delta = 60^0$. For $Re = 50$, the distribution of CO_2 from the block and wall heater is observed in the lower-left region of the enclosure because the amount of fresh air entered from inlet port inside the enclosure is not sufficient to drive the contaminants towards the outlet port due to slow movement of infiltrated air. Solutal obovate of CO_2 air is observed around the block directed towards the left side of the enclosure when $Re = 50$ for case-I, whereas the direction is shifted towards the bottom wall for case-II and case-III. The amount of infiltrated air can be increased by upgrading the Reynolds number so that the percentage of contaminants inside the enclosure will be decreased. For case-I, It is analyzed that, when Reynolds number is changed from 50 to 100, the region occupied by the contaminants is getting shrunk and the contaminants are diminished between block and wall heater by further increase in Re ($Re = 300$) and the region is occupied by the fresh air. For case-II, the fresh air is observed to be spread out in the upper-right region for $Re = 50$ and the contaminants are presented in the bottom-left region of the enclosure. Solutal lines having very less percentage of CO_2 is found to be exited through the outlet chimney for higher Reynolds number due to the mechanical driven force. When the inlet port is located in the upper section of the right

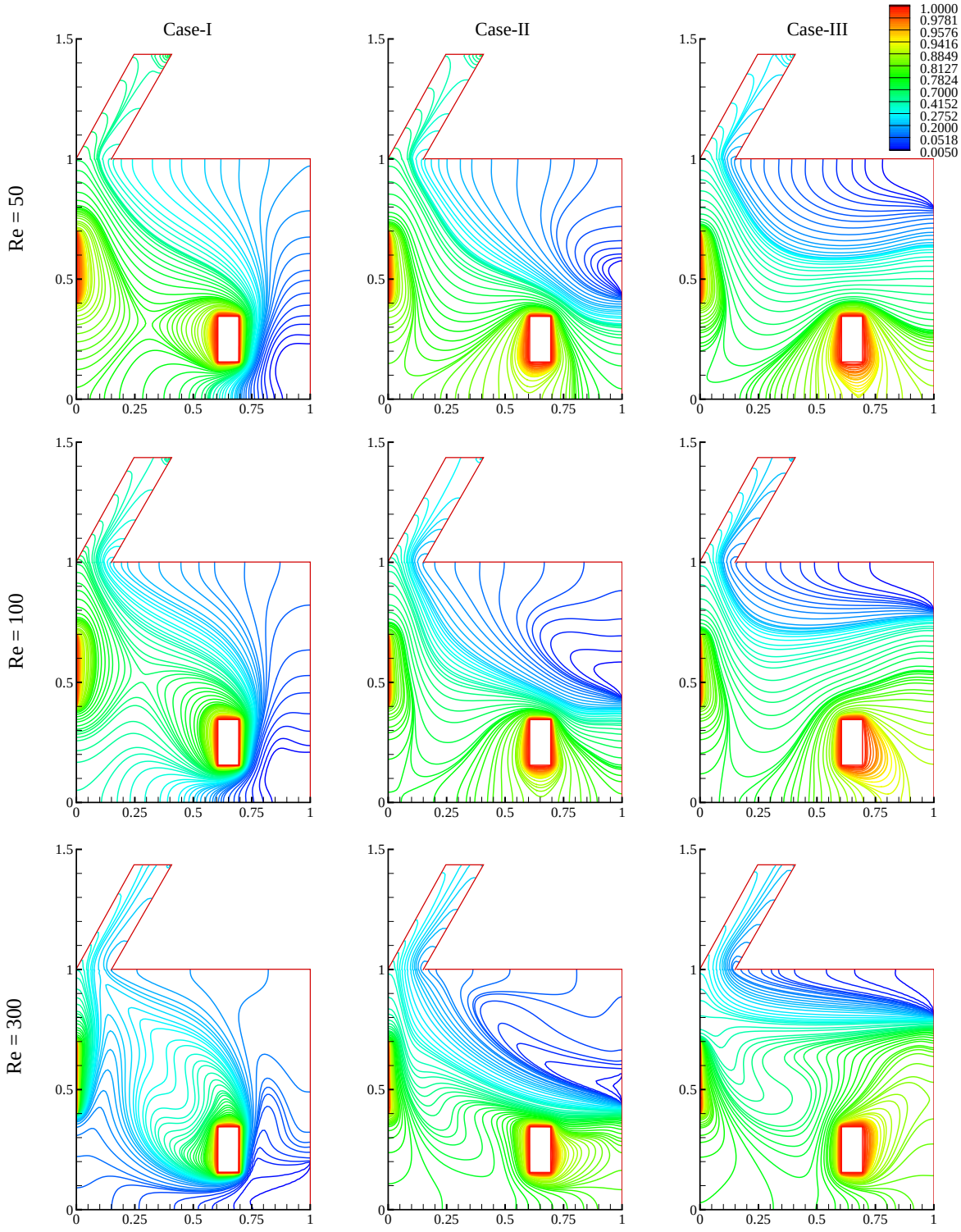

Figure 5.9: Effects of inlet port locations and infiltrated air velocity on isoconcentrations for $Ri = 0.1$ and $\delta = 60^0$.

vertical wall, the fresh air is not interacted with the block resulting denser solutal lines of CO_2 around the block. For $Ri = 0.1$, CO_2 percentage inside the enclosure is found to be minimum for case-I with $Re = 300$.

The effects of infiltrated air velocity along with the inlet port location on isoconcentration profiles for $Ri = 5.0$ and $\delta = 60^0$ are presented in Fig. 5.10. For $Re = 50$, lower-right section of the enclosure is occupied by the fresh air due to the infiltrated air through inlet port. The released CO_2 from the wall heater is flowing directing towards the outlet chimney. Contaminated air from the block is released in folium shape and is moving towards the outlet chimney for case-I, while the direction is slightly tilted towards the heater for case-II and case-III due to the change in location of the inlet port. By intensify the velocity of infiltrated fresh air ($Re = 100$), a sharp contaminated plume directed towards the upper wall is formed for all the cases and the bottom-right section is filled by fresh air due to forced convection effect (second raw of Fig. 5.10). Solutal lines having higher percentage of CO_2 from wall heater are shifted towards the chimney outlet due to mixed convection effect. Total percentage of contaminants inside the enclosure can be decreased by increasing the volume of the infiltrated fresh air to the enclosure i.e., contaminants can be removed by upgrading the Reynolds number value. A thick solutal ovate is observed around the block when Reynolds number is increased to 300 and the contaminants are completely removed from the bottom section due to the forced convection dominance. Deformation is observed between the solutal plume from block and the right vertical wall for case-III due to higher velocity of infiltrated fluid. From concentration profiles at $Ri = 5.0$, it is concluded that removal rate of contaminants is higher for higher velocity of inlet fluid i.e., higher value of Reynolds number.

5.4.4 Average Nusselt number, Entropy Generation, Performance evaluation Criterion and Bejan number

Average rate of heat transfer around the block is calculated for different flow governing parameters and a comparison is presented in Fig. 5.11 to show the effects of Reynolds number, Richardson number and inclination angle of chimney on Nu_{avg}. It is observed that average rate of heat transfer along the block is growing with the increasing value of Reynolds number for all the cases when $Ri > 1.0$ due to density difference. Average

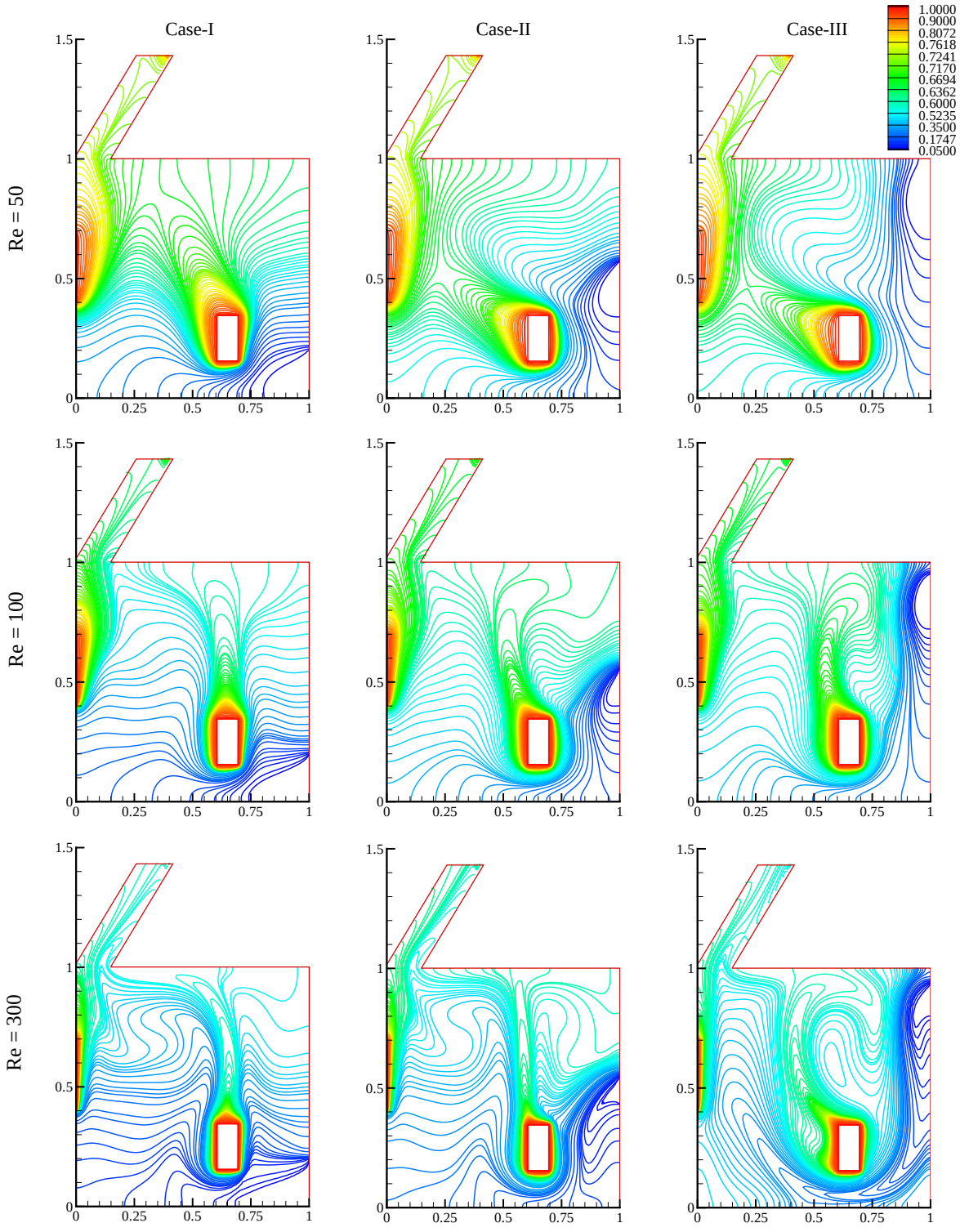

Figure 5.10: Effects of inlet port locations and various Reynolds number value on isoconcentrations for $Ri = 5.0$ and $\delta = 60^0$.

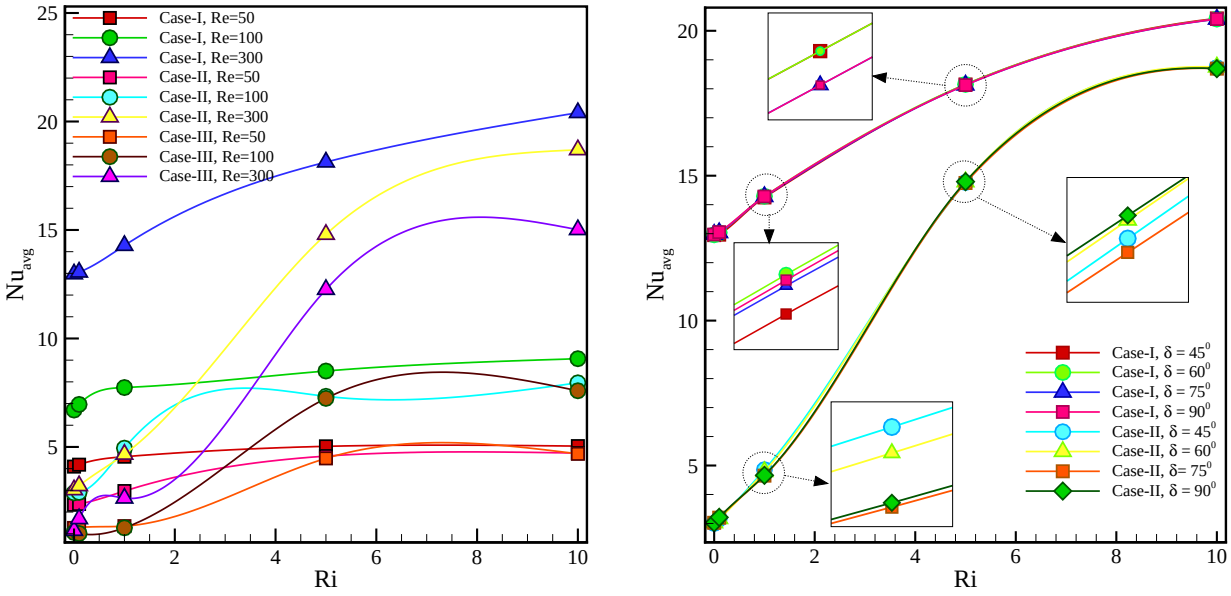

(a) (b)

Figure 5.11: Comparison of average Nusselt number along the block with the variation of Richardson number for (a) different Reynolds number with fixed $\delta = 90^0$ and (b) different values of δ with fixed $Re = 300$.

Nusselt number is higher for $Re = 300$ and $1.0 < Ri \leq 10.0$, since the volume of infiltrated cold air is maximum for higher Reynolds number value and the flow is dominated by mixed convection. Average Nusselt number is found to be increasing with the increase of Richardson number for all the cases and the maximum value is achieved for case-I at $Re = 300$. The effect of inclination angle is shown in Fig. 5.11(b) for case-I and case-II at $Re = 300$. It is observed that an infinitesimal change in heat transfer rate is found due to the change of inclination angle of the outlet chimney. For $Ri = 1.0$, the average heat transfer rate is maximum at $\delta = 60^0$ for case-I, while it is maximum for $\delta = 45^0$ in case-II. For case-I at $Ri = 5.0$, maximum value of average Nusselt number is found when $\delta = 45^0$ & 60^0, whereas for $Ri = 10.0$, maximum heat transfer rate is achieved at $\delta = 45^0$. For case-II at $Ri = 5.0$, the maximum heat transfer rate is observed with the vertical placement ($\delta = 90^0$) of the outlet chimney, while at $Ri = 10.0$, the heat transfer rate is maximum for $\delta = 60^0$.

Fig. 5.12 (a) represents the variation in average entropy generation due to the

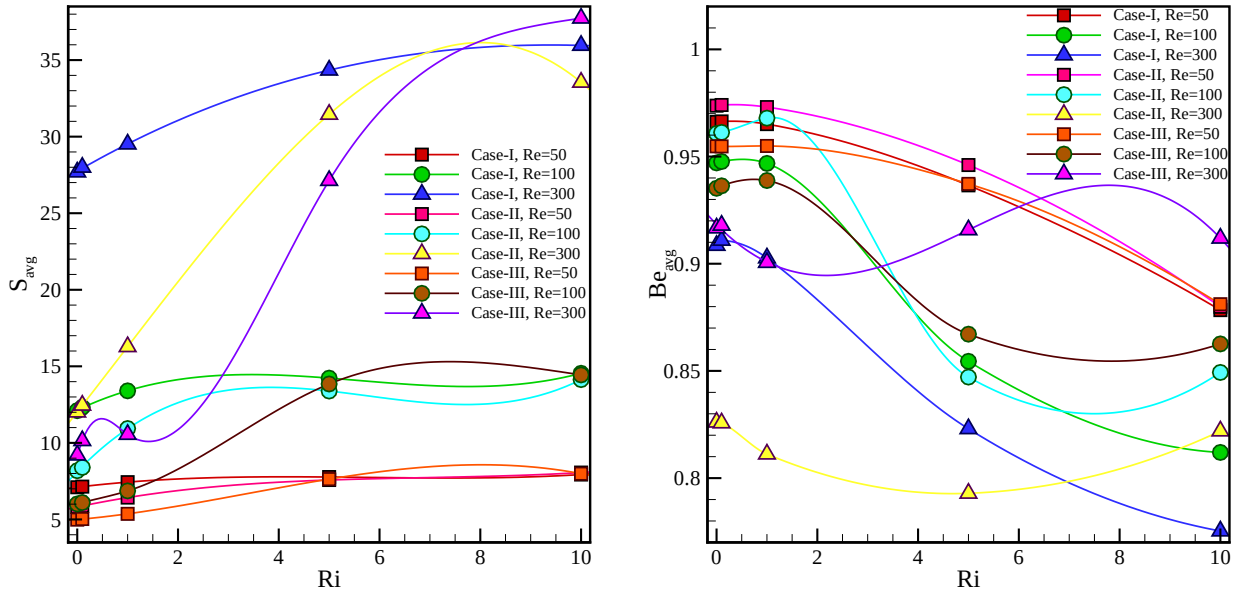

(a) (b)

Figure 5.12: Comparison of (a) average entropy generation and (b) average Bejan number with the variation of Richardson number for fixed $\delta = 90^0$.

change of Richardson number and inlet port location for different values of Reynolds number with $\delta = 90^0$. The rate of energy loss is minimum in case of weak forced convection i.e., $Re = 50$ for all the cases. Average entropy generation is increasing with the increasing values of Reynolds number as well as Richardson number. Case-III provides the minimum entropy generation (S_{avg}) for low Reynolds number with $Ri \leq 5.0$. For minimum energy loss, it is observed from Fig. 5.12 (a) that for low Richardson number ($Ri < 5.0$), inlet port must be located along the upper section of the right vertical wall but for $Ri = 10.0$, inlet must be located as of case-II. If $Re = 100$, then minimum entropy generation is achieved for case-III, since the flow is dominated by forced convection ($Ri < 5.0$), whereas case-II provides minimum entropy in case of natural convection dominated flow ($Ri \geq 5.0$). Fig. 5.12 (b) shows the effect of Richardson number on average Bejan number for different values of Reynolds number when outlet chimney is kept vertical. Be_{avg} is found to be greater than 0.75 for all the cases, which reflects the dominance of the heat transfer irreversibility over the fluid friction irreversibility. It is found that average Bejan number is decreasing with the increase in Reynolds number as well as Richardson number for case-I

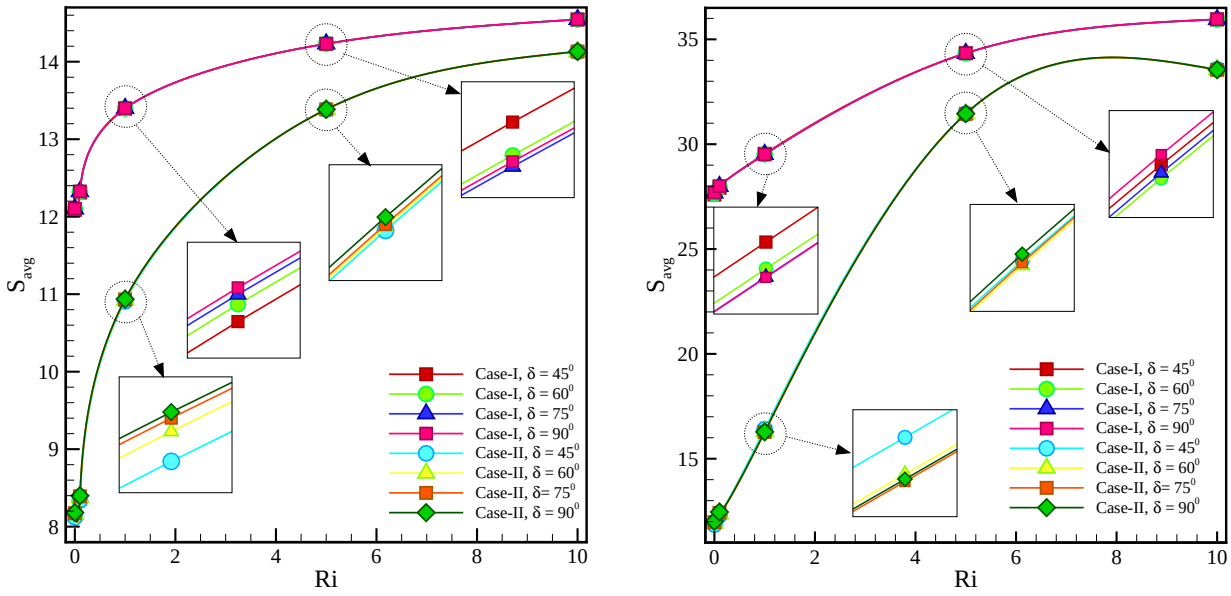

(a) (b)

Figure 5.13: Effect of inclination angle on average entropy generation when (a) $Re = 100$ and (b) $Re = 300$ with the variation of Richardson number for case-I and case-II.

and case-II. This demonstrate that fluid friction irreversibility increases with the increase in Reynolds number due to forced convection effect. Be_{avg} is maximum for low Reynolds number and Richardson number which makes clear that the fluid friction irreversibility is minimum for $Re = 50$ and $Ri < 1.0$ due to weak convection effect.

The effect of inclination angle on average entropy generation is compared for case-I and case-II in Fig. 5.13. It is interpreted that at $Re = 100$, the minimum entropy generation is obtained in case-II for $\delta = 45^0$. For case-I at $Re = 100$, minimum entropy generation is achieved for $\delta = 45^0$ at $Ri = 1.0$ whereas minimum S_{avg} is obtained for $\delta = 75^0$ by increasing the Richardson number to 5.0. For $Re = 300$, the value of average entropy is found to be minimum in case-II for $\delta = 75^0$ and $Ri = 1.0$ (Fig. 5.13 (b)) while for $Ri = 5.0$ average entropy is minimum at $\delta = 60^0$.

In order to find the best combination of fluid flow parameters for maximum heat transfer with minimum entropy generation, a comparison is made for performance evaluation criteria due to change in Richardson number and inlet port location for different values of Reynolds number with $\delta = 90^0$ in Fig. 5.14 (a). It is illustrated that for

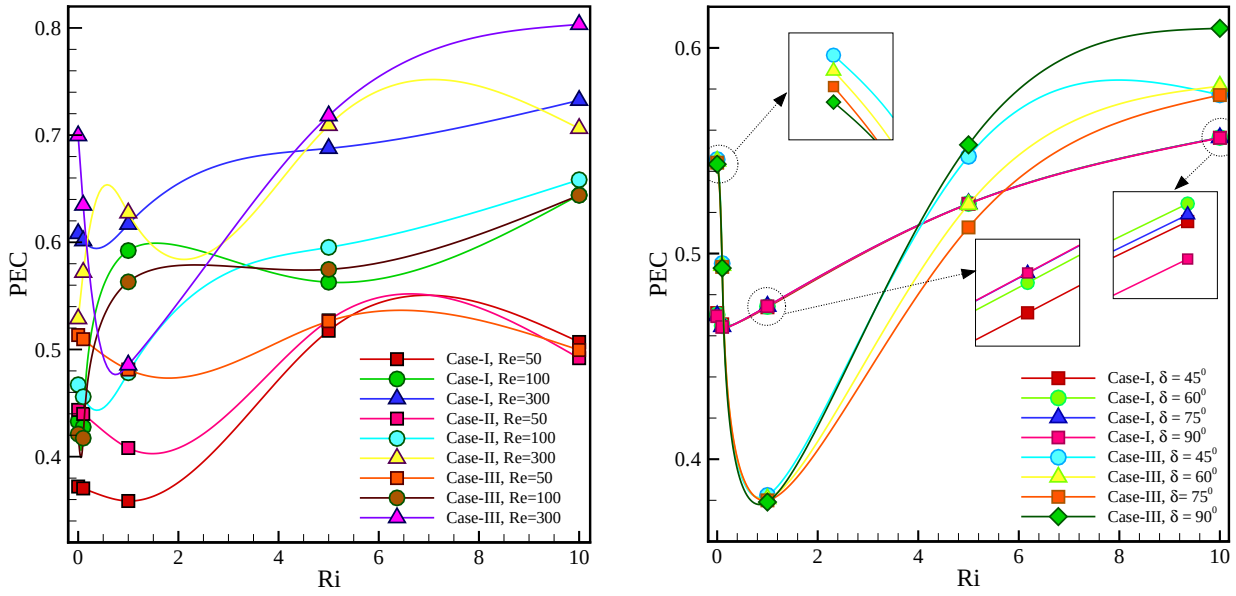

(a) (b)

Figure 5.14: Effect of Reynolds number and inlet port location on performance evaluation criteria with the variation of Richardson number for (a) vertical outlet chimney and (b) for different values of δ for case-I and case-III with $Re = 300$.

$Ri = 10.0$, the value of PEC is higher for case-I with $Re = 50$, for case-II with $Re = 100$ and for case-III with $Re = 300$. Maximum heat transfer with minimum entropy generation is achieved for case-III when $Ri < 1.0$ for all values of Reynolds number. In case of higher Richardson number ($Ri > 1.0$), maximum value of PEC is obtained in case-III for $Re = 100$ although maximum value of PEC is achieved in case-II for $Re = 100$. Fig. 5.14 (b) represents the variation in PEC due to the inclination angle for case-I and case-III at $Re = 300$. The maximum PEC is obtained in case-III with $\delta = 45^0$ and $Ri < 1.0$ while PEC is maximum in case-I for $Ri = 1.0$ due to mixed convection effect. Maximum Nusselt number with minimum entropy generation for $Ri > 1.0$ is obtained in case-III for $Re = 300$ with vertical outlet chimney ($\delta = 90^0$).

5.4.5 Average Sherwood number, air change per Hour, cooling Efficiency and average temperature

Fig. 5.15 (a) represents the variation of average Sherwood number for different values of Reynolds and Richardson number. It is found that the value of Sh_{avg} is increasing with

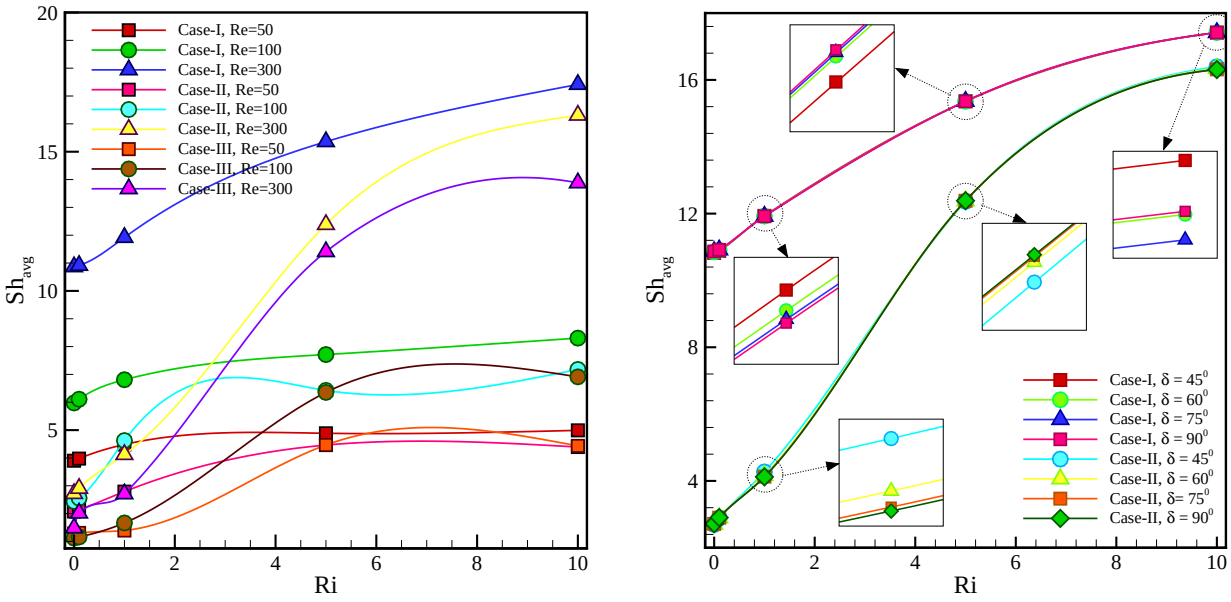

(a) (b)

Figure 5.15: Effect of Richardson number on average Sherwood number when (a) $\delta = 90^0$ for all cases with various Re values and (b) $Re = 300$ for different inclination angle for case-I and case-II.

the increase in Richardson number due to the variation of density. Increase in Reynolds number indicate higher mass transfer rate because increase in the velocity of infiltrated air reduces the amount of contaminated air of the enclosure due to forced convection. For higher Richardson number, contaminated hot air moves quickly towards the outlet chimney due to higher density differences inside the enclosure. From the figure, it is visualize that mass transfer is higher for case-I for all Reynolds number and maximum mass transfer rate is obtained for $Re = 300$. This signifies that the rate of mass transfer is higher when the flow is dominated by forced convection effect. The angle of inclination of outlet chimney is analyzed for case-I and case-II at $Re = 300$ and presented in from Fig. 5.15(b). For $Ri = 1.0$, the value of Sh_{avg} is maximum for $\delta = 45^0$ in both these cases. Maximum amount of mass transfer is occurring for vertical outlet chimney in case of $Ri = 5.0$ due to mixed convection effect. In case of higher density difference i.e., $Ri = 10.0$, average Sherwood number is maximum for $\delta = 45^0$ with $Re = 300$. This indicates that the maximum removal of contaminated air from the enclosure is possible

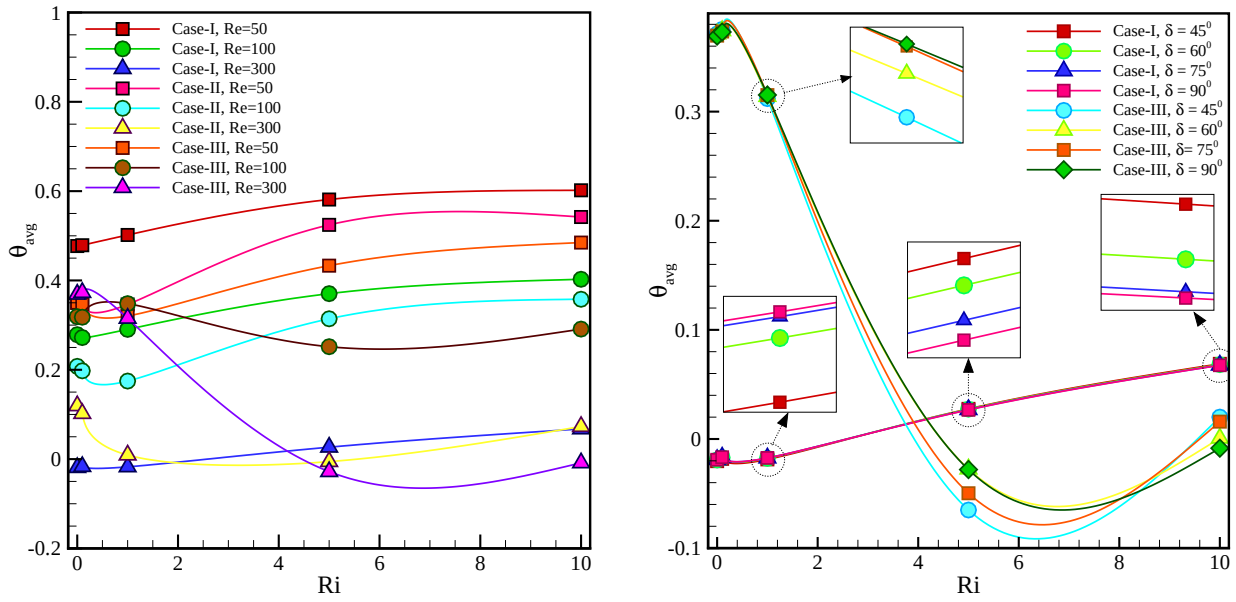

(a) (b)

Figure 5.16: Comparison of average temperature inside the enclosure with the variation of Richardson number for (a) different Reynolds number with fixed δ ($= 90^0$) and (b) different values of δ for case-I and case-III with fixed Re ($= 300$).

when the infiltrated cold air is entering through the bottom section of the right vertical wall and the outlet chimney is inclined at 45^0 with the horizontal axis.

The effect of Richardson number on average temperature inside the enclosure due to different Reynolds number is presented in Fig. 5.16 (a). It is obvious that cooling effects will be increased by increasing the volume of cold air inside the enclosure. This implies that minimum temperature can be obtained for higher values of Reynolds number ($Re = 300$) due to forced flow of fresh air. Maximum heating inside the enclosure is observed in case-I for low velocity of the infiltrated cold fluid i.e. $Re = 50$. For $Ri \leq 1.0$, minimum average temperature is achieved in case-I with fixed $Re = 300$, while θ_{avg} is minimum in case-II if Reynolds number is decreased to 100 and for $Re = 50$ minimum temperature is observed in case-III. It is observed from the figure that for $Ri > 1.0$, maximum cooling inside the enclosure is achieved in case-III with a fixed Reynolds number. The variation in average temperature due to inclination angle is shown in Fig. 5.16 (b) for case-I and case-III with $Re = 300$. Maximum cooling i.e., minimum average temperature is found for

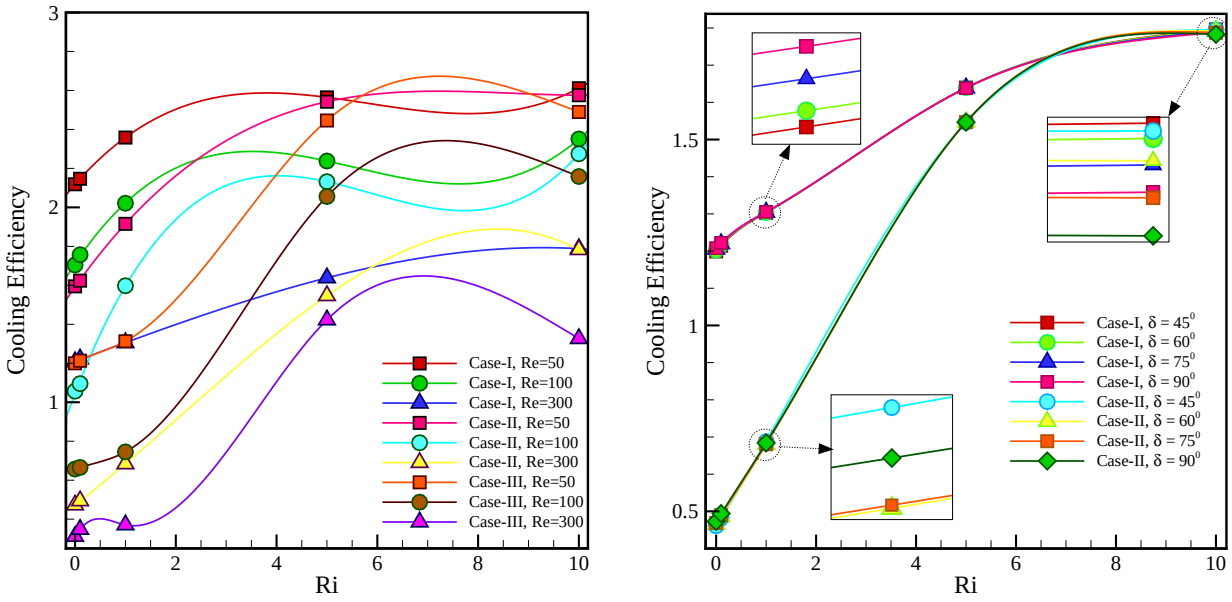

(a) (b)

Figure 5.17: Effect of Richardson number on cooling efficiency for (a) different Reynolds number when $\delta = 90^0$ and (b) different values of δ for case-I and case-II with fixed $Re = 300$.

$\delta = 45^0$ when $Ri \leq 5.0$, but average temperature is minimum for vertical outlet chimney when $Ri = 10.0$ for both these cases.

The variation in cooling efficiency due to Richardson number and Reynolds number are shown in Fig. 5.17 (a) for all the cases. Cooling efficiency is observed to be maximum in case-I for $Re = 50$ due to density differences. Increase in Richardson number implies the increasing of cooling efficiency inside the enclosure. This happens because increase in Ri implies the increment in temperature differences inside the enclosure that indicates the faster flow of heat towards the outlet chimney. From Fig. 5.17 (b), it is noted that for $Re = 300$ with $Ri = 1.0$, maximum cooling efficiency is obtained in case-I for $\delta = 90^0$ while for case-II, maximum cooling efficiency is achieved for $\delta = 45^0$. In case of higher density differences i.e., $Ri = 10.0$, maximum cooling efficiency is found for $\delta = 45^0$ due to the dominance of mixed convection.

Fig. 5.18 (a) represents the variation in air change per hour (ACH) due to Richardson number, Reynolds number and inlet port locations. ACH is higher for case-I when

$Ri \leq 1.0$, and its value is higher for case-III when $Ri > 1.0$. The location of inlet port affects the air change per hour significantly due to the interaction of infiltrated air with the thermosoluted block. The variation of ACH is found to be higher for case-III compared to case-I with the variation in Richardson number. It is pointed out that for case-III with higher Richardson number, the hot air is moving in the upward direction while cold air is moving in the downward direction by occupying most of the bottom-right region. But, when inlet port is placed according to case-I, the section near right vertical wall is not dominated by infiltrated air. This implies that there is huge variation in the value of ACH for case-III rather than case-I due to variation in Richardson number. Effect of inclination angle on ACH is shown in Fig. 5.18 (b) for case-II with the variation in Ri with two different values of Re. It is found that maximum ACH is obtained when outlet chimney is vertical due to straight flow of air.

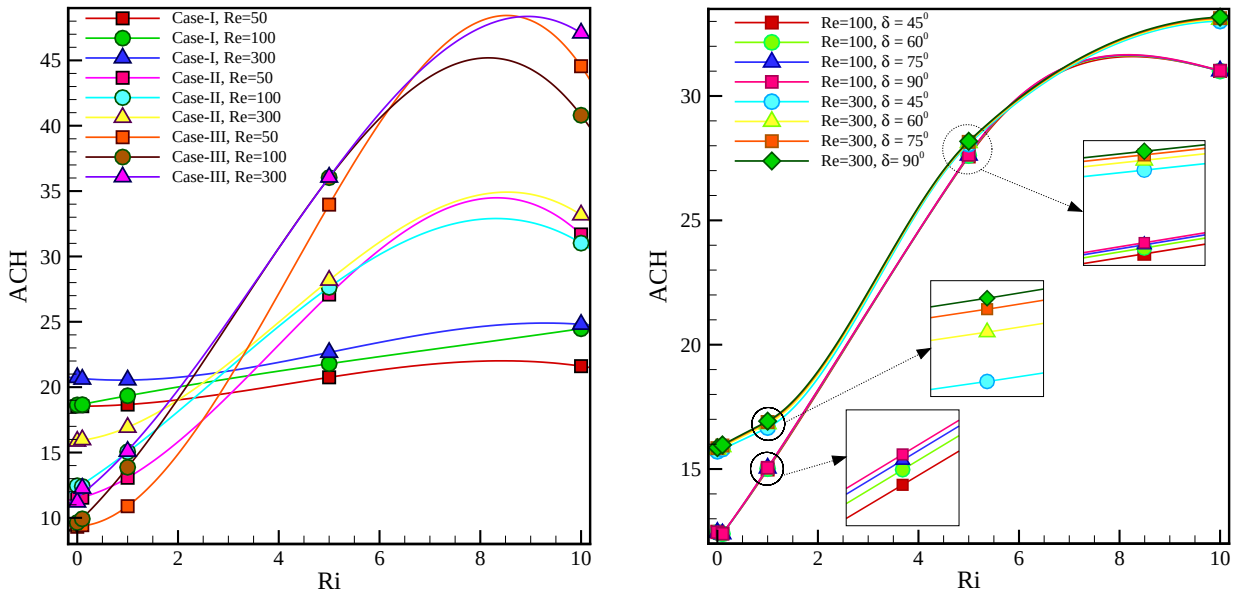

(a) (b)

Figure 5.18: Effect of Richardson number on air change per Hour (ACH) for (a) different Reynolds number for fixed $\delta(= 90^0)$ and (b) different values of δ for case-II.

5.5 Conclusion

A numerical study is presented in a slot-ventilated enclosure for removal of the heat and contaminants generated due to wall heater and a thermosoluted object. Fresh cold air is considered to be infiltrated inside the enclosure through various ports of right vertical wall and an outlet chimney is placed along the upper wall inclined at various angles with x-axis to flush out the contaminated air. The effect of Richardson number, Reynolds number, inclination angle of outlet chimney and location of inlet port on fluid, heat and mass transfer phenomena is visualized and summarized through the average Nusselt number, Sherwood number, entropy generation, cooling efficiency, performance evaluation criteria and air change per hour. Based on the above simulations, following remarks can be concluded:

1. Maximum average heat transfer rate is observed in case-I for $Re = 300$. At $Ri = 1.0$, maximum Nu_{avg} is obtained when outlet chimney is inclined at 60^0 with the horizontal axis although maximum heat transfer is achieved for $\delta = 45^0$ when $Ri = 10.0$,.

2. Minimum entropy generation is found for case-III when forced convection dominance is weak ($Re = 50$). For $Re = 100$ and $Ri > 1.0$, minimum value of S_{avg} is obtained in case-II for $\delta = 45^0$.

3. The heat and mass transfer irreversibility dominates the fluid friction irreversibility since Be_{avg} is greater than 0.75 for all the cases.

4. Maximum heat transfer rate with minimum energy loss for $Ri < 1.0$ is obtained in case-III at $\delta = 45^0$ when $Re = 300$. Although, the maximum value of PEC at $Ri = 1.0$ is obtained for case-II when $Re = 300$. For $Ri > 1.0$, maximum PEC is obtained in case-III when outlet chimney is vertical with $Re = 300$.

5. Maximum mass transfer rate (Sh_{avg}) is found in case-I for $\delta = 45^0$ at $Ri = 1.0$ but Sh_{avg} is maximum for vertical outlet chimney at $Ri = 5.0$. For $Ri = 10.0$, case-I provides the maximum removal of contaminated air from the enclosure when $\delta = 45^0$.

6. Maximum cooling is achieved when the flow is dominated by forced convection effect i.e., $Re = 300$. For $Ri < 5.0$, maximum cooling is found in case-I at $\delta = 45^0$. In case of higher density differences, minimum temperature inside the enclosure is obtained in case-III at $Ri = 5.0$ with $\delta = 45^0$. For $Ri = 10.0$, maximum cooling is obtained in case-III for vertical outlet chimney.

7. Air change per hour is higher in case-I for $Ri \leq 1.0$, and maximum ACH is achieved for case-III when $Ri \geq 5.0$ corresponding to $Re = 300$.

Chapter 6

Three-dimensional parametric study of airflow, heat and mass transfer characteristics in a slot-ventilated enclosure

6.1 Introduction

Three dimensional study of mixed convection flow to predict airflow rates between different zones in a slot-ventilated enclosure is getting prominent attention due to its applicability in many industrial and engineering processes, like chemical processing, space heating/cooling, thermal design of buildings, heat exchangers and cooling of electronic devices [108, 29, 125, 71]. A slot ventilated enclosure with discrete heat and contaminant sources can be considered as a general human living room in which the heat and mass transfer structures are needed to be investigated to obtain the air flow patterns. Thermal comfort with high indoor air quality by removing the airborne pollutants, are the primary aims in building design, although ventilation is found to be the best way to improve the quality of indoor air for optimal heating/cooling. The indoor air quality of the enclosure depends on the humidity, temperature and pollutants concentration. The two dimensional work on slot ventilated enclosures are sizably published in the past decades but the three dimensional work is needed to be simulated, since three dimensional geometry can probe the effects of vents in realistic applications [124]. For higher Richardson number, the flow adjacent to the substrate surface clearly signifies a three dimensional effect in case of vented flow which can not be predicted in two dimensional setups.

A number of experimental and numerical studies in the literature shows the behavior of heat and fluid flow through mixed convection in ventilated enclosures, and modifies the boundary conditions for a realistic room flow. The characteristics of fluid flow, heat and contaminant transport structures in a displacement ventilated system due to discrete heat and contaminant sources are analyzed by Deng et al. [29] using two-dimensional contour functions for different flow governing parameters. The temperature distribution and air flow patterns in an enclosure with fixed inlet and outlet port was investigated by Tripathi et al. [116]. They summarized that the buoyancy force intensifies the air circulation, and forces the cold air to move towards the outlet port which leads a uniform temperature distribution inside the enclosure. Koufi et al. [57] numerically analyzed the mixed convection flow due to heating floor inside a ventilated cavity to find a suitable configuration in terms of inlet and outlet port locations to achieve the optimum ventilation efficiency for the temperature distribution and heating intensity. A numerical study is conducted by Zhang et al. [125] to remove the airborne pollutants from a slot-ventilated enclosure in which a contaminant source is located in the lower section and two discrete heat sources are placed along the bottom and right vertical walls. They determined an optimal configuration based on the location of outlet port, heat source and higher efficiency of contaminant removal from the enclosure and found that the fluid flow, heat and contaminant transport phenomena are strongly dependent on the Reynolds number and Grashof number.

The natural convection flow in three dimension is numerically investigated for heat transfer in a cubical enclosure due to thermally active faces for a wide range of Rayleigh number to express the overall heat transfer rate in the enclosure [36]. Three dimensional parametric study for lid-driven enclosure with vertical thermal gradient was done by Iwatsu et al. [51] to visualize the realistic flow patterns and heat transfer characteristics. Yang et al. [123] numerically investigated the turbulent flow and heat transfer characteristics in a three-dimensional channel to correlate the heat transfer rates with Reynolds number. Mahannta et al. [63] and Nayak et al. [80] presented three dimensional parametric studies on fluid flow over a stretching sheet for convective boundary conditions to discuss the velocity and temperature fields. The numerical work of Sezai et al. [103] represented the three dimensional flow patterns of thermosolutal natural convection inside

a cubical enclosure because of opposing and assisting buoyancy force due to horizontal thermal and solutal gradients. Frederick et al. [37] investigated the steady-state, laminar natural convection flow inside a cubical enclosure with a heater placed along the vertical wall to study the heat transfer behavior for different values of Rayleigh number.

An experimental study for mixed convection flow was shown by He et al. [45] to remove the indoor contaminants under different air distribution methods in a building enclosure. They also validated their CFD model with the experimental observed results and numerically presented the results of air flow under additional contaminant sources and air diffusor layouts. The influence of flow governing parameters on indoor contaminants in a three-dimensional enclosure was numerically studied by Liu et al. [59] They reported the decrease in the level of contaminants with increasing Reynolds number. A three dimensional numerical investigation of mixed convection flow in a rectangular enclosure is presented by Moraga and Lopez [75] to find the effects of variation in Reynolds and Richardson number. Doghmi et al. [31] studied the effects of fluid flow and thermal transport phenomena due to the presence of isothermal heating block in a three-dimensional ventilated enclosure. They concluded that an optimal choice of flow governing parameters with different placement of inlet-outlet port can significantly enhance the fluid flow intensity and rate of heat transfer.

The simulations of thermosolutal systems are more realistic in three-dimensional, whereas most of the research works found in the literature are simulated in two dimensions. In past decades, the research work done is either related to natural convection or thermal mixed convection. For the best of authors' knowledge, there is no research work that deals with the simulation of three-dimensional mixed convection due to thermosolutal gradients in a slot-ventilated enclosure under different flow methods, which are applicable in various industrial heating/cooling processes and removal of indoor pollutants from residential buildings. This chapter deals with a three-dimensional numerical study of mixed convection air cooling in a slot-ventilated enclosure due to discrete heat and contaminant sources under different flow methods. The numerical simulations are performed for a wide range of flow governing parameters to find the effects of inlet and outlet port locations for achieving acceptable average temperature of the enclosure and maximum rates of heat and mass transfer with minimum entropy generation.

6.2 Physical description and Mathematical Modeling

The schematic geometry investigated in this chapter consists of a three-dimensional slot-ventilated rectangular enclosure (Fig. 6.1) of length L, width W and height H, filled with air-CO_2 mixture for thermosolutal mixed convection flow to represent different airflow paths in buildings. In fact, using two-dimensional modeling in room ventilation problems does not provide a realistic simulation of airflow, as it does not consider same phenomena that determine airflow characteristics, such as air flow separation over building sharp edges. In this model, fresh cold air is penetrating into the enclosure via an inlet port of height $0.2L$ located along left wall and the polluted air is expelling naturally via an outlet port located along the right wall. Two discrete heat sources of length $0.2L$ with higher temperature are considered to be located along the right vertical wall, whereas two discrete contaminant sources of width $0.25L$ having higher concentration are considered along the bottom face (shown in Fig. 6.1). The other walls are maintained as insulated and adiabatic. The modelled prototype represents two configurations (BT and TB) with respect to the position of inlet and outlet port: in BT configuration, inlet port is placed at the bottom section of left vertical face and outlet is placed at the top section of opposite vertical face (Fig. 6.1 (a)); while for TB configuration, inlet port is located along the top section of left vertical face and outlet is along the bottom section of opposite vertical face (Fig. 6.1 (b)).

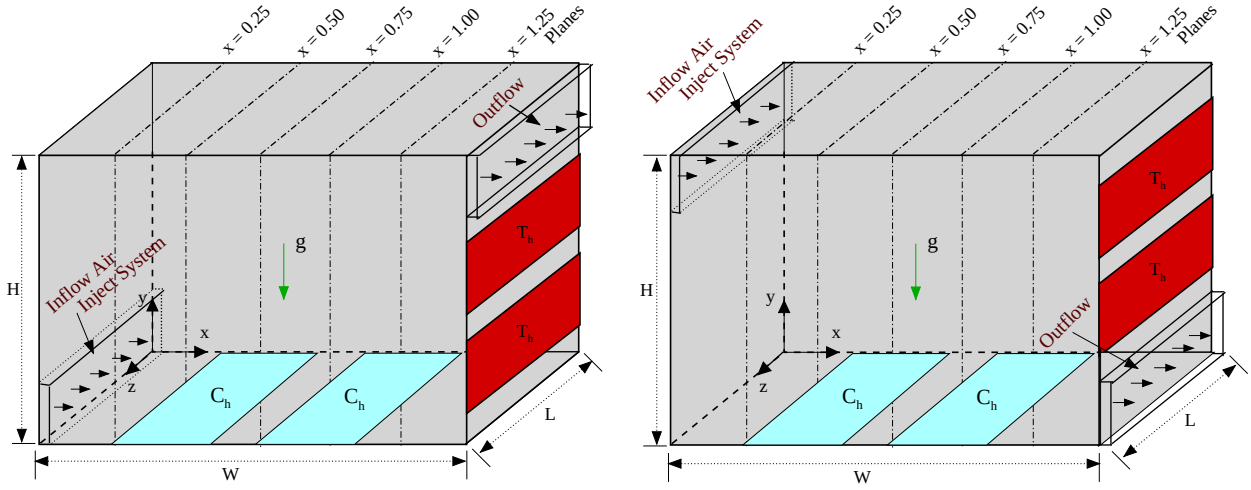

(a) BT (b) TB

Figure 6.1: Schematic diagram of the fluid flow configuration.

The three-dimensional governing equations for fluid, heat and mass flow inside the slot-ventilated enclosure include the equation of continuity (conservation of mass), Navier-Stokes equations (conservation of momentum), energy equation (conservation of energy) and concentration equation (conservation of species) which are based on the pre-assumptions that the fluid is Newtonian, viscous and incompressible. Thermal radiation inside the system is assumed to be negligible and the thermosolutal properties except density are considered to be independent of temperature and concentration. Therefore, Boussinesqs approximation is used for density variation due to temperature and concentration as:

$$\rho = \rho_0[1 - \beta_T(T^* - T_0) - \beta_C(C^* - C_0)], \tag{6.1}$$

where $\beta_T = -\frac{1}{\rho}\frac{\partial \rho}{\partial T^*}$ is the volumetric coefficient of thermal expansion and $\beta_C = -\frac{1}{\rho}\frac{\partial \rho}{\partial C^*}$ is the solutal expansion coefficient. The value of β_T is always greater than zero, since the density decreases with increasing temperature, whereas the value of β_c has random nature [39].

To process these calculations, an appropriate mathematical model has to be applied for the solution domain. Most of the airflow problems in buildings consider the airflow to be laminar and the characteristics have been specified using the intensity and length scale options. The governing equations are:

$$\frac{\partial u}{\partial x} + \frac{\partial v}{\partial y} + \frac{\partial w}{\partial z} = 0, \tag{6.2}$$

$$\frac{\partial u}{\partial t} + u\frac{\partial u}{\partial x} + v\frac{\partial u}{\partial y} + w\frac{\partial u}{\partial z} = -\frac{\partial p}{\partial x} + \frac{1}{Re}\left(\frac{\partial^2 u}{\partial x^2} + \frac{\partial^2 u}{\partial y^2} + \frac{\partial^2 u}{\partial z^2}\right), \tag{6.3}$$

$$\frac{\partial v}{\partial t} + u\frac{\partial v}{\partial x} + v\frac{\partial v}{\partial y} + w\frac{\partial v}{\partial z} = -\frac{\partial p}{\partial y} + \frac{1}{Re}\left(\frac{\partial^2 v}{\partial x^2} + \frac{\partial^2 v}{\partial y^2} + \frac{\partial^2 v}{\partial z^2}\right) + \frac{Gr}{Re^2}(T + Br.C), \tag{6.4}$$

$$\frac{\partial w}{\partial t} + u\frac{\partial w}{\partial x} + v\frac{\partial w}{\partial y} + w\frac{\partial w}{\partial z} = -\frac{\partial p}{\partial z} + \frac{1}{Re}\left(\frac{\partial^2 w}{\partial x^2} + \frac{\partial^2 w}{\partial y^2} + \frac{\partial^2 w}{\partial z^2}\right), \tag{6.5}$$

$$\frac{\partial T}{\partial t} + u\frac{\partial T}{\partial x} + v\frac{\partial T}{\partial y} + w\frac{\partial T}{\partial z} = \frac{1}{Re.Pr}\left(\frac{\partial^2 T}{\partial x^2} + \frac{\partial^2 T}{\partial y^2} + \frac{\partial^2 T}{\partial z^2}\right), \tag{6.6}$$

$$\frac{\partial C}{\partial t} + u\frac{\partial C}{\partial x} + v\frac{\partial C}{\partial y} + w\frac{\partial C}{\partial z} = \frac{1}{Re.Sc}\left(\frac{\partial^2 C}{\partial x^2} + \frac{\partial^2 C}{\partial y^2} + \frac{\partial^2 C}{\partial z^2}\right). \tag{6.7}$$

The characteristic length and reference inlet velocity are considered as L and u_i, respectively. The dimensionless variables x, y, z, u, v, w, p, T and C are obtained as:

$$(x,\ y,\ z) = \frac{(x^*, y^*, z^*)}{L};\ \ (u,\ v,\ w) = \frac{(u^*, v^*, w^*)}{u_i};\ \ p = \frac{p^*}{\rho u_i^2};\ \ T = \frac{(T^* - T_o)}{(T_h - T_o)};\ \ C = \frac{(C^* - C_o)}{(C_h - C_o)}. \tag{6.8}$$

The non-dimensional parameters namely, buoyancy ratio, Grashof number, Reynolds number, Richardson number, Prandtl number and Schmidt number in above flow governing equations are defined as:

$$Br = \frac{\beta_C(C_h - C_0)}{\beta_T(T_h - T_0)};\ \ Gr = \frac{g\beta_T(T_h - T_0)L^3}{\nu^2};\ \ Re = \frac{u_i L}{\nu};\ \ Ri = \frac{Gr}{Re^2};\ \ Pr = \frac{\nu}{\alpha};\ \ Sc = \frac{\nu}{D}. \tag{6.9}$$

Initially, the fluid is assumed to be stationary with uniform temperature T_0 and concentration C_0, therefore the initial conditions for time $t = 0$ in computational domain are given as follows:

$$u = 0,\ v = 0,\ w = 0,\ T = 0,\ C = 0. \tag{6.10}$$

The boundary conditions associated with the problem geometry at $t > 0$ are defined as: along the inlet port:

$$u = 1, \quad v = 0, \quad w = 0, \quad T = -0.5 \quad C = 0; \tag{6.11}$$

outlet port:

$$\frac{\partial u}{\partial x} = 0, \quad \frac{\partial v}{\partial x} = 0, \quad \frac{\partial w}{\partial x} = 0, \quad \frac{\partial T}{\partial x} = 0; \quad \frac{\partial C}{\partial x} = 0; \tag{6.12}$$

solid walls:

$$\begin{aligned} u = 0, \quad v = 0, \quad w = 0, \quad T = 1 \text{ (for heat source) and } \frac{\partial T}{\partial n} = 0 \text{ (elsewhere)}, \\ C = 1 \text{ (for contaminant source) and } \frac{\partial C}{\partial n} = 0 \text{ (elsewhere)}. \end{aligned} \tag{6.13}$$

The average rate of heat transfer along the right wall is obtained in the form of an average Nusselt number as:

$$Nu_{avg} = -\frac{1}{h_2 - h_1}\int_0^1 \int_{h_1}^{h_2} \left[\frac{\partial T}{\partial x}\right]_{x=1.5} dydz, \tag{6.14}$$

and the average rate of mass transfer along the bottom wall is obtained in the form of an average Sherwood number as:

$$Sh_{avg} = -\frac{1}{w_2 - w_1}\int_0^1 \int_{w_1}^{w_2} \left[\frac{\partial C}{\partial y}\right]_{y=0} dxdz. \tag{6.15}$$

The fluid flow is always accompanied by entropy generation due to irreversibilities. The main factors for irreversible flow in the mixed convection system are fluid friction, heat transfer and mass transfer. Based on the local thermodynamic equilibrium condition of the linear transport theory, the entropy generation in dimensional form can be expressed as [16, 40, 5, 2]:

$$\begin{aligned} S^*_{gen} = {} & \frac{k}{T_0^2}\left[\left(\frac{\partial T^*}{\partial x^*}\right)^2 + \left(\frac{\partial T^*}{\partial y^*}\right)^2 + \left(\frac{\partial T^*}{\partial z^*}\right)^2\right] + \frac{\mu}{T_0}\left[2\left\{\left(\frac{\partial u^*}{\partial x^*}\right)^2 + \left(\frac{\partial v^*}{\partial y^*}\right)^2 + \left(\frac{\partial w^*}{\partial z^*}\right)^2\right\}\right. \\ & \left. + \left(\frac{\partial v^*}{\partial x^*} + \frac{\partial u^*}{\partial y^*}\right)^2 + \left(\frac{\partial w^*}{\partial y^*} + \frac{\partial v^*}{\partial z^*}\right)^2 + \left(\frac{\partial u^*}{\partial z^*} + \frac{\partial w^*}{\partial x^*}\right)^2\right] \\ & + \frac{RD}{C_0}\left[\left(\frac{\partial C^*}{\partial x^*}\right)^2 + \left(\frac{\partial C^*}{\partial y^*}\right)^2 + \left(\frac{\partial C^*}{\partial z^*}\right)^2\right] \\ & + \frac{RD}{T_0}\left[\left(\frac{\partial T^*}{\partial x^*}\right)\left(\frac{\partial C^*}{\partial x^*}\right) + \left(\frac{\partial T^*}{\partial y^*}\right)\left(\frac{\partial C^*}{\partial y^*}\right) + \left(\frac{\partial T^*}{\partial z^*}\right)\left(\frac{\partial C^*}{\partial z^*}\right)\right]. \end{aligned} \tag{6.16}$$

The right hand side of the above equation represents: first term is the dimensional entropy generation due to thermal diffusion (S^*_T), second term is the dimensional entropy generation due to fluid friction (S^*_ψ), third term is the dimensional entropy generation due to species diffusion (S^*_C) and the last term is the dimensional entropy generation due to coupling between thermal and species diffusion ($S^*_{T,C}$). Using the non-dimensional parameters, the entropy generation in dimensionless form can be expressed as:

$$\begin{aligned} S_{gen} = {} & \left[\left(\frac{\partial T}{\partial x}\right)^2 + \left(\frac{\partial T}{\partial y}\right)^2 + \left(\frac{\partial T}{\partial z}\right)^2\right] + \phi_1\left[2\left\{\left(\frac{\partial u}{\partial x}\right)^2 + \left(\frac{\partial v}{\partial y}\right)^2 + \left(\frac{\partial w}{\partial z}\right)^2\right\}\right. \\ & \left. + \left(\frac{\partial v}{\partial x} + \frac{\partial u}{\partial y}\right)^2 + \left(\frac{\partial w}{\partial y} + \frac{\partial v}{\partial z}\right)^2 + \left(\frac{\partial u}{\partial z} + \frac{\partial w}{\partial x}\right)^2\right] \\ & + \phi_2\left[\left(\frac{\partial C}{\partial x}\right)^2 + \left(\frac{\partial C}{\partial y}\right)^2 + \left(\frac{\partial C}{\partial z}\right)^2\right] \\ & + \phi_3\left[\left(\frac{\partial T}{\partial x}\right)\left(\frac{\partial C}{\partial x}\right) + \left(\frac{\partial T}{\partial y}\right)\left(\frac{\partial C}{\partial y}\right) + \left(\frac{\partial T}{\partial z}\right)\left(\frac{\partial C}{\partial z}\right)\right], \end{aligned} \tag{6.17}$$

where ϕ_1, ϕ_2 and ϕ_3 are the irreversibility distribution ratios which are given by

$$\phi_1 = \frac{\mu T_0}{k}\left(\frac{u_i}{\Delta T}\right)^2, \quad \phi_2 = \frac{RD}{k}\frac{T_0^2}{C_0}\left(\frac{\Delta C}{\Delta T}\right)^2, \quad \phi_3 = \frac{RDT_0}{k}\left(\frac{\Delta C}{\Delta T}\right)$$

In general, eq. 6.17 can also be written as:

$$S_{gen} = S_T + S_\psi + S_C + S_{T,C}, \tag{6.18}$$

where S_T, S_ψ, S_C and $S_{T,C}$ denote the dimensionless entropy generation due to thermal gradients, viscosity effects, concentration gradients and the combined effect of thermal and concentration gradients, respectively. The average entropy generation can be calculated by using the formula:

$$S_{avg} = \frac{1}{V}\int_V S_{gen} dV. \tag{6.19}$$

The relative dominance of entropy generation due to heat and mass transfer irreversibility to the total irreversibility is given by the Bejan number which is formulated as [40, 2]:

$$Be_{T,C} = \frac{S_T + S_C + S_{T,C}}{S_{gen}}, \tag{6.20}$$

and the average Bejan number inside the enclosure is given by:

$$Be_{avg} = \frac{1}{V}\int_V Be_{T,C}\ dV. \tag{6.21}$$

From the formulation of the Bejan number; the fluid friction irreversibility is dominant for $Be < 0.5$, whereas the heat and mass transfer irreversibility is dominant for $Be > 0.5$ and $Be = 0.5$ implies equal contributions of fluid friction irreversibility and heat and mass transfer irreversibility to the entropy generation.

Performance evaluation criterion (PEC) is calculated in this study to achieve the maximum rate of heat transfer with minimum entropy generation, which is defined as the ratio of the average Nusselt number to the total entropy generation [67] i.e.,

$$PEC = \frac{Nu_{avg}}{S_{avg}}. \tag{6.22}$$

Air change per hour (ACH) [56] is specified by the ventilation rate which is calculated as:

$$ACH = \frac{Q\ 3600}{V}, \tag{6.23}$$

where Q is the volumetric flow rate and V denotes the volume of the enclosure.
The cooling efficiency [42] inside the enclosure is formulated as:

$$\epsilon = 1 - \left(\frac{\overline{T}_{out}}{\overline{T}_{in}}\right), \tag{6.24}$$

where $\overline{T}_{in}$ is the average temperature along the inlet port and $\overline{T}_{out}$ is the average temperature along the outlet port.

6.3 Numerical Procedure and Code validation

The flow governing equations for the conjugate problem are solved using SIMPLE (Semi Implicit Method for Pressure Linked Equations) algorithm [86] using a staggered grid arrangement. In the first step, above mentioned equations are discretized by the integration over control volumes (Fig. 6.2) to obtain a set of algebraic equations. The scalar control volume (Fig. 6.2 (a)) is used for the integration of continuity equation, heat equation and concentration equation, whereas momentum equations are integrated over their respective control volumes. Now, integrating the continuity equation over the $(i,j,k)^{th}$ scalar control volume as shown in Fig. 6.2 (a) at $(n+1)^{th}$ time level, we obtain,

$$(u^{n+1}_{i,j,k} - u^{n+1}_{i-1,j,k})\Delta y\Delta z + (v^{n+1}_{i,j,k} - v^{n+1}_{i,j-1,k})\Delta x\Delta z + (w^{n+1}_{i,j,k} - w^{n+1}_{i,j,k-1})\Delta x\Delta y = 0. \tag{6.25}$$

On integrating the x-momentum equation at $(n+1)^{th}$ time step over the $(i,j,k)^{th}$ control volume for u as shown in Fig. 6.2 (b), we obtain the discretized equation as,

$$a^u_i u^{n+1}_{i-1,j,k} + b^u_i u^{n+1}_{i,j,k} + c^u_i u^{n+1}_{i+1,j,k} = d^u_i - \left(p^{n+1}_{i+1,j,k} - p^{n+1}_{i,j,k}\right)\Delta y\Delta z, \tag{6.26}$$

where

$$a^u_i = -\frac{1}{4}(u^n_{i,j,k} + u^n_{i-1,j,k})\Delta y\Delta z - \frac{1}{Re.\Delta x}\Delta y\Delta z,$$

$$\begin{aligned} b^u_i = \frac{\Delta x\Delta y\Delta z}{\Delta t} + \frac{2}{Re}\left(\frac{\Delta y\Delta z}{\Delta x} + \frac{\Delta x\Delta z}{\Delta y} + \frac{\Delta x\Delta y}{\Delta z}\right) + \frac{1}{4}(u^n_{i+1,j,k} - u^n_{i-1,j,k})\Delta y\Delta z \\ + \frac{1}{4}(v^n_{i,j,k} + v^n_{i+1,j,k} - v^n_{i,j-1,k} - v^n_{i+1,j-1,k})\Delta x\Delta z \\ + \frac{1}{4}(w^n_{i,j,k} + w^n_{i+1,j,k} - w^n_{i,j,k-1} - w^n_{i+1,j,k-1})\Delta x\Delta y, \end{aligned}$$

$$c^u_i = \frac{1}{4}(u^n_{i,j,k} + u^n_{i+1,j,k})\Delta y\Delta z - \frac{1}{Re.\Delta x}\Delta y\Delta z,$$

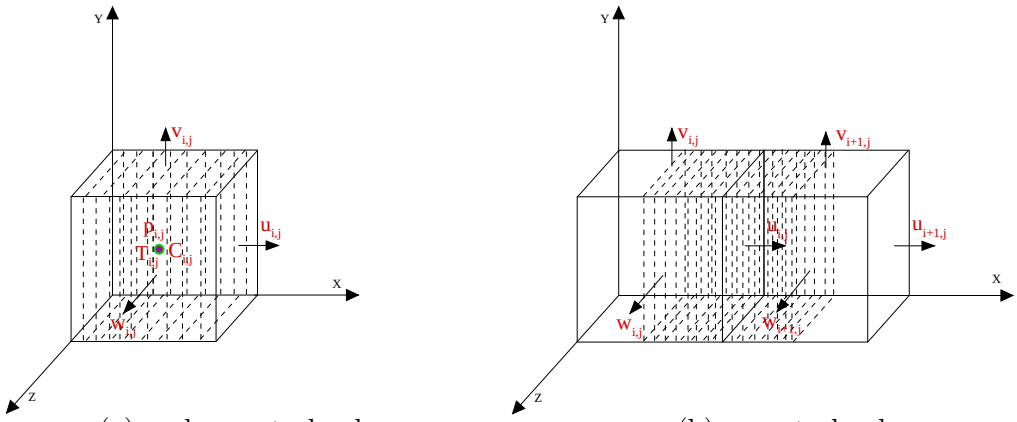

(a) scalar control volume (b) u-control volume,

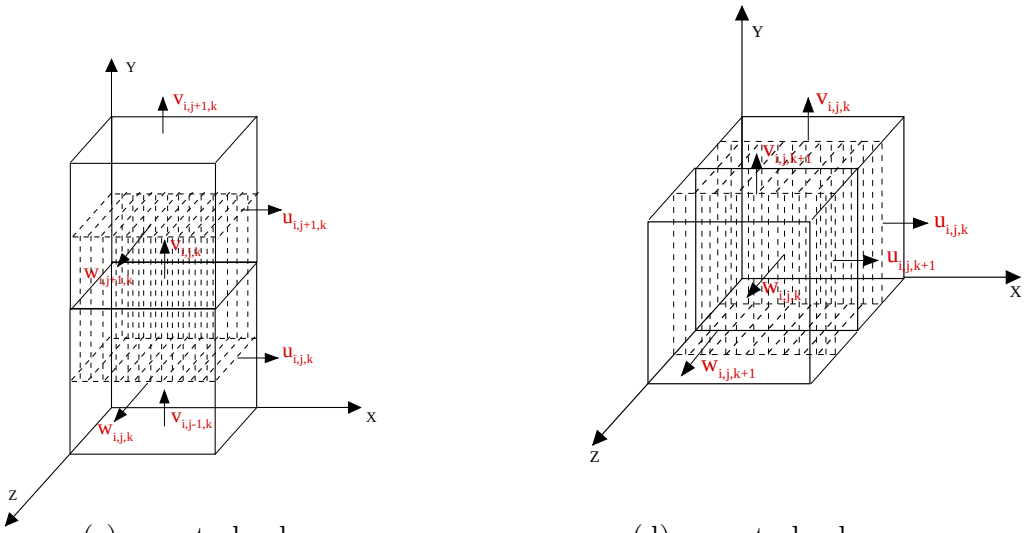

(c) v-control volume (d) w-control volume

Figure 6.2: Three-dimensional control volumes for staggered grid

$$
\begin{aligned}
d_i^u = \frac{\Delta x \Delta y \Delta z}{\Delta t} u_{i,j,k}^n + \frac{\Delta x \Delta z}{Re \Delta y}(u_{i,j-1,k}^{n+1} + u_{i,j+1,k}^{n+1}) + \frac{\Delta x \Delta y}{Re \Delta z}(u_{i,j,k-1}^{n+1} + u_{i,j,k+1}^{n+1}) \\
- \frac{1}{4}\Delta x \Delta z (v_{i,j,k}^n + v_{i+1,j,k}^n) u_{i,j+1,k}^{n+1} + \frac{1}{4}\Delta x \Delta z (v_{i,j-1,k}^n + v_{i+1,j-1,k}^n) u_{i,j-1,k}^{n+1} \\
- \frac{1}{4}\Delta x \Delta y (w_{i,j,k}^n + w_{i+1,j,k}^n) u_{i,j,k+1}^{n+1} + \frac{1}{4}\Delta x \Delta y (w_{i,j,k-1}^n + w_{i+1,j,k-1}^n) u_{i,j,k-1}^{n+1},
\end{aligned}
$$

Similarly, integrating the y-momentum equation at $(n+1)^{th}$ time step over the $(i,j,k)^{th}$ control volume for v as shown in Fig. 6.2 (c), we obtain the discretized equation as,

$$
a_i^v v_{i-1,j,k}^{n+1} + b_i^v v_{i,j,k}^{n+1} + c_i^v v_{i+1,j,k}^{n+1} - (Ri.T_{i,j,k}^{n+1} + Br.C_{i,j,k}^{n+1})\Delta x.\Delta y.\Delta z = d_i^v - \left(p_{i,j+1,k}^{n+1} - p_{i,j,k}^{n+1}\right)\Delta x \Delta z, \tag{6.27}
$$

where

$$a_i^v = -\frac{1}{4}(u_{i-1,j,k}^n + u_{i-1,j+1,k}^n)\Delta y\Delta z - \frac{1}{Re.\Delta x}\Delta y\Delta z,$$

$$\begin{aligned} b_i^v = \frac{\Delta x\Delta y\Delta z}{\Delta t} &+ \frac{2}{Re}(\frac{\Delta y\Delta z}{\Delta x} + \frac{\Delta x\Delta z}{\Delta y} + \frac{\Delta x\Delta y}{\Delta z}) \\ &+ \frac{1}{4}(u_{i,j,k}^n + u_{i,j+1,k}^n - u_{i-1,j,k}^n - u_{i-1,j+1,k}^n)\Delta y\Delta z + \frac{1}{4}(v_{i,j+1,k}^n - v_{i,j-1,k}^n)\Delta x\Delta z \\ &+ \frac{1}{4}(w_{i,j,k}^n + w_{i,j+1,k}^n - w_{i,j,k-1}^n - w_{i,j+1,k-1}^n)\Delta x\Delta y, \end{aligned}$$

$$c_i^v = \frac{1}{4}(u_{i,j,k}^n + u_{i,j+1,k}^n)\Delta y\Delta z - \frac{1}{Re.\Delta x}\Delta y\Delta z,$$

$$\begin{aligned} d_i^v = \frac{\Delta x\Delta y\Delta z}{\Delta t}v_{i,j,k}^n &+ \frac{\Delta x\Delta z}{Re\Delta y}(v_{i,j+1,k}^{n+1} + v_{i,j-1,k}^{n+1}) + \frac{\Delta x\Delta y}{Re\Delta z}(v_{i,j,k+1}^{n+1} + v_{i,j,k-1}^{n+1}) \\ &- \frac{1}{4}\Delta x\Delta z(v_{i,j,k}^n + v_{i,j+1,k}^n)v_{i,j+1,k}^{n+1} + \frac{1}{4}\Delta x\Delta z(v_{i,j,k}^n + v_{i,j-1,k}^n)v_{i,j-1,k}^{n+1} \\ &- \frac{1}{4}\Delta x\Delta y(w_{i,j,k}^n + w_{i,j+1,k}^n)v_{i,j,k+1}^{n+1} + \frac{1}{4}\Delta x\Delta y(w_{i,j,k-1}^n + w_{i,j+1,k-1}^n)v_{i,j,k-1}^{n+1}, \end{aligned}$$

Similarly, integrating the w-momentum equation at $(n+1)^{th}$ time step over the $(i,j,k)^{th}$ control volume for w as shown in Fig. 6.2 (d), we obtain the discretized equation as,

$$a_i^w w_{i-1,j,k}^{n+1} + b_i^w w_{i,j,k}^{n+1} + c_i^w w_{i+1,j,k}^{n+1} = d_i^w - \left(p_{i,j,k+1}^{n+1} - p_{i,j,k}^{n+1}\right)\Delta x\Delta y \tag{6.28}$$

where

$$a_i^w = -\frac{1}{4}(u_{i-1,j,k}^n + u_{i-1,j,k+1}^n)\Delta y\Delta z - \frac{1}{Re.\Delta x}\Delta y\Delta z,$$

$$\begin{aligned} b_i^w = \frac{\Delta x\Delta y\Delta z}{\Delta t} &+ \frac{2}{Re}(\frac{\Delta y\Delta z}{\Delta x} + \frac{\Delta x\Delta z}{\Delta y} + \frac{\Delta x\Delta y}{\Delta z}) \\ &+ \frac{1}{4}(u_{i,j,k}^n + u_{i,j,k+1}^n - u_{i-1,j,k}^n - u_{i-1,j,k+1}^n)\Delta y\Delta z \\ &+ \frac{1}{4}(v_{i,j,k}^n + v_{i,j,k+1}^n - v_{i,j-1,k}^n - v_{i,j-1,k+1}^n)\Delta x\Delta z + \frac{1}{4}(w_{i,j,k+1}^n - w_{i,j,k-1}^n)\Delta x\Delta y, \end{aligned}$$

$$c_i^w = \frac{1}{4}(u_{i,j,k}^n + u_{i,j,k+1}^n)\Delta y\Delta z - \frac{1}{Re.\Delta x}\Delta y\Delta z,$$

$$\begin{aligned} d_i^w = \frac{\Delta x\Delta y\Delta z}{\Delta t}w_{i,j,k}^n &+ \frac{\Delta x\Delta z}{Re\Delta y}(w_{i,j+1,k}^{n+1} + w_{i,j-1,k}^{n+1}) + \frac{\Delta x\Delta y}{Re\Delta z}(w_{i,j,k+1}^{n+1} + w_{i,j,k-1}^{n+1}) \\ &- \frac{1}{4}\Delta x\Delta z(v_{i,j,k}^n + v_{i,j,k+1}^n)w_{i,j+1,k}^{n+1} + \frac{1}{4}\Delta x\Delta z(v_{i,j-1,k}^n + v_{i,j-1,k+1}^n)w_{i,j-1,k}^{n+1} \\ &- \frac{1}{4}\Delta x\Delta y(w_{i,j,k}^n + w_{i,j,k+1}^n)w_{i,j,k+1}^{n+1} + \frac{1}{4}\Delta x\Delta y(w_{i,j,k}^n + w_{i,j,k-1}^n)w_{i,j,k-1}^{n+1}, \end{aligned}$$

Integrating the energy equation and species transport equation at $(n+1)^{th}$ time step over the $(i,j,k)^{th}$ control volume over scalar control volume Fig. 6.2 (a) results in,

$$a_i^T T_{i-1,j,k}^{n+1} + b_i^T T_{i,j,k}^{n+1} + c_i^T T_{i+1,j,k}^{n+1} = d_i^T \tag{6.29}$$

and

$$a_i^C C_{i-1,j,k}^{n+1} + b_i^C C_{i,j,k}^{n+1} + c_i^C C_{i+1,j,k}^{n+1} = d_i^C \tag{6.30}$$

where

$$a_i^T = -\frac{\Delta y \Delta z}{2} u_{i-1,j,k}^n - \frac{\Delta y \Delta z}{Re.Pr.\Delta x},$$

$$b_i^T = \frac{\Delta x \Delta y \Delta z}{\Delta t} + \frac{2}{Re.Pr}\left(\frac{\Delta y \Delta z}{\Delta x} + \frac{\Delta x \Delta z}{\Delta y} + \frac{\Delta x \Delta y}{\Delta z}\right) + \frac{1}{2}(u_{i,j,k}^n - u_{i-1,j,k}^n)\Delta y \Delta z + \frac{1}{2}(v_{i,j,k}^n - v_{i,j-1,k}^n)\Delta x \Delta z + \frac{1}{2}(w_{i,j,k}^n - w_{i,j,k-1}^n)\Delta x \Delta y,$$

$$c_i^T = \frac{\Delta y \Delta z}{2} u_{i,j,k}^n - \frac{\Delta y \Delta z}{Re.Pr.\Delta x},$$

$$d_i^T = \frac{\Delta x \Delta y \Delta z}{\Delta t} T_{i,j,k}^n + \frac{\Delta x \Delta z}{Re.Pr \Delta y}(T_{i,j+1,k}^{n+1} + T_{i,j-1,k}^{n+1}) + \frac{\Delta x \Delta y}{Re.Pr \Delta z}(T_{i,j,k+1}^{n+1} + T_{i,j,k-1}^{n+1}) - \frac{1}{2}\Delta x \Delta z (T_{i,j+1,k}^{n+1} v_{i,j,k}^n - T_{i,j-1,k}^{n+1} v_{i,j-1,k}^n) - \frac{1}{2}\Delta x \Delta y (T_{i,j,k+1}^{n+1} w_{i,j,k}^n - T_{i,j,k-1}^{n+1} w_{i,j,k-1}^n),$$

$$a_i^C = -\frac{\Delta y \Delta z}{2} u_{i-1,j,k}^n - \frac{\Delta y \Delta z}{Re.Sc.\Delta x},$$

$$b_i^C = \frac{\Delta x \Delta y \Delta z}{\Delta t} + \frac{2}{Re.Sc}\left(\frac{\Delta y \Delta z}{\Delta x} + \frac{\Delta x \Delta z}{\Delta y} + \frac{\Delta x \Delta y}{\Delta z}\right) + \frac{1}{2}(u_{i,j,k}^n - u_{i-1,j,k}^n)\Delta y \Delta z + \frac{1}{2}(v_{i,j,k}^n - v_{i,j-1,k}^n)\Delta x \Delta z + \frac{1}{2}(w_{i,j,k}^n - w_{i,j,k-1}^n)\Delta x \Delta y,$$

$$c_i^C = \frac{\Delta y \Delta z}{2} u_{i,j,k}^n - \frac{\Delta y \Delta z}{Re.Sc.\Delta x},$$

and

$$d_i^C = \frac{\Delta x \Delta y \Delta z}{\Delta t} C_{i,j,k}^n + \frac{\Delta x \Delta z}{Re.Sc \Delta y}(C_{i,j+1,k}^{n+1} + C_{i,j-1,k}^{n+1}) + \frac{\Delta x \Delta y}{Re.Sc \Delta z}(C_{i,j,k+1}^{n+1} + C_{i,j,k-1}^{n+1}) - \frac{1}{2}\Delta x \Delta z (C_{i,j+1,k}^{n+1} v_{i,j,k}^n - C_{i,j-1,k}^{n+1} v_{i,j-1,k}^n) - \frac{1}{2}\Delta x \Delta y (C_{i,j,k+1}^{n+1} w_{i,j,k}^n - C_{i,j,k-1}^{n+1} w_{i,j,k-1}^n),$$

The above algebraic equations are solved using the pressure correction based SIMPLE algorithm which includes a cyclic procedure of guessed and corrected operations. Momentum equations are solved to obtain the velocity fields using a guessed pressure field

and then a correction is introduced so that the equation of continuity is satisfied. A pressure link between the continuity and momentum equations is involved in this procedure which is established by the conversion of the continuity equation into a Poisson equation for the pressure. The Poisson equation implements a pressure correction for the divergent velocity field. The velocity field $u^*_{i,j,k}$, $v^*_{i,j,k}$ and $w^*_{i,j,k}$ are obtained from the momentum equations using the guessed pressure field $p^*_{i,j,k}$ (which is equal to the previous time step solution) at any intermediate stage. Hence $u^*_{i,j,k}$, $v^*_{i,j,k}$ and $w^*_{i,j,k}$ satisfies the equations 6.26 to 6.28, therefore,

$$a^u_i u^*_{i-1,j,k} + b^u_i u^*_{i,j,k} + c^u_i u^*_{i+1,j,k} = d^u_i - \big(p^*_{i+1,j,k} - p^*_{i,j,k}\big)\Delta y \Delta z, \tag{6.31}$$

$$a^v_i v^*_{i-1,j,k} + b^v_i v^*_{i,j,k} + c^v_i v^*_{i+1,j,k} - (Ri.T^{n+1}_{i,j,k} + Br.C^{n+1}_{i,j,k})\Delta x.\Delta y.\Delta z = d^v_i - \big(p^*_{i,j+1,k} - p^*_{i,j,k}\big)\Delta x \Delta z, \tag{6.32}$$

$$a^w_i w^*_{i-1,j,k} + b^w_i w^*_{i,j,k} + c^w_i w^*_{i+1,j,k} = d^w_i - \big(p^*_{i,j,k+1} - p^*_{i,j,k}\big)\Delta x \Delta y. \tag{6.33}$$

But this $u^*_{i,j,k}$, $v^*_{i,j,k}$ and $w^*_{i,j,k}$ may not satisfy the continuity equation 6.25. The continuity equation is justified through a pressure correction $p^c_{i,j,k}$ at each cell (i, j, k) as

$$p^{n+1}_{i,j,k} = p^*_{i,j,k} + p^c_{i,j,k}, \tag{6.34}$$

which implies a correction in the velocity field $u^c_{i,j,k}$, $v^c_{i,j,k}$ and $w^c_{i,j,k}$ as

$$u^{n+1}_{i,j,k} = u^*_{i,j,k} + u^c_{i,j,k}, \tag{6.35}$$

$$v^{n+1}_{i,j,k} = v^*_{i,j,k} + v^c_{i,j,k}, \tag{6.36}$$

$$w^{n+1}_{i,j,k} = w^*_{i,j,k} + w^c_{i,j,k}, \tag{6.37}$$

where $u^{n+1}_{i,j,k}$, $v^{n+1}_{i,j,k}$ and $w^{n+1}_{i,j,k}$ are satisfied by the continuity equation. The corrected velocity fields ($u^{n+1}_{i,j,k},\ v^{n+1}_{i,j,k},\ w^{n+1}_{i,j,k}$) can be obtained from the momentum equations as,

$$u^{n+1}_{i,j,k} = u^*_{i,j,k} + \alpha_u \bigg[- \frac{\Delta t}{\Delta x}(p^c_{i+1,j,k} - p^c_{i,j,k}) \bigg], \tag{6.38}$$

$$v^{n+1}_{i,j,k} = v^*_{i,j,k} + \alpha_v \bigg[- \frac{\Delta t}{\Delta y}(p^c_{i,j+1,k} - p^c_{i,j,k}) \bigg], \tag{6.39}$$

$$w^{n+1}_{i,j,k} = w^*_{i,j,k} + \alpha_w \bigg[- \frac{\Delta t}{\Delta z}(p^c_{i,j,k+1} - p^c_{i,j,k}) \bigg]. \tag{6.40}$$

$\alpha_u,\ \alpha_v$ and α_w are considered as relaxation parameters and convergence is achieved for a relaxation parameter of $\frac{2}{3}$. With the substitution of the corrected velocity fields $(u^{n+1}_{i,j,k},\ v^{n+1}_{i,j,k},\ w^{n+1}_{i,j,k})$ in the discretized continuity equation, the Poisson equation reduces to,

$$
\begin{aligned}
2\left(\alpha_u\frac{\Delta t\Delta y\Delta z}{\Delta x}+\alpha_v\frac{\Delta t\Delta x\Delta z}{\Delta y}+\alpha_w\frac{\Delta t\Delta x\Delta y}{\Delta z}\right)p^c_{i,j,k}&\\
=-\Big[(u^*_{i,j,k}-u^*_{i-1,j,k})\Delta y\Delta z+(v^*_{i,j,k}-v^*_{i,j-1,k})\Delta x\Delta z+(w^*_{i,j,k}-w^*_{i,j,k-1})\Delta x\Delta y\Big]&\\
+\alpha_u(p^c_{i-1,j,k}+p^c_{i+1,j,k})\frac{\Delta t\Delta y\Delta z}{\Delta x}+\alpha_v(p^c_{i,j-1,k}+p^c_{i,j+1,k})\frac{\Delta t\Delta x\Delta z}{\Delta y}&\\
+\alpha_w(p^c_{i,j,k-1}+p^c_{i,j,k+1})\frac{\Delta t\Delta x\Delta y}{\Delta z}.&
\end{aligned}
\tag{6.41}
$$

The numerical solution is considered to be converged when the maximum change to the flow variables are,

$$|\varphi^{k+1}_{i,j,k}-\varphi^{k}_{i,j,k}|\le 10^{-6}, \tag{6.42}$$

here $\varphi=(u,\ v,\ w,\ T,\ C)$ are the flow variables, k is the iteration number and (i,j,k) denotes the computational grid point.

The code is validated by solving three-dimensional mixed convection flow in a rectangular enclosure for the results of average Nusselt number with the published results of Moraga and Lopez [75] by computing the same geometry. Both of these studies considered the mixed convection flow in three-dimensional rectangular ventilated enclosures with an inlet opening along the top section of left vertical wall and the outlet opening along the bottom section of opposite vertical wall. The left vertical wall was maintained at a higher temperature, whereas the right vertical wall was maintained at low temperature and the other four walls were adiabatic. The comparison of the average Nusselt number (Nu_{avg}) along the hot wall for various values of the Richardson number at $Re = 80$ and 300 are presented in Fig. 6.3 (a). An excellent coordination of our results with the results of Moraga and Lopez [75] is observed within 2% maximum difference. A grid independency test is also performed in Fig. 6.3 (b) by considering different grid sizes $110\times70\times70$, $130\times85\times85$, $150\times100\times100$, $170\times115\times115$ and $190\times130\times130$. The grid size $150\times100\times100$ is found to be optimal, since changes in the solution are occurring just at the fourth decimal place.

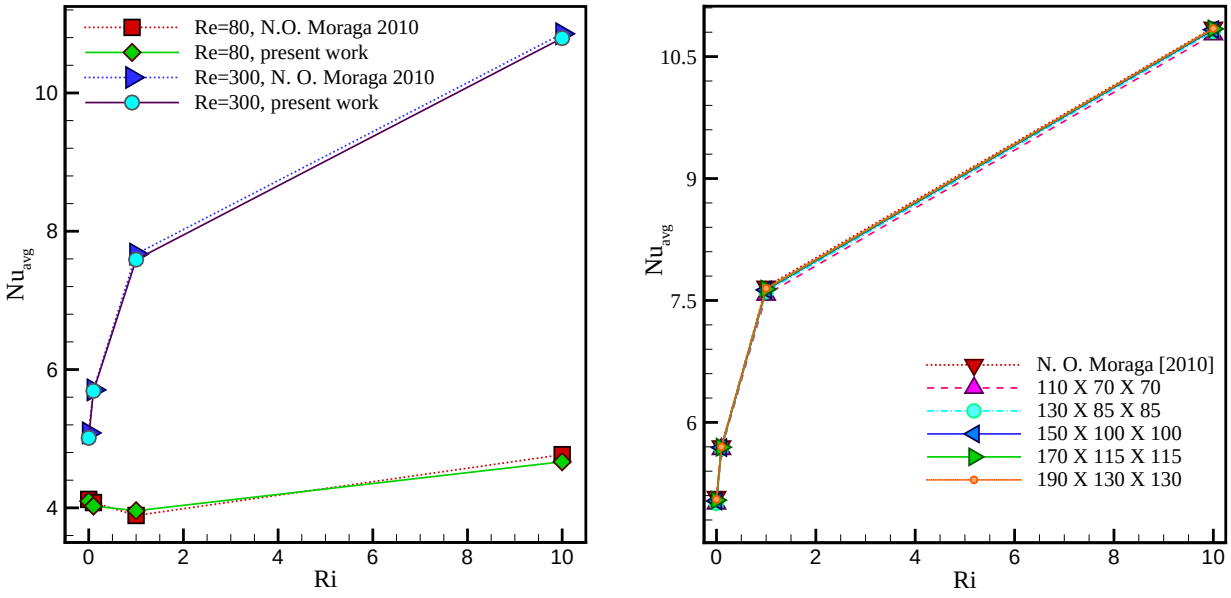

(a) (b)

Figure 6.3: (a) Comparison of 3D average Nusselt number along the hot wall with the results of Nelson O. Moraga and Sergio E. Lopez [75] and (b) grid independency test at $Re = 300$ with $Br = 1.0$.

6.4 Results

Computations are carried out to study the conjugated effects of thermal and solutal parameters on three-dimensional double diffusive mixed convection inside a slot-ventilated enclosure with discrete heat and contaminant sources. The flow of fluid, heat and concentration are visualized by streamlines, isotherms and isoconcentrations for two different configurations based on the location of inlet and outlet port. Air is assumed as working fluid inside the enclosure, therefore, Pr is taken to be 0.71 and carbon dioxide is diffusing into the air which results $Sc = 1.14$ [41]. The results are presented for a wide range of flow governing parameters: Reynolds number as $Re = 100,\ 300$ and 500, Richardson number and buoyancy ratio are ranging as $0.0 \leq Ri \leq 10.0$ and $-10.0 \leq Br \leq 10.0$. The Richardson number measures the importance of buoyancy-driven natural convection relative to the forced convection. The buoyancy force ratio, Br, is zero for pure thermal regime, positive for the assisting flow and negative for the opposing flow. The impact of Reynolds number, Richardson number and buoyancy ratio on average Nusselt number and

Sherwood number, bulk average temperature, entropy generation, Bejan number, cooling efficiency, air change per hour and performance evaluation criterion inside the system are evaluated for both the configurations.

6.4.1 Dynamic Field

Fig. 6.4 displays the streamlines in the xy-plane at $z = 0.5$ for different values of the Reynolds number corresponding to a low Richardson number ($Ri = 0.1$). For the BT-configuration, the cold fluid is flowing from inlet to outlet port through the bottom-right region of the enclosure for $Re = 100$. But with increasing Reynolds number ($Re = 300$), a clockwise circulation zone of the fluid is observed in the bottom-right corner of the enclosure which is increasing in size for $Re = 500$ (first column of Fig. 6.4). For the TB-configuration, the streamlines formed due to inlet cold fluid are moving diagonally towards the outlet port corresponding to $Re = 100$ due to the smaller forced convection effect, while these streamlines are shifted towards the upper section for the case of higher Reynolds number (300 and 500) due to the increased inlet velocity of the fluid. A downstream circulation zone is observed in the bottom-left region which is getting bigger in size with increasing Re due to the density difference, whereas the upstream eddy in the upper-right corner is shrinking with the increasing Reynolds number due to forced convection effects.

For higher Richardson number ($Ri = 5.0$), the streamlines in the xy-plane at $z = 0.5$ are represented in Fig. 6.5 corresponding to different values of the Reynolds number. For the BT-configuration, the cold fluid that enters from inlet port is moving towards the outlet port through the lower-right section of the enclosure, that is adjacent to the bottom wall and right vertical wall, since the density of the cold fluid is larger compared to the hot fluid. An upstream circulation zone is formed in the upper region of the enclosure when $Re = 100$ and this circulation zone is splitting into multiple vortices with increasing Reynolds number due to density variations. In case of the TB-configuration, the region adjacent to left wall and the bottom wall is observed to be fully occupied with the cold fluid, whereas an upstream circulation zone adjacent to the upper wall is formed in the middle-right region of the enclosure for $Re = 100$. For higher Reynolds number, two tiny downstream vortices are also found near the inlet port and bottom-left corner due to the

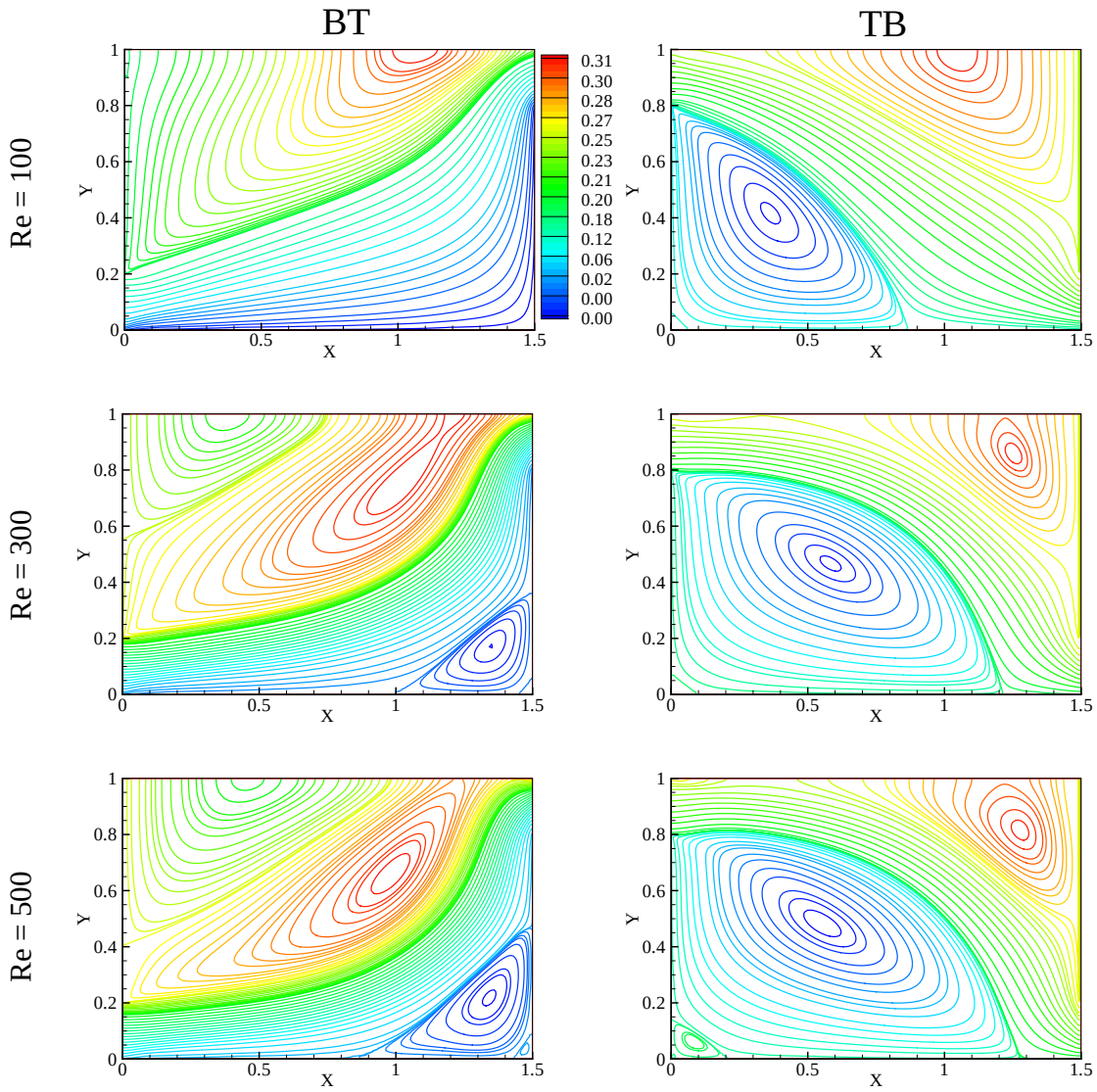

Figure 6.4: Streamlines in the xy-plane at $z = 0.5$ for different Reynolds numbers with fixed $Br(= 1.0)$ and $Ri = 0.1$.

forced convection dominated flow.

6.4.2 Thermal Field

To show the three dimensionality of the flow, three-dimensional isotherms are presented in Fig. 6.6 for different values of the Reynolds number at $Ri = 5.0$ and $Br = 1.0$ for both configurations (BT and TB). For the BT-configuration at $Re = 100$, the cold air is moving in the lower region of the enclosure very smoothly and fluid with higher temperature is moving towards the upper-right region. With increasing Reynolds number, the cold air enters sharply inside the enclosure and forces the hot air to move towards the outlet port.

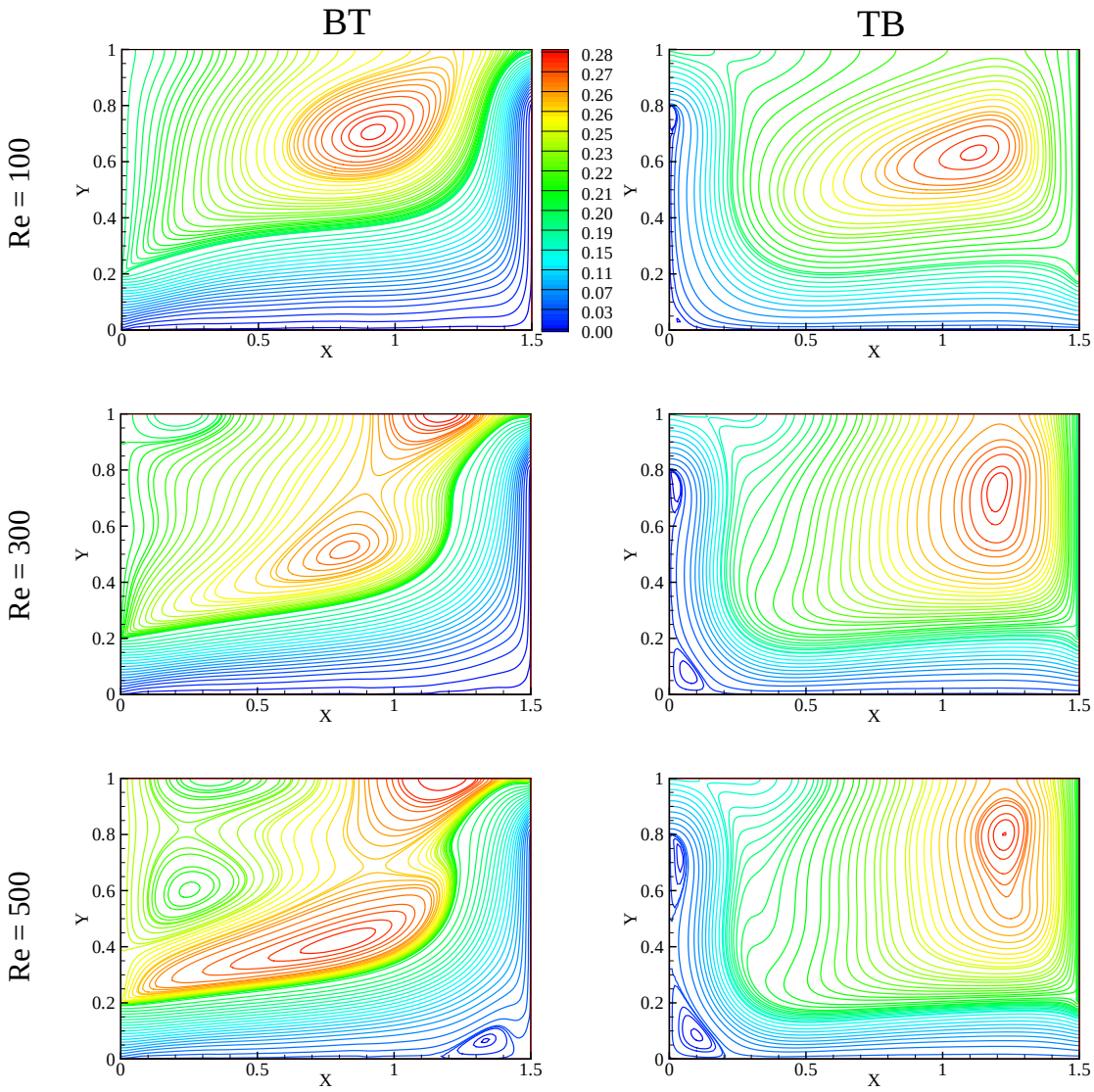

Figure 6.5: Streamlines in the xy-plane at $z = 0.5$ for different Reynolds numbers with fixed $Br = 1.0$ and $Ri = 5.0$.

The enclosure is colder in case of a higher Reynolds number value (500) due to forced convection dominated flow. When the outlet is shifted from the upper section to the bottom section of the right vertical wall (TB-configuration), the hot air is gathered in the upper-right corner of the enclosure due to its low density. Whereas, the cold fluid from the inlet port is diffusing towards the bottom section of the enclosure through the left region.

Two dimensional isotherms in the xy-plane at $z = 0.5$ are shown in Fig. 6.7 for a low Richardson number ($Ri = 0.1$) for different values of the Reynolds number. For BT-configuration with $Re = 100$, the bottom-left and the middle region of the enclosure

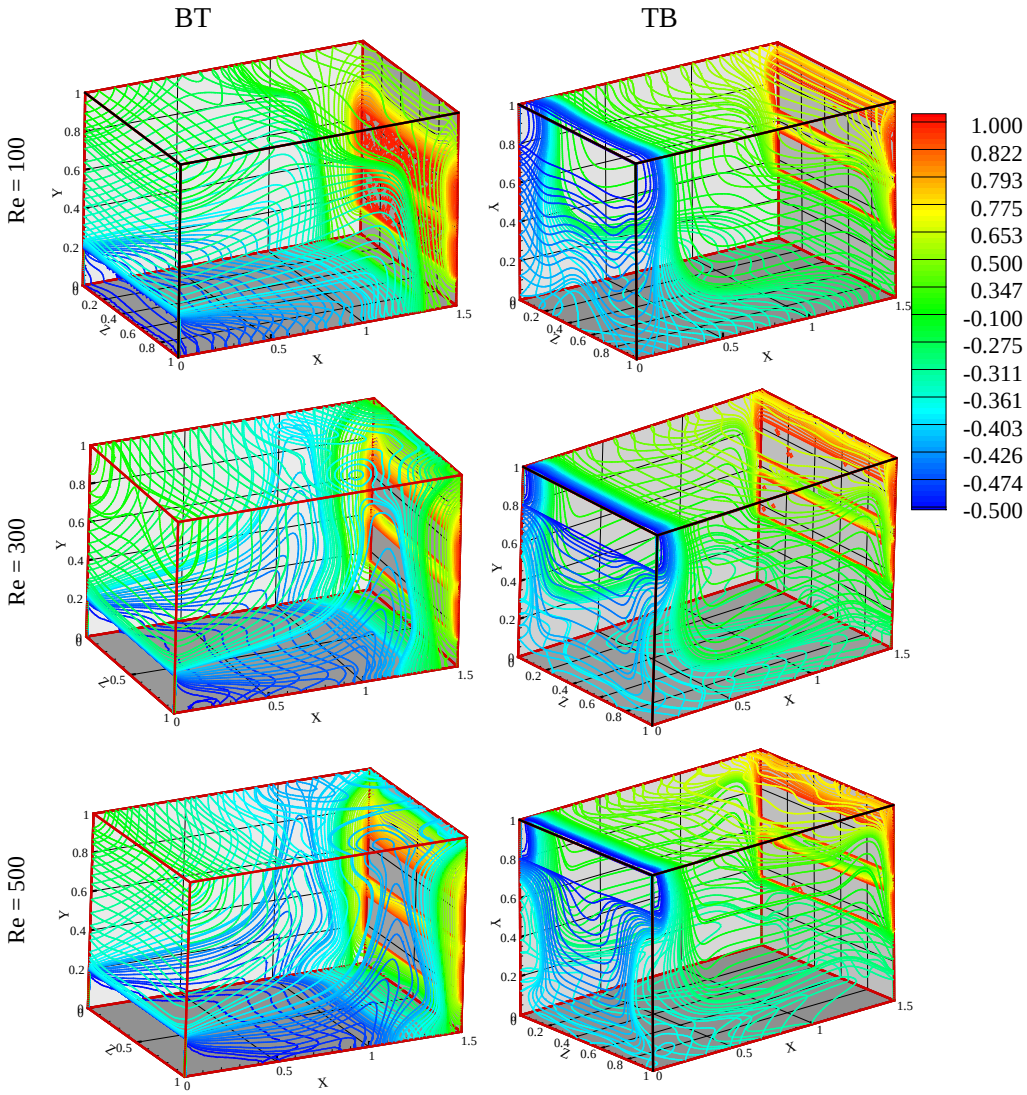

Figure 6.6: Three dimensional isotherms profiles for different Reynolds numbers at $Ri = 5.0$ for both the cases.

are occupied by cold fluid, while a thick thermal layer of higher temperature is observed around the heat source near to the right vertical wall due to density differences. The perseverance of cold fluid in the bottom region of the enclosure is increasing with an increase in Reynolds number, due to which the isotherms having higher values are moving from the heating source towards the bottom-right corner due to forced convection effects. In case of the TB-configuration, heated fluid from the heat source are moving towards the upper-right corner due to the lower density of the hot fluid for Reynolds numbers. The cold fluid that enters through the upper section of the left vertical wall is moving diagonally

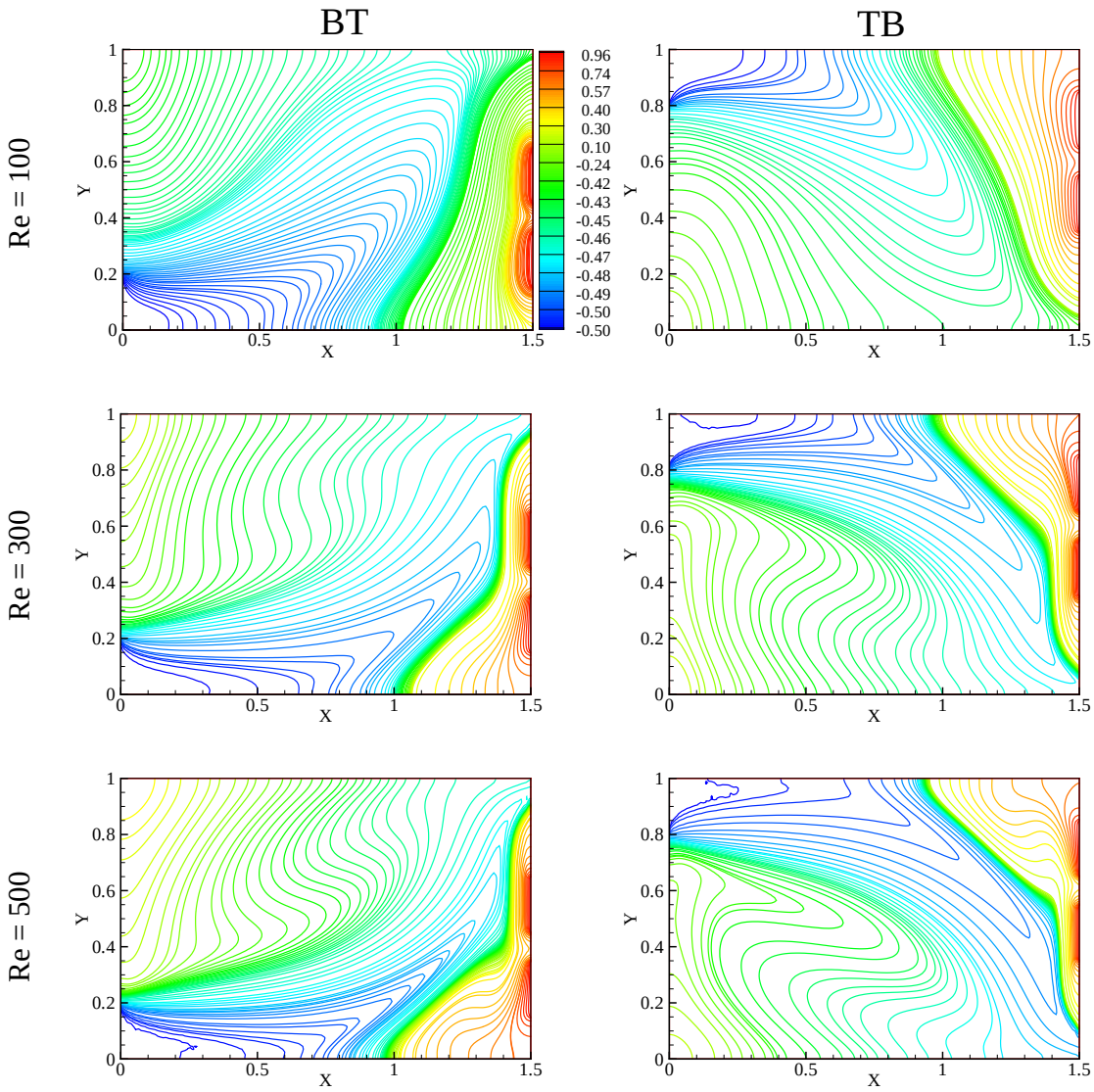

Figure 6.7: Isotherms in a xy-plane at $z = 0.5$ for different Reynolds number with fixed $Ri = 0.1$.

towards the lower region due to convection effects. In case of a higher Richardson number ($Ri = 5.0$), heat transfer along the xy-plane at $z = 0.5$ is found to be dominated by natural convection (Fig. 6.8). Bottom region of the enclosure becomes colder in the BT-configuration due to the inlet air, whereas a thick layer of heated air is found along the right vertical wall near the heat source due to forced convection dominated flow. For the TB-configuration, horizontal isotherms are observed in the middle section of the enclosure, whereas cold air from the inlet port is moving vertically in the downward direction parallel to the left wall which is gathered in the bottom section due to higher density of the cold air. Fluid having higher temperature from the heat source is moving upwards and is

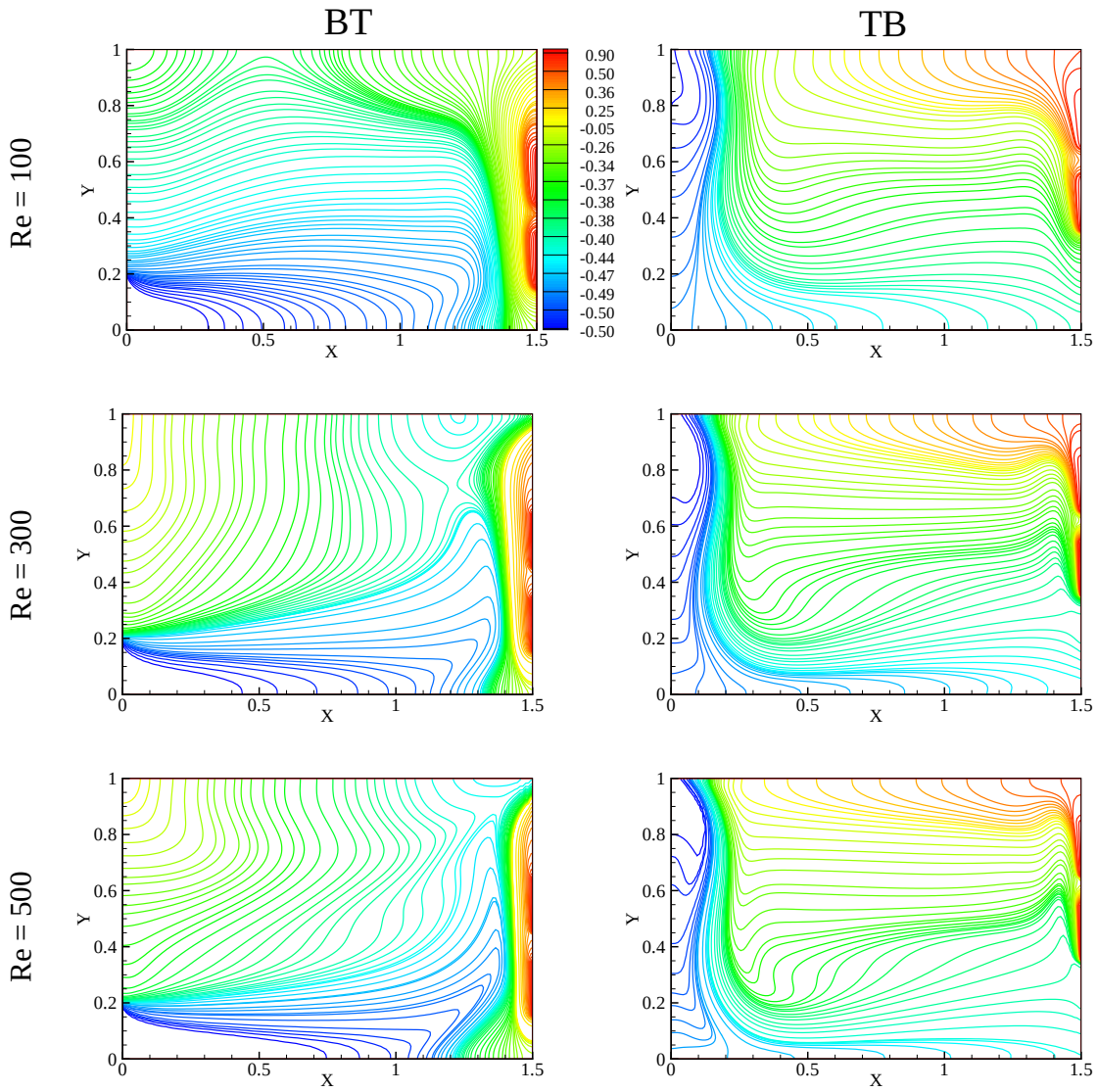

Figure 6.8: Isotherms in the xy-plane at $z = 0.5$ for different Reynolds number and fixed $Ri = 5.0$.

accumulated in the upper-right region adjacent to upper wall. With increasing value of Reynolds number, the thermal boundary layer along the heat source is getting thinner due to forced convection dominated flow and higher heat transfer is found at higher Reynolds number.

Isotherms in the xz-plane for different values of y ($= 0.2,\ 0.5,\ 0.8$) are represented in Fig. 6.9 for fixed values of $Ri = 5.0$, $Br = 1.0$ and $Re = 300$. In BT-configuration, the xz-plane at $y = 0.2$ is occupied by cold fluid except a thin layer adjacent to the heat source. Multiple vortices are also formed in this section due to forced convection dominated flow. These vortices vanish with the increasing values of y due to the weaker

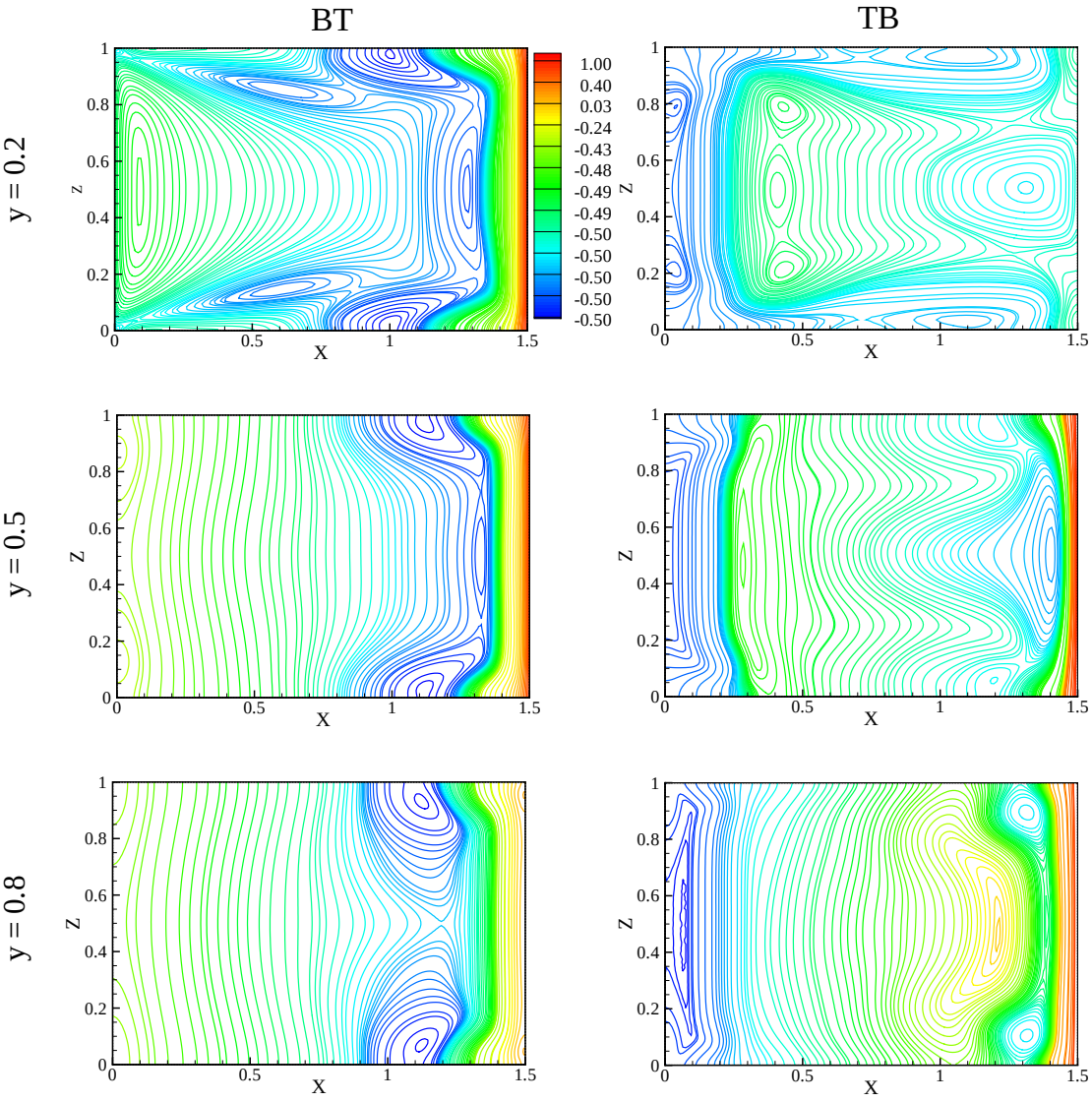

Figure 6.9: Isotherms in the xz-plane at different values of y for fixed $Ri = 5.0$, $Br = 1.0$ and $Re = 300$.

effect of inlet air. At the mid-plane ($y = 0.5$), the right section is observed to be colder than the left section due to forced convection effects, while at $y = 0.8$, the thermal layer of heated air is exiting through the outlet port. In case of the TB-configuration, the xz-plane at $y = 0.2$ is colder due to a higher density of the inlet air, which is flowing in downward direction towards the lower section of the enclosure, whereas the right section of xz-plane at $y = 0.8$ is at a higher temperature due to the upward flow of hot air from the heat source.

6.4.3 Concentration Field

Fig. 6.10 represents the isoconcentration profiles in three-dimension for different values of the Reynolds number with fixed $Ri = 1.0$ and $Br = 1.0$ for both configurations. For $Re = 100$, the left region is occupied by fresh air, whereas the contaminated air is moving towards the lower-right section of the enclosure in the BT-configuration. On the other hand for the TB-configuration, fresh air is moving in the upper-right region and the contaminated air is turning towards left section from the bottom wall due to forced convection effect. With the increase in Reynolds number, fluid is flowing under the dominance of forced convection effect and therefore, a thick solutal layer is forming near the contaminant source. In case of higher Reynolds number (500) for the BT-configuration, fresh air is forcing the contaminated air to move upwards and ovate shaped isoconcentration lines of higher concentration are forming around the second contaminant source due to density difference. The core fluid is well mixed at these higher values of the Reynolds number. When the inlet port is shifted from the bottom section to the upper section of left vertical wall (TB-configuration), the contaminated air is moving towards the left section and is gathered near the left vertical wall of the enclosure due to the convection effects. Whereas, fresh air from the inlet port is diffusing towards the upper-right section of the enclosure, indicates that three dimensionality is observed at higher values of Re due to its end wall effects.

Two dimensional isoconcentration lines in the xy-plane at $z = 0.5$ are represented in Fig. 6.11 for a low Richardson number ($Ri = 0.1$) for different values of Reynolds number with fixed buoyancy ratio $Br = 1.0$. For the BT-configuration at $Re = 100$, fresh air is observed to be diffusing in the upper-left section, whereas the contaminated air is slightly moving towards the right section from the contaminant source due to an intensification of the inertial effect. While for the TB-configuration, the fresh air is moving in the upper-right region, and the contaminated air is diffusing into the bottom section near the contaminated source due to weak convection effects. For higher values of the Reynolds number ($Re = 300$ and 500), the circulation of the air zones spread more so that the inlet air is contracted in the upper-right region and squeezes the contaminated air near the bottom wall due to higher velocity of the inlet air. In case of the BT-configuration, thick

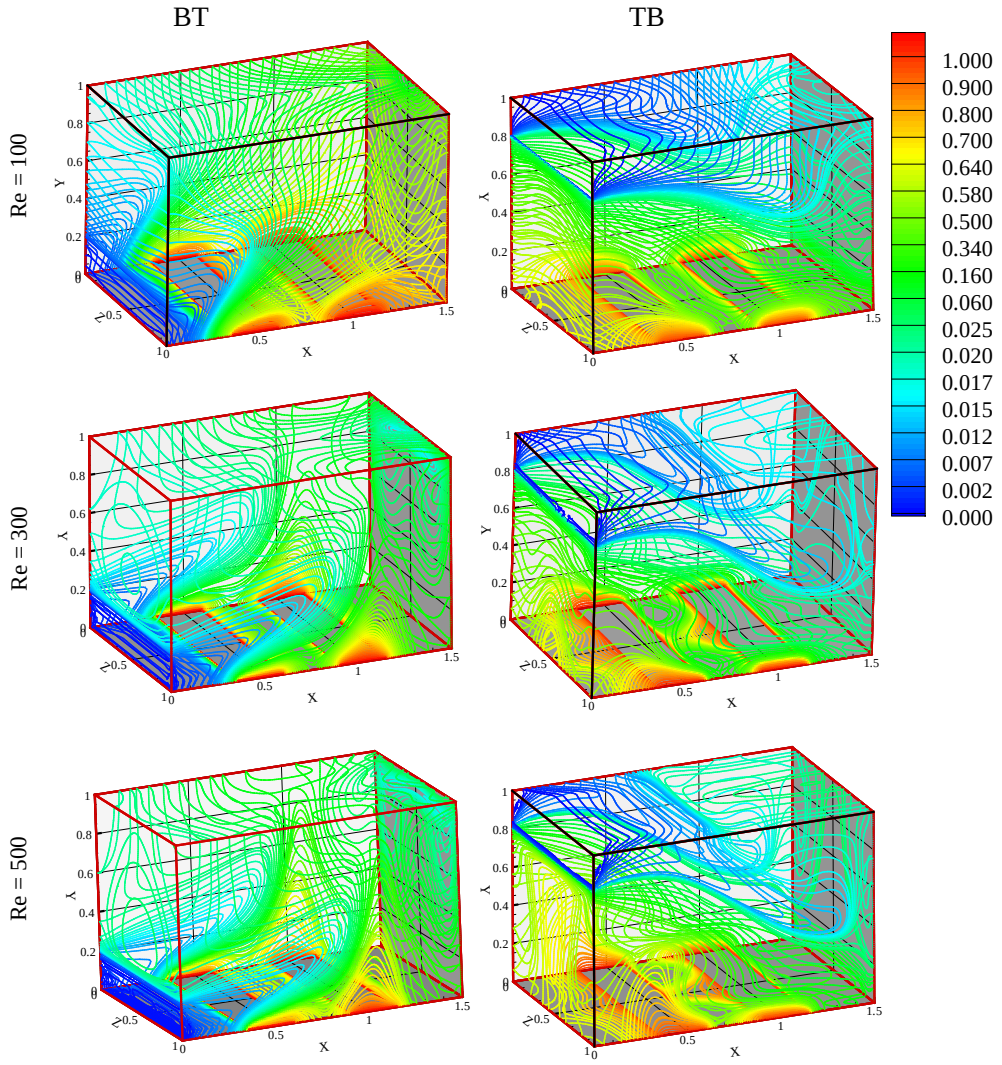

Figure 6.10: Three dimensional isoconcentration profiles for different values of Reynolds number at $Ri = 1.0$ and $Br = 1.0$.

solutal layers having higher concentration are observed around the contaminant sources, since the bottom region is dominated by forced convection due to higher velocity of the inlet air. Whereas, for TB-configuration, the solutal lines from contaminant sources are moving towards the bottom-left corner because of forced convection. For higher Richardson number ($Ri = 5.0$), the solutal distribution in a xy-plane at $z = 0.5$ is shown in Fig. 6.12 for $Br = 1.0$. In case of BT-configuration, the induced air flows faster towards the middle section of the enclosure because the diffused solute can not propagate to the top layers of fluid. A thick solutal layer of contaminated air is found along the contaminant source which is getting thinner with the increase in Reynolds number. For

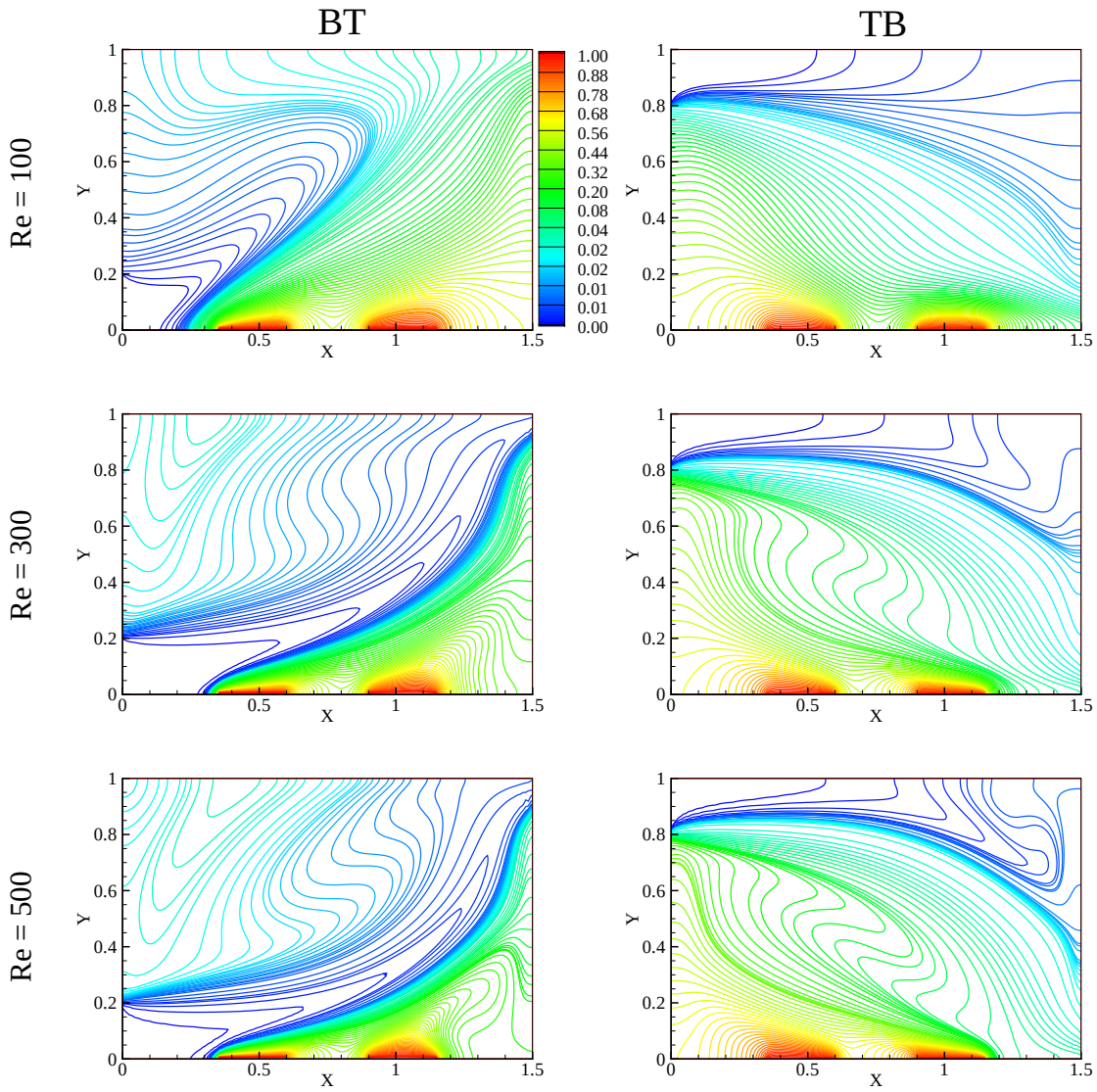

Figure 6.11: Isoconcentrations in a xy-plane at $z = 0.5$ for different Reynolds number with fixed $Ri = 1.0$.

the TB-configuration, fresh air from the inlet port is moving vertically in downward direction parallel to the left wall due to density effects, while the solutal lines having higher concentration from the contaminated source are moving towards the outlet port, which causes an enhancement of the buoyancy force and flow intensity. With increasing Reynolds number, the solutal boundary layer is getting thinner and the flow pattern changes remarkably in comparison with $Re = 100$. In this case the induced flow has a higher energy which causes the formation of recirculation cells.

Isoconcentrations in a xz-plane at different values of y $(= 0.2,\ 0.5,\ 0.8)$ are represented in Fig. 6.13 for fixed values of $Ri = 1.0$, $Br = 1.0$ and $Re = 300$. In the

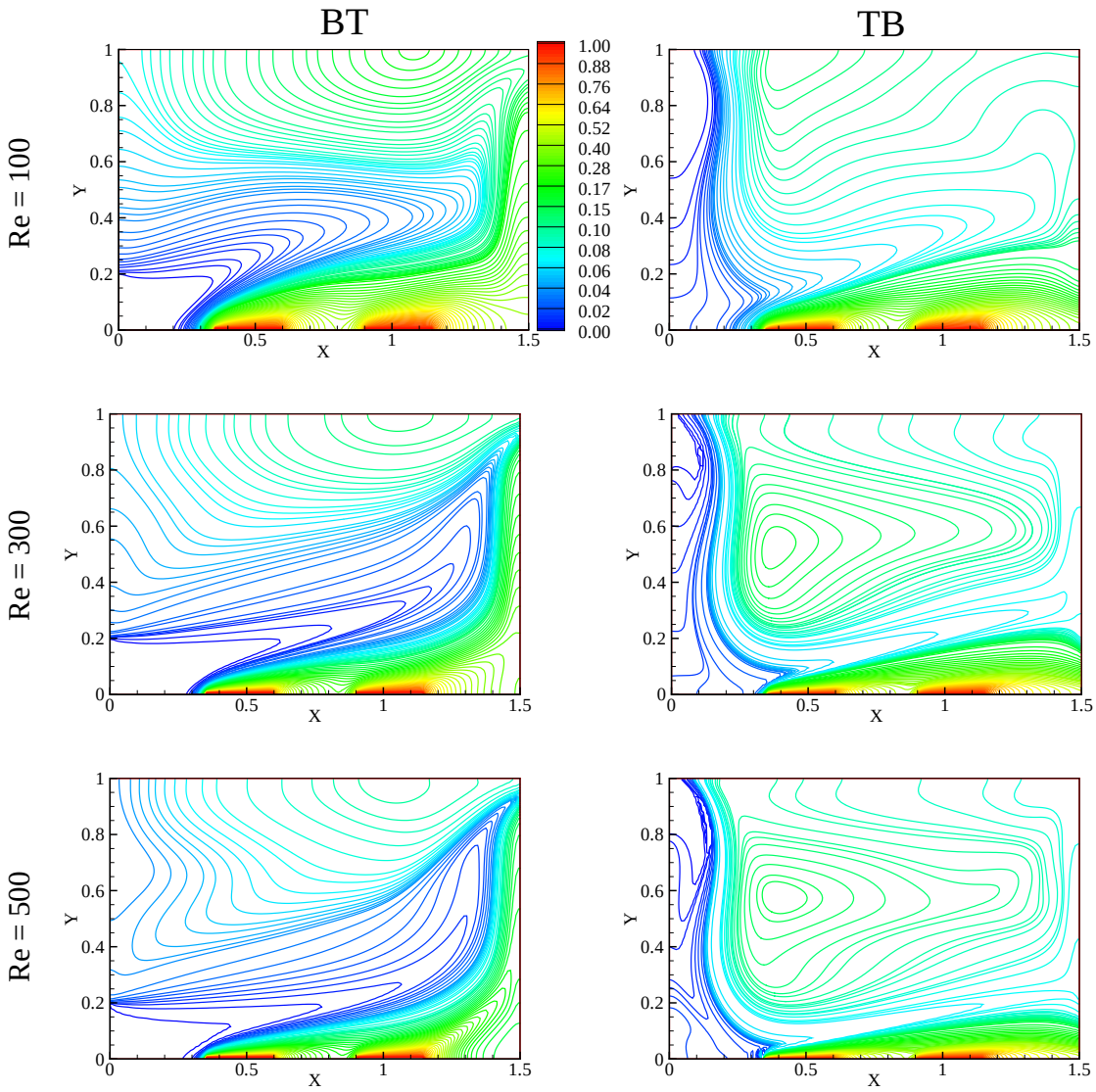

Figure 6.12: Isoconcentrations in xy-plane at $z = 0.5$ for different Reynolds number with fixed $Ri = 5.0$.

BT-configuration, the left section of xz-plane at $y = 0.2$ is occupied by fresh air, while the right section is occupied by the contaminated air. Multiple circulation zones are also formed in this plane due to mixed convection effects, and these vortices are disappearing with increasing values of y due to weaker effect of the inlet air. At $y = 0.5$ and $y = 0.8$, the induced flow spreads over the xz-plane and solutal layer of contaminated air is exiting through the outlet port. By moving from $y = 0.2$ to $y = 0.8$, the central circulating zones spread more and disappears gradually. In case of TB-configuration, the left region of xz-plane at $y = 0.2$ is contaminating due to forced flow of the inlet air, whereas the right section is less contaminated due to the presence of fresh air. Fresh air is existing along

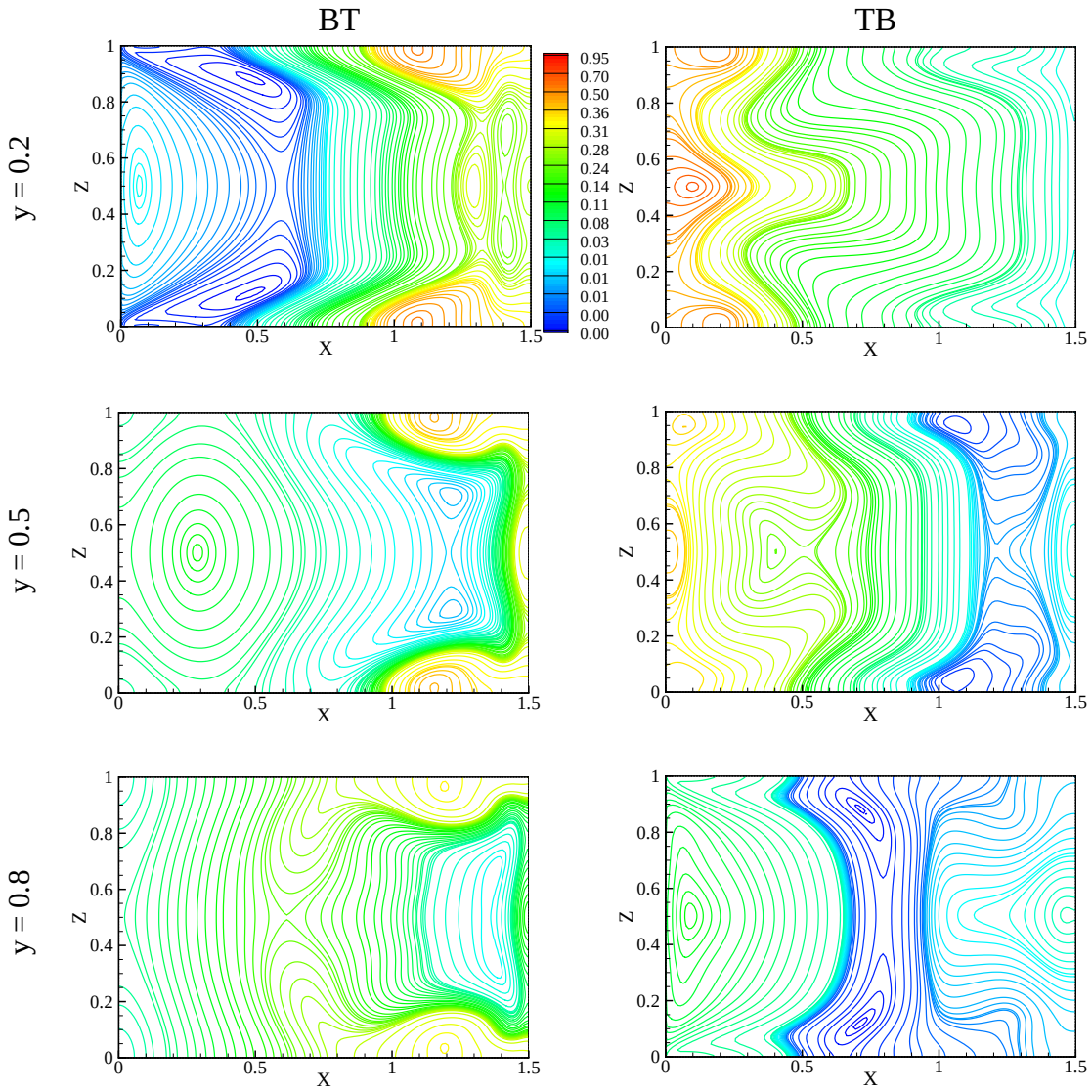

Figure 6.13: Isoconcentrations in the xz-planes for different values of y at fixed $Ri = 1.0$, $Br = 1.0$ and $Re = 300$.

the right section of xz-plane at $y = 0.5$ and the middle section of xz-plane at $y = 0.8$ due to the diagonal flow of fresh air from the inlet port. Enhancement in the buoyancy force and flow intensity is the reason of faster removal of contaminants in the upper section.

6.4.4 Three dimensional Effects

The three-dimensionality of the flow is shown in Fig. 6.14 and Fig. 6.15 by the distribution of the transverse velocity (w) in different xy-planes for $Re = 500$, $Ri = 1.0$ and $Br = 1.0$. Figure 6.14 presents the w-velocity profiles at $z = 0.25$, $z = 0.5$ and $z = 0.75$ for the BT-configuration. It is observed that the w-velocity is very low in the symmetry

plane, $z = 0.5$, for both configurations. With a variation of the z-coordinate, a distinguishable variation in w is observed due to end wall effects. Figures 6.14 and 6.15 show the prominent effect of transverse flow close to the end walls.

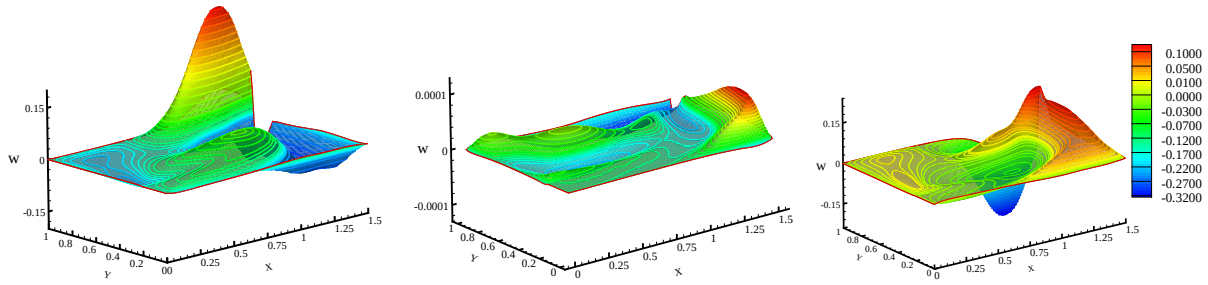

(a) (b) (c)

Figure 6.14: w-velocity profiles on a xy-plane for different z cross-sections, (a) $z = 0.25$, (b) $z = 0.5$ and $z = 0.75$, for $Ri = 1.0$, $Re = 500$ and $Br = 1.0$ for the BT-configuration.

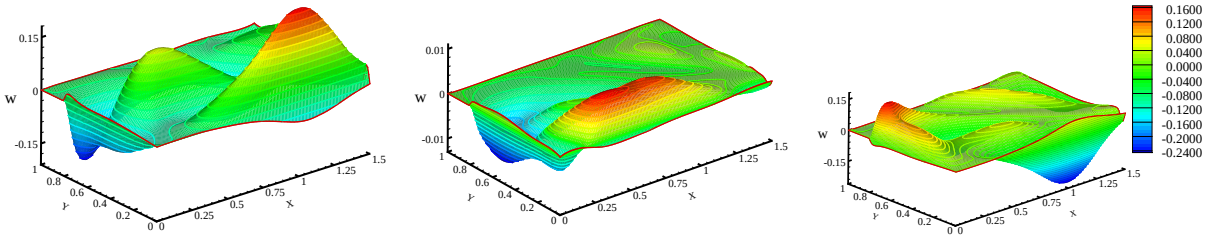

(a) (b) (c)

Figure 6.15: w-velocity profiles on a xy-plane for different z cross-sections, (a) $z = 0.25$, (b) $z = 0.5$ and $z = 0.75$, for $Ri = 1.0$, $Re = 500$ and $Br = 1.0$ for the TB-configuration.

6.4.5 Average Nusselt number, Entropy Generation, Performance evaluation Criterion and Bejan number

Average rate of heat transfer along the right wall is calculated for different flow governing parameters and a comparison is presented in Fig. 6.16 to show the effect of Reynolds number, Richardson number and buoyancy ratio on Nu_{avg}. Fig. 6.16 (a) shows that the average rate of heat transfer is increasing with the increasing value of Reynolds number for both the configurations due to dominating forced convection flow. In case of the BT-configuration, the value of average Nusselt number is found to be increasing with the increasing Richardson number from 0.0 to 10.0 and a maximum value is obtained at $Ri = 10.0$ for $Re = 500$, because the flow is dominated by mixed convection. Whereas

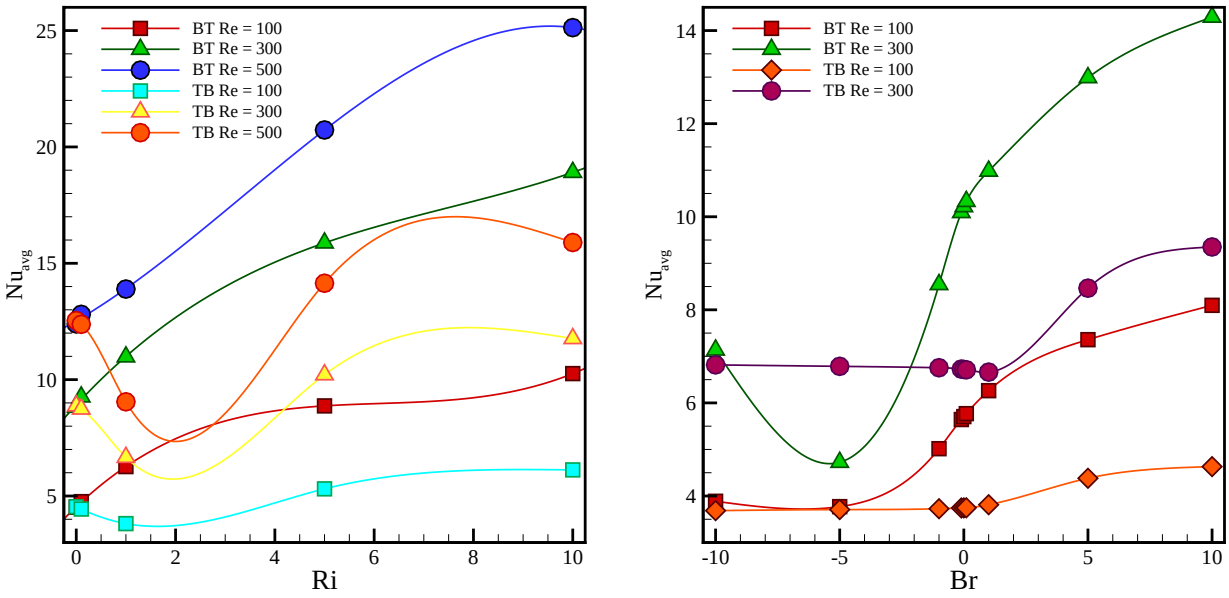

(a) (b)

Figure 6.16: Comparison of average Nusselt number along right vertical wall due to the variation of (a) Richardson number with fixed $Br = 1.0$ and (b) buoyancy ratio with fixed $Ri = 1.0$ for different Reynolds numbers for both the cases.

for the TB-configuration, the value of Nu_{avg} is decreasing when Ri is increasing from 0.0 to 1.0, and Nu_{avg} is increasing with further increase in Ri from 1.0 to 10.0. The vent location including the two combinations has a significant effect on the heat transfer rate although a higher percentage of heat loss is obtained from the component port to the air caused by the large mass flow rate. Fig. 6.16 (b) shows the effect of buoyancy ratio on Nu_{avg} for fixed $Ri = 1.0$. In case of the BT-configuration, the rate of average heat transfer is found to be increasing when Br is increasing from -5.0 to 10.0 for $Re = 100$ and 300. It is observed that there exist an infinitesimal change in the heat transfer rate when Br varies from -10.0 to 1.0 in case of the TB-configuration, whereas, the value of Nu_{avg} is increasing with the increase of Br from 1.0 to 10.0. Higher rate of heat transfer is obtained in case of higher Reynolds number corresponding to $Br = 10.0$. This predicts the influence of vent locations on the heat loss frictions.

A comparison of average entropy generation with the variation of flow governing parameters are presented in Fig. 6.17. Minimum entropy generation is obtained in case

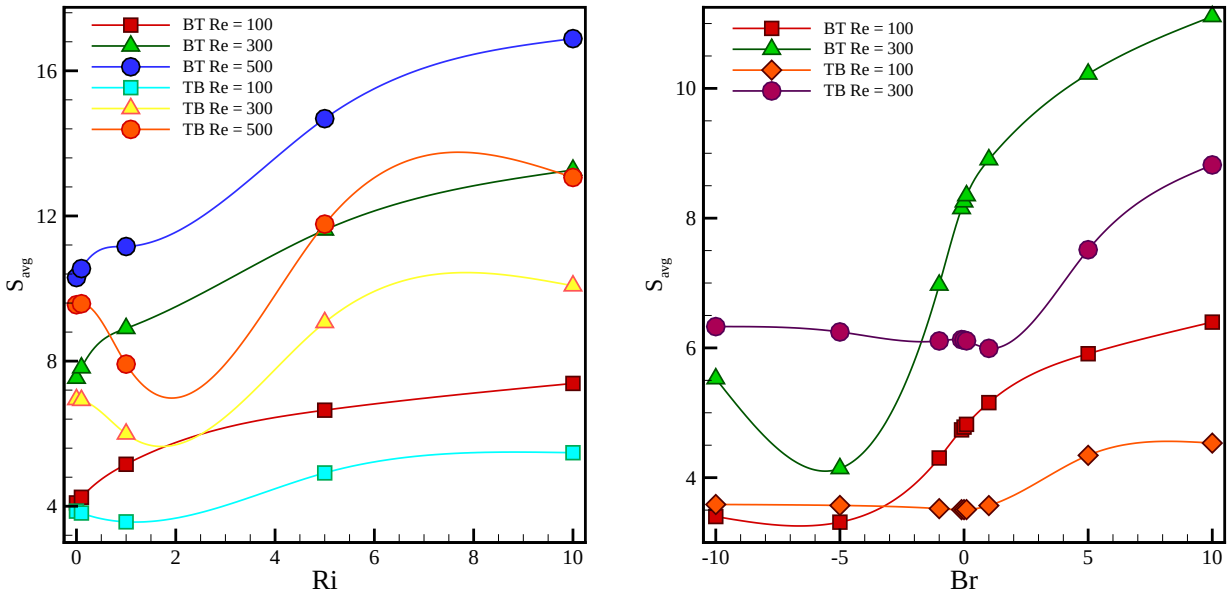

(a) (b)

Figure 6.17: Comparison of average Entropy generation due to the variation of (a) Richardson number with fixed $Br = 1.0$ and (b) buoyancy ratio with fixed $Ri = 1.0$ at different Reynolds number for both the cases.

of low Reynolds number ($Re = 100$) due to the convection effects. The energy loss is higher in case of higher Richardson number ($Ri \geq 5.0$) corresponding to higher Reynolds number ($Re \geq 300$) due to the larger gradients in the boundary layer adjacent to the heated wall. From Fig. 6.17 (b), it can be seen that the average entropy generation is minimum for BT-configuration when $Br < -1.0$, whereas average entropy generation is minimum for TB-configuration for $Br \geq -1.0$ corresponding to $Re = 100$. In order to obtain the best combination of flow governing parameters for a maximum heat transfer with minimum entropy generation, a comparison is made for performance evaluation criteria with the variation in Richardson number for different values of the Reynolds number with $Br = 1.0$ in Fig. 6.18 (a). It shows that for $Ri < 1.0$, a higher value of PEC is obtained for the TB-configuration corresponding to $Re \geq 300$. It is evident that in case of higher Richardson number ($Ri > 1.0$), a higher value of PEC is obtained for the BT-configuration corresponding to $Re \geq 300$. Maximum heat transfer rate with minimum entropy generation is achieved for BT-configuration at $Ri = 10.0$ and $Re = 500$.

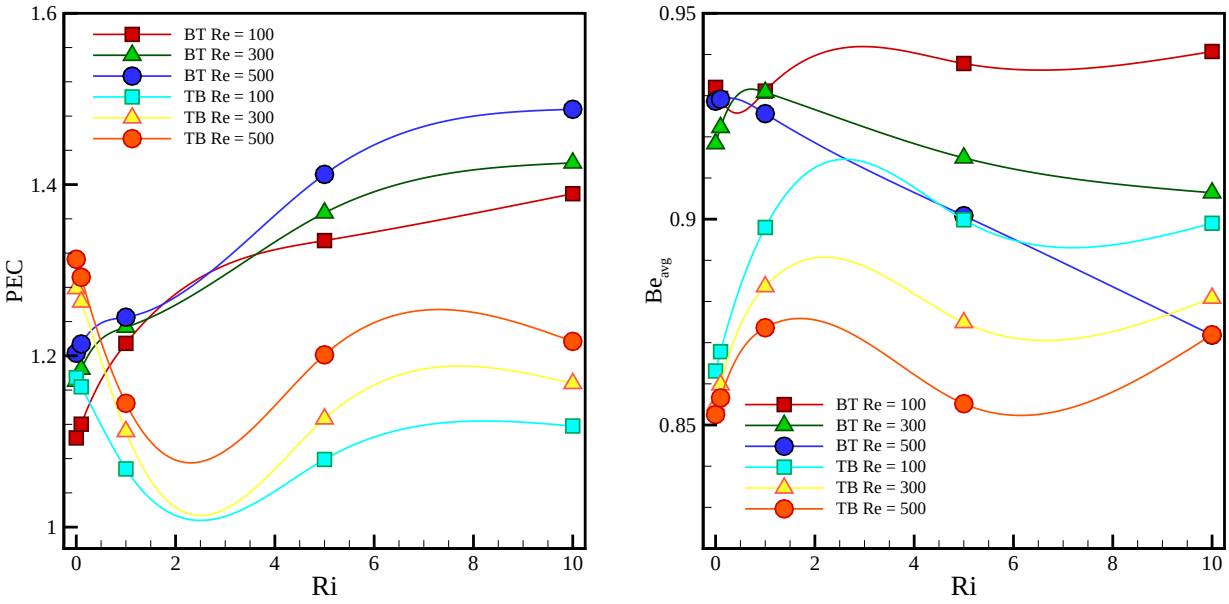

(a) (b)

Figure 6.18: Effect of Richardson number on (a) performance evaluation criterion and (b) average Bejan number at different Reynolds number with fixed $Br = 1.0$ for both the cases.

The effect of Richardson number on average Bejan number is shown in Fig. 6.18 (b) for different values of Reynolds number. Be_{avg} is found to be larger than 0.85 for all cases, which reflects the dominance of the heat transfer irreversibility over the fluid friction irreversibility. Be_{avg} is maximum for low Reynolds number which makes clear that the fluid friction irreversibility is minimum for $Re = 100$ due to the weak convection effects.

6.4.6 Average Sherwood number, air change per Hour, cooling Efficiency and average temperature

Fig. 6.19 shows the variation in average Sherwood number for different values of Reynolds number, Richardson number and buoyancy ratios. It is found that the value of Sh_{avg} is increasing with the increase in Richardson number as well as Reynolds number due to convection effects. For lower Reynolds and Richardson numbers, the internal flow contributes much to the convection, which is less influenced by the mass flow induced by weaker buoyancy. A higher mass transfer rate is obtained for $Re = 500$ due to the

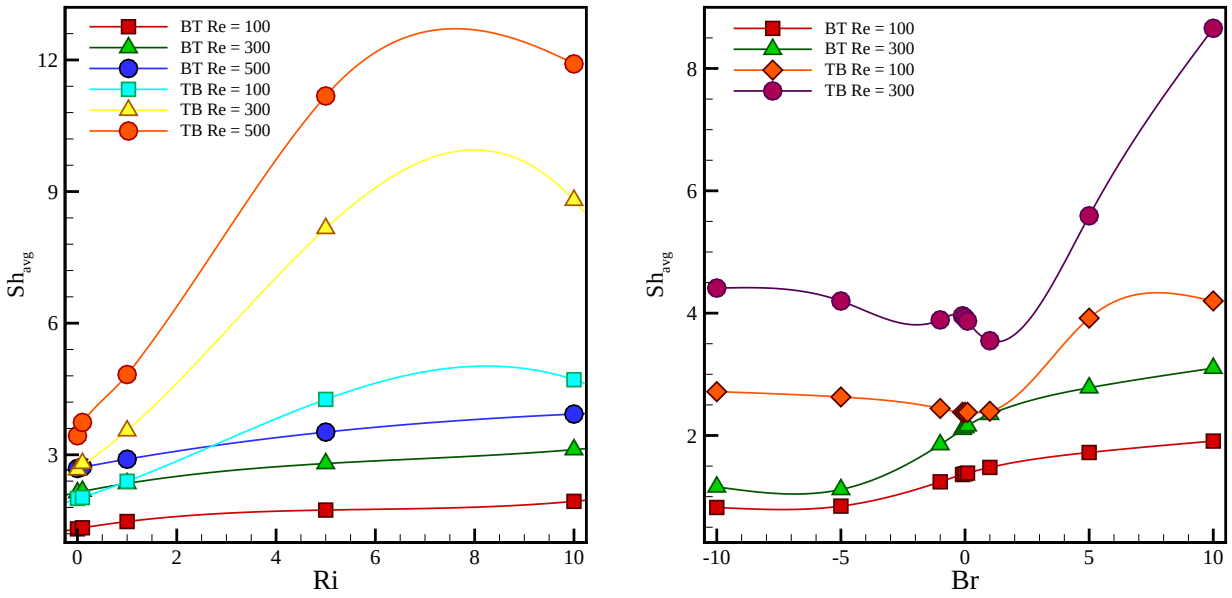

(a) (b)

Figure 6.19: Comparison of average Sherwood number along the bottom wall due to the variation of (a) Richardson number with fixed $Br = 1.0$ and (b) buoyancy ratio with fixed $Ri = 1.0$ at different Reynolds number for both cases.

increased velocity of infiltrated inlet air. For fixed values of Reynolds number, Richardson number and buoyancy ratio, the average value of mass transfer rate is always higher in case of TB-configuration compared to the BT-configuration because of the distance between contaminant source and the outlet port. Also, the maximum value of Sh_{avg} is achieved for $Ri = 10.0$ and $Re = 500$ in the TB-configuration because contaminated air moves quickly towards the outlet port due to forced convection dominated flow inside the enclosure. The average convective coefficients of species approximate a correlation between the soluted surface with the appropriate inflow specified on the openings. Fig. 6.19 (b) shows that mass transfer rate is slightly decreasing for the TB-configuration when buoyancy ratio varies from -10.0 to -1.0, while Sh_{avg} is increasing significantly when Br is increasing from 1.0 to 10.0. Maximum value of Sh_{avg} is achieved for the TB-configuration corresponding to $Br = 10.0$.

Average temperature inside the enclosure is calculated and presented in Fig. 6.20 for different values of Reynolds number, Richardson number and buoyancy ratio. It is

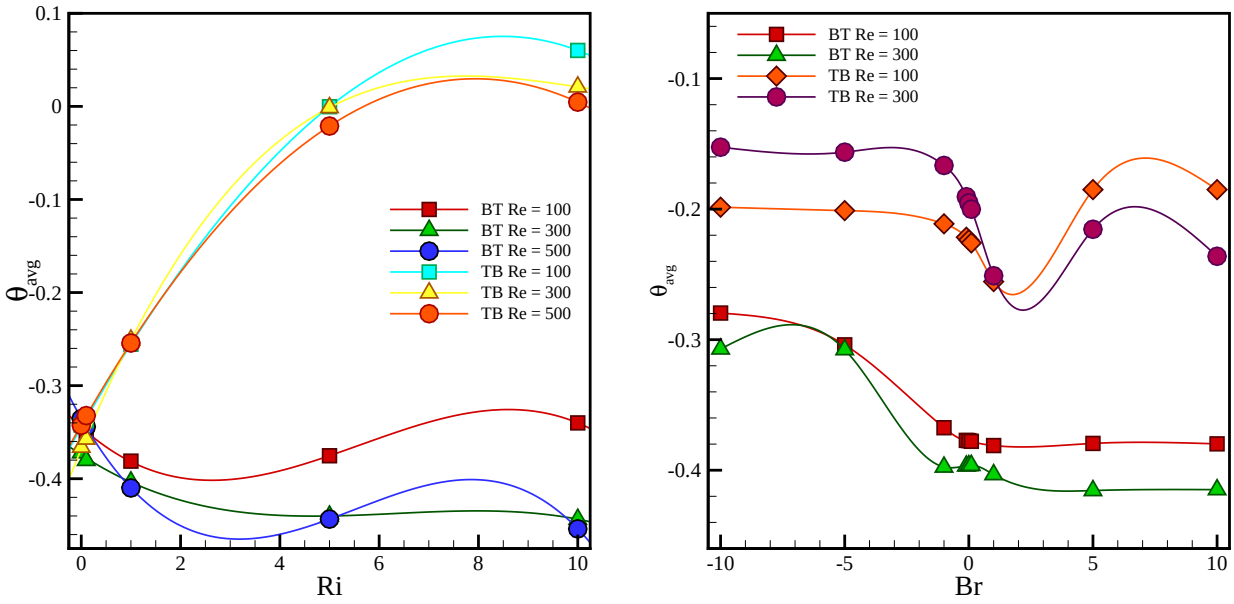

(a) (b)

Figure 6.20: Comparison of average temperature inside the enclosure due to the variation of (a) Richardson number with fixed $Br = 1.0$ and (b) buoyancy ratio with fixed $Ri = 1.0$ at different Reynolds number for both cases.

obvious that cooling effects will be increased by increasing the volume of cold air inside the enclosure. This indicates less pronounced convection mode in the fluid where minimum temperature is obtained for higher values of the Reynolds number ($Re \geq 300$). In case of TB-configuration, the hot air is moving towards the upper section and gathered near the upper wall of the enclosure due to which the average temperature of the enclosure became higher. Average temperature is sharply increasing with the increase in Richardson number for TB-configuration due to increased temperature of the heat source. Maximum cooling i.e., minimum average temperature inside the enclosure is obtained for the BT-configuration corresponding to higher Reynolds number ($Re \geq 300$) due to the dominance of forced convection effect and location of the outlet port. At $Ri = 10.0$ (Fig. 6.20 (a)), a negative average temperature region enlarges near the left wall which means that the inlet fluid cools the substance there. Fig. 6.20 (b) shows that maximum cooling is obtained for positive values of Br in case of BT-configuration. The variation in cooling efficiency due to the changes in Richardson number and Reynolds number are shown in Fig. 6.21 (a) for

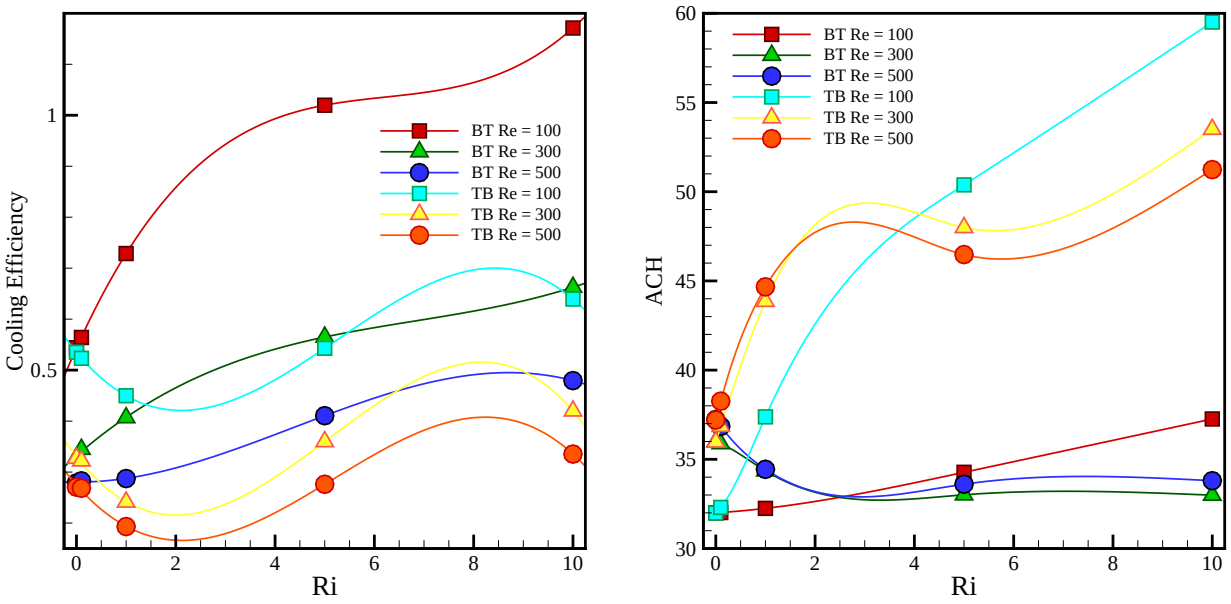

(a) (b)

Figure 6.21: Effect of Richardson number on (a) cooling efficiency and (b) air change per hour for different Reynolds number with fixed $Br = 1.0$ for both cases.

both configurations. Cooling efficiency is maximum in BT-configuration for $Re = 100$ due to mixed convection effects. An increase in Richardson number from 1.0 to 10.0 implies increasing cooling efficiency inside the enclosure, because the temperature difference inside the enclosure is increasing with the increase in Ri which accelerates the fluid velocity. It is observed that there exist a significant variation in average temperature of the enclosure with the variation of vented port locations for higher Reynolds number. Cooling efficiency is always higher in the BT-configuration compared to the TB-configuration for fixed value of flow parameters. Fig. 6.21 (b) shows a significant variation in air change per hour (ACH) due to change in Richardson number, Reynolds number and location of inlet and outlet port. The variation in ACH with the variation in Richardson number is observed to be higher in TB-configuration compared to the BT-configuration. For BT-configuration, ACH is higher for low Reynolds number corresponding to $Ri = 10.0$. Maximum value of ACH is obtained in case of the TB-configuration when $Ri \geq 5.0$ and $Re = 100$.

6.5 Conclusion

In this chapter, the ventilation of a simple room was investigated for two different geometrical models (BT and TB) considering the position of inlet and outlet ports. Three dimensional aspect of mixed convection is considered numerically for the effective cooling with the removal of heat and contaminants. Fresh cold air is considered to be infiltrated inside the enclosure through various ports of left vertical face and expelled through the outlet port placed along the right vertical face. The effect of Richardson number, Reynolds number and buoyancy ratio on fluid, heat and mass transfer phenomena has been visualized and summarized in the form of average Nusselt number, Sherwood number, entropy generation, cooling efficiency, performance evaluation criteria and air change per hour. Based on the above three-dimensional simulations, following remarks can be concluded:

1. The flow is dominated by mixed convection effects when Ri values shifts from 0.1 to 5.0. The heat transfer rate is also higher for higher values of the Richardson number.

2. Maximum heat transfer rate is found in the BT-configuration for higher Reynolds number due to forced convection dominated flow. But the minimum entropy is obtained in TB-configuration for low Reynolds number.

3. Higher values of Nu_{avg} is obtained for $Br = 10.0$ and minimum value of S_{avg} is obtained for $Br < 1.0$ for the BT-configuration.

4. For $Ri < 1.0$, maximum heat transfer rate with minimum entropy generation, i.e., maximum value of PEC is achieved for TB-configuration, and $Ri \geq 1.0$ produces maximum value of PEC for BT-configuration at $Re = 500$.

5. The heat and mass transfer irreversibility dominate the fluid friction irreversibility since Be_{avg} is greater than 0.85 for both cases.

6. The average rate of mass transfer is increasing with the increase in Richardson number as well as Reynolds number due to convection effects. The value of Sh_{avg} is maximum for TB-configuration corresponding to the higher values of Reynolds number, Richardson number and buoyancy ratio.

7. Maximum value of average temperature inside the enclosure is obtained for TB-configuration because the temperature of the fluid adjacent to the top surface becomes higher. Whereas, the BT-configuration provides maximum cooling inside the enclosure corresponding to higher Reynolds number.

8. The cooling efficiency is found to be higher for low values of Reynolds number in BT-configuration and the maximum value is achieved for $Ri = 10.0$.

Chapter 7

Summary and Future Scope

7.1 Overall Summary

This thesis dealt with the fluid flow, heat and mass transfer in slot-ventilated enclosures due to the presence of different discrete heat and contaminated sources/objects for Newtonian, viscous and incompressible fluids. Major contribution of this thesis includes:

- Effect of inlet and outlet port location on mixed convection with thermosolutal exchanger in ventilated system.
- Impact of positioning of thermo-contaminated block on heat and species transfer in an air filled ventilated enclosure.
- Investigation of mixed convection in a parallelogrammic shaped slot-ventilated system filled with discrete heat and contaminant (CO_2) sources.
- Removal of heat and airborne pollutants from a slot-ventilated enclosure due to wall heater and thermosoluted block using a chimney shaped outlet port.
- Three-dimensional parametric study of airflow, heat and mass transfer characteristics in a slot-ventilated enclosure.

In Chapter 2, the fluid flow, heat and mass transfer effects are studied inside a ventilated enclosure due to a thermo-solutally activated square block, embedded at the center of the enclosure. Two different configurations are considered by changing the locations of inlet and outlet port. The block is at higher temperature and concentration than those of inlet fluid which is at ambient temperature and concentration. The results for

flow, temperature and concentration are presented in terms of streamlines, isotherms and isoconcentrations with the variation of Richardson number, buoyancy ratio and Schmidt number. The average Nusselt number and Sherwood number around the block are calculated to find the effective variation of temperature that provides an insight on cooling efficiency factor of the enclosure. The simulated results shows that increment in Ri from 1.0 to 10.0 always produces an increment in average heat transfer rate, mass transfer rate and cooling efficiency for both the configurations due to convection effects. Last section of this chapter concludes that for $Br = 1.0$, maximum heat transfer rate is achieved in configuration-I, when the outlet is placed along the upper section of vertical wall.

In Chapter 3, a numerical study is conducted for the double diffusive mixed convection due to different locations and various aspect ratios of a thermo-contaminated block inside the ventilated enclosure. The block is maintained with higher temperature and species concentration compared to the injected cold fluid. Cooling efficiency inside the enclosure, average fluid temperature, heat and species transfer rate along the surface of the block are compared for different values of Richardson number, Reynolds number and buoyancy ratio to find the most suitable size and position of the block in order to obtain the maximum heat and mass transfer rate inside the enclosure. The simulated results concluded that block must be placed near the outlet port in upper section of the enclosure in order to obtain the maximum cooling inside the enclosure. Higher heat and mass transfer rates are achieved in case-II and case-V as compared to other cases corresponding to higher values of Reynolds number.

In Chapter 4, a numerical simulation is performed for mixed convection flow inside a parallelogrammic shaped ventilated enclosure with uniform discrete heat and contaminant (CO_2) sources. The horizontal walls of the enclosure are inclined at different angles with x-axis and their respective length is considered as of the order of vertical walls. Cold fresh air through the inlet port is considered at different locations of the left vertical wall and flush out through the outlet port along the right vertical wall. A suitable co-ordinate transformation is used to avoid the complicated interpolation of the data along the boundary points for the computational domain. The impact of inclination angle on average rate of heat transfer and mass transfer, average temperature, entropy generation, Bejan number, cooling efficiency and performance evaluation criterion inside the system

is discussed over a wide range of parameters. It is found that to obtain maximum cooling inside the enclosure, heat source must be kept along the right vertical wall, whereas for maximum heating, the heat source must be placed along the left vertical wall.

In Chapter 5, numerical study for slot-ventilated enclosure was presented for the removal of heat and contaminants generated due to wall heater and a thermosoluted object. Fresh cold air was considered to be infiltrated inside the enclosure through various ports of right vertical wall and an outlet chimney was placed along the upper wall inclined at various angles with x-axis to flush out the contaminated air. The effect of Richardson number, Reynolds number, inclination angle of outlet chimney and location of inlet port on fluid, heat and mass transfer phenomena was visualized and summarized through the average Nusselt number, Sherwood number, entropy generation, cooling efficiency, performance evaluation criteria and air change per hour. The results depicted that higher rates of heat and mass transfer were obtained in case-I for higher Reynolds number, but lower energy loss was obtained for low values of Reynolds number. Thus to achieve maximum heat transfer with minimum entropy generation, PEC (ratio of heat transfer to entropy generation) is calculated. It is found that, higher values of PEC is obtained for case-III corresponding to higher Reynolds number. In case of low Ri, maximum cooling inside the enclosure is achieved for case-I. Whereas for $Ri \geq 5.0$, maximum cooling is obtained in case-III.

In Chapter 6, a comparative numerical study for three dimensional characteristics of fluid flow, heat and contaminant transport in a slot-ventilated enclosure with the functionality of inlet and outlet opening system. Inflow of cold air was assumed through the left vertical wall that creates the mixed convection flow when combined with the buoyancy driven flow. Discrete heat sources and contaminant sources were considered along the right vertical wall and bottom wall, respectively. Three dimensional numerical study concerning airflow characteristics and cooling efficiency was made over a wide range of physical parameters namely, Reynolds number, Richardson number and buoyancy ratio to maximize the removal rate of heat and contaminants. The trends of thermal Nusselt number, species Sherwood number, entropy generation, Bejan number, average temperature, cooling efficiency, air change per hour and performance evaluation criterion inside the system were evaluated to find the impact of inflow and outflow port locations. The

results show that the removal rate of heat and mass transfer is increased with the increment of Reynolds number for both these cases. It is important to mention here that, BT-configuration provides the maximum cooling inside the enclosure for higher Reynolds number, whereas maximum heating inside the enclosure is obtained for TB-configuration because the temperature of the fluid adjacent to the top surface becomes higher. Hence, for cooling purpose, outlet port must be placed in the upper section of vertical walls.

7.2 Future Scope

In this thesis, the study is restricted to mixed convection in slot-ventilated enclosures for laminar flow. However, this work can be extended for natural ventilation considering turbulent flow. In addition, mixed convection study is restricted within regular computational domains due to its simplicity, that can also be extended for irregular computational domains. We can highlight some of the proposed extensions of the work made in the thesis are as follows:

- The present study for thermosoluted block can be extended for multiple thermosoluted objects in a ventilated enclosure with different combinations of inlet and outlet ports.
- The effect of flow turbulence on heat transfer in a ventilated enclosure with CO_2 contaminant source.
- Three dimensional numerical simulation of slot-ventilated enclosure due to the presence of thermosoluted blocks.
- Numerical study of mixed convection in a ventilated cavity utilizing nanofluids.
- Parametric study of mixed convection in an open channel with discrete heat and contaminant sources.

Appendix A

Successive Over Relaxation (SOR)

The relaxation technique is a finite-difference method particularly suited for the solution of elliptic partial differential equations. Successive over-relaxation (SOR) is a technique which can be used in an attempt to accelerate any iteration procedure but we will propose it here primarily as a refinement to the Gauss-Seidel method. As we apply Gauss-Seidel iteration to a system of simultaneous algebraic equation, we expect to make several recalculations or iterations before convergence to an acceptable level is achieved. A major disadvantage of the otherwise attractive Gauss-Seidel method is that its convergence is too slow, especially when a large number of grid points are involved. The reason for the slowness is easy to understand; the method transmits the boundary condition information at a rate of one grid interval per iteration.

In the iterative solution of the algebraic equation or in the overall iterative scheme employed for handing nonlinearity, it is often desirable to speed up or to slow down the changes. This process is called over-relaxation or under-relaxation depending on whether the variable changes are accelerated or slowed down. An arbitrary correction to the intermediate values of the unknowns from any iteration procedure according to the form

$$u_{i,j}^{n+1'} = \omega u_{i,j}^{n+1} + (1-\omega) u_{i,j}^{n'} \tag{A.1}$$

is known as over-relaxation or successive over-relaxation (SOR).

Here, n denotes iteration level and $u_{i,j}^{n+1}$ is the most recent value of $u_{i,j}$ calculated from the Gauss-Seidel procedure, $u_{i,j}^{n'}$ is the value from the previous iteration as a adjusted

by previous application of this formula if the over-relaxation is being applied successively and $u_{i,j}^{n+1'}$ is newly adjusted for $u_{i,j}$ at the $n+1$ iteration level. ω is the relaxation parameter whose value is usually found by trail-and-error experimentation for a given problem. For over-relaxation, generally the value of ω is bounded by $1 < \omega < 2$ and for under-relaxation, ω is bounded by $0 < \omega < 1$.

Appendix B

Tridiagonal Matrix Algorithm (TDMA)

Suppose we have to solve a linear system of algebraic equations

$$AV = D \tag{B.1}$$

where

$$A = \begin{bmatrix} b_1 & c_1 & & & & & \\ a_2 & b_2 & c_2 & & & & \\ & . & . & . & & & \\ & & a_i & b_i & c_i & & \\ & & & . & . & . & \\ & & & & a_{N-1} & b_{N-1} & c_{N-1} \\ & & & & & a_N & b_N \end{bmatrix}$$

is a $N \times N$ tri-diagonal matrix,

$$V = \begin{bmatrix} v_1 \\ v_2 \\ . \\ v_i \\ . \\ v_{N-1} \\ v_N \end{bmatrix}$$

is the vector of unknowns and

$$D = \begin{bmatrix} d_1 \\ d_2 \\ . \\ d_i \\ . \\ d_{N-1} \\ d_N \end{bmatrix}$$

is the known vector. All elements in A, other than those shown, are zero.

The Thomas algorithm for solving (B.1) consists of two parts. First (B.1) is manipulated into the form

$$\begin{bmatrix} 1 & c_1^1 & & & & & \\ & 1 & c_2^1 & & & & \\ & & . & . & & & \\ & & & 1 & c_i^1 & & \\ & & & & . & . & \\ & & & & & 1 & c_{N-1}^1 \\ & & & & & & 1 \end{bmatrix} \begin{bmatrix} v_1 \\ v_2 \\ . \\ v_i \\ . \\ v_{N-1} \\ v_N \end{bmatrix} = \begin{bmatrix} d_1^1 \\ d_2^1 \\ . \\ d_i^1 \\ . \\ d_{N-1}^1 \\ d_N^1 \end{bmatrix}$$

i.e., the a_i coefficients have been eliminated and the b_i coefficients normalized to unity. For the first equation

$$c_1^1 = \frac{c_1}{b_1}, d_1^1 = \frac{d_1}{b_1}$$

and for the general equation

$$c_i^1 = \frac{c_i}{b_i - a_i c_{i-1}^1}, d_i^1 = \frac{d_i - a_i d_{i-1}^1}{b_i - a_i c_{i-1}^1}. \tag{B.2}$$

The equation are modified as in (B.2). The second stage consists of a back substitution

$$v_N = d_N^1, v_i = d_i^1 - v_{i+1} c_i^1.$$

The Thomas algorithm is particularly economical, it requires only $5N - 4$ operations (multiplications and divisions). But to present ill conditioning, it is necessary that

$$\mid b_i \mid > \mid a_i \mid + \mid c_i \mid$$

Appendix C

Block Tridiagonal Matrix Algorithm (Varga's Algorithm)

A block tri-diagonal system of equations can be written as

$$\overline{AV} = \overline{D} \tag{7.1}$$

where

$$\overline{A} = \begin{bmatrix} B_1 & C_1 & & & & \\ A_2 & B_2 & C_2 & & & \\ & . & . & . & & \\ & & A_i & B_i & C_i & \\ & & . & . & . & \\ & & & A_{N-1} & B_{N-1} & C_{N-1} \\ & & & & A_N & B_N \end{bmatrix}$$

is a block tri-diagonal matrix, each element being a third order square matrix. Let

$$V_1 = (0,0,0)^T, \quad V_N = (0,0,0)^T$$

$$\overline{V} = (V_2, V_3, ..., V_{N-1})^T$$

is the vector of unknowns vectors and

$$\overline{D} = (D_2, D_3, ..., D_{N-1})^T$$

is the vector of known vectors. The matrix equation $(D.1)$ can be solved using Varga's Algorithm.

The algorithm is as follows

$$V_n = -E_n V_{n+1} + J_n, \qquad 2 \leq n \leq N-1$$

where

$$E_n = (B_n - A_n E_{n-1})^{-1} C_n, \qquad 2 \leq n \leq N-1$$

$$J_n = (B_n - A_n E_{n-1})^{-1} (D_n - A_n J_{n-1}), \qquad 2 \leq n \leq N-1$$

$$E_1 = E_N = \begin{bmatrix} 0 & 0 & 0 \\ 0 & 0 & 0 \\ 0 & 0 & 0 \end{bmatrix}$$

$$J_1 = V_1, \quad J_N = V_N$$

Bibliography

[1] Adamu, G. and Sinha, P.: 2012, Thermal and roughness effects in a tilted pad slider bearing considering heat conduction through the pad and slider, *Proceedings of the National Academy of Sciences, India Section A: Physical Sciences* **82**(4), 323–333.

[2] Al-Rashed, A. A., Oztop, H. F., Kolsi, L., Boudjemline, A., Almeshaal, M. A., Ali, M. E. and Chamkha, A.: 2019, CFD study of heat and mass transfer and entropy generation in a 3D solar distiller heated by an internal column, *International Journal of Mechanical Sciences* **152**, 280–288.

[3] Anderson, D. A., Tannehill, J. C. and Pletcher, R. H.: 1984, *Computational fluid dynamics and heat transfer*, Hemisphere, Washington.

[4] Anderson, J.: 1995, *Computational fluid dynamics: the basics with applications*, McGrawhill Inc, New York.

[5] Aouachria, Z., Haddad, D. and Benzemit, F.: 2015, Double diffusion effects on entropy generation in convective heat and mass transfer, *Progress in Clean Energy: Analysis and Modeling* **1, chapter 31**, 433–447.

[6] Bairi, A.: 2008, On the nusselt number definition adapted to natural convection in parallelogrammic cavities, *Applied Thermal Engineering* **28**, 1267–1271.

[7] Bairi, A.: 2011, Transient free convection in passive buildings using 2D air-filled parallelogram-shaped enclosures with discrete isothermal heat sources, *Energy and Buildings* **43**, 366–373.

[8] Bairi, A.: 2013, Correlations for transient natural convection in parallelogrammic enclosures with isothermal hot wall, *Applied Thermal Engineering* **51**, 833–838.

[9] Bairi, A., Garcia de Maria, J. and Laraqi, N.: 2010, Transient natural convection in parallelogrammic enclosures with isothermal hot wall. experimental and numerical study applied to on-board electronics, *Applied Thermal Engineering* **30**, 1115–1125.

[10] Bairi, A., Zarco-Pernia, E. and Garcia de Maria, J.-M.: 2014, A review on natural convection in enclosures for engineering applications. the particular case of the parallelogrammic diode cavity, *Applied Thermal Engineering* **63**, 304–322.

[11] Baker, A. J.: 1983, *Finite element computational fluid mechanics*, Taylor & Francis US.

[12] Basak, T., Roy, S., Sharma, P. K. and Pop, I.: 2009, Analysis of mixed convection flows within a square cavity with linearly heated side wall (s), *International Journal of Heat and Mass Transfer* **52**(9-10), 2224–2242.

[13] Basak, T., Roy, S., Singh, A. and Balakrishnan, A.: 2009, Natural convection flows in porous trapezoidal enclosures with various inclination angles, *International Journal of heat and mass transfer* **52**, 4612–4623.

[14] Bassiouny, R. and Korah, N. S.: 2009, Effect of solar chimney inclination angle on space flow pattern and ventilation rate, *Energy and Buildings* **41**, 190–196.

[15] Beg, O., Bakier, A., Prasad, R. and Ghosh, S.: 2011, Numerical modelling of non-similar mixed convection heat and species transfer along an inclined solar energy collector surface with cross diffusion effects, *World Journal of mechanics* **1**, 185–196.

[16] Bejan, A.: 1987, The thermodynamic design of heat and mass transfer processes and devices, *International Journal of Heat and Mass transfer* **8**(4), 258–276.

[17] Bejan, A.: 1996, *Entropy Generation Minimization: The Method of Thermodynamic Optimization of Finite-Size Systems and Finite-Time Processes*, CRC Press, Boca Raton, FL.

[18] Bhattacharyya, S., Maiti, D. and Dhinakaran, S.: 2006, Influence of buoyancy on vortex shedding and heat transfer from a square cylinder in proximity to a wall, *Numerical Heat Transfer, Part A: Applications* **50**(6), 585–606.

[19] Biegger, C. and Weigand, B.: 2015, Flow and heat transfer measurements in a swirl chamber with different outlet geometries, *Experiments in Fluids* **56**(4), 78.

[20] Biswas, N., Mahapatra, P. S. and Manna, N. K.: 2015, Thermal management of heating element in a ventilated enclosure, *International Communications in heat and Mass Transfer* **66**, 84–92.

[21] Bolster, D. T. and Linden, P. F.: 2007, Contaminants in ventilated filling boxes, *Journal of Fluid Mechanics* **591**, 97–116.

[22] Bouabid, M., Hidouri, N., Magherbi, M. and Brahim, A.: 2011, Analysis of the magnetic field effect on entropy generation at thermosolutal convection in a square cavity, *Entropy* **13**, 1034–1054.

[23] Chamkha, A. J., Hussain, S. H. and Abd-Amer, Q. R.: 2011, Mixed convection heat transfer of air inside a square vented cavity with a heated horizontal square cylinder, *Numerical Heat Transfer, Part A: Applications* **59**(1), 58–79.

[24] Chorin, A. J.: 1967, A numerical method for solving incompressible viscous flow problems, *Journal of computational physics* **2**(1), 12–26.

[25] Chung, T.: 1978, Finite element analysis in fluid dynamics, *NASA STI/Recon Technical Report A* **78**.

[26] Costa, V.: 2004, Double-diffusive natural convection in parallelogrammic enclosures, *International journal of Heat and Mass transfer* **47**, 2913–2926.

[27] Crespy, A., Boleve, A. and Revil, A.: 2007, Influence of the dukhin and reynolds numbers on the apparent zeta potential of granular porous media, *Journal of Colloid and Interface Science* **305**(1), 188–194.

[28] Deepika, N. and Narayana, P.: 2016, Nonlinear stability of double-diffusive convection in a porous layer with throughflow and concentration based internal heat source, *Transport in Porous Media* **111**(3), 751–762.

[29] Deng, Q.-H., Zhou, J., Mei, C. and Shen, Y.-M.: 2004, Fluid, heat and contaminant transport structures of laminar double-diffusive mixed convection in a two-dimensional ventilated enclosure, *International Journal of Heat and Mass Transfer* **47**(24), 5257–5269.

[30] Deresse, G. A. and Sinha, P.: 2011, Thd analysis for finite slider bearing with roughness: special reference to load generation in parallel sliders, *Acta mechanica* **222**(1-2), 1–15.

[31] Doghmi, H., Abourida, B., Belarche, L., Sannad, M. and Ouzaouit, M.: 2018, Numerical study of mixed convection inside a three-dimensional ventilated cavity in the presence of an isothermal heating block, *International Journal of Heat and Technology* **36**(2), 447–456.

[32] Famouri, M. and Hooman, K.: 2008, Entropy generation for natural convection by heated partitions in a cavity, *International Communications in Heat and Mass Transfer* **35**(4), 492–502.

[33] Fechter, S., Terzis, A., Ott, P., Weigand, B., Von Wolfersdorf, J. and Cochet, M.: 2013, Experimental and numerical investigation of narrow impingement cooling channels, *International Journal of Heat and Mass Transfer* **67**, 1208–1219.

[34] Ferziger, J. H. and Peric, M.: 1996, *Computational methods for fluid dynamics*, Springer-Verlag, New York.

[35] Fletcher, C.: 1991, *Computational techniques for fluid dynamics-I & II*, Springer-Verlag, Berlin Heidelberg.

[36] Frederick, R.: 1997, Natural convection heat transfer in a cubical enclosure with two active sectors on one vertical wall, *International Communications in Heat and Mass Transfer* **24**(4), 507–520.

[37] Frederick, R. L. and Quiroz, F.: 2001, On the transition from conduction to convection regime in a cubical enclosure with a partially heated wall, *International journal of Heat and Mass Transfer* **44**(9), 1699–1709.

[38] Garcia de Maria, J., Bairi, A. and Costa, V.: 2010, Empirical correlations at high Ra for steady-state free convection in 2D air-filled parallelogrammic enclosures with isothermal discrete heat sources, *International Journal of heat and mass transfer* **53**, 3831–3838.

[39] Gebhart, B. and Pera, L.: 1971, The nature of vertical natural convection flows resulting from the combined buoyancy effects of thermal and mass diffusion, *International journal of Heat and Mass transfer* **14**, 2025–2050.

[40] Ghachem, K., Kolsi, L., Maatki, C., Hussein, A. and Borjini, M.: 2012, Numerical simulation of three-dimensional double diffusive free convection flow and irreversibility studies in a solar distiller, *International Communications in Heat and Mass Transfer* **39**, 869–876.

[41] Gualtieri, C., Angeloudis, A., Bombardelli, F., Jha, S. and Stoesser, T.: 2017, On the values for the turbulent schmidt number in environmental flows, *Fluids* **2**(2), 17.

[42] Gupta, N. and Nayak, A. K.: 2018, Effects of heat induced pollutants due to thermosolutal exchanger in ventilation system, *Journal of Thermophysics and Heat Transfer* **32**(1), 172–183.

[43] Gupta, S. K., Chatterjee, D. and Mondal, B.: 2014, Investigation of mixed convection in a ventilated cavity in the presence of a heat conducting circular cylinder, *Numerical Heat Transfer, Part A: Applications* **67**(1), 52–74.

[44] Guta, L. and Sundar, S.: 2010, Navier-stokes-brinkman system for interaction of viscous waves with a submerged porous structure, *Tamkang journal of mathematics* **41**(3), 217–243.

[45] He, G., Yang, X. and Srebric, J.: 2005, Removal of contaminants released from room surfaces by displacement and mixing ventilation: modeling and validation, *Indoor air* **15**(5), 367–380.

[46] Hirt, C.: 1975, A numerical solution algorithm for transient fluid flow, *Los Alamos Scientific Laboratory Report* .

[47] Hsu, T. and How, S.: 1999, Mixed convection in an enclosure with a heat-conducting body, *Acta Mechanica* **133**, 87–104.

[48] Hyun, H. and Choi, B.: 1990, Transient natural convection in a parallelogram-shaped enclosure, *International Journal of heat and Fluid Flow* **11**(2), 129–134.

[49] Inman, W. S.: 1835, *Report of the committee of the house of Commons, on ventilation, warming and transmission of sound*, London: John Weale, Architectural Library, 59, High Holborn.

[50] Issa, R. I.: 1986, Solution of the implicitly discretised fluid flow equations by operator-splitting, *Journal of computational physics* **62**(1), 40–65.

[51] Iwatsu, R. and Hyun, J. M.: 1995, Three-dimensional driven-cavity flows with a vertical temperature gradient, *International journal of Heat and Mass Transfer* **38**(18), 3319–3328.

[52] Jardani, A., Revil, A., Slob, E. and Söllner, W.: 2010, Stochastic joint inversion of 2d seismic and seismoelectric signals in linear poroelastic materials: A numerical investigation, *Geophysics* **75**(1), N19–N31.

[53] Jerry, A. E., Hidouri, N., Magherbi, M. and Brahim, A. B.: 2010, Effect of an external oriented magnetic field on entropy generation in natural convection, *Entropy* **12**, 1391–1417.

[54] Kaluri, R. S., Basak, T. and Roy, S.: 2010, Heatline approach for visualization of heat flow and efficient thermal mixing with discrete heat sources, *International Journal of Heat and Mass Transfer* **53**(15-16), 3241–3261.

[55] Karimi, F., Xu, H., Wang, Z. and Yang, M.: 2014, Numerical simulation of steady mixed convection around two heated circular cylinders in a square enclosure, *Heat transfer Engineering* **37**(1), 64–75.

[56] Khanal, R. and Lei, C.: 2015, A numerical investigation of buoyancy induced turbulent air flow in an inclined passive wall solar chimney for natural ventilation, *Energy and Buildings* **93**, 217–226.

[57] Koufi, L., Younsi, Z., Cherif, Y. and Naji, H.: 2017, Numerical investigation of turbulent mixed convection in an open cavity: Effect of inlet and outlet openings, *International Journal of Thermal Sciences* **116**, 103–117.

[58] Kumar, D. S., Murugesan, K. and Thomas, H. R.: 2011, Effect of the aspect ratio of a heated block on the interaction between inertial and thermosolutal buoyancy forces in a lid-driven cavity, *Numerical Heat Transfer, Part A: Applications* **60**(7), 604–628.

[59] Liu, D., Zhao, F.-Y. and Tang, G.-F.: 2008, Numerical analysis of two contaminants removal from a three-dimensional cavity, *International journal of Heat and Mass Transfer* **51**(1), 378–382.

[60] Liu, D., Zhao, F.-Y., Yang, H., Chen, J. and Ye, C.: 2016, Probability adjoint identification of airborne pollutant sources depending on one sensor in a ventilated enclosure with conjugate heat and species transports, *International Journal of Heat and Mass Transfer* **102**, 919–933.

[61] Lomax, H., Pulliam, T. H. and Zingg, D. W.: 2013, *Fundamentals of computational fluid dynamics*, Springer-Verlag, New York.

[62] Madadi, R. and Balaji, C.: 2008, Optimization of the location of multiple discrete heat sources in a ventilated cavity using artificial neural networks and micro genetic algorithm, *International Journal of Heat and Mass Transfer* **51**, 2299–2312.

[63] Mahanta, G. and Shaw, S.: 2015, 3D casson fluid flow past a porous linearly stretching sheet with convective boundary condition, *Alexandria Engineering Journal* **54**(3), 653–659.

[64] Maiti, D., Gupta, A. and Bhattacharyya, S.: 2008, Stable/unstable stratification in thermosolutal convection in a square cavity, *Journal of Heat Transfer* **130**(12), 122001.

[65] Maiti, D. K.: 2011, Numerical study on heat/mass transfer by shear/thermal/solutal-convection in a cavity under counteracting buoyancies, *Heat and mass transfer* **47**(3), 245–257.

[66] Maiti, D. K. and Bhatt, R.: 2014, Numerical study on flow and aerodynamic characteristics: Square cylinder and eddy-promoting rectangular cylinder in tandem near wall, *Aerospace Science and Technology* **36**, 5–20.

[67] Malik, S. and Nayak, A.: 2017, Mhd convection and entropy generation of nanofluid in a porous enclosure with sinusoidal heating, *International Journal of Heat and Mass Transfer* **111**, 329–345.

[68] Mamum, M., Rahman, M., Billah, M. and Saidur, R.: 2010, A numerical study on the effect of a heated hollow cylinder on mixed convection in a ventilated cavity, *International Communications in Heat and Mass Transfer* **37**(9), 1326–1334.

[69] Matle, S. and Sundar, S.: 2012a, A 2D finite element study on the flow pattern and temperature distribution for an isothermal spherical furnace with the aperture, *Open Journal of Applied Sciences* **2**(04), 319.

[70] Matle, S. and Sundar, S.: 2012b, Axi symmetric 2d simulation and numerical heat transfer characteristics for the calibration furnace in a rectangular enclosure, *Applied Mathematical Modelling* **36**(3), 878–893.

[71] Matta, A., Narayana, P. and Hill, A. A.: 2016, Nonlinear thermal instability in a horizontal porous layer with an internal heat source and mass flow, *Acta Mechanica* **227**(6), 1743–1751.

[72] Minaei, A., Ashjaee, M. and Goharkhah, M.: 2014, Experimental and numerical study of mixed and natural convection in an enclosure with a discrete heat sources and ventilation ports, *Heat transfer Engenering* **35**(1), 63–73.

[73] Moallemi, M. and Jang, K.: 1992, Prandtl number effects on laminar mixed convection heat transfer in a lid-driven cavity, *International Journal of Heat and Mass Transfer* **35**(8), 1881–1892.

[74] Montazeri, H. and Montazeri, F.: 2018, CFD simulation of cross-ventilation in buildings using rooftop windcatchers: Impact of outlet openings, *Renewable Energy* **118**, 502–520.

[75] Moraga, N. O. and Lopez, S. E.: 2004, Numerical simulation of three-dimensional mixed convection in an air-cooled cavity, *Numerical Heat Transfer, Part A: Applications* **45**(8), 811–824.

[76] Mourad, M., Hassen, A., Nejib, H. and Ammar, B.: 2006, Second law analysis in convective heat and mass transfer, *Entropy* **8**(1), 1–17.

[77] Navier, C.: 1823, Mémoire sur les lois du mouvement des fluides, *Mémoires de lAcadémie Royale des Sciences de lInstitut de France* **6**, 389–440.

[78] Nayak, A., Jena, P. and Narayana, P. L.: 2014, Flow simulation and mixed convection in a lid-driven square cavity with saturated porous media, *Journal of Porous Media* **17**(6).

[79] Nayak, A. K. and Bhattacharyya, S.: 2012, Double-diffusive convection in a cubical lid-driven cavity with opposing temperature and concentration gradients, *Theoretical and Computational Fluid Dynamics* **26**(6), 565–581.

[80] Nayak, M., Shaw, S. and Chamkha, A. J.: 2017, Impact of variable magnetic field and convective boundary condition on a stretched 3D radiative flow of Cu-H2O Nanofluid, *Advances in Modelling and Analysis A* **86**(3), 658–678.

[81] Nayak, R., Bhattacharyya, S. and Pop, I.: 2015, Numerical study on mixed convection and entropy generation of Cuwater nanofluid in a differentially heated skewed enclosure, *International journal of Heat and Mass transfer* **85**, 620–634.

[82] Nazari, M., Louhghalam, L. and Kayhani, M.: 2015, Lattice boltzmann simulation of double diffusive natural convection in a square cavity with a hot square obstacle, *Chinese Journal of Chemical Engineering* **23**, 22–30.

[83] Nikbakhti, R. and Khodakhah, J.: 2016, Numerical investigation of double diffusive buoyancy forces induced natural convection in a cavity partially heated and cooled from sidewalls, *Engineering Science and Technology, an International Journal* **19**, 322–337.

[84] Oden, J. T.: 1972, Finite elements of nonlinear continua.

[85] Omri, A. and Nasrallah, S.: 1999, Control volume finite element numerical simulation of mixed convection in an air-cooled cavity, *Numerical Heat transfer Part A: Applications* **36**(6), 615–637.

[86] Patankar, S.: 1980, *Numerical heat transfer and fluid flow*, Hemisphere, Washington, DC.

[87] Patil, P., Pop, I. and Roy, S.: 2012, Unsteady heat and mass transfer over a vertical stretching sheet in a parallel free stream with variable wall temperature and concentration, *Numerical Methods for Partial Differential Equations* **28**(3), 926–941.

[88] Peyret, R. and Taylor, T. D.: 1986, *Computational methods for fluid flow*, Springer Series in Computational Physics (Springer, New York, 1983).

[89] Radhakrishnan, T., Balaji, C. and Venkateshan, S.: 2010, Optimization of multiple heaters in a vented enclosure-a combined numberical and experimental study, *International journal of Thermal Sciences* **49**, 721–732.

[90] Radhakrishnan, T., Verma, A., Balaji, C. and Venkateshan, S.: 2007, An experimental and numerical investigation of mixed convection from a heat generating element in a ventilated cavity, *Experimental thermal and Fluid Science* **32**, 502–520.

[91] Rahman, M., Alim, M., Saha, S. and Chowdhury, M.: 2008a, Mixed convection in a vented square cavity with a heat conducting horizontal solid circular cylinder, *Journal of naval architecture and marine engineering* **5**(2), 37–46.

[92] Rahman, M., Alim, M., Saha, S. and Chowdhury, M.: 2008b, A numerical study of mixed convection in a square cavity with a heat conducting square cylinder at different locations, *Journal of Mechanical Engineering* **ME39**(2), 78–85.

[93] Rahman, M., Parvin, S., Rahim, N., Islam, M., Saidur, R. and Hasanuzzaman, M.: 2012, Effects of reynolds and prandtl number on mixed convection in a ventilated cavity with a heat-generating solid circular block, *Applied Mathematical Modelling* **36**, 2056–2066.

[94] RamReddy, C., Narayana, P. L. and Motsa, S. S.: 2015, A spectral relaxation method for linear and non-linear stratification effects on mixed convection in a porous medium, *Applied Mathematics and Computation* **268**, 991–1000.

[95] Ren, X.-H., Hu, J.-T., Liu, D., Zhao, F.-Y., Li, X.-H. and Wang, H.-Q.: 2016, Combined convective heat and airborne pollutant removals in a slot vented enclosure under different flow schemes: Parametric investigations and non unique flow solutions, *Applied Thermal Engineering* **94**, 159–169.

[96] Ren, X., Hu, J., Liu, D., Liu, C., Zhao, F. and Wang, H.: 2017, Heterogeneous convective thermal and airborne pollutant removalsfrom a partial building enclosure with a conducting baffle: Parametricinvestigations and steady transition flow solutions, *Energy and Buildings* **138**, 280–300.

[97] Revil, A.: 2007, Thermodynamics of ions and water transport in porous media, *Journal of colloid and interface science* **307**(1), 254–264.

[98] Roy, M., Basak, T., Roy, S. and Pop, I.: 2015, Analysis of entropy generation on mixed convection in square enclosures for various thermal boundary conditions, *Numerical Heat transfer, Part A: Applications* **68**, 44–74.

[99] Roy, M., Roy, S. and Basak, T.: 2015, Analysis of entropy generation on mixed convection in a square enclosures for various horizontal or vertical moving wall(s), *International Communications in Heat and mass transfer* **68**, 258–266.

[100] Selimefendigil, F. and Oztop, H. F.: 2014a, Effects of an adiabatic fin on the mixed convection heat transfer in a square cavity with two ventilation ports, *Thermal Science* **18**(2).

[101] Selimefendigil, F. and Öztop, H. F.: 2014b, Numerical investigation and dynamical analysis of mixed convection in a vented cavity with pulsating flow, *Computers & Fluids* **91**, 57–67.

[102] Selimefendigil, F. and Öztop, H. F.: 2015, Effects of phase shift on the heat transfer characteristics in pulsating mixed convection flow in a multiple vented cavity, *Applied Mathematical Modelling* **39**(13), 3666–3677.

[103] Sezai, I. and Mohamad, A. A.: 2000, Double diffusive convection in a cubic enclosure with opposing temperature and concentration gradients, *Physics of Fluids* **12**(9), 2210–2223.

[104] Shaw, S., Mahanta, G. and Sibanda, P.: 2016, Non-linear thermal convection in a casson fluid flow over a horizontal plate with convective boundary condition, *Alexandria Engineering Journal* **55**(2), 1295–1304.

[105] Shen, X., Zhou, J., Chang, V. W. and Yang, E.: 2016, Comparing mixing and displacement ventilation in tutorial rooms: Students' thermal comfort, sick building syndromes, and short-term performance, *Building and Environment* **102**, 128–137.

[106] Shuja, S., Yilbas, B. and Iqbal, M.: 2000, Mixed convection in a square cavity due to heat generating rectangular body: Effect of cavity exit port locations, *International Journal of Numerical Methods for Heat and Fluid flow* **10**(8), 824–841.

[107] Siddiqa, S., Abrar, M., Hossain, M. and Gorla, R.: 2017, Double diffusive natural convection flow over a wavy surface situated in a non-absorbing medium, *International Journal of Heat and Mass Transfer* **109**, 200–208.

[108] Singh, S. and Sharif, M.: 2003, Mixed convective cooling of a rectangular cavity with inlet and exit openings on differentially heated side walls, *Numerical Heat Transfer: Part A: Applications* **44**(3), 233–253.

[109] Sinha, P. and Adamu, G.: 2009, Thd analysis for slider bearing with roughness: special reference to load generation in parallel sliders, *Acta mechanica* **207**(1-2), 11–27.

[110] Smith, G. D.: 1985, *Numerical solution of partial differential equations: finite difference methods*, Oxford university press.

[111] Solsvik, J., Chao, Z. and Jakobsen, H. A.: 2014, Numerical evaluation of a one-dimensional two-fluid model applied to gas–solid cold-flows in fluidised beds, *The Canadian Journal of Chemical Engineering* **92**(3), 401–420.

[112] Solsvik, J., Chao, Z. and Jakobsen, H. A.: 2015, Modeling and simulation of bubbling fluidized bed reactors using a dynamic one-dimensional two-fluid model, *Advances in Engineering Software* **80**(C), 156–173.

[113] Solsvik, J., Sanchez, R. A., Chao, Z. and Jakobsen, H. A.: 2013, Simulations of steam methane reforming/sorption-enhanced steam methane reforming bubbling fluidized bed reactors by a dynamic one-dimensional two-fluid model: Implementation issues and model validation, *Industrial & Engineering Chemistry Research* **52**(11), 4202–4220.

[114] Stokes, G.: 1845, On the theories of the internal friction of fluids in motion, and of the equilibrium and motion of elastic solids, *Transactions of the Cambridge Philosophical Society* **8**, 287–305.

[115] Teodosiu, C., Rusaouen, G. and Hohota, R.: 2003, Influence of boundary conditions uncertainities on the simulation of ventilated enclosures, *Numerical Heat transfer Part A: Applications* **44**(5), 483–504.

[116] Tripathi, B. and Moulic, S.: 2007, Investigation of the buoyancy affected airflow patterns in the enclosure subjected at the different wall temperatures, *Energy and Building* **39**, 906–912.

[117] Venkateshwarlu, K., Nayak, A., Singh, B., Katiyar, V. and Gupta, N.: 2015, Thermosolutal mixed convection in an air filled ventilated enclosure with slot wise embedded heat and contaminant sources, *Journal of Heat transfer* **138**(3), 032501.

[118] VERSTEEG, H. and MALALASEKERA, W.: 1995, An introduction to computational fluid dynamics-the finite volume method, *Technical report*, Pearson Education Limited.

[119] Weigand, B., Schwartzkopff, T. and Sommer, T.: 2002, A numerical investigation of the heat transfer in a parallel plate channel with piecewise constant wall temperature boundary conditions, *Journal of heat transfer* **124**(4), 626–634.

[120] Xaman, J., Ortiz, A., Alvarez, G. and Chavez, Y.: 2011, Effect of a contaminant source (CO_2) on the air quality in a ventilated room, *Energy* **36**, 3302–3318.

[121] Xu, H., Xiao, R., Karimi, F., Yang, M. and Zhang, Y.: 2014, Numerical study of double diffusive mixed convection around a heated cylinder in an enclosure, *International journal of Thermal Sciences* **78**, 169–181.

[122] Xu, X., Wang, Z. Y., Karimi, F., Yang, M. and Zhang, Y.: 2014, Numerical simulation of double diffusive mixed convection in an open enclosure with different cylinder locations, *International Communications in Heat and Mass Transfer* **52**, 33–45.

[123] Yang, G., Weigand, B., Terzis, A., Weishaupt, K. and Helmig, R.: 2018, Numerical simulation of turbulent flow and heat transfer in a three-dimensional channel coupled with flow through porous structures, *Transport in Porous Media* **122**(1), 145–167.

[124] Yu, E. and Joshi, Y.: 1997, A numerical study of three-dimensional laminar natural convection in a vented enclosure, *International journal of Heat and Fluid Flow* **18**(6), 600–612.

[125] Zhang, D. D., Zhong, H., Liu, D., Zhao, F., Li, Y. and Wang, H. Q.: 2018, Multi-objective-oriented removal of airborne pollutants from a slot-ventilated enclosure subjected to mechanical and multicomponent buoyancy flows, *Applied mathematical modelling* **60**, 333–353.